Model-Based Processing in Ultrasound Imaging: Sparse Reconstruction and Coded Excitation

Doğan, D.

DOI
10.4233/uuid:00682d8e-de4b-4a7f-a311-ed4f721df7d4

Publication date
2025

Document Version
Final published version

Citation (APA)
Doğan, D. (2025). *Model-Based Processing in Ultrasound Imaging: Sparse Reconstruction and Coded Excitation*. [Dissertation (TU Delft), Delft University of Technology]. https://doi.org/10.4233/uuid:00682d8e-de4b-4a7f-a311-ed4f721df7d4

Important note
To cite this publication, please use the final published version (if applicable).
Please check the document version above.

Model-Based Processing in Ultrasound Imaging: Sparse Reconstruction and Coded Excitation

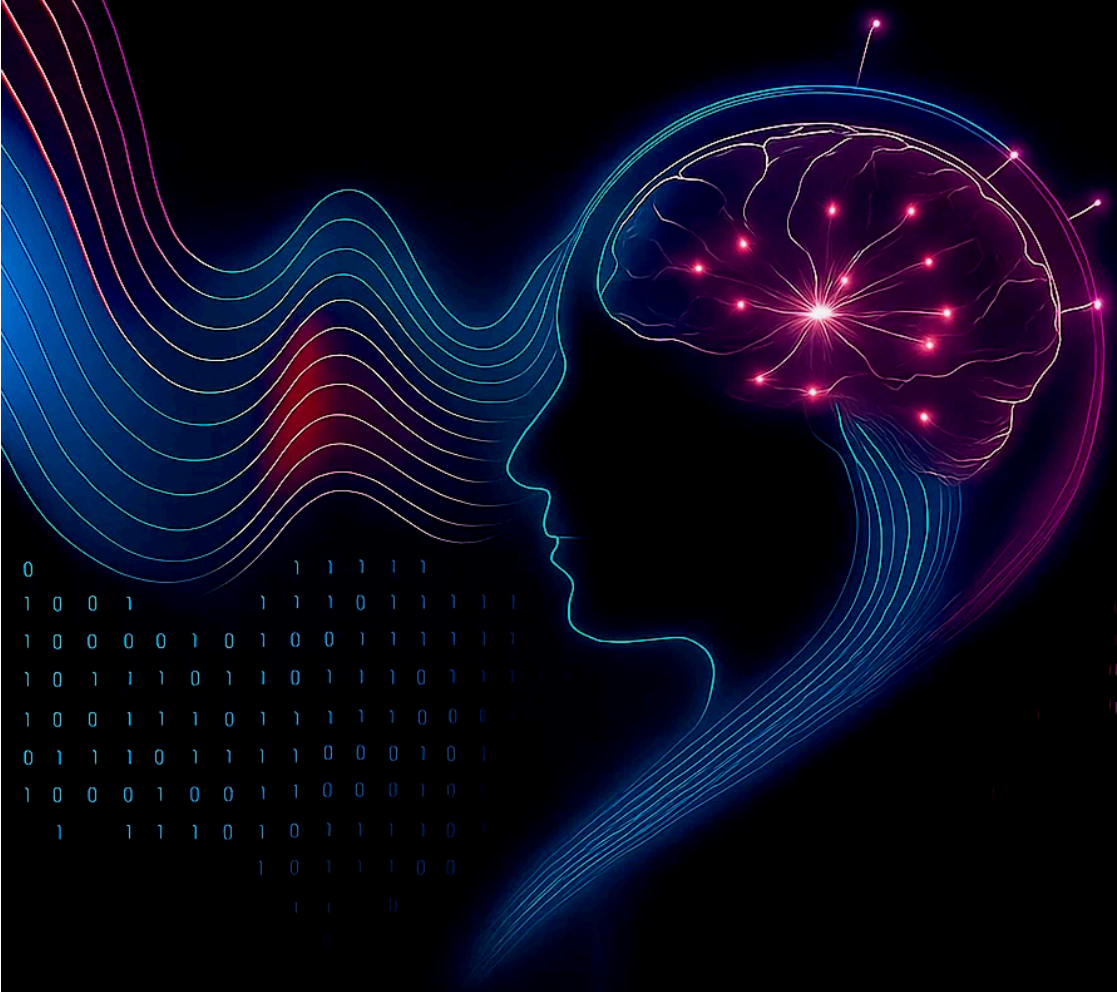

Didem Doğan

Model-Based Processing in Ultrasound Imaging: Sparse Reconstruction and Coded Excitation

Model-Based Processing in Ultrasound Imaging: Sparse Reconstruction and Coded Excitation

Dissertation

for the purpose of obtaining the degree of doctor
at Delft University of Technology
by the authority of the Rector Magnificus prof. dr. ir. T.H.J.J van der Hagen,
chair of the Board for Doctorates
to be defended publicly on
thursday 3 december 2025 at 17:30.

by

Didem Doğan

Master of Science in Electrical and Electronics Engineering
Orta Doğu Teknik Üniversitesi, Türkiye
born in Yozgat, Türkiye.

This Dissertation has been approved by the promotors.

Composition of the doctoral committee:

Rector Magnificus,	chairperson
Prof. dr. ir. G. J. T. Leus	Delft University of Technology, promotor
Dr. ir. P. Kruizinga	Erasmus University Medical Center, copromotor
Independent members:	
Prof. dr. ir. A. J. van der Veen	Delft University of Technology
Prof. dr. B. Cox	University College London
Prof. dr. P. Pal	University of California San Diego
Prof. dr. B. Rieger	Delft University of Technology
Dr. ir. R. J. G. van Sloun	Eindhoven University of Technology

Keywords: Model-based ultrasound imaging, sparse Bayesian learning, coded excitation

Front & Back: Cover art capturing the unintended parts of the work.

ISBN 978-94-6518-148-6

An electronic version of this dissertation is available at
http://repository.tudelft.nl/.

CONTENTS

SUMMARY

Ultrasound is a widely used real-time imaging modality to diagnose patients. Ultrasound imaging has several modes of operation such as ultrafast Doppler which, due to the high frame-rates, is particularly suited to image blood flow inside bodily organs such as the brain. Despite its success, the ultrafast imaging technique has some downsides such as lower overall signal-to-noise ratio (SNR), especially in deeper regions due to the use of unfocussed transmissions. This thesis explores the use of advanced signal processing methods such as model-based image reconstruction to regain some of the loss in SNR.

Chapters 3, 4, 5, and 6 of the thesis focus on advanced model-based image reconstruction techniques, incorporating complex priors or statistical assumptions about the signal and noise instead of using a simple physical propagation model. Conventional ultrasound beamforming techniques, such as the delay-and-sum (DAS) beamformer, perform well in many clinical settings; however, they face challenges in applications requiring high structural detail or SNR, such as vascular imaging. This thesis explores deterministic and statistical model-based vascular image reconstruction techniques to improve SNR, resolution, and clarity of fine vascular details. The proposed techniques exploit the joint sparsity of the vasculature images at different time instants. These methods enhance the depiction of vascular structures while increasing SNR and suppressing background noise and artifacts. A large part of the thesis, including Chapters 4, 5 and 6, focuses on the sparse Bayesian learning (SBL) techniques. Starting with classical SBL, this thesis introduces the application of block-sparsity-based SBL techniques, such as pattern-coupled sparse Bayesian learning with fixed-point iterations and correlated sparse Bayesian learning. Although some of the proposed techniques are not computationally efficient yet for real-time ultrasound imaging, they do provide a new contribution to signal processing and computational imaging fields.

Chapter 7 of the thesis focuses on improving the ultrasound transmission to enhance the SNR. An optimized coded excitation technique has been proposed as an alternative to standard coded excitation techniques. By keeping the computational complexity to a modest level, the codes are optimized to increase the SNR without a significant loss in the image resolution. The Cramér-Rao lower bound (CRB) minimization and a faster alternative Fisher information matrix (FIM) maximization have been proposed to optimize the codes. The optimized codes are tested on simulated data to demonstrate their potential for flow imaging.

To sum up, this thesis contributes to the ultrasound blood flow imaging area through solutions on image reconstruction algorithms and ultrasound transmissions to overcome current limitations and challenges. This thesis explores using advanced model-based signal processing methods to improve image quality. Therefore, this work contributes new strategies that can inspire future research and clinical applications in vascular ultrasound imaging.

SAMENVATTING

Echografie is een veelgebruikte real-time beeldvormingstechniek voor het stellen van diagnoses bij patiënten. Echobeelden kunnen op verschillende manieren worden verkregen, waaronder ultrageluid Doppler-technieken met een zeer hoge beeldsnelheid. Dankzij deze hoge frame rates is deze methode bijzonder geschikt om de bloedstroom in organen zoals de hersenen zichtbaar te maken. Ondanks het succes kent ultrageluid met hoge beeldsnelheid ook nadelen, zoals een lager signaal-ruisverhouding (SNR), vooral in diepere weefsels vanwege het gebruik van ongefocuste pulsen. In dit proefschrift wordt onderzocht hoe geavanceerde signaalverwerkingstechnieken, zoals modelgebaseerde beeldreconstructie, kunnen worden ingezet om het signaalverlies deels te compenseren.

Hoofdstukken 3, 4, 5 en 6 richten zich op geavanceerde modelgebaseerde reconstructietechnieken, waarbij complexe priors of statistische aannames over het signaal en de ruis worden gebruikt in plaats van een eenvoudig fysisch voortplantingsmodel. Traditionele beamforming-methoden zoals delay-and-sum (DAS) werken goed in veel klinische toepassingen, maar zijn beperkt bij beeldvorming die een hoge structurele resolutie of SNR vereist, zoals vasculaire beeldvorming. In dit proefschrift worden deterministische en statistische modelgebaseerde reconstructietechnieken voor vasculaire beeldvorming onderzocht om de SNR, resolutie en zichtbaarheid van fijne vaatstructuren te verbeteren. De voorgestelde methoden maken gebruik van de gezamenlijke sparsiteit van vasculaire beelden op verschillende tijdstippen. Deze aanpak verbetert de weergave van vaatstructuren en onderdrukt tegelijkertijd achtergrondruis en artefacten. Een groot deel van het proefschrift, met name hoofdstukken 4, 5 en 6, richt zich op sparse Bayesian learning (SBL). Beginnend met klassieke SBL introduceert dit proefschrift block-sparsity-gebaseerde SBL-technieken, zoals pattern-coupled sparse Bayesian learning met fixed-point iteraties en correlated sparse Bayesian learning. Hoewel sommige van deze technieken nog niet efficiënt genoeg zijn voor real-time echobeeldvorming, dragen ze wel bij aan de vakgebieden van signaalverwerking en computationele beeldvorming.

Hoofdstuk 7 richt zich op het verbeteren van ultrasone transmissies om de SNR te verhogen. Een geoptimaliseerde gecodeerde excitatie wordt voorgesteld als alternatief voor standaard gecodeerde excitatietechnieken. Met een bescheiden rekentijd worden de codes geoptimaliseerd om de SNR te verbeteren zonder noemenswaardig verlies aan resolutie. Optimalisatie wordt uitgevoerd via Cramér-Rao lower bound (CRB) minimalisatie en een snellere benadering op basis van de Fisher-informatiematrix (FIM). De geoptimaliseerde codes zijn getest op gesimuleerde data om hun potentieel voor flow imaging te laten zien.

Samenvattend draagt dit proefschrift bij aan het gebied van echografie van bloedstroming door oplossingen te bieden voor zowel beeldreconstructie-algoritmen als transmissietechnieken, met als doel bestaande beperkingen en uitdagingen te overwin-

nen. In dit werk wordt het gebruik van geavanceerde modelgebaseerde signaalverwerkingstechnieken onderzocht om de beeldkwaliteit te verbeteren. Daarmee biedt dit onderzoek nieuwe strategieën die toekomstige studies en klinische toepassingen in vasculaire echobeeldvorming kunnen inspireren.

1

INTRODUCTION

Ultrasound imaging is a critical tool in modern medicine, offering real-time visualization for accurate diagnosis and monitoring. In cardiovascular medicine, high-quality ultrasound scans can simplify the detection of anomalies. In maternal-fetal medicine, detailed images of the fetus help identify potential developmental issues in the baby. Furthermore, ultrasound imaging plays a significant role in medical research and daily patient care, providing valuable insights across various medical fields.

The demand for accurate and detailed ultrasound imaging motivates the advancements in image reconstruction techniques. Ultrasound imaging continues to rely heavily on traditional delay-and-sum (DAS) beamforming techniques [1], which offer reliable and efficient performance in many clinical settings. On the other hand, there is increasing interest in exploring model-based image reconstruction techniques [2, 3], which have the potential to enhance image quality and address challenges in specific applications, such as blood flow imaging [4, 5, 6, 7, 8]. These model-based methods aim to improve resolution and signal-to-noise ratio (SNR) by offering better detection of subtle features and enhancing the overall quality of images. Over time, ultrasound imaging research has explored various approaches, with model-based techniques gaining increasing attention as a promising alternative to traditional methods [9, 10, 11, 12, 13]. Model-based methods represent the ultrasound imaging process as a linear inverse problem, and they are flexible to incorporate deterministic or statistical prior knowledge in order to enhance the imaging of flow.

The formalization of the model/system matrix to be used for the inversion allows for a variety of well-developed signal processing techniques, such as least squares and compressive sensing. The latter has been studied by our group and enabled good reconstructions from fewer data samples [9, 10, 11, 12, 13]. Compressed sensing reduces the number of required measurements and the number of sensors; hence, the manufacturing costs of the devices become lower and the amount of data to transfer and process smaller, making real-time assessments more accessible. However, it causes a loss in image quality, such as SNR and resolution, due to the reduction in the number of measurements. While the DAS beamformer is not convenient for solving compressive ultrasound

imaging problems, model-based techniques offer a solution by incorporating prior information and optimization frameworks to regain or enhance the image reconstruction quality [2]. Overall, model-based ultrasound for compressive sensing is promising for improved diagnostic capabilities and broader clinical applications, in cases where the number of sensors pose a restriction such as for 3D imaging.

The advantage of the model-based approach is also shown when we consider the topic of coded excitation. Ultrasound imaging with coded excitation also exploits model-based imaging, especially when the codes do not have a standard structure. Previously, it has been shown that applying coded excitation techniques can enhance the SNR, resolution, and penetration depth in ultrasound imaging [14, 15, 16, 17]. Instead of using standard coding techniques such as Barker and Golay codes, random coding is an alternative method and provides benefits for improving the resolution [18]. However, DAS does not work optimally when each element in the transducer is excited with different pulses, as the interference between different pulses will result in incoherent summation and delay mismatch. Therefore, model-based beamforming is adopted, which exploits the linear system model. Besides, further innovative coding designs, such as optimized codes, require model-based imaging techniques.

1.1. RESEARCH MOTIVATION

In specific applications, particularly those involving compressive spatial coding, model-based ultrasound imaging methods can face limitations in achieving high spatial resolution, fine detail, or SNR [9, 10, 11]. In particular, compressive spatial coding for flow imaging may benefit from more specialized and advanced algorithms beyond matched filtering and least squares methods [12]. As the compressive scenarios typically do not align with the assumptions of DAS beamforming, exploring model-based techniques becomes relevant. Therefore, this thesis aims to develop model-based image reconstruction algorithms applicable to non-compressive and compressive scenarios.

Previous works have examined the sparsity assumption in contrast-enhanced vascular ultrasound imaging using microbubbles, but mostly did not make assumptions for vascular data itself [6, 8]. Although contrast-enhanced ultrasound imaging (CEUS) provides certain advantages, normal ultrasound imaging (ultrasound imaging without the use of contrast agents) is more practical and accessible [19, 20]. Besides, due to the short lifespan of microbubbles within the body, the microbubble injection method exhibits low stability and consistency in imaging. Therefore, there is a need to discover and exploit prior information related to the vasculature data without contrast agents, such as the sparsity of vascular structures in tissue-separated images. However, since it increases the computational demands, it is necessary to reduce the computational burden using advanced techniques.

To develop image reconstruction algorithms for ultrasound flow imaging, it's crucial to consider different characteristics of the tissue and flow components in these images. In ultrasound imaging, flow represents the movement of blood through the vasculature, while tissue refers to the static structures of the surrounding soft tissue. The separation of flow from tissue is fundamental in creating accurate models of vascular networks. Sparsity arises in this context, as the vascular network can often be represented using

fewer data points when isolated from the surrounding tissue. Note that the characteristics of the vasculature are not limited to sparsity, and it also presents a connected network structure.

Deterministic sparsity-based priors may not fully capture the complex prior information beyond the bare sparsity of the tissue-separated vascular network, as they primarily focus on representing the network with the fewest non-zero elements, without accounting for other important characteristics such as structure or shape [21]. Capturing more prior information requires further assumptions on the vascular image data and more sophisticated deterministic priors, which might increase the number of parameters in the ultrasound imaging problem and result in a substantial computational burden and parameter tuning step. On the other hand, probabilistic models such as sparse Bayesian learning (SBL) assume that unknown data elements are random variables with a zero-mean Gaussian distribution. This might be more flexible in embracing other properties of the vasculature in addition to the sparsity. Although SBL was employed for super-resolution ultrasound imaging with contrast-enhancing microbubbles (which exhibit sparsity), its performance for tissue-separated vascular networks has remained unexplored [22]. The SBL algorithm is notably slow for large-scale vascular ultrasound imaging, especially when it relies on the expectation-maximization (EM) technique. Hence, reducing the computational burden of the classical SBL is crucial, particularly for large-size real-time ultrasound imaging problems.

Classical SBL assumes statistical independence between image voxels, which might not be sufficient to handle dependence between the vascular image voxels. Block sparsity naturally arises in practical applications such as in radar images [23, 24, 25], fetal ECG [26], ultrasound signals [27], and so on. Classical SBL might remain insufficient to capture the vasculature exhibiting a connected structure, which can be associated with block sparsity. Investigating block sparse approaches such as pattern-coupled sparse Bayesian learning (PCSBL) might improve the reconstruction quality of sparse and connected structures [28]. However, existing PCSBL techniques exploit the EM algorithm and are extremely slow for vascular ultrasound imaging as the real data is of large-size. Thus, there is a need for a faster version of the PCSBL algorithm [29]. Besides, PCSBL requires tuning of the hyperparameters to achieve its optimal performance. An algorithm not requiring manual parameter tuning can be more useful in computationally intensive problems such as ultrasound imaging.

The PCSBL approach, widely used for block sparsity, exploits the relation between neighboring elements but does not capture their correlations [28, 30, 31, 32]. The statistical correlation of the neighboring pixels can be beneficial in capturing block sparsity in vascular ultrasound imaging. The dynamic flow is likely to exhibit a correlation between neighboring blood cells and might result in a correlation between neighboring image pixels. Existing correlation-based sparse reconstruction methods include block sparse Bayesian learning (BSBL) and extended block sparse Bayesian learning (EBSBL) algorithms [33]. While BSBL requires prior knowledge of the block partition, EBSBL offers an alternative that does not require block information, which is the case for natural signals such as tissue-separated vasculature data. However, EBSBL uses a large dictionary, which results in high computational complexity. Henceforth, developing a faster alternative that uses block correlations could be beneficial. Furthermore, their perfor-

mance is inferior to the PCSBL algorithm. Hence, improving the performance of the correlation-based block sparsity methods is required while reducing the computational complexity.

The motivation for this thesis also includes improving the image quality within advancements in ultrasound transmission strategies. While unfocused transmissions in Doppler ultrasound allow for high frame rate imaging, they often suffer from low SNR, especially when imaging deeper structures or smaller blood vessels. Although image reconstruction algorithms improve image quality, they mostly have high computational complexity and memory requirements, particularly the model-based methods that exploit deterministic or statistical prior information [21, 29, 34]. On the other hand, advancements in ultrasound transmission can also improve image quality without significantly increasing the computational demands. Using coded excitation techniques such as Barker and Golay codes also improves the SNR and the penetration depth up to a limit [14, 15, 16, 35, 36, 18]. However, there is still a gap in the literature on utilizing optimized code design to increase image reconstruction performance in ultrasound imaging.

In summary, this research explores the use of new computational techniques to advance ultrasound imaging. While many chapters of the thesis address the limitations regarding the vascular ultrasound image reconstruction algorithms and prior information, one chapter is motivated by limitations on ultrasound transmission strategies.

1.2. RESEARCH OBJECTIVES

The main objective of this thesis is to develop and explore a new set of algorithms that can leverage model-based image reconstruction applied to the imaging of blood flow. In this regard, we try to answer three main questions.

Q1. *How well can the joint sparsity (i.e., the shared sparsity between different time-instants of vascular networks) of tissue-separated frames improve the image reconstruction quality in vascular ultrasound imaging?*

One of the primary goals of this thesis in addressing **Q1** is to explore how the joint sparsity of vascular networks at different time instants can be leveraged using a deterministic framework [21]. We will study whether joint sparsity is a valid assumption for the tissue-separated vascular data. Existing methods assume the sparsity only in the vasculature's power Doppler image (PDI) and assume the statistical independence between image voxels [6, 8]. This research aims to achieve higher resolution and better depiction of vascular structures by developing new algorithms that exploit joint sparsity of the tissue-separated vasculature.

We also attempt to answer **Q1** by exploiting probabilistic joint sparsity methods for the tissue-separated vascular data in ultrasound image reconstruction, such as sparse Bayesian learning (SBL) [37, 38]. Our approach seeks to investigate its performance for vascular ultrasound imaging and improve the resolution, SNR, noise suppression, and accurate depiction of the details of the vascular structure with a statistical method.

Q2. *Can we design efficient algorithms to enhance the image reconstruction quality by exploiting the block sparsity in the spatial domain?*

In addition to examining the algorithm performance in vascular ultrasound imaging, this question opens a way for developing block sparsity algorithms for general signal processing problems, including one-dimensional inverse problems. To approach the answer of **Q2**, we first pursue incorporating the block sparsity information in the SBL algorithm. Firstly, we aim to use pattern-coupling, namely, the relations between neighboring parameters, which inherently enforce block sparsity [28]. However, PCSBL relies on the EM algorithm, which exhibits slow convergence. To finally answer **Q2**, our objective is to develop a version of the pattern-coupled sparse Bayesian learning (PCSBL) algorithm based on the fixed-point iterations method, which offers a faster convergence [39]. To our knowledge, such an algorithm has not been described in the literature before. Another goal is avoiding manual hyperparameter update rules in PCSBL, which requires a parameter tuning stage. We aim to develop an efficient method and examine its performance for the one-dimensional direction-of-arrival (DOA) estimation problem and two-dimensional vascular ultrasound image reconstruction problem, thereby presenting a novel contribution to the field.

Alternatively, we focus on enforcing block sparsity using the correlations between neighboring elements/pixels. Block sparse Bayesian Learning (BSBL) and extended block sparse Bayesian learning (EBSBL) have been an inspiration for adopting this approach. Since BSBL involves knowledge of the block partition, EBSBL has become our primary focus. To answer **Q2**, a novel approach is needed to improve the performance and reduce the computational cost of the existing correlation-based SBL algorithm. Therefore, another objective of this thesis is developing an efficient correlated sparse Bayesian learning algorithm without the prior block partition information [34]. To demonstrate the enhanced signal/image reconstruction quality, numerical experiments on DOA and amplitude estimation, as well as ultrasound imaging problems, are pursued.

Q3. *Can we improve the imaging of blood flow at greater depths by optimizing transmission codes?*

We aim to employ optimized coded excitation for vascular ultrasound imaging to answer **Q3**. A linear signal model will optimize the coding scheme, where the code sequences appear in a coding matrix. To design optimal codes, we minimize the Cramér-Rao lower bound (CRB)[40] as a proxy for minimizing the mean square error[41, 42]. We also introduce a trace-constrained variant of the optimization problem to reduce computational complexity based on the Fisher information matrix. This approach allows us to investigate whether the designed codes can improve image quality at greater depths under ultrafast imaging conditions.

1.3. OUTLINE OF THE THESIS

This thesis is organized as follows. First, we present model-based vascular ultrasound imaging and the related mathematical model in Chapter 2. In Chapter 3, we propose a multiple-measurement vector (MMV) model to enforce the joint sparsity of the images at different time instants, which provides an answer to **Q1**. We propose the MMV FISTA method as an image reconstruction technique and evaluate its performance for

1

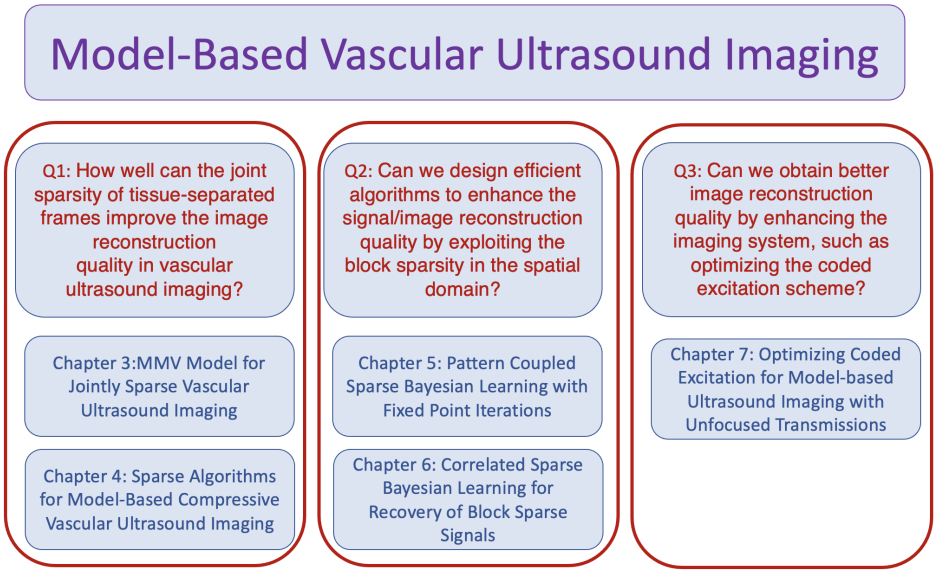

Figure 1.1: Thesis outline.

synthetic data. In the subsequent Chapter 4, we present the compressive vascular ultrasound imaging model and propose SBL with fixed point iterations to solve the image reconstruction problem. We seek an answer to **Q1** by statistically enforcing the joint sparsity. In Chapter 5, a novel pattern coupled sparse Bayesian learning algorithm with fixed point iterations (FP-SBL) is developed, which is tested on the direction-of-arrival (DOA) estimation problem in radar and the compressive vascular ultrasound imaging problem using experimental data obtained from mouse brain. We address **Q2** by exploiting the block sparsity in the spatial domain. Then, in Chapter 6, a correlated sparse Bayesian learning algorithm for recovery of block sparse signals is introduced to provide an additional answer to **Q2**. However, as the computational complexity of the developed algorithm is significantly high for ultrasound imaging problems, its application is limited to synthetic one-dimensional data and DOA estimation problems. Then, we present an advancement in ultrasound transmissions, which is the subject of **Q3**. At this point, Chapter 7 presents a novel optimization scheme for coded excitation in model-based ultrasound imaging to enhance the signal-to-noise ratio. The thesis outline is given in Fig. 1.1.

CHAPTER 2:

This chapter starts by explaining the mechanism of ultrasound imaging, where both focused and unfocused transmissions are presented. The chapter then presents Doppler ultrasound imaging, which focuses on power Doppler imaging (PDI) to visualize blood flow using the signal power intensity. Next, it introduces model-based vascular ultra-

sound image reconstruction and emphasizes its difference from traditional delay-and-sum (DAS) beamforming. It presents how this approach exploits matrix-vector formulations and iterative algorithms to improve image quality compared to traditional methods. The chapter also discusses various image reconstruction methods, such as least squares estimation and regularized techniques, which can enhance image resolution, contrast, and noise reduction. To further boost the performance, we introduce the coded excitation techniques in ultrasound literature to improve the image quality by modifying the imaging system. Thereafter, we address the challenges in computational complexity to obtain a high-quality image, which might require additional prior information related to vascular imaging data. Finally, the chapter summarizes the approaches we focus on in this thesis to enhance the ultrasound image quality by increasing the SNR and resolution and by removing the artifacts. It also emphasizes further research to refine these techniques by addressing their limitations.

CHAPTER 3:

To answer **Q1**, this chapter introduces a multiple measurement vector model (MMV) with joint sparsity across ultrasound frames. It starts by addressing the limitations in existing methods due to limited spatial resolution and long acquisition times. Conventional methods often assume statistical independence between voxels, which can distort the signal model. A novel image reconstruction approach is proposed using the MMV model to exploit joint sparsity across images obtained at different time instants to eliminate the distortion of the signal model. To reduce the computational complexity, the ℓ_1-SVD method is employed. Our approach enhances the spatial resolution and improves the separation between blood vessels compared to existing methods, albeit with slightly increased computation time.

CHAPTER 4:

This chapter introduces the vascular ultrasound imaging system with compressive measurements. As in the previous chapter, it exploits the vasculature's jointly sparse and connected structure with the MMV model. However, this time, a statistical method is exploited to seek an answer to **Q1**, named SBL, solved with the fixed-point iterations method. Here, the methods from Chapters 3 and 4 are applied to two-dimensional vascular ultrasound scenarios for mouse brain data. However, they could not successfully reveal the detailed vasculature, which requires future advancements.

CHAPTER 5:

This chapter presents a novel approach for recovering block-sparse signals with unknown boundaries for answering **Q2**, a problem that naturally seems to arise in various applications, such as tissue-separated vasculature. It introduces a pattern-coupled sparse Bayesian learning (PCSBL) algorithm that utilizes fixed-point iterations, unlike the traditional expectation-maximization (EM) algorithm, to achieve faster convergence. The chapter demonstrates that the proposed fixed-point iteration method offers a simple hyperparameter update rule, which does not require manual adjustments. It also includes numerical results showing that the method performs comparably to PCSBL with the EM algorithm in one-dimensional scenarios such as direction of arrival (DOA)

and amplitude estimation problems while achieving faster convergence. Thanks to the faster convergence of the algorithm, it is now tested on mouse brain data for the two-dimensional case. It exhibits slight improvements compared to the conventional SBL algorithm.

CHAPTER 6:

This chapter aims to answer **Q2** by introducing a novel approach for recovering complex-valued block sparse signals with unknown block partitions. The proposed method reduces the computational complexity of previous correlation-based EBSBL method by employing a tridiagonal correlation matrix. The tridiagonal matrix structure represents the correlation between neighboring sparse coefficients. The proposed algorithm reduces the computational complexity and the number of unknowns compared to EBSBL. Furthermore, it provides superior performance over the state-of-the-art by reconstructing both block and non-block sparse patterns. We aim to apply this novel algorithm to the presented compressive ultrasound imaging problem. However, due to the high computational cost of the algorithm, which exploits the EM, the applications of the algorithm are only the limited to one-dimensional data such as randomly generated block sparse data as well as data related to the DOA estimation problem.

CHAPTER 7:

This chapter focuses on the optimization of coded excitation for model-based ultrasound imaging with unfocused transmissions to answer **Q3**. This chapter introduces a novel approach to enhance SNR by optimizing the coding matrix via the minimization of the Cramér-Rao lower bound (CRB) and the maximization of the Fisher information matrix (FIM). The proposed method results in superior SNR in deep imaging regions compared to conventional sparse codes. Although it reduces the axial resolution, this is mitigated by the least squares QR (LSQR) method. Simulations using the optimized code show an improvement of the SNR in ultrasound imaging. Furthermore, the effectiveness and limitations of coded excitation in practical scenarios are discussed.

CHAPTER 8:

This chapter summarizes the conclusions driven by the findings and scientific contributions throughout this dissertation. Lastly, it also reviews the insights obtained from the previous chapters as well as potential research directions.

1.4. LIST OF CONTRIBUTIONS

Finally, we provide an overview of the contributions made to the scientific literature during this Ph.D. thesis.

Journal Publications

- J1: **D. Dogan**, L. Zhu, Y. Hu, J. G. Bosch, P. Kruizinga and G. Leus, "Optimizing Coded Excitation for Model-Based Ultrasound Imaging With Unfocused Transmissions," in IEEE Transactions on Computational Imaging, vol. 11, pp. 609-624, 2025.

- J2: **D. Dogan**, G. Leus, Correlated Sparse Bayesian Learning for Recovery of Block Sparse Signals with Unknown Borders, IEEE Open Journal of Signal Processing 5, p.421-435, 2024.
- J3: Y. Hu, **D. Dogan**, M. Brown, G. Leus, T. van der Steen, P. Kruizinga, Computational Ultrasound Carotid Artery Imaging with a Few Transceivers: An Emulation Study. Accepted for a publication in IEEE Transactions on Ultrasonics, Ferroelectrics, and Frequency Control

Conference Publications

- C1: **D. Dogan**, G. Leus, Pattern Coupled Sparse Bayesian Learning with Fixed Point Iterations for DOA and Amplitude Estimation, Asilomar Conference on Signals, Systems, and Computers 2023, paper 1308, p.1303-1307
- C2: **D. Dogan**, P. Kruizinga, J.G. Bosch, G. Leus, Multiple Measurement Vector Model for Sparsity-Based Vascular Ultrasound Imaging. Proceedings IEEE Statistical Signal Processing Workshop 2021, p. 501-505, 2021
- C3: Y. Hu, M. Brown, M. Bulot, M. Cheppe, G. Ferin, **D Dogan**, G. Leus, L. Wei, A.F.W. van der Steen, P. Kruizinga, J.G. Bosch, Volumetric Computational Ultrasound Imaging of Carotid Artery using 20×12 Elements Matrix Transducer with Aberration Mask: Phantom Studies, IEEE International Ultrasonics Symposium 2024
- C4: Y. Hu, **D. Dogan**, M. Brown, M. Bulot, G. Ferin, G. Leus, P. Kruizinga, A.F.W. van der Steen, J.G. Bosch, 3D Carotid Artery Flow Imaging Using Compressive Sensing with a Spatial Coding Mask: A Simulation Study. Proceedings IEEE International Ultrasonics Symposium 2023.
- C5: Y. Hu, M. Brown, **D. Dogan**, G. Leus, P. Kruizinga, A. F.W. Steen, J.G. Bosch., Compressive Imaging with Spatial Coding Masks on Low Number of Elements: An Emulation Study, Proceedings IEEE International Ultrasonics Symposium 2022

2

Model-Based Vascular Ultrasound Imaging

This chapter presents the fundamental concepts of vascular Doppler ultrasound imaging and model-based Doppler ultrasound imaging, an alternative to the conventional image reconstruction techniques, such as delay-and-sum beamforming. We first present the power Doppler imaging process and then explain the reconstruction techniques. We then give the mathematical model for the model-based imaging technique under non-compressive scenarios and discuss how various deterministic and statistical priors can be obtained to solve that problem. Furthermore, we introduce the existing coded excitation techniques as a background for the thesis content.

2.1. ULTRASOUND IMAGING MECHANISM

In ultrasound imaging, a transducer consisting of an array of piezoelectric elements is used to transmit and receive mechanical pressure waves. When a voltage is applied to a piezoelectric element, it vibrates and generates a mechanical pressure wave. The frequency of vibration is determined by the material of the element, typically ranging from 1 to 30 MHz for medical applications. When the transmitted pressure wave encounters various acoustic impedances and echoes will return to the piezoelectric elements. Then, the transducer elements convert these echoes into small voltage potentials, known as radio frequency (RF) signals which can be subsequently digitized and used to create an image of the acoustic impedance differences within the medium.

Conventional ultrasound imaging employs focused ultrasonic waves. It sends a single focused wave during each transmission, reconstructing one image line at a time, as shown in Fig. 2.1. This process is repeated for each neighbouring image line, requiring multiple transmission events before generating a single image. For Doppler imaging, where we aim to image motion (such as flowing blood), we need multiple transmissions per line. Due to the multiple transmissions for every line, this scanning method might not achieve high sampling frequency for high-frame-rate imaging [43]. An alternative to constructing an image line by line is using unfocused transmissions. First, a synthetic aperture ultrasound imaging technique can be employed, where a single transmitter can illuminate the entire region of interest (ROI) instead of focusing on a single angular sector. Since the signal-to-noise ratio (SNR) decreases for such a case, multiple images are compounded to obtain the final image. Each image is acquired by firing the different sensors in the transducer array [44]. Although synthetic aperture imaging increases the image quality in terms of resolution, it stll suffers from a limited frame rate. To reach a higher frame rate, a plane-wave imaging approach illustrated in Fig. 2.1 can be embraced where all the sensors transmit to illuminate the entire field of view [9]. Hence, the entire image can be reconstructed with parallel beamforming from a single transmission. Compared to synthetic aperture imaging, plane-wave transmissions still reach a decent level of contrast, SNR, and resolution. This level is achieved via coherent compounding of multiple images with different steering angles. Since plane-wave imaging uses all elements in the transducer array simultaneously for a few steering angles, it avoids the repeated firing of individual transmitters, leading to a higher frame rate compared to line-by-line imaging and synthetic aperture methods. Note that plane-wave imaging is particularly advantageous for high-frame-rate imaging such as Doppler imaging [43].

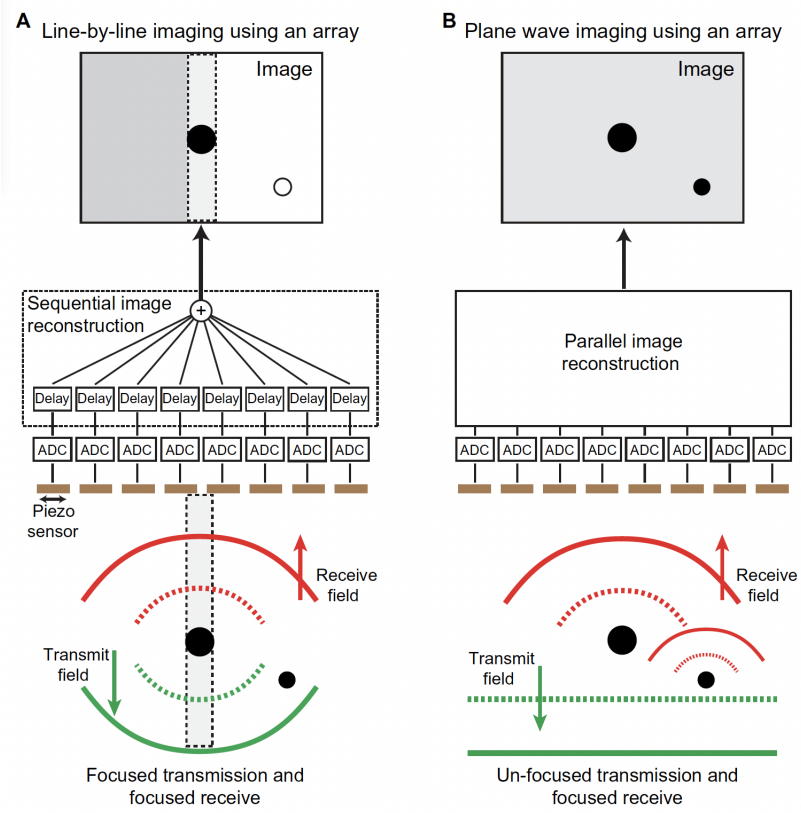

Figure 2.1: Two different methods of ultrasound imaging. (a) Conventional ultrasound imaging method using line by line focused ultrasonic waves. (b) Demonstration of a plane-wave imaging scheme. [45]

2.2. VASCULAR POWER DOPPLER IMAGING

Doppler ultrasound imaging is an imaging technique that exploits the interaction between mechanical pressure waves, tissues, and red blood cells. Doppler shift occurs with the scattering of red blood cells where the Doppler frequency is related to the velocity of the blood cells. The visualization of the blood flow and the detection of vascular abnormalities or pathologies are enabled by Doppler ultrasound imaging.

Spectral and color Doppler imaging enables the detection and visualization of the blood flow velocity and direction. The angle towards the scatterer is the same for the same transmitting and receiving element. The Doppler frequency f_D is given by [43]:

$$f_D = f_R - f_T = -\frac{2v}{c_0} f_0 \cos\theta, \tag{2.1}$$

where v is the velocity of the scatterer, c_0 is the speed of sound in the medium, f_0 is the transmitted frequency, and θ is the angle between the ultrasound beam and the flow di-

rection. A negative f_D indicates that the scatterer is moving away from the transducer, while a positive f_D indicates movement towards the transducer. Thus, the Doppler frequency shift is related to both the velocity of the blood cells and the insonation angle. However, these methods face challenges in detecting blood flow in cases of low-flow, where it is difficult to separate the flow from tissue moving at similar speeds, and in deep-lying vessels, where the weak SNR limits accurate detection.

In tasks where flow direction is not significant, but sensitive detection of the presence of blood flow is essential, such as imaging the small and deep vessels, power Doppler imaging (PDI) is a valuable method. In PDI, the flow direction is not measured, and the amplitude or power of these scattered signals is considered rather than their frequency shift [46]. It is an imaging technique that visualizes blood flow based on the amplitude or power of the Doppler signal [46]. The total energy of the moving blood cells is achieved by calculating the integrated power of the Doppler signal. PDI highlights the regions with strong Doppler signals irrespective of their velocity, where the power increases by the moving scatterer concentration. Note that color Doppler imaging can miss the low-velocity or weak blood flow regions, and PDI can mitigate this, which uses the intensity of the signals rather than the phase [47]. Furthermore, PDI is advantageous in settings where the insonation angle is challenging to control as it is less angle-dependent.

Now we present the steps of PDI, from raw radio frequency (RF) data acquisition to PDI formation as shown in Fig. 2.2.

- **Raw Data RF Acquisition:** The first step given in the first row of Fig. 2.2 is raw RF data acquisition from D transmissions, such as with D steering angles.

- **Beamforming:** The next step is using the acquired raw data to generate an ultrasound image via delay-and-sum (DAS) beamforming [48] or model-based beamforming [49]. Beamforming is the most crucial step of ultrasound processing as it determines the contrast and resolution of the resulting image. As DAS is a fast and efficient method, it is widely used, but model-based techniques can be advantageous in some scenarios that require superior imaging quality.

- **Compounding:** After that, the coherent summation and averaging of the D images produces a single high-resolution and high-SNR compounded frame of size $L_z \times L_x$. Here, L_z and L_x represent the number of samples in the spatial depth and spatial width (along the transducer array), respectively. Compounding the images that belong to D steering angles is beneficial for visualizing low-contrast structures, such as small vessels, as it reduces speckle noise and enhances the SNR.

- **Sequential Image Acquisition:** Then, M compounded frames are sequentially acquired over time. This results in $L_z \times L_x \times M$ data. Here, M represents the temporal (slow-time) dimension and can also be called the number of frames or ensemble size. Then, each frame is vectorized and stacked as a 2D space-time matrix $\mathbf{S}$ with dimensions $L_z L_x \times M$.

- **SVD Filtering:** A singular value decomposition (SVD) [50] or a high-pass filter [51] can be applied to this 2D space-time matrix to distinguish between the slow-moving tissue and faster-moving blood vessels, enabling the explicit depiction of

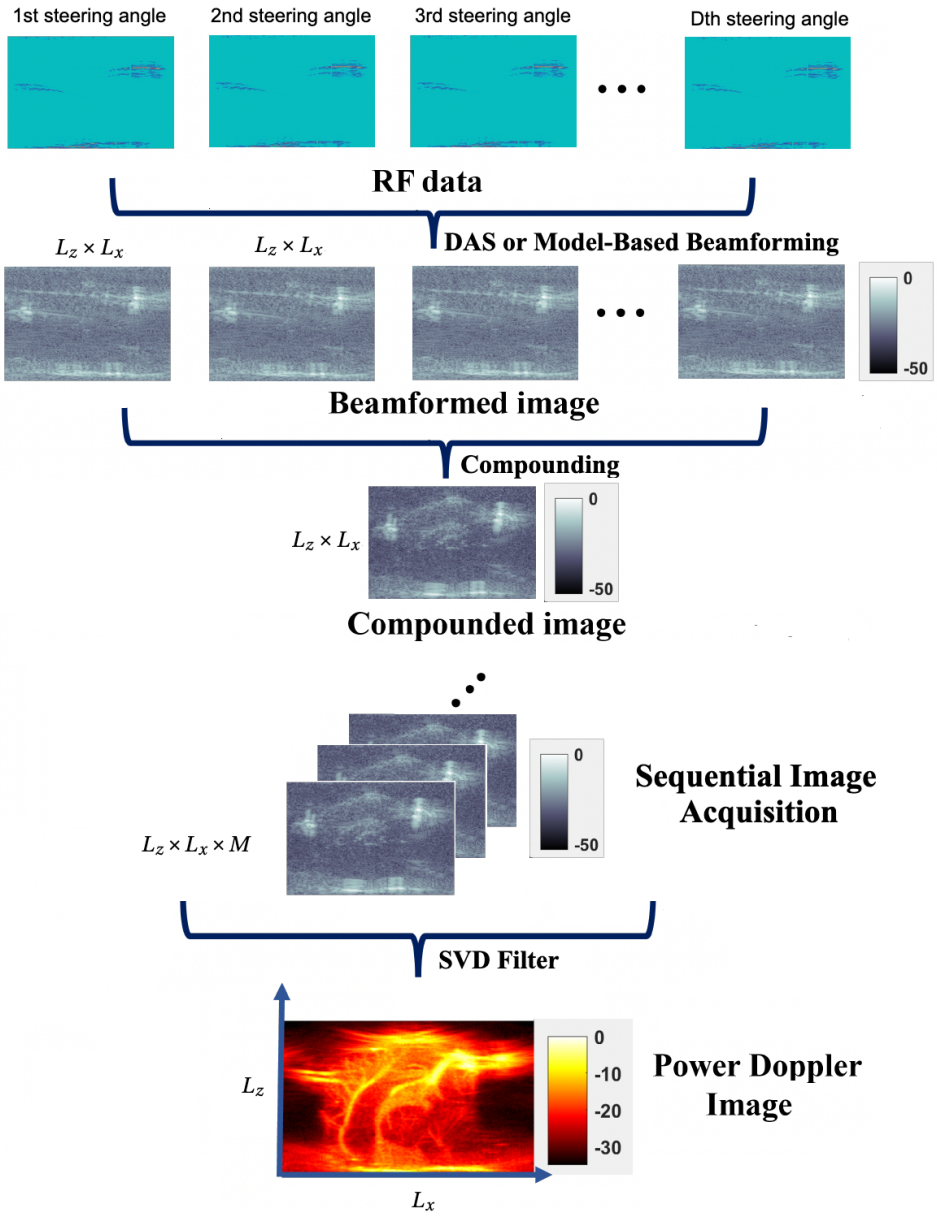

Figure 2.2: Data processing chain for Doppler ultrasound imaging.

vascular structures. In the SVD filter case, we take the SVD decomposition of this 2D space-time matrix $\mathbf{S}$ as $\mathbf{S} = \mathbf{U\Gamma V}^{\mathsf{H}}$. Then, we set the tissue-related first M_t singular values of $\mathbf{\Gamma}$ to zero, where M_t can be selected empirically. Then, the new di-

agonal matrix is given by $\tilde{\mathbf{\Gamma}}$ and the tissue separated 2D space-time matrix is given by $\tilde{\mathbf{S}} = \mathbf{U}\tilde{\mathbf{\Gamma}}\mathbf{V}^{\mathsf{H}}$.

- **PDI formation**: The final PDI image is formed by averaging all power of the filtered temporal frames and reshaping the result into an image with dimensions $L_z \times L_x$.

Note that Fig. 2.2 presents the steps for conventional PDI. For some model-based imaging applications with sophisticated image reconstruction techniques, the order can be modified so that sequential RF data acquisition and SVD filtering are performed before beamforming and compounding. Since prior information on the cleaned/filtered signal is used in some estimation problems, SVD filtering is applied first to the RF data instead of sequentially acquired compounded frames.

2.3. MODEL-BASED ULTRASOUND IMAGE RECONSTRUCTION

2.3.1. TRADITIONAL DELAY-AND-SUM BEAMFORMING

Delay-and-sum (DAS) is the most basic digital beamformer for traditional ultrasound imaging [1]. Thanks to its simplicity and efficiency, it is widely used in high-frame-rate ultrasound, such as power Doppler imaging. Calculating the arrival time of an echo to a specific location is simple when the propagation speed of sound in the body is assumed to be constant. Since the same pulse is transmitted to and reflected by all pixels and the time-of-arrival of each echo can be calculated, the complex signals across all sensors are coherently summed at the corresponding arrival times. In the final image, high intensities correspond to scattering caused by high impedance differences, while low intensities represent regions with no scattering or low scattering and thus tissue with homogeneous impedance.

To clarify the effect of coherent summation in DAS beamforming, block diagrams of the DAS beamforming for two scatterers at different locations, S_1 and S_2, are shown in Fig. 2.3. The top subfigure shows the coherent summation with delay correction for scatterer S_1. The ultrasound echoes reflected from the scatterer S_1 arrive at different receivers, J_0, J_1, and J_2, at different times, μ_0, μ_1 and μ_2, as each receiver element has a different distance from the scatterer. To compensate for varying arrival times, we apply time delays, d_0, d_1, and d_2, to the received signals. Then, these aligned signals are coherently summed and yield a strong response in the beamformed image, resulting in constructive interference. On the other hand, in the bottom subfigure of Fig. 2.3, the signals reflected from S_2 cannot be coherently summed as they are not aligned using the delays previously applied for S_1 and produce a weak response in the beamformed image. In some cases where the signals partially overlap, it might even cause destructive interference and reduce the signal strength. To obtain the coherent summation for each pixel in the region of interest (ROI), the required delays need to be calculated explicitly for each location. If the system geometry is known in ultrasound imaging, the correct delays for each pixel location, including the scatterers S_1 and S_2, can be computed. Ultimately, the overall ROI can be reconstructed with DAS beamforming.

DAS beamforming is applicable to several medical ultrasound imaging techniques such as Doppler imaging. Since all the techniques have the knowledge of the system geometry and time-of-arrival for all the echoes, DAS beamforming is suitable for all those

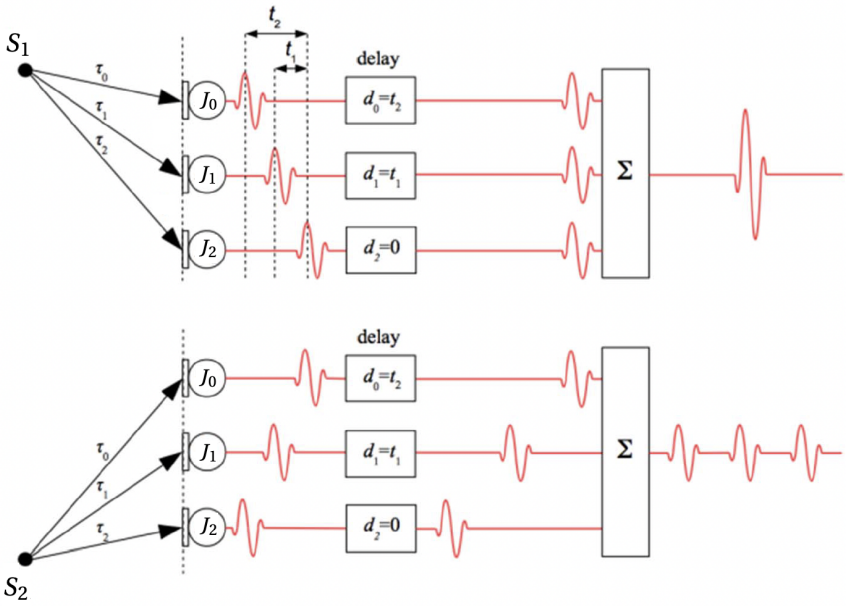

Figure 2.3: The block diagram of the delay-sum beamforming (DAS) method [52].

techniques. DAS beamforming can be combined with compounding to enhance image quality and reduce artifacts. The DAS approach assumes that waves can travel uninterruptedly with only small inhomogeneities so that the background medium speed of sound can be assumed constant. Furthermore, the same pulse waveform is received on each sensor, making coherent summation possible.

2.3.2. MODEL-BASED VASCULAR ULTRASOUND IMAGING

In model-based imaging, the images are reconstructed with a matrix-vector formulation that best represents the measured ultrasound signals given the complete ultrasound propagation and scattering model with all parameters. Unlike traditional beamforming techniques with simple delay-and-sum operations, model-based techniques are suitable for exploiting iterative reconstruction techniques to enhance image quality. Model-based approaches can also employ regularization techniques to enhance the reconstruction quality [9, 53]. Incorporating prior information with regularization techniques might use assumptions related to the distribution of the scatterers and tissue smoothness, such as the sparsity of ultrasound images with a homogenous background. Compared to conventional beamforming, higher spatial resolution can be attained with model-based imaging, which enables the depiction of small vessels and the detection of slight changes [53]. Moreover, model-based approaches can enhance image contrast and SNR, which results in better separation between tissue and blood regions. Lastly, model-based approaches can mitigate imaging artifacts such as speckle noise, reverberation, and shadowing while preserving the image quality.

IMAGE FORMATION MODEL

We consider a scenario where we examine the transmission of a known pressure pulse into a region of interest (ROI) characterized by a homogeneous background medium. When pixels in the ROI exhibit contrast speed of sound or density compared to the surrounding medium, a scattering event occurs. Although there are multiple reflections between scatterers, they can be ignored in ultrasound imaging as these differences are relatively small. This Born approximation [54, 55] simplifies the relationship between the unknown image and measurement data, effectively rendering it linear. Consequently, the output signal received by a sensor becomes a linear superposition of the echo from each pixel, as the echo is not significantly altered.

The proposed setup consists of I elements in a linear transducer array. A plane-wave transmit scheme was employed to acquire signals. All elements are excited jointly with appropriate delays (e.g., when a plane-wave transmission under a non-zero angle is considered) and received signals from all elements are recorded. In vascular Doppler ultrasound imaging, at every period Δt, a pulse $a(t)$ is sent from each transmitter, where t is assumed to be continuous time, and the pulse peak is assumed to be located at $t = 0$. At sensor $j = 1,\dots,I$ and pulse period $m = 1,\dots,M$ the sensor output is modeled as

$$z(j,t,m) = \sum_{z,x}\sum_{i} a_{j,i}(z,x,t)s(z,x,m) + n(j,t,m), \tag{2.2}$$

where $s(z,x,m)$ is the time-varying scattering signal related to the position (z,x), $n(j,t,m)$ corresponds to the white Gaussian noise for the measurement $z(j,t,m)$, and $a_{j,i}(z,x,t) = a(t-\tau_{z,x,j,i})$, where $\tau_{z,x,j,i}$ is the sum of the pulse delay adopted at transmitter i and the delay related to the distance from the transmitter i to the receiver j through the pixel at (z,x). In the remainder of this chapter, we work in the frequency domain instead of the time domain since faster computation in the frequency domain is possible. Note that (2.2) is equally valid in the frequency domain if $z(j,t,m)$ and $a_{j,i}(z,x,t)$ are replaced by their frequency domain equivalents [10]. We denote the Fourier transform of $z(j,t,m)$ and $a_{j,i}(z,x,t)$ by $z(j,\omega,m)$ and $a_{j,i}(z,x,\omega)$, respectively.

Here, all $a_{j,i}(z,x,t)$ and eventually $a_{j,i}(z,x,\omega)$ are known beforehand as the transmitted pulses and the geometry of the problem is known. The only unknowns are the coefficients $s(z,x,m)$. Now, the problem boils down to the linear equation (2.2). By sampling and exploiting the matrix-vector formulation, this relation can be compactly denoted as

$$\mathbf{Z} = \mathbf{AS} + \mathbf{N}, \tag{2.3}$$

with

$$\mathbf{A} = \begin{bmatrix} \mathbf{a}_{1,1} & \dots & \mathbf{a}_{1,L} \\ \vdots & \ddots & \vdots \\ \mathbf{a}_{I,1} & \dots & \mathbf{a}_{I,L} \end{bmatrix}, \mathbf{a}_{j,l} = \begin{bmatrix} a_{j,l}(\omega_1) \\ \vdots \\ a_{j,l}(\omega_F) \end{bmatrix} = \begin{bmatrix} \sum_{i=1}^{I} a_{j,i}(z_l,x_l,\omega_1) \\ \vdots \\ \sum_{i=1}^{I} a_{j,i}(z_l,x_l,\omega_F) \end{bmatrix},$$

$$\mathbf{Z} = \begin{bmatrix} \mathbf{z}_1 & \dots & \mathbf{z}_M \end{bmatrix} = \begin{bmatrix} \mathbf{z}_{1,1} & \dots & \mathbf{z}_{1,M} \\ \vdots & \ddots & \vdots \\ \mathbf{z}_{I,1} & \dots & \mathbf{z}_{I,M} \end{bmatrix}, \mathbf{z}_{j,m} = \begin{bmatrix} z(j,\omega_1,m) \\ \vdots \\ z(j,\omega_F,m) \end{bmatrix},$$

$$\mathbf{S} = \begin{bmatrix} \mathbf{s}_1 & \dots & \mathbf{s}_M \end{bmatrix} = \begin{bmatrix} s(z_1, x_1, 1) & \dots & s(z_1, x_1, M) \\ \vdots & \ddots & \vdots \\ s(z_L, x_L, 1) & \dots & s(z_L, x_L, M) \end{bmatrix},$$

$$\mathbf{N} = \begin{bmatrix} \mathbf{n}_1 & \dots & \mathbf{n}_M \end{bmatrix} = \begin{bmatrix} \mathbf{n}_{1,1} & \dots & \mathbf{n}_{1,M} \\ \vdots & \ddots & \vdots \\ \mathbf{n}_{I,1} & \dots & \mathbf{n}_{I,M} \end{bmatrix}.$$

Here, $\omega \in \Omega$ is sampled at F frequencies in the set $\Omega = \{\omega_1, ..., \omega_F\}$. We use equidistant samples taken from the positive side of the frequency spectrum. Further, (z_l, x_l) is the sample of the spatially continuous (z, x) related to the lth pixel. $\mathbf{z}_{j,m}$ is the received signal at receiver j for pulse m and $\mathbf{a}_{j,l}$ is the received echo signal at receiver j for pixel l. Note that stacking the data into $\mathbf{Z}$ and $\mathbf{S}$ matrices corresponds to the multiple measurement vector (MMV) model. In the single measurement vector (SMV) case, each column of $\mathbf{Z}$ and $\mathbf{S}$ can be represented as

$$\mathbf{z}_m = \mathbf{A}\mathbf{s}_m + \mathbf{n}_m, \tag{2.4}$$

where $\mathbf{z}_m$ and $\mathbf{s}_m$ are columns of $\mathbf{Z}$ and $\mathbf{S}$.

The model in (2.3) is then generalized to include multiple measurements involving different transmissions, such as various steering angles or differently coded transmissions. In such a case, D distinct measurement sets are stacked vertically into a larger system of equations as follows:

$$\begin{bmatrix} \mathbf{Z}_1 \\ \vdots \\ \mathbf{Z}_D \end{bmatrix} = \begin{bmatrix} \mathbf{A}_1 \\ \vdots \\ \mathbf{A}_D \end{bmatrix} \mathbf{S} + \begin{bmatrix} \mathbf{N}_1 \\ \vdots \\ \mathbf{N}_D \end{bmatrix}, \tag{2.5}$$

where $\mathbf{A}_d$, $\mathbf{Z}_d$, and $\mathbf{N}_d$ are the sensing matrix, measurements, and noise for the dth transmission, respectively. This concatenated model in (2.5) is an extended version of the above model in (2.3). For simplicity, we keep the same notation for (2.5) as in (2.3) and do not introduce new variables for the concatenated model with different transmissions.

IMAGE RECONSTRUCTION METHODS

Here, we present the image reconstruction methods which are applicable to classical vascular ultrasound imaging. The methods aim to enhance the SNR, contrast, image detail, and resolution.

Matched Filter: To obtain the estimated image frames $\mathbf{S}$ from $\mathbf{Z}$, the simplest and the computationally most efficient way is the matched filter given by

$$\hat{\mathbf{S}} = \mathbf{A}^{\mathsf{H}}\mathbf{Z}, \tag{2.6}$$

even though it does not exactly solve the problem in (2.3). Note that if $\mathbf{A}^{\mathsf{H}}\mathbf{A}$ can be approximated as an identity matrix, the estimator solves (2.3). The matched filter actually comes close to applying the DAS beamformer. To demonstrate this, assume a delta-pulse $a(t) = \delta(t)$. Therefore, each $\mathbf{a}_{j,l}$ consists of zeros except for a unity magnitude on the sample at which an echo is expected to arrive for pixel l at sensor j. Since only I

values are non-zero in every column of the **A** matrix, the matched filter sums I values of each column of **Z** for each pixel, namely the samples in **Z** at which an echo is expected at sensor j. By denoting the lth column vector of **A** as $\mathbf{a}_l$ and the mth column of **Z** as $\mathbf{z}_m$ with $\tau_{z_l,x_l,j}$, the expected time of arrival for an echo from pixel l on the sensor j, the element at the lth pixel is given by

$$\begin{aligned}\hat{s}(z_l, x_l, m) &= \mathbf{a}_l^{\mathsf{H}} \mathbf{z}_m \\ &= \sum_{j=1}^{I} \mathbf{a}_{j,l}^{\mathsf{H}} \mathbf{z}_{j,m} \\ &= \sum_{j=1}^{I} z(j, \tau_{z_l,x_l,j}, m).\end{aligned} \tag{2.7}$$

Hence, this is equivalent to DAS beamforming. Here, if we include D different RF signals in a single column for mth pulse response, it corresponds to applying traditional DAS beamforming and compounding within the matched filter framework.

Least Squares Estimation: As an alternative method, the least squares estimation can be leveraged, which minimizes the sum of the squared differences between the measurement matrix **Z** and estimated model **AS**. This leads to the following optimization problem:

$$\hat{\mathbf{S}} = \arg\min_{\mathbf{S}} ||\mathbf{Z} - \mathbf{AS}||_F^2, \tag{2.8}$$

with closed-form solution

$$\hat{\mathbf{S}} = \mathbf{A}^{\dagger}\mathbf{Z} = (\mathbf{A}^{\mathsf{H}}\mathbf{A})^{-1}\mathbf{A}^{\mathsf{H}}\mathbf{Z}, \tag{2.9}$$

where $\mathbf{A}^{\dagger}$ is the pseudoinverse of **A**. This holds only when **A** is full rank and invertible.

Tikhonov Regularization: When **A** is an ill-posed matrix, incorporating prior information available for the images, we formulate the inverse problem as follows:

$$\hat{\mathbf{S}} = \arg\min_{\mathbf{S}} \frac{1}{2} ||\mathbf{Z} - \mathbf{AS}||_F^2 + \lambda \mathscr{R}(\mathbf{S}). \tag{2.10}$$

This is a regularized least squares problem, which can also be related to maximum posterior estimation (MAP). Here, the first term controls data fidelity, whereas the second term $\mathscr{R}(\mathbf{S})$ controls how well the reconstruction matches our prior knowledge of the solution, with the scalar parameter λ trading off between these two terms. The regularization function can exploit prior knowledge about **S**.

The most-used regularization term is the Tikhonov regularizer where $\mathscr{R}(\mathbf{S}) = ||\mathbf{S}||_F^2$. It can be expressed as follows:

$$\hat{\mathbf{S}} = \arg\min_{\mathbf{S}} \frac{1}{2} ||\mathbf{Z} - \mathbf{AS}||_F^2 + \lambda ||\mathbf{S}||_F^2. \tag{2.11}$$

It penalizes the large values in **S** and provides a unique solution. However, it smoothens **S** and results in reduced resolution. The solution now becomes

$$\hat{\mathbf{S}} = (\mathbf{A}^{\mathsf{H}}\mathbf{A} + \lambda \mathbf{I})^{-1}\mathbf{A}^{\mathsf{H}}\mathbf{Z}. \tag{2.12}$$

As an alternative to least squares estimation with ℓ_2-norm regularization, minimum mean squared error minimization (MMSE) can be used, which is given by

$$\hat{\mathbf{S}} = \arg\min_{\mathbf{S}} \mathbb{E}\big((\mathbf{S}-\hat{\mathbf{S}})^{\mathsf{H}}(\mathbf{S}-\hat{\mathbf{S}})\big), \tag{2.13}$$

if $\mathbf{S}$ and $\mathbf{N}$ are random. Assume for instance that $\mathbf{S}$ has prior distribution $\mathcal{N}(\mu_{\mathbf{S}}, \mathbf{C}_{\mathbf{S}})$ and $\mathbf{N}$ has distribution $\mathcal{N}(\mathbf{0}, \mathbf{C}_{\mathbf{N}})$, then $\hat{\mathbf{S}}$ is given by,

$$\hat{\mathbf{S}} = \mathbb{E}(\mathbf{S}|\mathbf{Z}) = \mu_{\mathbf{S}} + (\mathbf{C}_{\mathbf{S}}^{-1} + \mathbf{A}^{\mathsf{H}}{\mathbf{C}_{\mathbf{N}}}^{-1}\mathbf{A})^{-1}\mathbf{A}^{\mathsf{H}}{\mathbf{C}_{\mathbf{N}}}^{-1}(\mathbf{Z}-\mathbf{A}\mu_{\mathbf{S}}). \tag{2.14}$$

The prior distribution of $\mathbf{S}$ is often unknown and needs an assumption. Note that (2.14) will be equal to the Tikhonov least squares estimation (2.12) when $\mathbf{S}$ is zero mean with covariance matrix $\mathbf{C}_{\mathbf{S}} = \frac{1}{\lambda}\mathbf{I}$ and $\mathbf{N}$ is zero mean with covariance matrix $\mathbf{C}_{\mathbf{N}} = \mathbf{I}$.

Sparse Regularization: The other widely used regularization term is the sparsity-enforcing regularizer. In the single measurement case, it is given as follows

$$\hat{\mathbf{s}}_m = \arg\min_{\mathbf{s}_m} \frac{1}{2}||\mathbf{z}_m - \mathbf{A}\mathbf{s}_m||_2^2 + \lambda||\mathbf{s}_m||_0. \tag{2.15}$$

Here, we use $\mathscr{R}(\mathbf{s}_m) = ||\mathbf{s}_m||_0$ where the ℓ_0-norm is used as a sparse regularizer. This method can precisely reconstruct $\mathbf{s}_m$ if the true $\mathbf{s}_m$ is known to be sparse, and under certain conditions on $\mathbf{A}$. Fortunately, several methods have been proposed to solve the sparse reconstruction. One popular approach is a greedy pursuit method, which approximates the solution iteratively. Examples of techniques from this group for the single measurement vector form are matching pursuit (MP) [56] and orthogonal matching pursuit (OMP) [57], which can produce fast results with moderate accuracy. Instead of solving the ℓ_0-norm, the cost function can also be relaxed by replacing the ℓ_0-norm by the ℓ_p-norm for $p \in (0,1]$. For example, the focal underdetermined system solver (FOCUSS) [58] applies iterative reweighted least squares to solve the ℓ_0-norm problem. When the ℓ_1-norm is used, it results in a convex optimization problem with a unique global solution. The single measurement vector version of the problem that accounts for measurement noise is named basis pursuit denoising (BPDN) [59] (also known as LASSO [60]).

Sparsity-based methods can be adapted to the multiple measurement vector (MMV) case. Since the vasculature at different time instants is similar, the joint sparsity assumption for the vasculature may hold. Joint sparsity here means that only the pixels related to vasculature are non-zero, and the background is zero. Furthermore, non-zero elements in different frames correspond to the same pixel positions. However, the sequentially acquired frames do not exhibit a sparse structure, as shown in the fourth row of Fig. 2.2, where the tissue background has a similar intensity to the vasculature. Only the tissue-separated vascular data can be assumed to be sparse or partially sparse. In the DAS beamforming or other beamforming techniques, such as the matched filter and least-squares estimation, the SVD filtering is applied in the last stage of power Doppler imaging as shown in Fig. 2.2. However, to exploit the joint sparsity information in the vascular imaging problem, we first apply SVD filtering on the RF data before applying model-based beamforming. Since SVD filtering and compounding are linear operations, applying them before or after beamforming should not make a significant difference.

Note that there can be slight differences in practical applications due to complex noise characteristics or imperfections in the imaging system.

With the considered assumptions, we can generalize the sparsity-based model given for the SMV case. In the MMV case, the $\ell_{2,1}$-norm can be used as the generalized version of the ℓ_1-norm. Here, the ℓ_2-norm of all rows of $\mathbf{S}$ is computed. Then, the $\mathbf{s}^{(\ell_2)}$ vector is contructed, which stacks the ℓ_2-norms of the rows of $\mathbf{S}$. Finally, $||\mathbf{S}||_{2,1} = ||\mathbf{s}^{(\ell_2)}||_1$ is computed [61]. Hence, we finally obtain the problem

$$\hat{\mathbf{S}} = \arg\min_{\mathbf{S}} \frac{1}{2}||\mathbf{Z} - \mathbf{A}\mathbf{S}||_F^2 + \lambda||\mathbf{S}||_{2,1} \tag{2.16}$$

Sparse Bayesian Learning: There are also other methods under the probabilistic framework for sparsity. Note in this context that probabilistic sparse reconstruction methods are mostly Gaussian [62]. With a reasonable probabilistic model for the unknown data, these methods outperform deterministic approaches. One well-known method in the probabilistic framework is sparse Bayesian learning (SBL). It was initially developed for the relevance vector machine (RVM) [37]. Later, it was applied to the inversion of compressive measurements [38]. The classical SBL algorithm assumes that unknown data elements are independent random variables with a zero-mean Gaussian distribution as follows:

$$p(s(z_l, x_l), \gamma_l) = \mathscr{CN}(0, \gamma_l). \tag{2.17}$$

The variance γ_l of the coefficients is treated as a hyperparameter learned from the observations by maximizing the likelihood function, usually using the expectation-maximization (EM) algorithm. The fixed-point iterations method can be a faster alternative than the EM algorithm to solve the likelihood problem. The fixed point iterations method is an empirical strategy, but it provides a fast convergence rate in most applications [63, 64].

2.4. CODED EXCITATION

In ultrasound imaging, it is observed that applying coded excitation [14, 15, 16],i.e., sending out longer encoded pulses, can enhance the SNR of ultrasound images and penetration depth. Long-bit streams of a Barker code can significantly improve ultrasound color flow imaging sensitivity [17]. Coded excitation involves using longer encoded pulses, enabling an extended pulse duration without causing a rise in amplitude and tissue heating issues. It can increase the SNR notably without exceeding the safety limits of medical ultrasound imaging devices. Besides, the decoding of the echoes mostly mitigates the degradation in the axial resolution.

Coded excitation methods in ultrasound imaging can be improved with various methods. The first way is exploring hybrid coding techniques with a combination of different coding sequences. The convolution of Barker and Golay codes partially or fully suppresses sidelobe levels, which increases SNR [65]. Chirp-modulated Golay codes, that multiply the chirp signal with an orthogonal binary sequence, enhance the SNR significantly [66]. Advanced signal processing algorithms can be effective in reconstructing received echoes. A finite impulse response (FIR) filter reconstructs the echoes transmitted with Barker codes by suppressing sidelobe energy [67]. Finally, longer Barker codes

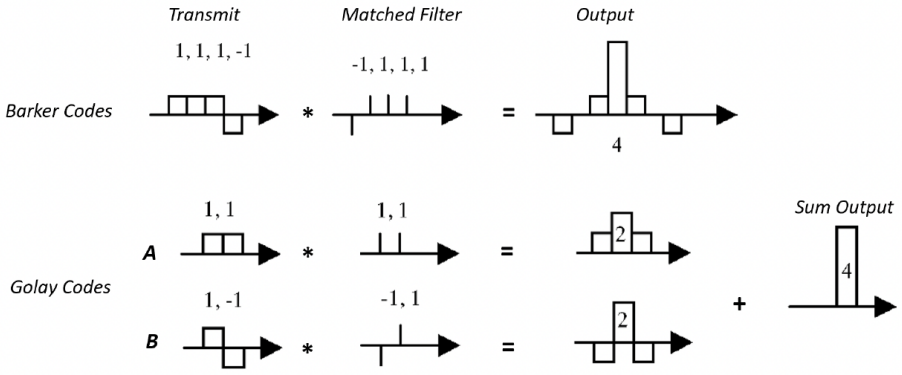

Figure 2.4: The Barker and Golay codes after matched filtering.

can be attained via Kronecker products for several applications, including functional ultrasound imaging.

In coded excitation, specially designed longer encoded pulses are used. They aim to reach a high mainlobe-to-sidelobe ratio, albeit with a slightly worse axial resolution than a single short pulse. Frequency and phase encoding techniques are widely applied in coded excitation [68]. While frequency encoding linearly modulates the carrier signal frequency with a chirp [15], phase encoding is achieved via phase modulation of the transmitted pulse either with linear or bi-phase modulation [14]. While the former applies linear modulation, the latter encodes the transmitted pulse with a 0-degree or 180-degree phase shift, respectively represented by 1 and -1. The Golay and Barker codes are the most common bi-phase modulation techniques, as they increase the SNR.

Barker Code: A Barker code results in a high mainlobe-to-sidelobe ratio after matched filtering as shown in Fig. 2.4. It results in a $10\log10(K)$ gain for the SNR, where K is the code length. However, existing Barker codes only have specific lengths $(2,3,4,5,7,11$ and $13)$, limiting the total transmitted energy. On the other hand, the Kronecker product of two Barker codes is a way to generate longer codes [67], at the expense of degraded autocorrelation. The inverse filter [67] and or spiking filter [68] can provide a sidelobe suppression, but they decrease the SNR.

Golay Code: The Golay code consists of a pair of finite equal-length binary sequences. As shown in Fig. 2.4, the Golay pair is designed to cancel out the range sidelobes, which can be observed in single transmit signals. The Golay complementary pairs cancel the sidelobes of length K sequences A and B when $A(k) * A(-k) + B(k) * B(-k) = 2K\delta(k)$, where the $*$ denotes the convolution operator. Now, the SNR gain of the Golay codes is given by $10\log10(2K)$. Due to the two transmissions, the Golay pairs' frame rate is halved. To mitigate this, [69] proposed the transmission of two pairs of mutually orthogonal Golay complementary sequences.

Random Code: While Barker and Golay codes use phase encoding, random codes exploit both time and space encoding [18]. In previous methods, the transducers transmit the same pulse for every element. In random codes, however, each transmitter

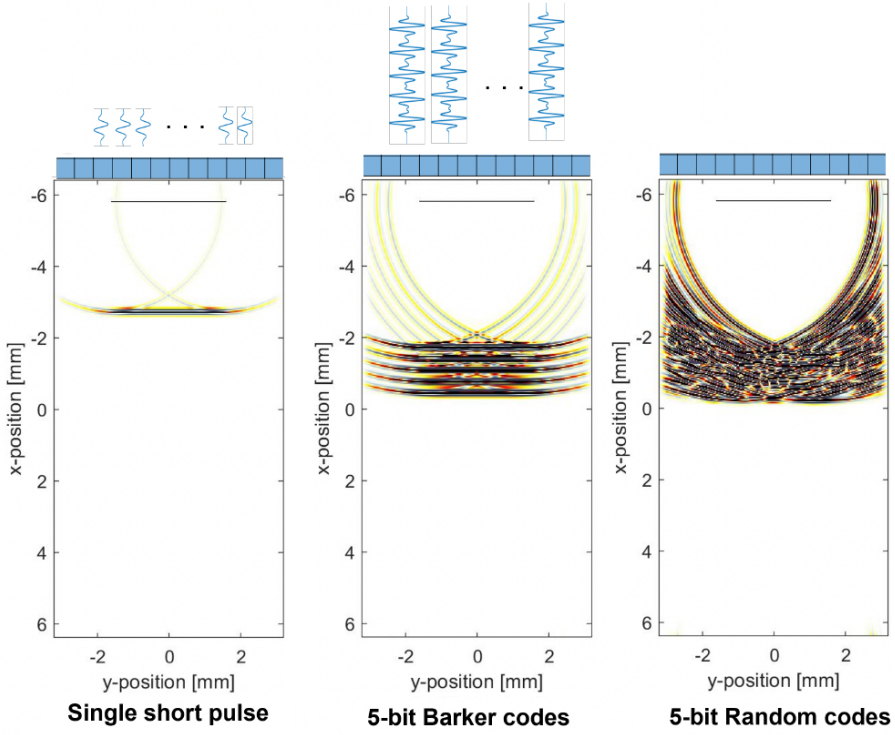

Figure 2.5: The wavefield of simultaneously transmitting a single short pulse, 5-bit Barker, and 5-bit random codes.

transmits different randomly encoded pulses, resulting in ultrasound waves with spatiotemporal interference. This results in low pixel-to-pixel correlations and, hence, high-resolution images. The wavefields of the single short pulse, 5-bit Barker codes, and 5-bit random codes are shown in Fig. 2.5.

2.5. CHALLENGES IN VASCULAR ULTRASOUND IMAGING

The first challenge is that low image quality and artifacts in conventional ultrasound imaging impact its accuracy and reliability [70, 71]. Accurately distinguishing between blood and tissue in ultrasound images is challenging due to the complex acoustic interactions between the ultrasound waves and heterogeneous tissue structures. Various types of noise, such as speckle and artifacts like shadowing, reverberation, and mirror images, distort the ultrasound images [71]. The interaction of ultrasound waves with different tissue types results in artifacts and insufficient interpretation of the structures. Especially in deep tissues, the limited resolution hinders the detection of immediate changes in the body [72]. Model-based imaging results in advancements in image quality compared to conventional ultrasound imaging. However, the earlier mentioned is-

sues are still observed due to the limited enhancement of commonly used model-based imaging techniques such as the matched filter and least squares estimation. More advanced image reconstruction techniques are required to improve the image quality by filtering out the noise and correcting the artifacts. Model-based imaging enables the enforcement of prior information related to the ultrasound images. However, the knowledge of the characteristics of the prior information is still limited and requires further understanding of the blood and tissue properties. Enforcing sparsity is helpful for the representation of microbubbles [22]. On the other hand, sparsity might not be sufficient to represent the blood flow characteristics if there is no microbubble injection. Therefore, statistical priors can improve the ultrasound image reconstruction performance.

Another challenge is that model-based imaging is computationally inefficient compared to delay-and-sum beamforming [73]. Model-based imaging requires advanced and computationally expensive techniques to visualize real-time blood flow. Computational efficiency is significant, especially in real-time applications. Since DAS is computationally more efficient and does not require the pre-computation or storage of a large matrix, it is generally preferred [53]. However, in compressive settings, when for instance a lower number of sensors or distorted unfocused transmissions are used [9, 11, 12], DAS is not applicable, and model-based beamforming is essential. The fast Fourier transform can be applied to reduce the computational complexity; however, it still provides a limited reduction of the computational cost [74]. But, as compression reduces the size of the measurements, it can reduce the computational cost of the algorithms. Another way is to exploit iterative algorithms instead of applying methods that require large inverses.

This thesis focuses on enhancing image quality (SNR and resolution) and reducing artifacts to overcome model-based vascular ultrasound imaging challenges. In several chapters, this work aims to develop image reconstruction algorithms to eliminate noise and artifacts. The approach exploits prior information related to vascular images to improve the SNR and image detail. By utilizing sparsity-based deterministic and statistical priors, the thesis aims to improve the effectiveness of the image reconstruction process. In Chapter 7, this work focuses on enhancements in ultrasound transmission to increase the SNR, penetration depth, and resolution. More specifically, we focus on optimizing the coded excitation scheme for model-based ultrasound imaging. We employ the minimization of the Cramér-Rao lower bound (CRB) over the unknown coding matrix to optimize the code. Due to the high computational cost of the resulting optimization problems, we also introduce a trace-constraint optimization problem based on the Fisher information matrix (FIM).

While noticeable progress has been shown in these areas in the thesis, the computational challenges associated with model-based imaging are only addressed partially, and they mostly remain beyond the scope of this thesis. These issues can be considered in future research.

2.6. CONCLUSION

In this chapter, we have explored the fundamental principles of Doppler and model-based vascular imaging, which offer significant advantages and flexibility over traditional methods in ultrasound imaging systems. Model-based imaging, with mathemat-

ical models and regularization techniques, significantly enhances image quality (SNR, resolution, and artifact suppression). The chapter also detailed model-based reconstruction methods, including least squares estimation and regularization techniques, focusing on sparsity-based regularization and probabilistic frameworks. On the other hand, model-based techniques face substantial computational challenges, particularly in real-time applications. They also partially suffer from the disadvantages of conventional ultrasound imaging regarding image quality, but they are open to improvement with the usage of prior information. The thesis aims to address these issues by developing advanced reconstruction algorithms and optimizing imaging systems to improve SNR, resolution, and penetration depth. Future research must tackle the computational inefficiencies inherent in model-based approaches, exploring new methods and technologies to overcome these limitations.

3

MMV Model for Jointly Sparse Vascular Ultrasound Imaging

Ultrasound imaging of the vasculature has major significance for the detection of cardiovascular diseases and cancer. However, limited spatial resolution or long acquisition times of existing techniques limit the visualization of the microvascular structures. Enforcing sparsity in the underlying vasculature as well as exploiting statistical independence between voxels have become prominent for fast super-resolution imaging. However, such a statistical independence may not be valid for all voxels and may hence lead to a distorted signal model. Here we present an image reconstruction method that exploits the sparsity of the vasculature data without distorting the original signal model. We employ a multiple measurement vector (MMV) model to enforce the joint sparsity over the images at different time instants. To reduce the computational complexity of obtaining the solution, the ℓ_1-SVD method is applied to the MMV model. We demonstrate that our method improves spatial resolution and provides a clear separation between blood vessels. Although our method is slightly slower than existing approaches, it outperforms them in terms of image reconstruction quality.

Part of this chapter is published as: D. Dogan, P. Kruizinga, J.G. Bosch, G. Leus, Multiple Measurement Vector Model for Sparsity-Based Vascular Ultrasound Imaging (2021), [21].

3.1. INTRODUCTION

Ultrasound imaging is widely used in medicine as it is a non-invasive and cost-effective imaging technique [9]. Visualization of the vasculature has major significance for the detection of cardiovascular diseases and cancer. Cancer treatments cause structural changes in the microvascular structures, and hence exposing the microvasculature using ultrasound imaging can provide fast treatment [75]. However, fast detection of the hemodynamic changes over the microvasculature is prevented by spatial resolution limitations [8]. Therefore, there is a need for fast imaging methods that improve the spatial resolution of identifying the microvasculature structures.

Recently, sparse representations of signals [76, 77] have gained popularity in areas such as radar [78], magnetic resonance imaging (MRI) [79], and ultrasound imaging [4]. The specific regularization to solve the ultrasound imaging problem is the sparse structure of the vascular network [8]. A signal is sparse if it can be represented by a vector with most coefficients zero, in an appropriate transform domain [80].

Here, we focus on the sparsity-based ultrasound hemodynamic imaging problem presented in [7, 8]. A method named SUSHI has been developed to improve the spatial resolution in contrast-enhanced ultrasound imaging. It is a fast method exploiting sparsity in the correlation domain of the underlying vasculature structure [6, 5]. This method assumes that the temporal fluctuations in volume cells that belong to different vessels are statistically independent [8].

In this chapter, we propose an image reconstruction method named MMV FISTA that directly uses the sparse structure of the vasculature instead of enforcing sparsity in the correlation domain. Although assuming statistical independence between the flows in different vessels is computationally advantageous, this assumption ignores that blood cells from the same vessel are correlated to each other. Here we aim to avoid such a statistical independence assumption. Since the vasculature at different time instants does not change considerably, we, on the other hand, exploit the temporal correlation of the frames to improve the spatial resolution. For this, we employ a multiple measurement vector (MMV) model and enforce the joint sparsity of the vasculature in different frames [81]. Note that such a joint sparsity problem can be considered as a group lasso problem, with ℓ_1-relaxation [82]. Furthermore, the number of measurements can be decreased using the ℓ_1-SVD method thereby reducing the computational complexity of solving the MMV problem [61].

The remainder of this chapter is organized as follows. In the next section, we define the signal model for the ultrasound imaging problem of the vasculature. In Section 3.3, we present the inverse problem by incorporating the available joint sparsity information. In Section 3.4, we express the steps of the optimization method that solves the inverse problem. Then, we comparatively evaluate the performance of the proposed method with the state-of-the-art. In the final section, we discuss the results and conclude this chapter.

3.2. FORWARD MODEL

In this section, we introduce the problem and relate our proposed approach to an existing method from the literature. In ultrasound imaging, we first construct the image formation model and represent this in the form of a matrix-vector multiplication. For simplicity, we consider an imaging model for a system with a single transmitter that transmits a series of pulses. However, the model can easily be extended to multiple transmitters. At every period Δt a pulse $a(t)$ is sent, where t is assumed to be continuous time and the peak of the pulse is assumed to be located at $t = 0$. At sensor j and pulse period m, the sensor output is modeled as

$$\begin{aligned} z(j,t,m) &= \sum_{z,x} a_j(z,x,t) \sum_{v} f(z,x,v) \exp^{j v m \Delta t} \\ &= \sum_{z,x} a_j(z,x,t) s(z,x,m), \end{aligned} \tag{3.1}$$

where $f(z,x,v)$ is the total amount of scattering of all blood cells in a high resolution volume cell centered at position (z,x) and radial velocity v. Note that $a_j(z,x,t) = a(t - \tau_{z,x,j})$, where $\tau_{z,x,j}$ is the delay related to the distance from the transmitter to the receiver j through the pixel at (z,x). Lastly, $s(z,x,m)$ is the time-varying scattering signal related to the position (z,x).

In commercial ultrasound imaging, users generally only have access to the beamformed data. Applying delay-and-sum (DAS) beamforming on $z(j,t,m)$ from (3.1) at a low resolution, the output of the DAS beamformer for the uth low-resolution pixel at position (z_u, x_u) and pulse period m is given by

$$\begin{aligned} y(z_u,x_u,m) &= \sum_{j} z(j, \tau_{z_u,x_u,j}, m) \\ &= \sum_{j} \sum_{z,x} a(\tau_{z_u,x_u,j} - \tau_{z,x,j}) s(z,x,m) \\ &= \sum_{z,x} h_{z_u,x_u}(z,x) s(z,x,m), \end{aligned} \tag{3.2}$$

where h_{z_u,x_u} is assumed to be the point spread function (PSF) of the imaging system. Note that instead of a DAS, a matched filter can also be used as beamformer for the above formulation. In literature, several works assume h_{z_u,x_u} as a shift-invariant point spread function [83, 84], but this assumption generally does not hold for realistic systems.

After obtaining $y(z_u,x_u,m)$ in (3.2), several preprocessing steps are performed on $y(z_u,x_u,m)$ prior to performing sparse reconstruction. First, a singular value decomposition (SVD) is applied to separate the tissue and blood flow subspaces, and we obtain the blood-related part of $y(z_u,x_u,m)$ [85]. Sparsity will only be enforced over the blood flow subspace. Subsequent to SVD filtering, the phase of the received signal is manipulated to separate different flows (in terms of direction and/or speed) with Doppler processing. This separation is expected to provide additional anatomical information and a sparser structure compared to the original signal [8]. A bank of B bandpass filters is applied to $y(z_u,x_u,m)$ to obtain different videos with different velocities:

$$y^{(b)}(z_u,x_u,m) = \sum_{z,x} h_{z_u,x_u}(z,x) s^{(b)}(z,x,m). \tag{3.3}$$

For $B = 2$, the blood flow is separated into a positive and negative flow, which corresponds to positive and negative frequencies in the Doppler domain. Note that this filterbank is not crucial and we will not use it for all our experiments. To simplify the presentation, in the remainder of this chapter, we will drop the superscript b but keep in mind that the presented models and methods apply to any of the frequency bands.

Some approaches such as SUSHI assume that the signal fluctuations in volume cells that belong to different blood vessels are statistically independent [8, 7]. With this assumption, the autocorrelation of the beamformed and preprocessed measurements $y(z_u, x_u, m)$ in (3.3) can be approximated as

$$r_y(z_u, x_u) = \sum_m |y(z_u, x_u, m)|^2 \approx \sum_{z,x} |h_{z_u,x_u}(z,x)|^2 r_s(z,x), \tag{3.4}$$

where $r_s(z,x) = \sum_m |s(z,x,m)|^2$. In (3.4), the cross-correlation terms are ignored as the signals from different vessels are assumed uncorrelated. Signals from pixels that are in the same vessel are not uncorrelated, but for those signals, the cross terms are still dropped since they are not deemed important for obtaining super-resolution imaging. Notice how the approximation results in a squared absolute-valued PSF, which is narrower than the original PSF and therefore provides improved separation between vessels [8]. Although this approach has some clear advantages, we want to investigate some techniques that do not distort the original signal model of (3.3). Therefore, we propose not to solve the problem in the correlation domain and to directly work with the original signal model in (3.3).

While (3.4) is based on a single measurement vector (SMV) model in the correlation domain [8], we employ an MMV model based on (3.3) which exploits different pulse periods in synergy [81, 61]. Such an MMV model is obtained by stacking the $y(z_u, x_u, m)$ and $s(z,x,m)$ values respectively into a space-time matrix $\mathbf{Y}$ and $\mathbf{S}$, resulting in the model

$$\mathbf{Y} = \mathbf{H}\mathbf{S} + \mathbf{N}, \tag{3.5}$$

where the $\mathbf{H}$ matrix contains $h_{z_u,x_u}(z_l, x_l)$, which is sample of $h_{z_u,x_u}(z,x)$ for pixel $l = 1,\ldots,L$. Here $\mathbf{Y} = [\mathbf{y}_1 ... \mathbf{y}_M]$ and $\mathbf{S} = [\mathbf{s}_1 ... \mathbf{s}_M]$ represent a horizontal concatenation of respectively the vectorized measurements $\mathbf{y}_m$ and unknown images $\mathbf{s}_m$ related to the mth pulse period. Note that $\mathbf{s}_m$ and $\mathbf{y}_m$ include vertically concatenated elements of $s(z_l, x_l, m)$, which corresponds to the lth pixel of $s(z,x,m)$, and $y(z_u, x_u, m)$ for a particular m, respectively. Finally, $\mathbf{N}$ is similarly defined as $\mathbf{Y}$ and represents additional noise that is picked up at the receiving elements.

3.3. INVERSE PROBLEM

In the inverse problem, the goal is to recover the unknown images, $\mathbf{S}$, from their noisy and distorted measurements, $\mathbf{Y}$. Here, the image data is reconstructed by combining information from the measurements with some additional prior (statistical or structural) knowledge about the unknown image data. The sparsity-based MMV image reconstruction problem is formulated as

$$\min_{\boldsymbol{s}} \frac{1}{2} ||\mathbf{Y} - \mathbf{H}\mathbf{S}||_F^2 + \lambda ||\mathbf{S}||_{2,1} \tag{3.6}$$

where the $\ell_{2,1}$-norm is the sparse regularizer enforcing the joint sparsity of the image over different time instants [61]. In the matrix $\mathbf{S}$, the sparsity is enforced only in the spatial domain as the signal is not sparse over the time dimension. Since the vasculature at different time instants is similar, we expect that all columns have the same sparsity pattern. As a result, we exploit the temporal correlation to obtain a better spatial resolution. This is referred to as joint (or group) sparsity in the literature [86], and it can be enforced via the $\ell_{2,1}$-norm. We first compute the ℓ_2-norm of all rows of $\mathbf{S}$. Then, we construct the $\mathbf{s}^{(\ell_2)}$ vector, which stacks the ℓ_2-norms of the rows of $\mathbf{S}$. Finally, $||\mathbf{S}||_{2,1} = ||\mathbf{s}^{(\ell_2)}||_1$ is computed [61].

The main disadvantage of the MMV model is computational complexity. To reduce this cost, the number of measurements is decreased via the SVD, which relies on the fact that the set of vectors $\{\mathbf{y}_m\}_{m=1}^{M}$ lies in a P-dimensional subspace with $P \ll M$. To find this subspace, we first take the SVD of $\mathbf{Y}$ resulting in $\mathbf{Y} = \mathbf{U}\mathbf{L}\mathbf{V}^{\mathsf{H}}$. Then a reduced matrix which contains most of the signal power is obtained as $\tilde{\mathbf{Y}} = \mathbf{U}\mathbf{L}\mathbf{D}_P = \mathbf{Y}\mathbf{V}\mathbf{D}_P$ where $\mathbf{D}_P = [\mathbf{I}_P\,\mathbf{0}]^{\mathsf{T}}$. Similary, we multiply $\mathbf{S}$ and $\mathbf{N}$ by these matrices and obtain $\tilde{\mathbf{S}} = \mathbf{S}\mathbf{V}\mathbf{D}_P$ and $\tilde{\mathbf{N}} = \mathbf{N}\mathbf{V}\mathbf{D}_P$. Now, instead of the large problem in (3.6) we solve the following problem

$$\min_{\tilde{\mathbf{S}}} \; \frac{1}{2}||\mathbf{H}\tilde{\mathbf{S}} - \tilde{\mathbf{Y}}||_F^2 + \lambda||\tilde{\mathbf{S}}||_{2,1}, \tag{3.7}$$

whose solution can be obtained faster. This approach is known at the ℓ_1-SVD method. If the model does not contain any noise and the signal subspace has exactly order P, the solutions of (3.6) and (3.7) are the same, i.e. $\tilde{\mathbf{S}} = \mathbf{S}$. In case of noise, the approach in (3.7) also has a denoising effect. Finally, note that the SVD was already adopted in the preprocessing stage and hence the SVD required to formulate (3.7) does not introduce any additional complexity.

3.4. IMAGE RECONSTRUCTION METHOD

The optimization problem (3.7) can now be solved using any off-the-shelf solvers for MMV inverse problems [87]. M-FOCUSS and standard sparse Bayesian learning (SBL) include a large inverse and thus are computationally complex for large-scale problems [88, 89]. On the other hand, inverse-free SBL [90], ADMM [91] and FISTA [87] do not include a large inverse and hence allow for a fast solution. However, for a fair comparison with SUSHI, which solves the problem using FISTA, we apply the MMV version of FISTA whose updating steps for solving (3.7) are given in Algorithm 1 [92]. Finally, note that $\mathbf{S}$ is easily obtained from $\tilde{\mathbf{S}}$ using a simple matrix product. In MMV FISTA, the computational complexity in each iteration is $\mathcal{O}(L^2P)$ where $s(z_l, x_l, m)$ has L pixels for the mth frame; however, SUSHI has a complexity of $\mathcal{O}(L^2)$.

3.5. NUMERICAL RESULTS

In this section, we comparatively evaluate the performance of the developed method with SUSHI for two scenarios [8].

Algorithm 1: MMV FISTA

Output: $\mathbf{S}$: vectorized unknown images
Input: $\tilde{\mathbf{Y}}$: vectorized measurements, $\mathbf{H}$: sensing matrix, E: number of iterations
initialize $\lambda > 0$, $L_f = ||\mathbf{H}^{\mathsf{H}}\mathbf{H}||_2$, $t^1 = 1$, $\tilde{\mathbf{S}}^0 = \mathbf{Z}^1$, $e = 1$
while $e < E$ **do**
calculate $\mathbf{Q}^e = \mathbf{Z}^e - \frac{1}{L_f}(\mathbf{H}^{\mathsf{H}}\mathbf{H}\mathbf{Z}^e - \mathbf{H}^{\mathsf{H}}\tilde{\mathbf{Y}})$
compute $\tilde{S}^e_{(a,b)} = Q^e_{(a,b)}(1 - \frac{\lambda}{||\mathbf{Q}^e_{(a)}||_2})^+$ where $Q^e_{(a,b)}$ is (a,b)th element of $\mathbf{Q}^e$ matrix, $\mathbf{Q}^e_{(a)}$ is the ath row of $\mathbf{Q}$ matrix and $(x)^+ = \max(x, 0)$.
update $t^{e+1} = 0.5(1 + \sqrt{1 + 4(t^e)^2})$
update $\mathbf{Z}^{e+1} = \tilde{\mathbf{S}}^e + \frac{t^e - 1}{t^{e+1}}(\tilde{\mathbf{S}}^e - \tilde{\mathbf{S}}^{e-1})$
end
$\mathbf{S} = \tilde{\mathbf{S}}^E \mathbf{D}_P^{\mathsf{T}} \mathbf{V}^{\mathsf{T}}$

3.5.1. RESULTS WITH SHIFT-INVARIANT SENSING MATRIX

In this section, we use a shift-invariant $\mathbf{H}$ matrix in (3.5) although the shift-invariancy assumption for the sensing matrix generally does not hold. Note that the sensing matrix for the SUSHI based on the model in (3.4) is equal to the element-wise square of the $\mathbf{H}$ matrix. The shift-invariant matrix-vector multiplication in (3.5) corresponds to a convolution with the point spread function (PSF) in the spatial domain, and hence to an element-wise multiplication in the spatial frequency domain. Therefore, both SUSHI and our method are implemented efficiently in the frequency domain. Here, we use the PSF from [8] to compare the different algorithms.

For the first simulation, we used 101 frames containing two parallel blood vessels where the blood flows in the same direction, represented by $s(z_l, x_l, m)$, for $m = 1, 2, ..., 101$. The high-resolution frames are of size 1024×1024 and their average absolute value is shown in Fig. 3.1a. The background is assumed to have an intensity of 1000 whereas the blood flow has an intensity of $1000 + 30 \times \mathcal{N}(0, 1)$. Here, the low-resolution beamformed images $y(z_u, x_u, m)$, are of size 128×128. White Gaussian noise with 20 dB SNR is added to the measurements. After obtaining $y(z_u, x_u, m)$, which is also displayed in Fig. 3.1a, the tissue is separated from the blood flow by using SVD filtering and keeping only the components related to the blood flow of $y(z_u, x_u, m)$. Since the flow direction is the same, Doppler processing is not considered here.

For SUSHI, the correlation image $r_y(z_u, x_u)$ consists of a single frame as shown in Fig. 3.1b. The temporal mean of the tissue separated image $y(z_u, x_u, m)$ is also given in Fig. 3.1c. To reduce the number of frames to a single frame in the MMV model, the ℓ_1-SVD is applied with $P = 1$. Since we only have a simple image and a well-conditioned sensing matrix of the PSF, a single frame is sufficient. Note though that the ℓ_1-SVD may require more frames for complex structures such as actual vasculature. We further select $\lambda = 0.5$ in (3.7) for 20 dB SNR. The reconstructions with SUSHI and MMV FISTA are shown in Fig. 3.1b and 3.1c, respectively. Here, we plot the reconstructed $r_s(z_l, x_l)$ in (3.4) for SUSHI and the temporal mean of the reconstructed $s(z_l, x_l, m)$ in (3.3) for the MMV FISTA. Although their image reconstruction times are the same for this simula-

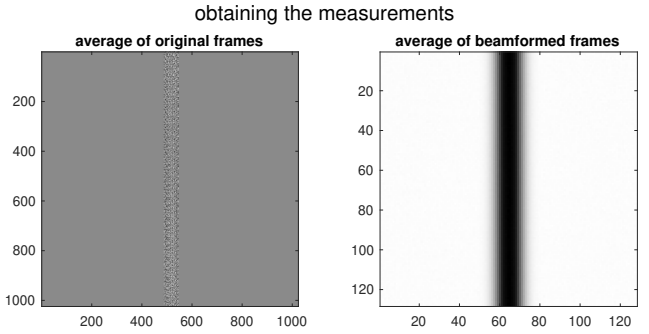

(a)

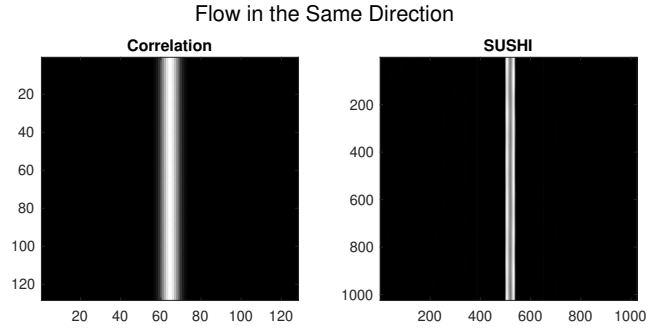

(b)

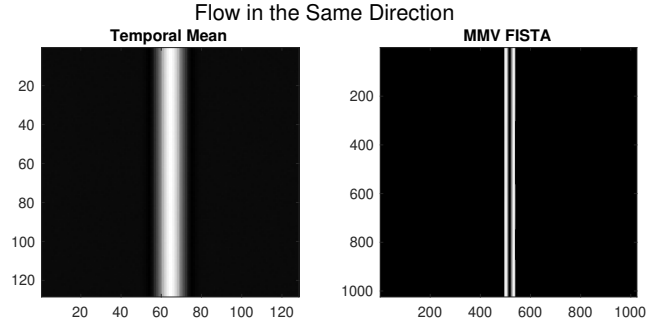

(c)

Figure 3.1: (a) The average absolute value of original and beamformed frames, (b) tissue separated correlation image of measurements and reconstructed correlation image with SUSHI, and (c) temporal mean of tissue separated measurements and reconstructed image with MMV FISTA

tion, the MMV FISTA algorithm outperforms SUSHI. Fig. 3.1b shows that SUSHI could not separate the blood vessels as they are very close to each other and their flow is correlated.

For the second simulation, we use the same setting but this time the synthetic flow moves downward in the right vessel and upward in the left one. We consider a simulation with and without Doppler processing to separate positive and negative flow. Both algorithms perform similarly for the opposing flow image (without Doppler processing) and the positive flow image (with Doppler processing) in Fig 3.2. Since the flow in the different vessels is uncorrelated now, SUSHI (with and without Doppler processing) can separate the vessels.

3.5.2. RESULTS WITH SENSING MATRIX OBTAINED FROM K-WAVE

In this section, instead of using a simulated shift-invariant $\mathbf{H}$ matrix, the image reconstruction is performed with a realistic sensing matrix. Here, we assume matched filter beamforming for $\mathbf{Z} = \mathbf{AS} + \mathbf{W}$, where $\mathbf{X}$ corresponds to the sensor measurements of the ultrasound imaging system (3.1). Using the matched filter $\mathbf{A}$, we can obtain the system in (3.2), $\mathbf{Y} = \mathbf{A}^{\mathsf{H}}\mathbf{X} = \mathbf{A}^{\mathsf{H}}\mathbf{AS} + \mathbf{N} = \mathbf{HS} + \mathbf{N}$, with $\mathbf{H} = \mathbf{A}^{\mathsf{H}}\mathbf{A}$, which is not a shift-invariant matrix. Here, $\mathbf{A}$ is constructed using the k-wave toolbox in MATLAB for an imaging system with 128 transmitters and receivers [93] [10]. Furthermore, the $\mathbf{A}$ matrix is constructed in the frequency domain instead of the time domain. The advantage of a frequency-domain implementation is that number of frequency samples is smaller than the number of time samples, and it provides fast beamforming [94]. Since the sensing matrix is not shift-invariant, a fast multiplication with $\mathbf{H}$ cannot be performed.

For these simulations, we use the same setting as in the second simulation of Section 3.5.1 with opposing flow. However, both $s(z_l, x_l, m)$ and $y(z_u, x_u, m)$ in Fig. 3.3a are now of size 101×101. Therefore, we do not solve a super-resolution problem but a simple image reconstruction problem. Note that, even though $\mathbf{H}$ is a square matrix, the system is still highly ill-posed and requires regularization. The tissue is separated from the blood flow by using SVD filtering to obtain the blood-related part of $y(z_u, x_u, m)$ but no Doppler processing is considered here.

The tissue separated correlation image $r_y(z_u, x_u)$ and the SUSHI reconstruction $r_s(z_l, x_l)$ are shown in Fig. 3.3b. The number of frames are reduced to 1, 5 and 10 using the ℓ_1-SVD method for the reconstructions with MMV FISTA. Finally, the full set of frames are used. The temporal mean of the tissue separated images $y(z_u, x_u, m)$ and recovered images $s(z_l, x_l, m)$ are displayed in Fig. 3.3c for several cases. When a single frame is used, the image reconstruction performance of SUSHI and MMV FISTA are similar. Still, the bottom part of the image is more visible with MMV FISTA. Since SUSHI squares the sensing matrix and the reconstructed image in the forward model, high-intensity parts become stronger, and low-intensity parts weaken. The image reconstruction performance of our method improves with an increasing number of frames. Each iteration of SUSHI and MMV FISTA with a single frame takes 0.04 seconds. Each iteration of MMV FISTA with 5, 10, and all frames takes 0.05, 0.06, and 0.2 seconds, respectively. Therefore, increasing the number of frames does not cause a huge increase in the computational time of the MMV FISTA algorithm.

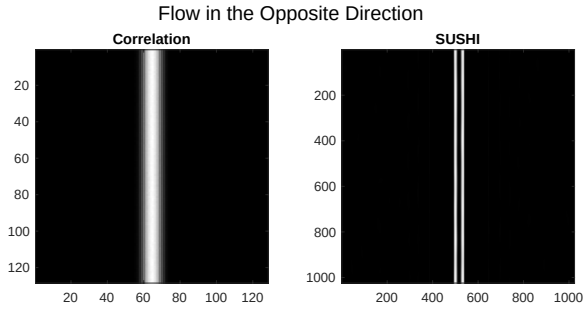

(a)

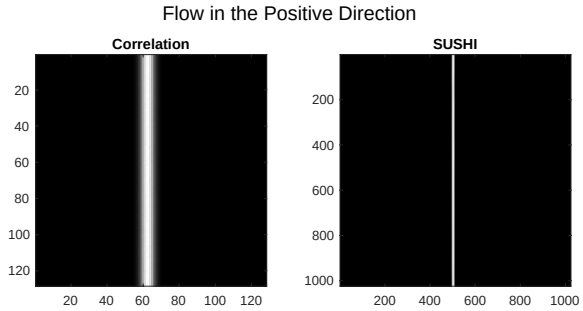

(b)

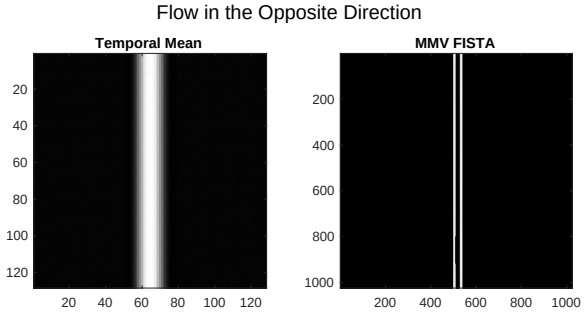

(c)

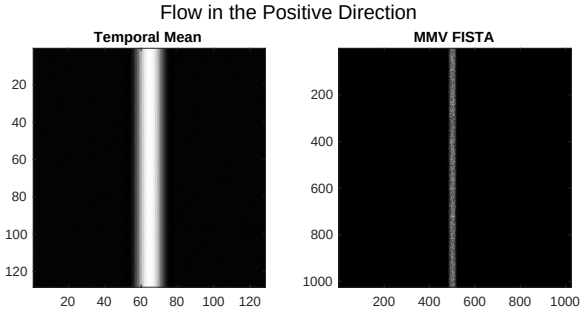

(d)

Figure 3.2: (a),(b) Tissue separated and reconstructed images with SUSHI, and (c),(d) temporal mean of tissue separated and reconstructed images with MMV FISTA

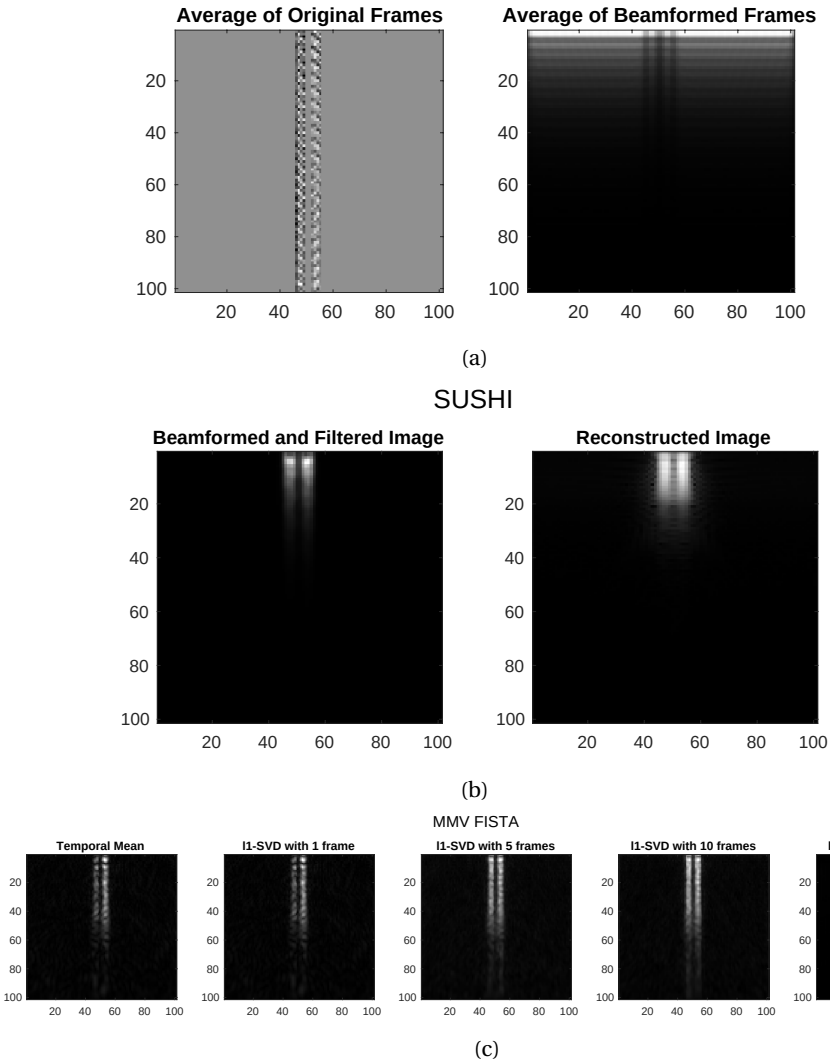

Figure 3.3: (a) The average absolute value of original and beamformed frames, (b) tissue separated and reconstructed correlation images with SUSHI, (c) temporal mean of tissue separated images and reconstructed images with MMV FISTA when 101 frames are reduced to 1, 5 and 10 frames, and all frames are used

3.6. CONCLUSION AND DISCUSSION

In this chapter, we have proposed an image reconstruction method that directly exploits the joint sparse structure of the vasculature. The ℓ_1-SVD algorithm is performed over the measurements to reduce the computational complexity. We evaluated the performance of our method within two different simulation settings. In the first set of experiments, we demonstrated that our method improves spatial resolution and provides a clear separation between very close vessels. Our method seems slightly slower than SUSHI for the second set of more realistic experiments, but its image reconstruction quality is better under appropriate settings.

We first exploited the joint sparse structure with deterministic prior. We aim to consider a statistical prior in the next section, which might be more suitable for the ultrasound imaging data. As the structure of the brain vasculature may include additional properties in addition to sparsity, the statistical priors can be more suitable for the target problem. The focus of the following sections will be the development of ultrasound image reconstruction algorithms with statistical priors such as sparse Bayesian learning and its variants.

4

SPARSE ALGORITHMS FOR MODEL-BASED COMPRESSIVE VASCULAR ULTRASOUND IMAGING

Recently, there has been a growing focus on reducing the amount of measured sensor data in the ultrasound imaging field while maintaining the image quality. Compressive sensing allows for a combination of signal compression with sensing to reduce the hardware complexity in applications such as three-dimensional ultrasound imaging. Unlike the classical delay-and-sum (DAS) beamforming approach, model-based image reconstruction techniques, such as matched filtering, are used to solve such problems. Given the number of measurements is often smaller than the number of unknowns, advanced reconstruction methods are required to solve these ill-conditioned problems. MMV FISTA, the deterministic image reconstruction method proposed in the previous chapter, can be useful for solving such problems using the vasculature's jointly sparse and connected structure. This chapter presents a statistical alternative method: sparse Bayesian learning (SBL) with fixed-point iterations. While SBL is well-established in the literature, its application to the ultrasound imaging domain without microbubbles is novel. In a two-dimensional compressive vascular ultrasound imaging problem, both SBL and MMV FISTA methods outperform the matched filter regarding signal-to-noise ratio (SNR). While MMV FISTA often has lower computational complexity than SBL, it requires a time-consuming manual parameter tuning procedure. Besides, the image reconstruction quality with SBL is slightly higher than MMV FISTA. However, the improvements obtained with both methods on real data are limited to SNR improvements rather than revealing fine vascular details. Therefore, further advancements are required to visualize the detailed structure of the vasculature.

4.1. INTRODUCTION

The compression of the measured sensor data in ultrasound imaging has been studied recently. In minimally invasive surgery, where the number of data cables is limited due to the space, data compression can have a potential [95]. Transferring all data from a dense imaging array is challenging for high-frame-rate, high-quality imaging. Instead of using a Nyquist-sampled sensor array, data compression during sensing can be an alternative. Hence, the data can be reduced without complex hardware compressing the array's signals.

Data compression can be useful in three-dimensional (3D) ultrasound, a powerful imaging tool for many biomedical diagnostic applications [9, 10]. However, it does not have a vast application area as conventional 3D ultrasound requires high hardware complexity and two-dimensional (2D) arrays that consist of thousands of sensors. In previous studies [9, 10], a compressive sensing-based method is proposed using a single channel sensor for 3D imaging. A spatially coded acoustic field that allows detailed 3D reconstructions is generated by placing an aberration mask upon the sensor. The compression is combined with sensing and realized by coding the ultrasound signals while they are transmitted or received by an acoustic transducer [9, 10]. As this approach required the rotation of the sensor to attain a sufficient number of measurements for the solution of the imaging problem, a more practical approach with a higher number of sensors is proposed [11, 12].

In these compressive ultrasound imaging systems, the number of measurements is often smaller than the number of unknowns. The matched filter or least-squares QR (LSQR) approaches might not be sufficient to capture inherent prior information related to ultrasound images. Therefore, advanced reconstruction methods that exploit the ultrasound image properties can be useful to solve this ill-conditioned problem. Sparse representations of signals [76, 77] are widely used in the areas such as radar [78], magnetic resonance imaging (MRI) [79], spectral imaging [96, 97] and ultrasound imaging [4, 53]. Specifically, the sparse structure of the vascular network is proposed as the specific regularization to solve the ultrasound imaging problem, which can be included as a statistical prior on the image [8].

A deterministic joint-sparsity-based approach to this problem was presented in Chapter 3. In this chapter, on the other hand, we develop methods under a probabilistic framework, focusing on the conventional sparse Bayesian learning (SBL) algorithm with fixed-point iterations. The classical SBL algorithm assumes that unknown data elements are independent random variables with zero-mean Gaussian distribution. Such a statistical approach is known to enforce the sparsity in the literature [63]. This Gaussian prior not only captures sparsity but also offers greater flexibility to encode prior knowledge about the data compared to deterministic approaches. The variance of the Gaussian data elements (e.g., pixel intensities in ultrasound imaging) is treated as a hyperparameter learned from the observations by maximizing the likelihood function, usually using the expectation-maximization (EM) algorithm [98]. Alternatively, the fixed-point iterations method is used to solve the likelihood problem instead of the EM algorithm for its speed. The fixed point iterations method is an empirical strategy, but it provides a faster convergence rate than EM algorithm [63, 64].

The novel contribution of this chapter is to introduce the usage of a statistical approach for a compressive vascular ultrasound imaging problem and compare its performance with the previously proposed algorithms. Although a similar application of the SBL can be found in the literature of super-resolution ultrasound imaging with contrast-enhanced microbubbles [22], we are the first to propose the presented methods for compressive ultrasound imaging scenario by enforcing the prior information regarding the tissue-separated vasculature data. While microbubbles present a sparse structure, the prior information regarding the vasculature data is still available to explore. The SBL algorithm with fixed-point iterations is presented to enforce the joint sparsity of the vascular data at different time instants.

We evaluate the performance of this statistical approach in comparison to the matched filter and MMV FISTA algorithms across various scenarios [63]. Although our method achieves improvements in signal-to-noise ratio (SNR), further work is required to visualize fine vascular details, as the improvements in real data are limited to SNR enhancements rather than revealing detailed structures.

The remainder of this chapter is organized as follows. In the next section, we define the signal model for the compressive vascular ultrasound imaging problem. Section 4.3 offers the SBL method that solves the presented problem. Then, we analyze the performance of the proposed methods in Section 4.4, followed by a discussion and conclusion in the final section.

4.2. IMAGE FORMATION MODEL

For the proposed compressive ultrasound imaging system, we first construct the image formation model and represent this in the form of a matrix-vector multiplication. For this, we consider a plane-wave imaging model for a system with multiple transmitters. The proposed setup consists of I elements in a linear transducer array. A plane-wave transmit scheme was employed to acquire signals. All elements are excited jointly with appropriate delays (e.g., when a plane-wave transmission under a non-zero angle is considered) and received signals from all elements are recorded.

To implement the compressive ultrasound imaging system, the transducer is divided into R equally sized groups of elements. The measurement of each group is constructed by summing the received signals of the individual elements within that group. This summation is not a subsampling strategy but an alternative method to reduce the number of measurements without losing valuable information from all elements.

A similar group summation has been previously implemented in the emulation of compressive ultrasound imaging with coded aperture [11, 12]. However, the scenario presented in this chapter differs from the emulation of coded aperture, as we do not implement any delays in group summation. We take the group summation of the non-neighboring receivers instead of the neighboring receivers. We have chosen this simple scenario to measure the performance of the proposed algorithm. Note that various types of realistic compressions can be attained in ultrasound imaging systems and the proposed imaging reconstruction method is applicable to both compressive and non-compressive scenarios.

In the proposed compressive ultrasound imaging system, at every period Δt, a pulse

$a(t)$ is sent from each transmitter, where t is assumed to be continuous time, and the pulse peak is assumed to be located at $t = 0$. At sensor $r = 1,\dots,R$ and the pulse period $m = 1,\dots,M$, the sensor output is modeled as

$$z(r,t,m) = \sum_j \sum_{z,x} \sum_i c_{r,j}\, a_{j,i}(z,x,t)\, s(z,x,m) + n(r,t,m), \tag{4.1}$$

where $s(z,x,m)$ is the time-varying scattering signal at position (z,x) and $n(r,t,m)$ corresponds to the white Gaussian noise for the measurement $z(r,t,m)$. Note that $a_{j,i}(z,x,t) = a(t-\tau_{z,x,j,i})$, where $\tau_{z,x,j,i}$ is the sum of the pulse delay adopted at the transmitter i and the delay related to the distance from the transmitter i to the receiver j through the pixel at (z,x). The binary coefficient $c_{r,j} \in \{0,1\}$ indicates whether the received signal from receiver j is included in the rth group summation. If the received signal j has contribution to the rth group, then $c_{r,j} = 1$; otherwise $c_{r,j} = 0$. In other words, it encodes the predefined grouping pattern of the receivers in the compressive setup. In the remainder of this chapter, we work in the frequency domain instead of the time domain since it enables faster computation. We denote the sampled continuous-time Fourier transform of $z(r,t,m)$ and $a_{j,i}(z,x,t)$ by $z(r,\omega,m)$ and $a_{j,i}(z,x,\omega)$, respectively.

Then, we employ an MMV model that exploits different pulse periods in synergy [81, 61]. Such an MMV model is obtained by stacking the $z(r,\omega,m)$ and $s(z,x,m)$ values respectively into a measurement matrix $\mathbf{Z}$ and space-time matrix $\mathbf{S}$, resulting in the model

$$\mathbf{Z} = \mathbf{AS} + \mathbf{N}, \tag{4.2}$$

where the matrix

$$\mathbf{A} = \mathbf{C}\begin{bmatrix} \mathbf{a}_{1,1} & \dots & \mathbf{a}_{1,L} \\ \vdots & \ddots & \vdots \\ \mathbf{a}_{I,1} & \dots & \mathbf{a}_{I,L} \end{bmatrix}, \mathbf{a}_{j,l} = \begin{bmatrix} \sum_{i=1}^{I} a_{j,i}(z_l,x_l,\omega_1) \\ \vdots \\ \sum_{i=1}^{I} a_{j,i}(z_l,x_l,\omega_F) \end{bmatrix}$$

and $\mathbf{Z}$, $\mathbf{S}$ and $\mathbf{N}$ are defined similar to the equation in (2.3). To briefly recap, L represents the number of pixels, F is the number of frequency samples, and M is the number of frames in the ultrasound imaging video. $\mathbf{Z} = [\mathbf{z}_1 ... \mathbf{z}_M]$ and $\mathbf{S} = [\mathbf{s}_1 ... \mathbf{s}_M]$ represent a horizontal concatenation of respectively the vectorized measurements $\mathbf{z}_m \in \mathbb{C}^{RF}$ and vectorized unknown images $\mathbf{s}_m \in \mathbb{C}^{L}$ related to the mth pulse period. Here, $\mathbf{z}_m$ and $\mathbf{s}_m$ include vertically concatenated elements of $z(r,\omega,m)$ and $s(z,x,m)$ for a particular m. Now we introduce $\mathbf{C} \in \mathbb{R}^{RF \times IF}$, which is a matrix that consists of 1s and 0s to select the candidate elements for receiver group summation. Then, in this chapter, $\mathbf{A} \in \mathbb{C}^{RF \times L}$ is defined as the compressive measurement matrix. From now on, the total number of measurements is given by $RF = N$ for simplicity. Finally, $\mathbf{N}$ is similarly defined as $\mathbf{Z}$ and represents additional Gaussian noise. The model is then generalized to include multiple measurements involving different steering angles and differently coded grouping combinations similar to the case in (2.5).

4.3. IMAGE RECONSTRUCTION METHOD

The optimization problem (4.2) can be solved using standard solvers for MMV inverse problems. FISTA for MMV problems [87] is presented in the previous section, and now

SBL [89] is proposed to solve the vascular ultrasound imaging problem. While SBL is slower than MMV FISTA due to the large inverse in each iteration, it does not require manual parameter optimization, such as for λ in (3.6). The conventional SBL algorithm is based on the expectation-maximization (EM) update rule, which converges slower. However, using fixed-point (FP) iterations for SBL results in faster convergence [39, 63].

In this section, we apply Bayesian inference to obtain the posterior distribution of the complex density magnitudes of the pixels from the likelihood and prior model [63]. The conditional probability density function (PDF) for $\mathbf{Z}$ given the sources $\mathbf{S}$ is complex Gaussian with noise variance σ^2:

$$p(\mathbf{Z}|\mathbf{S};\sigma^2) = \frac{\exp\left(-\frac{1}{\sigma^2}||\mathbf{Z}-\mathbf{AS}||_F^2\right)}{(\pi\sigma^2)^{NM}}. \tag{4.3}$$

In the classical SBL model, the complex pixel density magnitudes $s(z_l, x_l, m)$ are assumed independent across different frames and across each other as

$$p_m(s(z_l, x_l, m), \gamma_l) = \mathscr{CN}(0, \gamma_l). \tag{4.4}$$

Using Bayes' rule conditioned on $\mathbf{\Gamma}$ and σ^2, the posterior distribution of the sources is

$$p(\mathbf{S}|\mathbf{Z};\mathbf{\Gamma},\sigma^2) = \mathscr{CN}(\mu_\mathbf{S}, \mathbf{\Sigma_s}), \tag{4.5}$$

where the mean and covariance are given by

$$\mu_\mathbf{S} = \mathbf{\Gamma}\mathbf{A}^\mathsf{H}\mathbf{\Sigma}_\mathbf{z}^{-1}\mathbf{Z}, \tag{4.6}$$

$$\mathbf{\Sigma_s} = \mathbf{\Gamma} - \mathbf{\Gamma}\mathbf{A}^\mathsf{H}\mathbf{\Sigma}_\mathbf{z}^{-1}\mathbf{A}\mathbf{\Gamma}. \tag{4.7}$$

The data covariance matrix is

$$\mathbf{\Sigma_z} = \sigma^2\mathbf{I}_N + \mathbf{A}\mathbf{\Gamma}\mathbf{A}^\mathsf{H}. \tag{4.8}$$

Using MAP estimation, we obtain $\hat{\mathbf{S}}^{MAP} = \mu_\mathbf{S}$, where the diagonal of $\mathbf{\Gamma}$ controls the row sparsity of $\hat{\mathbf{S}}^{MAP}$.

The hyperparameters $\mathbf{\Gamma}$, σ^2 are estimated by type-II maximum likelihood. The probability density function is

$$p(\mathbf{Z};\mathbf{\Gamma},\sigma^2) = \frac{e^{-\mathrm{tr}(\mathbf{Z}^\mathsf{H}\mathbf{\Sigma}_\mathbf{z}^{-1}\mathbf{Z})}}{(\pi^N \det\mathbf{\Sigma_z})^M} \tag{4.9}$$

and its log-likelihood function is

$$\log p(\mathbf{Z};\mathbf{\Gamma},\sigma^2) \propto -\mathrm{tr}(\mathbf{Z}^\mathsf{H}\mathbf{\Sigma}_\mathbf{z}^{-1}\mathbf{Z}) - M\log\det\mathbf{\Sigma_z}. \tag{4.10}$$

The hyperparameters $\hat{\mathbf{\Gamma}}$ and $\hat{\sigma}^2$ are estimated as

$$(\hat{\Gamma}, \hat{\sigma}^2) = \mathrm{argmax}_{\hat{\Gamma}\geq 0, \hat{\sigma}^2\geq 0} \log p(\mathbf{Z};\mathbf{\Gamma},\hat{\sigma}^2). \tag{4.11}$$

After iteratively estimating $\hat{\mathbf{\Gamma}}$, $\hat{\sigma}^2$, and $\Sigma_\mathbf{z}^{-1}$, $\mathbf{S}$ is obtained from (4.6).

The key step is the estimation of $\mathbf{\Gamma}$, which controls the sparsity of $\mathbf{S}$. The derivative of (4.10) with respect to γ_l is

$$\frac{\partial \log p(\mathbf{Z};\mathbf{\Gamma},\sigma^2)}{\partial\gamma_l} = ||\mathbf{Z}^\mathsf{H}\mathbf{\Sigma}_\mathbf{z}^{-1}\mathbf{a}_l||_2^2 - M\mathbf{a}_l^\mathsf{H}\mathbf{\Sigma}_\mathbf{z}^{-1}\mathbf{a}_l. \tag{4.12}$$

Algorithm 2: SBL with fixed-point iterations method

Output: S: unknown data
Initialize $\sigma^2 = 0.1$, $\text{diag}(\mathbf{\Gamma}) = \mathbf{1}$, $\epsilon_{min} = 0.001$, $E_{max} = 500$
while $e < E_{max}$ *and* $\epsilon_{min} < \epsilon$ **do**
  $e = e + 1$, $\mathbf{\Gamma}^{old} = \mathbf{\Gamma}^{new}$
  calculate $\mathbf{\Sigma_z} = \sigma^2 \mathbf{I}_N + \mathbf{A\Gamma A}^{\mathsf{H}}$
  update γ_l^{new} with (4.14)
  $\mathbf{\Gamma} = \text{diag}(\gamma_1, ..., \gamma_l)$
  $\mathscr{K} = \{l \in \mathbb{N} | K \text{ largest peaks in } \mathbf{\Gamma}\} = \{l_1, \dots l_K\}$
  $\mathbf{A}_{\mathscr{K}} = (\mathbf{a}_{l_1}, \dots, \mathbf{a}_{l_K})$
  update $(\sigma^2)^{new}$ with (4.15)
  $\epsilon = ||\text{diag}(\mathbf{\Gamma}^{new} - \mathbf{\Gamma}^{old})||_1 / ||\text{diag}(\mathbf{\Gamma}^{old})||_1$
  end
$\tilde{\mathbf{S}} = \mathbf{\Gamma A}^{\mathsf{H}} \mathbf{\Sigma_z}^{-1} \mathbf{Z}$

Setting this equal to zero results in

$$||\mathbf{Z}^{\mathsf{H}} \mathbf{\Sigma_z}^{-1} \mathbf{a}_l||_2^2 = M \mathbf{a}_l^{\mathsf{H}} \mathbf{\Sigma_z}^{-1} \mathbf{a}_l. \tag{4.13}$$

This leads to the fixed-point update rule for γ_l:

$$\gamma_l^{new} = \frac{\frac{\gamma_l^{old}}{\sqrt{M}} ||\mathbf{Z}^{\mathsf{H}} \mathbf{\Sigma_z}^{-1} \mathbf{a}_l||_2}{\sqrt{\mathbf{a}_l^{\mathsf{H}} \mathbf{\Sigma_z}^{-1} \mathbf{a}_l}}. \tag{4.14}$$

To ensure convergence, we require $\gamma_l^{new} = \gamma_l^{old}$.

For fast convergence, a good estimate of the noise variance is crucial. We assume that the number of non-zero elements K is approximately known, and a rough guess for the number of sources suffices. The update rule for σ^2 follows [63]:

$$\sigma^2 = \frac{\text{tr}(\mathbf{S_z} - \mathbf{A}_{\mathscr{K}} \mathbf{A}^{\dagger} \mathbf{S_z})}{N - K} = \hat{\sigma}^2. \tag{4.15}$$

The overall SBL with fixed-point iterations is summarized in Algorithm 2.

4.4. NUMERICAL RESULTS

In this section, we comparatively evaluate the performance of the matched filter, MMV FISTA and SBL performance with the fixed-point iterations method for various scenarios. We use a linear plane-wave imaging system for two-dimensional ultrasound image reconstruction. The original ultrasound imaging system comprises 128 transmitters and receivers and $D = 20$ steering angles. This system's DAS/matched filter result is obtained as reference reconstruction data for the comparisons. We first use a compressive scenario with $I = 128$ elements in a linear array and $R = 16$ grouped measurements to implement the other algorithms. The number of steering angles is kept as $D = 20$. In the

second scenario, we consider a case without grouping the receiver measurements where $I = R = 128$ but reducing the number of steering angles to $D = 2$.

We generate a model-based $\mathbf{A}$ matrix to image $z \times x = 384 \times 512$ pixels in an imaging area of 19.2 mm by 25.6 mm with inter-pixel distances $dz = dx = 5 \times 10^{-5}$. To reduce the size of $\mathbf{A}$ matrix for efficient computation, only the elements of $\mathbf{A}$ matrix that corresponds to the imaging region of interest (ROI) of $z \times x = 254 \times 129$ pixels with inter-pixel distances of $dz = 5 \times 10^{-5}$ and $dx = 10^{-4}$ are considered. Here, the ROI covers 12.7 mm by 12.9 mm area. Lastly, the transmit center frequency of the probe is $f_0 = 15.625 \times 10^6$ for a Gaussian pulse.

We construct $\mathbf{A}$ matrix with k-Wave Toolbox. We first simulate the one-way wavefields for all the pixels in the ROI. For this, we first assume a single source in the center of the linear array and a flat plate of sensors corresponding to the simulation grid to calculate the one-way impulse response for each pixel location [99]. After computing the one-way wavefields for the element in the center of the transducer, we shift the simulation grid 128 times to the left and right to imitate the behavior of the transmitters at all locations. Since convolution in the time domain corresponds to element-wise multiplication in the frequency domain, we compute $a_{j,i}(z_l, x_l, \omega_f)$ by multiplying two one-way impulse responses element-wise in the frequency domain for I transmitters and receivers, F frequencies, and L pixels. The contribution of all transmitters to each pixel is summed as $\sum_{i=1}^{I} a_{j,i}(z_l, x_l, \omega_f)$, as given in (4.2). After concatenating over F frequencies, we obtain $\mathbf{a}_{j,l}$ for each receiver j and pixel l. Thereafter, we repeat it for all receivers and pixels and multiply the resulting matrix by $\mathbf{C}$ and create the final $\mathbf{A}$ matrix in (4.2).

The proposed RF data is measured using a 128 elements linear array transducer (L7-4) and a Vantage 256 system (Verasonics). The system was deployed in a mouse brain, and raw signals correspond to a typical region of interest for vasculature imaging. We first obtain RF measurements for 128 elements in the emulated linear array. The number of frames in the vasculature video is $M = 197$. Note that the measurements are taken at 20 different steering angles between $[-7.5, 7.5]^\circ$ to provide a sufficient variety of measurements.

Before enforcing the sparsity with the proposed algorithms, we separate the tissue from the vasculature data using the procedure in section 2.2. Since SVD filtering is a linear operation, we initially apply SVD filtering on the RF data and separate the first $M_t = 60$ components, which correspond to the tissue. M_t is determined empirically by observing the matched filter reconstructions. To enforce the joint sparsity on the vasculature data, applying SVD filtering on RF data is necessary. Otherwise, the vasculature with the tissue cannot be considered as sparse. Then, the unknown vasculature image is reconstructed with MMV FISTA and SBL algorithms in addition to matched filter results. $\lambda = 15 \times 10^8$ is set for MMV FISTA where manual tuning of λ takes significant time. In contrast, SBL does not require parameter optimization. After 10-15 iterations, neither MMV FISTA nor SBL significantly improved image quality, and hence the results are taken from the 10th iteration.

To form the final image for visualization, the reconstructed image data is cropped and its size is reduced to 171×99, which covers an area of 8.55 mm by 9.9 mm. As a post-processing step, the reconstructed images are upsampled with new pixel distances of $dz = dx = 2.5 \times 10^{-5}$. While upsampling, the Tukey window with fraction $r = 0.5$ elim-

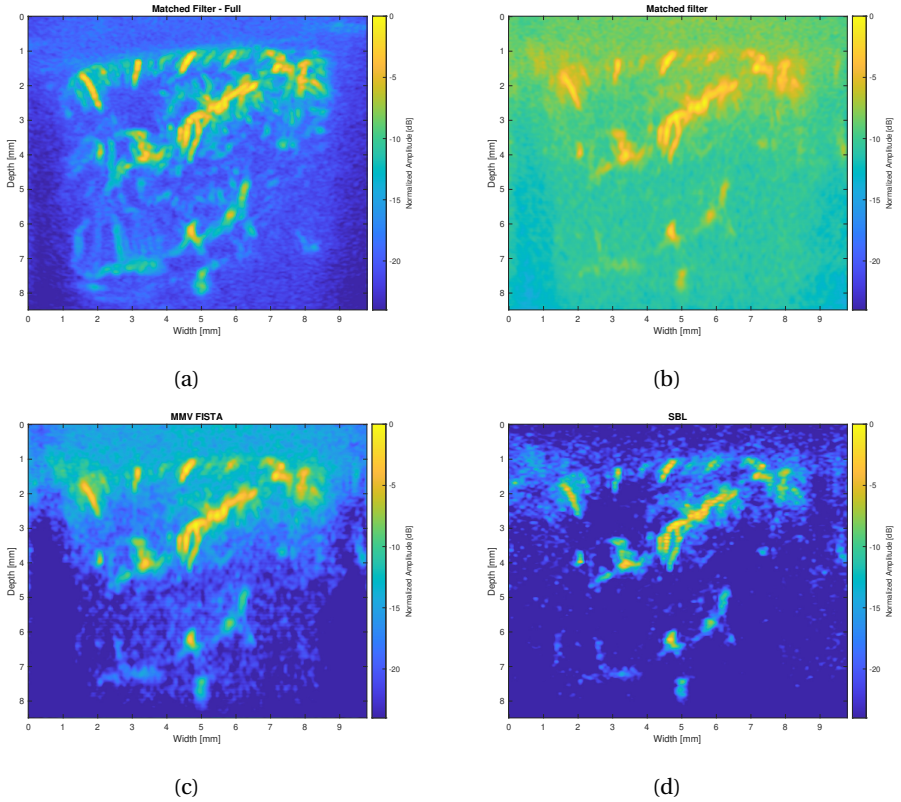

Figure 4.1: Comparison of MF, MMV FISTA and SBL for mouse brain with 16 receivers with 20 steering angles when we image them in the same dynamic range

inates the aliasing effects.

Delay-and-sum (DAS) beamformer or matched filter reconstructions with complete measurement set are shown in Fig. 4.1a. Since no ground truth is available, we consider these reconstructions as reference images from the non-compressive setting. We then evaluate the power Doppler image (PDI) quality of the reconstructions as shown in Fig. 4.1 and 4.2. In Fig. 4.1, the dynamic range is selected equally for all of the algorithms, but in Fig. 4.2, the dynamic range is selected to observe the vasculature with all algorithms in the best possible way. Since no ground truth exists, qualitative visual inspection is used for evaluation. In Fig. 4.1, MMV FISTA and SBL algorithms outperform the matched filter visually for the same dynamic range. While the matched filter has a low contrast between the vasculature and background reconstruction, the SNR and contrast is significantly improved via MMV FISTA and SBL algorithms. The sharpest image reconstruction is attained via SBL algorithm though it exhibits a slight grainy structure. Note also that, MMV FISTA requires manual parameter tuning of λ while SBL does not, making SBL more practical.

Then, in Fig. 4.2, the average power Doppler of an area outside the vascular region

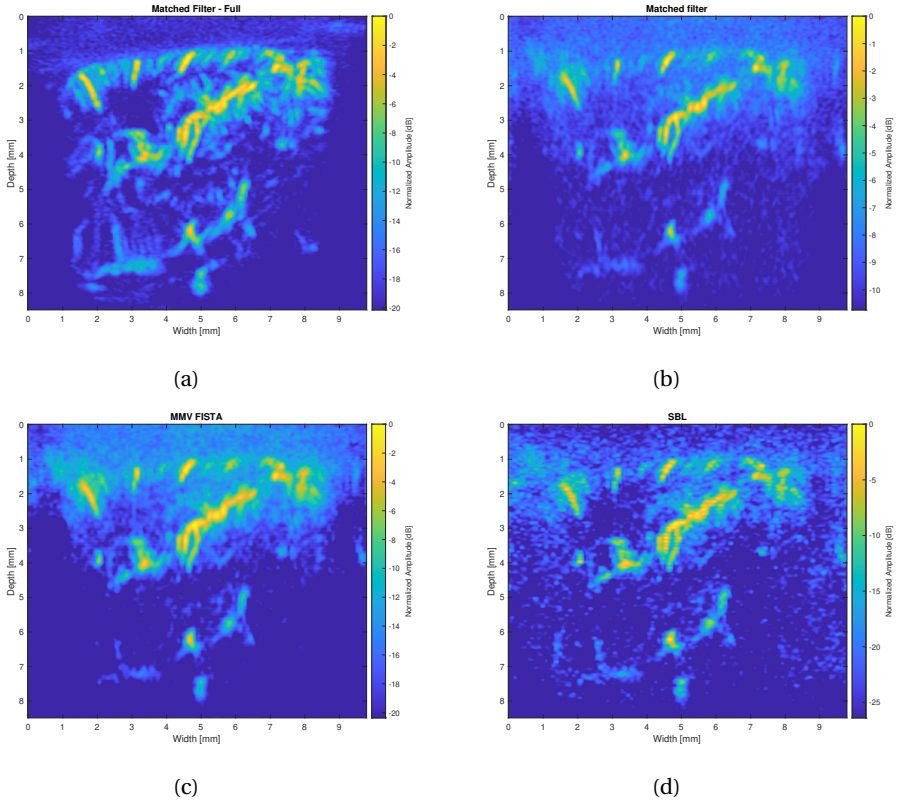

Figure 4.2: Comparison of MF, MMV FISTA and SBL for random scatterers with 16 receivers with 20 steering angles when we image them in the suitable dynamic range

was used as the minimum value for the dynamic range in each method for the best visualization of each method. Here, MMV FISTA and SBL provide a limited improvement over the matched filter. Enhancements are mainly in SNR, contrast, and background suppression rather than fine detail reconstruction. Note that none of the advanced algorithms fully recover the fine details in Fig. 4.1a, which is the DAS result of the non-compressive ultrasound imaging system by using the complete measurements. Since advanced algorithms are highly time-consuming compared to matched filter, their usage seems impractical to attain improved SNR without revealing the additional structural details.

As an additional setup, we consider the case without doing group summation over the measurements from 128 receivers. Instead, we only use 2 steering angles rather than 20. Although this does not involve compressing the array measurements, the aim is to observe how MMV FISTA and SBL perform with a limited number of steering angles. These angles are selected as the central two from the 20 steering angles, corresponding to $[-0.39, 0.39]^\circ$. In that case, the improvements obtained with the matched filter and SBL seem more noticeable both in Fig. 4.3, where images are visualized in the same

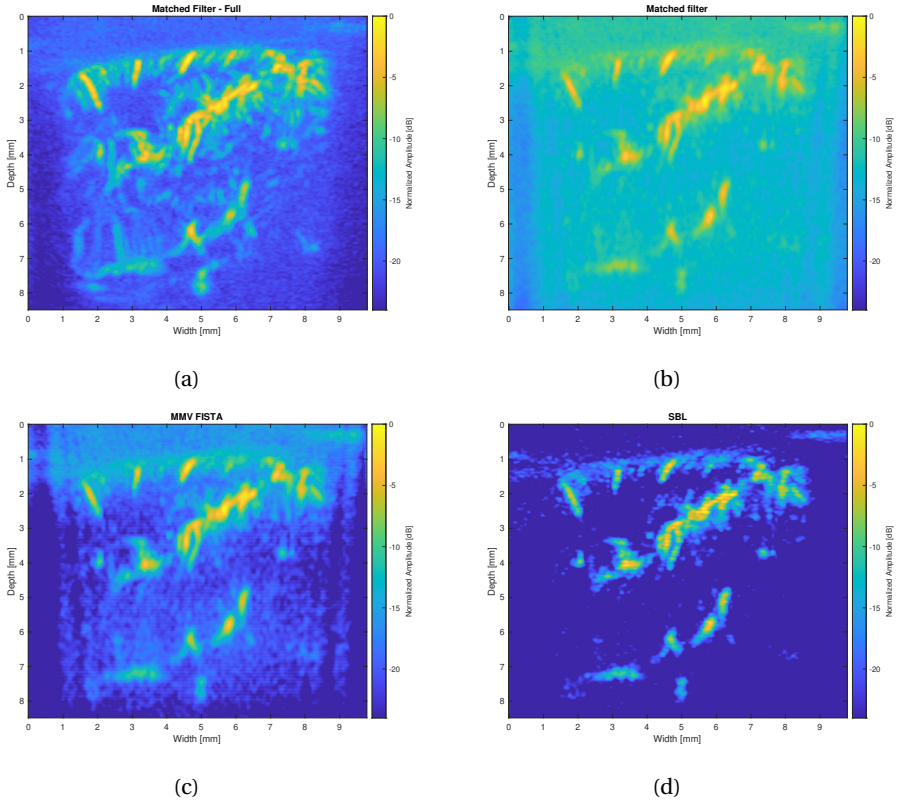

Figure 4.3: Comparison of MF, MMV FISTA and SBL for mouse brain with 128 receivers with 2 steering angles when we image them in the same dynamic range

dynamic range, and Fig. 4.4, where all images are shown in the best possible dynamic ranges. Even in Fig. 4.4, the image details seem more apparent with SBL compared to other algorithms, where MMV FISTA provides a decent result. Although it is not a drastic improvement, the superiority of advanced algorithms over the matched filter in SNR, contrast and image details is evident. Still, their usage is inconvenient due to the computational complexity of the advanced algorithms, and this improvement does not justify the computational time of these advanced algorithms.

The reason behind such a limited improvement with advanced methods can be explained by the inherent characteristics of the vascular imaging data or the ultrasound imaging system. Although theoretically, joint sparsity is expected to enhance image quality, the tissue-separated vascular data might not perfectly adhere to the joint sparsity assumption. It might require additional assumptions, such as jointly block sparsity or hierarchical sparsity, which can be exploited via statistical models, or sparsity in another domain, which can be leveraged within deterministic models. The other explanation for this limited improvement is that the matched filter is already well-suited for the physical constraints of the imaging system. These constraints may limit the visibility of

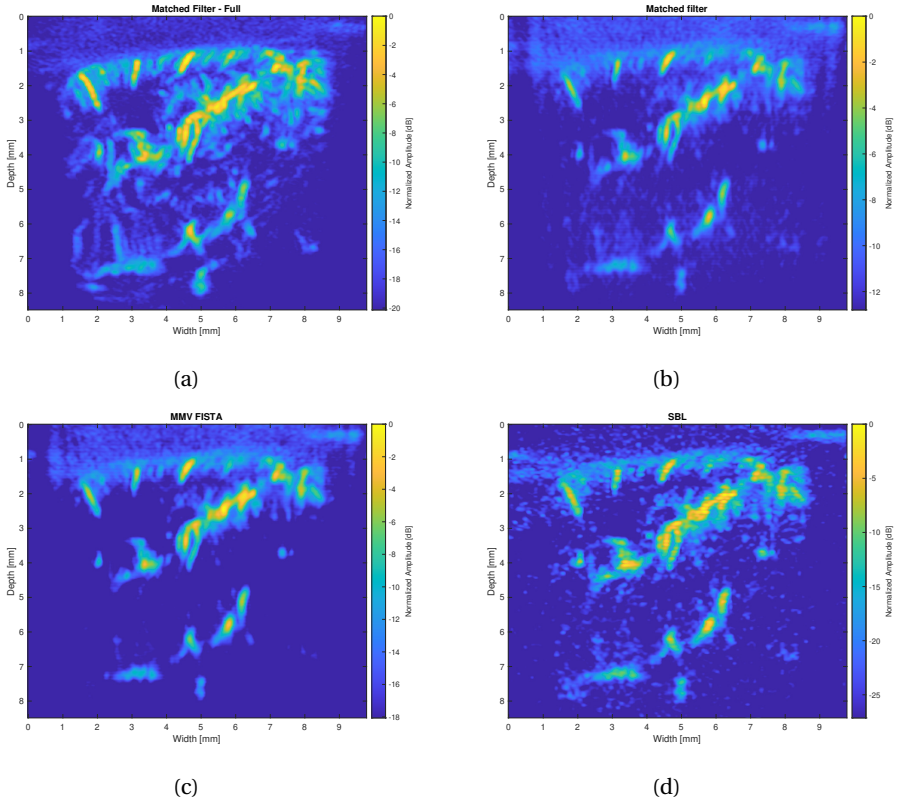

Figure 4.4: Comparison of MF, MMV FISTA and SBL for random scatterers with 128 receivers with 2 steering angles when we image them in the suitable dynamic range

the theoretical advantages of advanced reconstruction algorithms, and they may leave little room for improvement in the image details. Unfortunately, the computational cost of advanced algorithms makes their modest enhancements in contrast and background removal seems less attractive.

4.5. CONCLUSION AND DISCUSSION

In this chapter, we have proposed the SBL method that statistically exploits the sparse joint structure of the data for vascular ultrasound imaging. We evaluated the performance of the MMV FISTA and SBL within two compressive vascular imaging settings with mouse brain image data and compared their performance with a matched filter. We observed that the advanced algorithms are limited to increased contrast and better background removal and were insufficient to model the brain vasculature successfully to reveal fine image details. Hence, more sophisticated priors that consider the relationship between neighboring pixels might be required. Block sparsity can be efficient as vasculature seems to exhibit a connected structure. The following two chapters will focus on

block sparsity with pattern-coupled and correlated sparse Bayesian learning to improve the reconstruction performance of the ultrasound imaging data or other problems such as DOA estimation.

5

Pattern Coupled Sparse Bayesian Learning with Fixed Point Iterations

We consider the problem of recovering block-sparse signals with unknown boundaries. Such signals arise naturally in various applications. Recent literature introduced a pattern-coupled or clustered Gaussian prior, in which each coefficient involves its own hyperparameter as well as its immediate neighbors' hyperparameters. Some methods use a hierarchical distribution, making the solution vulnerable to the parameter choice. Besides, these methods mainly rely on the expectation-maximization (EM) algorithm and either require a suboptimal solution or an approximation of the hyperparameters. To address these difficulties, we propose to solve the pattern coupling problem via fixed point iterations instead of the EM algorithm. The proposed algorithm does not require any further assumptions on the hyperparameters and provides a simple update rule for the hyperparameters. Although the fixed point iterations method is an empirical strategy, it provides a fast convergence rate. The algorithm is presented for both one-dimensional and two-dimensional data. Firstly, the proposed algorithm is tested on a simple direction of arrival (DOA) and amplitude estimation problem for the one-dimensional scenario. Our simulations show that the proposed method achieves reconstruction results similar to those of the state-of-the-art method; however, the proposed method is faster than the existing counterparts. We also tested the algorithm for the mouse brain data for the two-dimensional case and observed slight improvement compared to the classical SBL.

Part of this chapter is published as: D. Dogan, G. Leus, Pattern Coupled Sparse Bayesian Learning with Fixed Point Iterations for DOA and Amplitude Estimation (2023) [29].

5.1. INTRODUCTION

Block sparsity has been observed for signals in numerous applications, such as the cluster structure of scatterers on radar images [23], fetal ECG [26], DOA estimation, and so on [100]. The block sparse model can be naturally exploited by further including the relation between sparse coefficients, such as the dependence of the sparsity patterns. Under noisy environments, correlated settings, or with very compressive measurements, algorithms properly leveraging such an underlying structure could achieve a robust recovery compared to their counterparts which merely exploit the sparsity.

The pattern-coupled sparse Bayesian learning (PCSBL) algorithm incorporates a pattern-coupled hierarchical Gaussian prior where each coefficient depends on its own hyperparameter and its immediate neighbors' hyperparameters to exploit interactions between neighboring coefficients [28, 31]. For this problem, a suboptimal solution is attained for the hyperparameters; however, the performance of the PCSBL depends on a proper selection of the hyperparameters. Clustered sparse Bayesian learning (CSBL) takes on a similar idea as the pattern-coupled prior used in PCSBL yet without relying on the hierarchical distribution over the hyperparameters [30]. Both algorithms use an EM-based update rule.

We propose to solve the pattern coupling problem via fixed point iterations instead of the EM algorithm [39]. The fixed point iterations method is an empirical strategy, but it provides a fast convergence rate in most applications [63, 64]. In [28], PCSBL uses a lower bound to approximate the optimal hyperparameter, whose performance always depends on a careful setting of the auxiliary parameter. Instead, our algorithm does not need such a bound since it does not require any selection of auxiliary parameters. Our algorithm can be seen as a fixed point update rule-based version of the EM update rule-based CSBL algorithm [30]. However, CSBL assumes neighboring sparse coefficients to share the same variance or precision. We do not make such an assumption. Finally, although a theoretical analysis of the convergence behavior is unavailable, the proposed algorithm demonstrates a fast convergence rate.

The remainder of this paper is organized as follows. In the next section, we define the signal model for the DOA and amplitude estimation problem. In Section 5.3, we present the proposed Bayesian formulation with a short discussion on the existing literature. Then, we compare the performance of our proposed method with the state-of-the-art. In the final section, we discuss the results and conclude this work.

5.2. FORWARD MODEL

In DOA and amplitude estimation, we employ a multiple measurement vector (MMV) model, which exploits different pulse periods in synergy [61]. Such an MMV model can be expressed as

$$\mathbf{Z} = \mathbf{AS} + \mathbf{N}, \tag{5.1}$$

where the system matrix $\mathbf{A} = [\mathbf{a}_1 ... \mathbf{a}_L] \in \mathbb{C}^{N \times L}$ contains the array steering vectors for all hypothetical DOAs as columns, with the (n,l)-th element given by $\exp(-j(n-1)\frac{\omega d}{c} sin\theta_l)$ (d is the element spacing, c the sound speed, ω the frequency, and θ_l the lth DOA, e.g., $\theta_l = -90° + \frac{l-1}{L}180°$); $\mathbf{S} \in \mathbb{C}^{L \times M}$ represents the complex source amplitudes

$s_{l,m}$; $\mathbf{Z} = [\mathbf{z}_1 ... \mathbf{z}_M] \in \mathbb{C}^{N \times M}$ represents the concatenation of the measurements $\mathbf{z}_m$ at the mth snapshot; and the additive white noise $\mathbf{N}$ is assumed independent across sensors and snapshots, where each element has a complex Gaussian distribution with zero mean and variance σ^2.

5.3. BAYESIAN FORMULATION

5.3.1. PRIORS ON THE SOURCES

Here, Bayesian interference is used. This involves determining the posterior distribution of the complex source amplitudes from the likelihood and a prior model. In (5.1), the probability density function is given by

$$p(\mathbf{Z}|\mathbf{S};\sigma^2) = \frac{\exp\left(-\frac{1}{\sigma^2}||\mathbf{Z}-\mathbf{AS}||_F^2\right)}{(\pi\sigma^2)^{NM}}. \tag{5.2}$$

as the noise is assumed to be Gaussian. In classical SBL, the complex source amplitudes $s_{l,m}$ are assumed independent across different snapshots and each other as

$$p_m(s_{l,m},\gamma_l) = \mathscr{CN}(0,\gamma_l). \tag{5.3}$$

On the other hand, the pattern-coupled model is proposed in this work to cope with block-sparse signals with unknown block-sparse structures. This model utilizes the fact that the sparsity patterns of neighboring coefficients are statistically dependent. Specifically, in this model, the Gaussian prior for each coefficient involves its own hyperparameter and its immediate neighbors' hyperparameters [28]. For a one-dimensional setup, such as the presented DOA and amplitude estimation problem, the pattern-coupled prior is given as follows:

$$p_m(s_{l,m},\gamma_l,\gamma_{l-1},\gamma_{l+1}) = \mathscr{CN}(0,\gamma_l+\beta\gamma_{l-1}+\beta\gamma_{l+1}). \tag{5.4}$$

Then, we can express their joint distribution as

$$p(\mathbf{S};\mathbf{\Gamma}) = \prod_{m=1}^{M}\prod_{l=1}^{L} p_m(s_{l,m},\gamma_l+\beta\gamma_{l-1}+\beta\gamma_{l+1}) \tag{5.5}$$

$$= \prod_{m=1}^{M} \mathscr{CN}(\mathbf{0},\mathbf{\Gamma}) \tag{5.6}$$

where $\mathbf{\Gamma} = \text{diag}(\gamma_1+\beta\gamma_0+\beta\gamma_2,...,\gamma_L+\beta\gamma_{L-1}+\beta\gamma_{L+1})$. Note that $\gamma_0 = \gamma_{l+1} = 0$. In this approach, the sparsity is controlled by the hyperparameters. If the γ_l is non-zero, then $s_{l,m}$ is also non-zero. Therefore, if any of the neighboring elements (i.e., $s_{l-1,m}$ and $s_{l+1,m}$) is non-zero, then the center element s_l is likely to be non-zero. It might not give an exact sparse reconstruction; however, it provides the continuity of the sparsity patterns and hence the block sparsity.

Note that in PCSBL [28], the pattern-coupling prior has the following form:

$$p_m(s_{l,m},\gamma_l,\gamma_{l-1},\gamma_{l+1}) = \mathscr{CN}(\mathbf{0},(\gamma_l+\beta\gamma_{l-1}+\beta\gamma_{l+1})^{-1}) \tag{5.7}$$

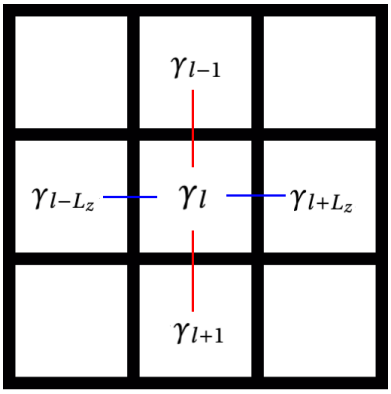

Figure 5.1: The pattern-coupling relations in two-dimensional case

Here, the motivation is the 'zero-coupling' effect. In this approach, if any of the neighboring elements (i.e. s_{l-1} and s_{l+1}) are zero, then the center element s_l is likely to be zero. In other words, if the $\gamma_l \to \infty$ for an element is zero, the neighboring elements are also zero. On the other hand, in CSBL [30], the prior has the following form:

$$p_m(s_{l,m}, \gamma_l, \gamma_{l-1}, \gamma_{l+1}) = \mathscr{CN}(\mathbf{0}, \gamma_l + \gamma_{l-1} + \gamma_{l+1}). \tag{5.8}$$

which has a similar formulation as the proposed one in (5.4), without the β term. They also provided an extension of that model, which takes the same formulation as given in (5.4). It is also possible to provide an update rule for β; however, it is out of the scope of this work. We select $\beta = 0.5$, resulting in a better reconstruction quality in most scenarios.

Apart from the DOA estimation problem, this method can be extended to reconstruct two-dimensional data in other problems, such as ultrasound imaging. Here, four neighboring pixels represent the dependence, as shown in Fig. 5.1. Therefore, the pattern-coupled prior is given for the two-dimensional case as follows:

$$\begin{aligned} &p_m(s(z_l, x_l, m), \gamma_l, \gamma_{l-1}, \gamma_{l+1}, \gamma_{l-L_z}, \gamma_{l+L_z}) \\ &= \mathscr{CN}(\mathbf{0}, \gamma_l + \beta_1\gamma_{l-1} + \beta_1\gamma_{l+1} + \beta_2\gamma_{l-L_z} + \beta_2\gamma_{l+L_z}). \end{aligned} \tag{5.9}$$

where L_z represents the number of pixels in the vertical direction. Note that $s(z_l, x_l, m)$ corresponds to the lth pixel of $s(z, x, m)$ given in (2.2). Now, we use β_1 and β_2 as coefficients for the vertical and horizontal directions. For many problems, $\beta_1 = \beta_2$, but they can be set differently regarding the level of correlation in the vertical and horizontal directions. For brevity, we only make the derivations for the one-dimensional scenario. Note that it can be simply extended to the two-dimensional case.

5.3.2. STOCHASTIC LIKELIHOOD

The posterior distribution of the sources can be attained using the Bayes rule conditioned on $\mathbf{\Gamma}$ and σ^2:

$$\begin{aligned} p(\mathbf{S}|\mathbf{Z};\mathbf{\Gamma},\sigma^2) &= \frac{p(\mathbf{Z}|\mathbf{S};\sigma^2)p(\mathbf{S};\mathbf{\Gamma})}{p(\mathbf{Z};\mathbf{\Gamma},\sigma^2)} \propto p(\mathbf{Z}|\mathbf{S};\sigma^2)p(\mathbf{S};\mathbf{\Gamma}) \\ &\propto \frac{e^{-tr((\mathbf{S}-\mu_\mathbf{S})^\mathsf{H}\mathbf{\Sigma}_\mathbf{s}^{-1}(\mathbf{S}-\mu_\mathbf{S}))}}{(\pi^L \det\Sigma_\mathbf{s})^M} = \mathscr{CN}(\mu_\mathbf{S},\mathbf{\Sigma}_\mathbf{s}). \end{aligned} \tag{5.10}$$

Since both $p(\mathbf{Z}|\mathbf{S};\sigma^2)$ and $p(\mathbf{S};\mathbf{\Gamma})$ are Gaussian $p(\mathbf{S}|\mathbf{Z};\mathbf{\Gamma},\sigma^2)$ is also Gaussian with mean $\mu_\mathbf{S}$ and covariance $\mathbf{\Sigma}_\mathbf{s}$:

$$\mu_\mathbf{S} = E\{\mathbf{S}|\mathbf{Z};\mathbf{\Gamma},\sigma^2\} = \mathbf{\Gamma}\mathbf{A}^\mathsf{H}\mathbf{\Sigma}_\mathbf{z}^{-1}\mathbf{Z} \tag{5.11}$$

$$\mathbf{\Sigma}_\mathbf{s} = \mathbf{\Gamma} - \mathbf{\Gamma}\mathbf{A}^\mathsf{H}\mathbf{\Sigma}_\mathbf{z}^{-1}\mathbf{A}\mathbf{\Gamma}. \tag{5.12}$$

Here, the data covariance matrix is given by

$$\mathbf{\Sigma}_\mathbf{z} = \sigma^2\mathbf{I}_N + \mathbf{A}\mathbf{\Gamma}\mathbf{A}^\mathsf{H}, \tag{5.13}$$

and its inverse can be computed using the matrix inversion lemma

$$\mathbf{\Sigma}_\mathbf{z}^{-1} = \sigma^{-2}\mathbf{I}_N - \sigma^{-2}\mathbf{A}\mathbf{\Sigma}_\mathbf{s}\mathbf{A}^\mathsf{H}\sigma^{-2}. \tag{5.14}$$

The denominator $p(\mathbf{Z};\mathbf{\Gamma},\sigma^2)$ is neglected here as it is only a normalization term and does not depend on $\mathbf{S}$. So in conclusion, we have $\mathbf{S} \sim \mathscr{CN}(\mu_\mathbf{S},\mathbf{\Sigma}_\mathbf{s})$. Using MAP estimation, we obtain

$$\hat{\mathbf{S}}^{MAP} = \mu_\mathbf{S} = E[\mathbf{S}|\mathbf{Z};\mathbf{\Gamma},\sigma^2] = \mathbf{\Gamma}\mathbf{A}^\mathsf{H}\mathbf{\Sigma}_\mathbf{z}^{-1}\mathbf{Z}. \tag{5.15}$$

Here the diagonal elements of $\mathbf{\Gamma}$ control the row sparsity of $\hat{\mathbf{S}}^{MAP}$. The hyperparameters $\mathbf{\Gamma}$, σ^2 are estimated by a type-II maximum likelihood, i.e., by maximizing the evidence that was treated as constant in (5.10). The evidence is the product of the likelihood $p(\mathbf{Z}|\mathbf{S};\sigma^2)$ and the prior $p(\mathbf{S};\mathbf{\Gamma})$ integrated over the complex source amplitudes $\mathbf{S}$. The resulting $p(\mathbf{Z};\mathbf{\Gamma},\sigma^2)$ is given by

$$p(\mathbf{Z};\mathbf{\Gamma},\sigma^2) = \int_{\mathbb{R}^{2ML}} p(\mathbf{Z}|\mathbf{S};\sigma^2)p(\mathbf{S};\mathbf{\Gamma})d\mathbf{Z} = \frac{e^{-tr(\mathbf{Z}^\mathsf{H}\mathbf{\Sigma}_\mathbf{z}^{-1}\mathbf{Z})}}{(\pi^N \det\Sigma_\mathbf{z})^M} \tag{5.16}$$

where $d\mathbf{Z} = \prod_{m=1}^{M}\prod_{l=1}^{N}\mathrm{Re}(d\mathbf{Z}_{mn})\mathrm{Im}(d\mathbf{Z}_{mn})$ and $\mathbf{\Sigma}_\mathbf{z}$ is the data covariance matrix. We can derive

$$\log p(\mathbf{Z};\mathbf{\Gamma},\sigma^2) \propto -\mathrm{tr}(\mathbf{Z}^\mathsf{H}\mathbf{\Sigma}_\mathbf{z}^{-1}\mathbf{Z}) - M\log\det\mathbf{\Sigma}_\mathbf{z}. \tag{5.17}$$

Finally, the hyperparameters $\mathbf{\Gamma}$ and σ^2 are estimated from the log-likelihood function as

$$(\hat{\mathbf{\Gamma}},\hat{\sigma}^2) = \mathrm{argmax}_{\Gamma\geq 0,\sigma^2\geq 0}\log p(\mathbf{Z};\mathbf{\Gamma},\sigma^2). \tag{5.18}$$

The parameters $\hat{\mathbf{\Gamma}}$, $\hat{\sigma}^2$ and $\Sigma_\mathbf{z}^{-1}$ are iteratively estimated and then finally $\mathbf{S}$ is attained by (5.15).

5.3.3. ESTIMATION OF Γ

Since $\mathbf{\Gamma}$ represents the source powers and controls the sparsity of $\mathbf{S}$, the most significant step is the estimation of $\mathbf{\Gamma}$. We need to find $\mathbf{\Gamma}$ for the estimation of $\mathbf{S}$ in (5.15). To iteratively compute $\mathbf{\Gamma}$, we form the derivatives of (5.17) with respect to the elements γ_l as follows:

$$\begin{aligned}\frac{\partial \mathrm{tr}(\mathbf{Z}^{\mathrm{H}}\mathbf{\Sigma}_z^{-1}\mathbf{Z})}{\partial \gamma_l} &= \mathrm{tr}\{(\frac{\partial \mathrm{tr}(\mathbf{Z}^{\mathrm{H}}\mathbf{\Sigma}_z^{-1}\mathbf{Z})}{\partial \mathbf{\Sigma}_z})^T \frac{\partial \mathbf{\Sigma}_z}{\partial \gamma_l}\} = \\ &\mathbf{a}_l^{\mathrm{H}}\mathbf{\Sigma}_z^{-1}\mathbf{Z}\mathbf{Z}^{\mathrm{H}}\mathbf{\Sigma}_z^{-1}\mathbf{a}_l + \beta\mathbf{a}_{l-1}^{\mathrm{H}}\mathbf{\Sigma}_z^{-1}\mathbf{Z}\mathbf{Z}^{\mathrm{H}}\mathbf{\Sigma}_z^{-1}\mathbf{a}_{l-1} + \\ &\beta\mathbf{a}_{l+1}^{\mathrm{H}}\mathbf{\Sigma}_z^{-1}\mathbf{Z}\mathbf{Z}^{\mathrm{H}}\mathbf{\Sigma}_z^{-1}\mathbf{a}_{l+1}\end{aligned} \tag{5.19}$$

$$\begin{aligned}\frac{\partial \log\det(\mathbf{\Sigma}_z)}{\partial \gamma_l} &= \mathrm{tr}(\mathbf{\Sigma}_z^{-1}\frac{\partial \mathbf{\Sigma}_z}{\partial \gamma_l}) = \\ &\mathbf{a}_l^{\mathrm{H}}\mathbf{\Sigma}_z^{-1}\mathbf{a}_l + \beta\mathbf{a}_{l-1}^{\mathrm{H}}\mathbf{\Sigma}_z^{-1}\mathbf{a}_{l-1} + \beta\mathbf{a}_{l+1}^{\mathrm{H}}\mathbf{\Sigma}_z^{-1}\mathbf{a}_{l+1}.\end{aligned} \tag{5.20}$$

After inserting (5.19) and (5.20) into (5.17), the derivative is formed as follows:

$$\begin{aligned}\frac{\partial \log p(\mathbf{Z};\mathbf{\Gamma},\sigma^2)}{\partial \gamma_l} &= ||\mathbf{Z}^{\mathrm{H}}\mathbf{\Sigma}_z^{-1}\mathbf{a}_l||_2^2 + \beta||\mathbf{Z}^{\mathrm{H}}\mathbf{\Sigma}_z^{-1}\mathbf{a}_{l-1}||_2^2 \\ &+ \beta||\mathbf{Z}^{\mathrm{H}}\mathbf{\Sigma}_z^{-1}\mathbf{a}_{l+1}||_2^2 - M\beta\mathbf{a}_{l-1}^{\mathrm{H}}\mathbf{\Sigma}_z^{-1}\mathbf{a}_{l-1} \\ &- M\mathbf{a}_l^{\mathrm{H}}\mathbf{\Sigma}_z^{-1}\mathbf{a}_l - M\beta\mathbf{a}_{l+1}^{\mathrm{H}}\mathbf{\Sigma}_z^{-1}\mathbf{a}_{l+1}.\end{aligned} \tag{5.21}$$

Here (5.21) is forced to be zero and we obtain the following equality:

$$\begin{aligned}&||\mathbf{Z}^{\mathrm{H}}\mathbf{\Sigma}_z^{-1}\mathbf{a}_l||_2^2 = M\mathbf{a}_l^{\mathrm{H}}\mathbf{\Sigma}_z^{-1}\mathbf{a}_l + \\ &M\beta\mathbf{a}_{l-1}^{\mathrm{H}}\mathbf{\Sigma}_z^{-1}\mathbf{a}_{l-1} - \beta||\mathbf{Z}^{\mathrm{H}}\mathbf{\Sigma}_z^{-1}\mathbf{a}_{l-1}||_2^2 + \\ &M\beta\mathbf{a}_{l+1}^{\mathrm{H}}\mathbf{\Sigma}_z^{-1}\mathbf{a}_{l+1} - \beta||\mathbf{Z}^{\mathrm{H}}\mathbf{\Sigma}_z^{-1}\mathbf{a}_{l+1}||_2^2.\end{aligned} \tag{5.22}$$

Thereafter, we introduce $(\frac{\gamma_l^{new}}{\gamma_l^{old}})^b$ and multiply the right side of (5.22) to obtain an iterative equation for γ_l [63, 64]. In this paper, $b = 2$. This leads to the following fixed-point update rule for γ_l:

$$\gamma_l^{new} = \frac{\gamma_l^{old}}{\sqrt{M}} \frac{||\mathbf{Z}^{\mathrm{H}}\mathbf{\Sigma}_z^{-1}\mathbf{a}_l||_2}{\sqrt{\mathbf{a}_l^{\mathrm{H}}\mathbf{\Sigma}_z^{-1}\mathbf{a}_l + \beta(\upsilon_{l-1} + \upsilon_{l+1})}} \tag{5.23}$$

where

$$\begin{aligned}\upsilon_{l-1} &= \mathbf{a}_{l-1}^{\mathrm{H}}\mathbf{\Sigma}_z^{-1}\mathbf{a}_{l-1} - (1/M)||\mathbf{Z}^{\mathrm{H}}\mathbf{\Sigma}_z^{-1}\mathbf{a}_{l-1}||_2^2, \\ \upsilon_{l+1} &= \mathbf{a}_{l+1}^{\mathrm{H}}\mathbf{\Sigma}_z^{-1}\mathbf{a}_{l+1} - (1/M)||\mathbf{Z}^{\mathrm{H}}\mathbf{\Sigma}_z^{-1}\mathbf{a}_{l+1}||_2^2.\end{aligned}$$

Note that γ_l^{old} and $\mathbf{\Sigma}_z$ are given from previous iterations. For the convergence of the fixed point iterations, we need to attain $\gamma_l^{new} = \gamma_l^{old}$.

Here, by following the steps between (5.19) and (5.23) for the one-dimensional case, the extension of the given update rule for the two-dimensional data is derived as follows:

$$\gamma_l^{new} = \frac{\gamma_l^{old}}{\sqrt{M}} \frac{||\mathbf{Z}^{\mathrm{H}}\mathbf{\Sigma}_z^{-1}\mathbf{a}_l||_2}{\sqrt{\mathbf{a}_l^{\mathrm{H}}\mathbf{\Sigma}_z^{-1}\mathbf{a}_l + \beta_1(\upsilon_{l-1} + \upsilon_{l+1}) + \beta_2(\upsilon_{l-L_z} + \upsilon_{l+L_z})}} \tag{5.24}$$

where

$$v_{l-i} = \mathbf{a}_{l-i}^{\mathsf{H}} \boldsymbol{\Sigma}_{\mathbf{z}}^{-1} \mathbf{a}_{l-i} - (1/M) ||\mathbf{Z}^{\mathsf{H}} \boldsymbol{\Sigma}_{\mathbf{z}}^{-1} \mathbf{a}_{l-i}||_2^2$$

with $i \in \{-1, +1, -L_z, +L_z\}$. For brevity, detailed derivations are not included. It is straightforward to attain (5.24) using the distribution in (5.9).

5.3.4. ESTIMATION OF THE NOISE PARAMETER σ^2

For fast convergence of the FP PCSBL method, it is important to develop a good noise variance estimate as it controls the sharpness of the peaks. In (5.15) and (5.13), we need to obtain σ^2 for the estimation of $\mathbf{S}$. This section estimates the noise variance σ^2, iteratively. We assume that the number of non-zero elements in the sparse vector is approximately known. Here stochastic maximum likelihood provides an asymptotically efficient estimate of σ^2 if the set of active sources is known. Note that we do not need to know the exact number of sources. A rough guess for the number of sources is also sufficient to obtain a good performance.

Let $\boldsymbol{\Gamma}_{\mathscr{K}}$ be the covariance matrix of the K estimated sources with corresponding steering matrix $\mathbf{A}_{\mathscr{K}}$. The corresponding data covariance matrix is

$$\boldsymbol{\Sigma}_{\mathbf{z}} = \sigma^2 \mathbf{I}_N + \mathbf{A}_{\mathscr{K}} \boldsymbol{\Gamma}_{\mathscr{K}} \mathbf{A}_{\mathscr{K}}^{\mathsf{H}}. \tag{5.25}$$

Note that the data covariance matrix (5.13) and (5.25) are identical. We first force (5.21) to zero as follows:

$$\begin{aligned} &\mathbf{a}_l^{\mathsf{H}} \boldsymbol{\Sigma}_z^{-1} (\mathbf{S}_{\mathbf{z}} - \boldsymbol{\Sigma}_z) \boldsymbol{\Sigma}_z^{-1} \mathbf{a}_l + \\ &\beta \mathbf{a}_{l-1}^{\mathsf{H}} \boldsymbol{\Sigma}_z^{-1} (\mathbf{S}_{\mathbf{z}} - \boldsymbol{\Sigma}_z) \boldsymbol{\Sigma}_z^{-1} \mathbf{a}_{l-1} + \\ &\beta \mathbf{a}_{l+1}^{\mathsf{H}} \boldsymbol{\Sigma}_z^{-1} (\mathbf{S}_{\mathbf{z}} - \boldsymbol{\Sigma}_z) \boldsymbol{\Sigma}_z^{-1} \mathbf{a}_{l+1} = 0 \end{aligned} \tag{5.26}$$

for all sources l. Here, the data sample covariance matrix is $\mathbf{S}_{\mathbf{z}} = \mathbf{Z}\mathbf{Z}^{\mathsf{H}}/M$. Note that (5.26) holds for the values of $l = 1, \ldots, L$ and results in the following:

$$\begin{bmatrix} 1 & \beta & \ldots & 0 \\ \beta & 1 & \ldots & 0 \\ \vdots & \vdots & \ddots & \vdots \\ 0 & 0 & \beta & 1 \end{bmatrix} \begin{bmatrix} u_1 \\ u_2 \\ \vdots \\ u_L \end{bmatrix} = \mathbf{0} \tag{5.27}$$

where $u_l = \mathbf{a}_l^{\mathsf{H}} \boldsymbol{\Sigma}_z^{-1} (\mathbf{S}_{\mathbf{z}} - \boldsymbol{\Sigma}_z) \boldsymbol{\Sigma}_z^{-1} \mathbf{a}_l$. By solving (5.27), we obtain the following equality

$$\mathbf{a}_l^{\mathsf{H}} \boldsymbol{\Sigma}_z^{-1} (\mathbf{S}_{\mathbf{z}} - \boldsymbol{\Sigma}_z) \boldsymbol{\Sigma}_z^{-1} \mathbf{a}_l = 0. \tag{5.28}$$

Jaffer [101] shows that for a full $\boldsymbol{\Gamma}$ matrix, the derivative in (5.21) is given by

$$\frac{\partial \log p(\mathbf{Z}; \boldsymbol{\Gamma}, \sigma^2)}{\partial \boldsymbol{\Gamma}} = \mathbf{A}_{\mathscr{K}}^{\mathsf{H}} \boldsymbol{\Sigma}_z^{-1} (\mathbf{S}_{\mathbf{z}} - \boldsymbol{\Sigma}_z) \boldsymbol{\Sigma}_z^{-1} \mathbf{A}_{\mathscr{K}} = 0. \tag{5.29}$$

and using the matrix inversion lemma, it is equivalent to the following condition:

$$\mathbf{A}_{\mathscr{K}}^{\mathsf{H}} (\mathbf{S}_{\mathbf{z}} - \boldsymbol{\Sigma}_z) \mathbf{A}_{\mathscr{K}} = \mathbf{0}, \tag{5.30}$$

Algorithm 3: FP PCSBL

Output: $\mathbf{S}$: unknown data

Initialize $\sigma^2 = 0.1$, $\text{diag}(\mathbf{\Gamma}) = \mathbf{1}$, $\epsilon_{min} = 0.001$, $E_{max} = 500$

while $e < E_{max}$ *and* $\epsilon_{min} < \epsilon$ **do**

$e = e + 1$, $\mathbf{\Gamma}^{old} = \mathbf{\Gamma}^{new}$

calculate $\mathbf{\Sigma_z} = \sigma^2 \mathbf{I}_N + \mathbf{A\Gamma A}^{\mathsf{H}}$

update γ_l^{new} with (5.23)

$\mathbf{\Gamma} = \text{diag}(\gamma_1 + \beta\gamma_0 + \beta\gamma_2, ..., \gamma_L + \beta\gamma_{L-1} + \beta\gamma_{L+1})$

$\mathscr{K} = \{l \in \mathbb{N} | K \text{ largest peaks in } \mathbf{\Gamma}\} = \{l_1, \dots l_K\}$

$\mathbf{A}_{\mathscr{K}} = (\mathbf{a}_{l_1}, \dots, \mathbf{a}_{l_K})$

update $(\sigma^2)^{new} = \frac{tr((\mathbf{I}_N - \mathbf{A}_{\mathscr{K}}\mathbf{A}_{\mathscr{K}}^{\dagger})\mathbf{S_z})}{N-K}$

$\epsilon = ||\text{diag}(\mathbf{\Gamma}^{new} - \mathbf{\Gamma}^{old})||_1 / ||\text{diag}(\mathbf{\Gamma}^{old})||_1$

end

$\tilde{\mathbf{S}} = \mathbf{\Gamma A}^{\mathsf{H}} \mathbf{\Sigma_z}^{-1} \mathbf{Z}$

5

by following the steps in [101]. In [63], Jaffer's condition is assumed to be correct, even though $\mathbf{\Gamma}$ is a diagonal matrix. On the other hand, when $\mathbf{\Gamma}$ is diagonal, we cannot guarantee that the following is always true

$$\mathbf{a}_l^{\mathsf{H}} \mathbf{\Sigma_z}^{-1} (\mathbf{S_z} - \mathbf{\Sigma_z}) \mathbf{\Sigma_z}^{-1} \mathbf{a}_{l'} = 0 \text{ for } l \neq l', \tag{5.31}$$

as this comes from the derivative $\frac{\partial \log p(\mathbf{Z};\mathbf{\Gamma},\sigma^2)}{\partial \mathbf{\Gamma}_{ll'}}$ for the off-diagonal elements of $\mathbf{\Gamma}$. However, we do not have any off-diagonal terms in $\mathbf{\Gamma}$. Therefore, Jaffer's condition might not hold for diagonal matrices. Unlike [63], instead of using Jaffer's condition, we estimate σ^2 by using the approximation $\text{tr}(\mathbf{S_z}) \approx \text{tr}(\mathbf{\Sigma_z})$. Then, by using (5.25) we attain

$$\begin{aligned} &\epsilon = \text{tr}(\mathbf{S_z} - \mathbf{\Sigma_z}) = \text{tr}(\mathbf{S_z} - \sigma^2 \mathbf{I}_N - \mathbf{A}_{\mathscr{K}} \mathbf{\Gamma}_{\mathscr{K}} \mathbf{A}_{\mathscr{K}}^{\mathsf{H}}) \Rightarrow \\ &\text{tr}(\mathbf{S_z}) - \text{tr}(\sigma^2 \mathbf{I}_N) - \epsilon = \text{tr}(\mathbf{A}_{\mathscr{K}} \mathbf{\Gamma}_{\mathscr{K}} \mathbf{A}_{\mathscr{K}}^{\mathsf{H}}) = \\ &\text{tr}(\mathbf{P}\mathbf{A}_{\mathscr{K}} \mathbf{\Gamma}_{\mathscr{K}} \mathbf{A}_{\mathscr{K}}^{\mathsf{H}} \mathbf{P}) = \text{tr}(\mathbf{P}(\mathbf{\Sigma_z} - \sigma^2 \mathbf{I}_N)\mathbf{P}) \end{aligned} \tag{5.32}$$

where $\mathbf{P}$ is the projection matrix onto the subspace spanned by the active components and is written by

$$\mathbf{P} = \mathbf{A}_{\mathscr{K}} \mathbf{A}_{\mathscr{K}}^{\dagger} = \mathbf{A}_{\mathscr{K}} (\mathbf{A}_{\mathscr{K}}^{\mathsf{H}} \mathbf{A}_{\mathscr{K}})^{-1} \mathbf{A}_{\mathscr{K}}^{\mathsf{H}} = \mathbf{P}^{\mathsf{H}} = \mathbf{PP}. \tag{5.33}$$

Thereafter we obtain

$$\text{tr}(\mathbf{S_z}) - \sigma^2 \text{tr}(\mathbf{I}_N) - \epsilon = \text{tr}(\mathbf{P\Sigma_z P}) - \sigma^2 \text{tr}(\mathbf{PP}). \tag{5.34}$$

Then, the trace in (5.34) is evaluated and it leads to $\text{tr}(\mathbf{PP}) = \text{tr}(\mathbf{P}^{\mathsf{H}}\mathbf{P}) = K$, $\text{tr}(\mathbf{I}_N) = N$ and $\text{tr}(\mathbf{P\Sigma_z P}) = \text{tr}(\mathbf{P}^2\mathbf{\Sigma_z}) = \text{tr}(\mathbf{P\Sigma_z})$. That gives

$$\text{tr}(\mathbf{S_z}) - N\sigma^2 - \epsilon = \text{tr}(\mathbf{P\Sigma_z}) - K\sigma^2. \tag{5.35}$$

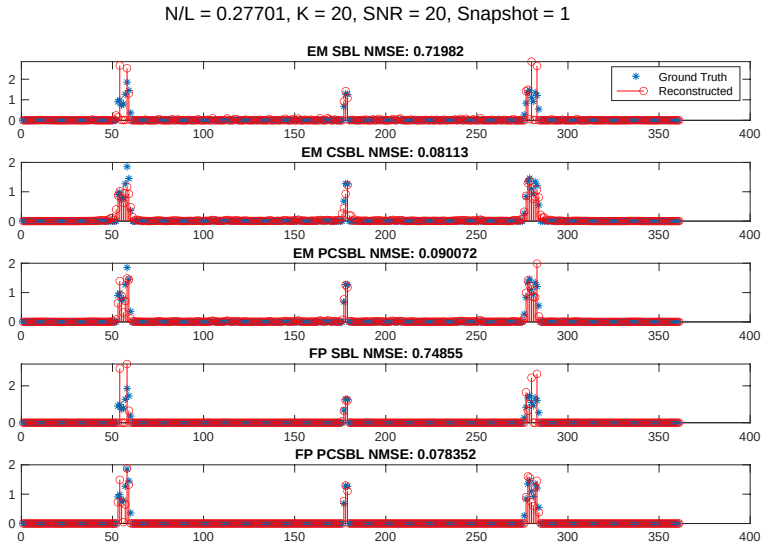

Figure 5.2: The reconstructions and NMSE performance of the sparse Bayesian algorithms for a single snapshot with correlated data under 20 dB SNR

Inserting $\theta = \text{tr}(\mathbf{P}(\mathbf{S_z} - \mathbf{\Sigma}_z))$ and solving (5.35) for σ^2 results in

$$\sigma^2 = \frac{\text{tr}(\mathbf{S_z} - \mathbf{PS_z}) + \theta - \epsilon}{N-K} \approx \frac{\text{tr}(\mathbf{S_z} - \mathbf{PS_z})}{N-K} = \hat{\sigma}^2, \tag{5.36}$$

which is the same variance estimator as in [63], although it is derived differently. This approximation makes the noise power estimation error-free if $\text{tr}(\mathbf{\Sigma_z}) = \text{tr}(\mathbf{S_z})$ and $\text{tr}(\mathbf{P}\Sigma_\mathbf{z}) = \text{tr}(\mathbf{PS_z})$ or $\text{tr}(\mathbf{P}(\mathbf{S_z} - \mathbf{\Sigma}_z)) = \text{tr}(\mathbf{S_z} - \mathbf{\Sigma}_z)$, unbiased as $E[\epsilon] = 0$ and $E[\theta] = 0$, consistent since its variance tends to zero for $M \to \infty$ and asymptotically efficient as it approaches the Cramér-Rao lower bound (CRLB) as $M \to \infty$.

5.4. NUMERICAL RESULTS

5.4.1. RESULTS FOR DOA AND AMPLITUDE ESTIMATION

The proposed algorithm is tested on a DOA and amplitude estimation problem with block sparse sources. It should be noted that most analysis in the literature has been done with randomly designed sensing matrices [28, 33]. However, such a random design is not realistic to evaluate the performance of our algorithm. Hence, we tested and compared different algorithms for a simple DOA and amplitude estimation problem. The performance of the proposed algorithm is close to both PCSBL and CBSL; however, it is faster than both algorithms. Here, we consider an array with various numbers of elements and various numbers of snapshots and SNR values. The DOAs are on an angular grid $[-90 : 0.5 : 90]^\circ$, and $L = 361$. The noise is modeled as i.i.d. complex Gaussian. The single snapshot array signal-to-noise ratio (SNR) is SNR $= 10\log_{10}[E[||\mathbf{A}\mathbf{s}_m||_2^2]/E[||\mathbf{n}_m||_2^2]]$. For M snapshots the noise power becomes

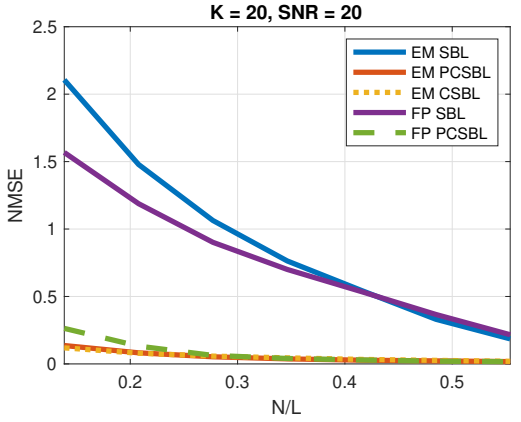

(a)

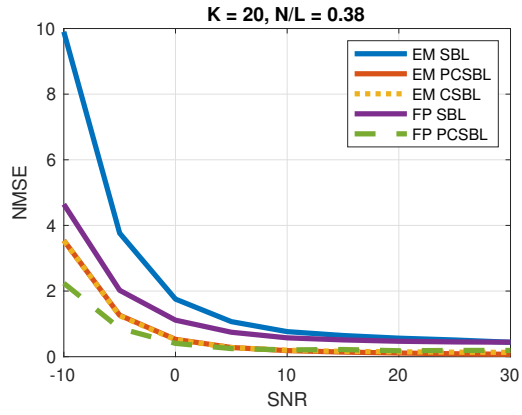

(b)

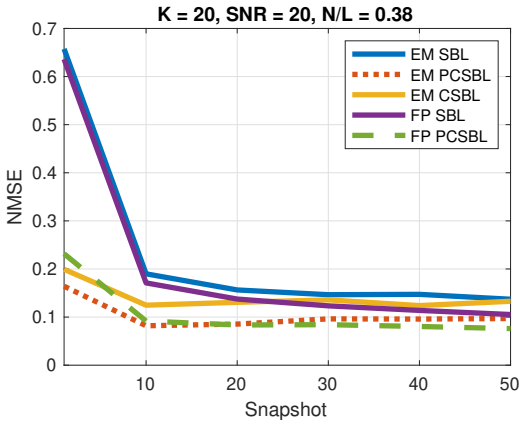

(c)

Figure 5.3: Performance comparison of the sparse Bayesian algorithms for different (a) N/L ratios; (b) SNR values for a single snapshot problem and (c) different number of snapshots

$$E[||\mathbf{N}||_{\mathscr{F}}^2]/(MN) = 10^{-SNR/10}[E[||\mathbf{AS}||_2^2]/(MN). \tag{5.37}$$

Here, we examine a scenario with $K = 20$ random sources at random three DOA groups with $s_{l,m}$ having random complex amplitudes. The sources are chosen to be correlated to see the robustness of the algorithms with such a setting. The correlated sources are created as $\mathbf{S} = \mathbf{R}^{1/2}\mathbf{W}$ where $\mathbf{W}$ is complex random noise with unit variance. We choose

$$\mathbf{R} = \begin{bmatrix} 1 & a & \dots & 0 \\ a & 1 & \dots & 0 \\ \vdots & \vdots & \ddots & \vdots \\ 0 & \dots & \dots & 1 \end{bmatrix} \tag{5.38}$$

where $a = 0.5$. $\mathbf{R}$ is chosen to be a tridiagonal correlation matrix; hence, only the neighboring correlations are considered.

The reconstructed amplitudes and their NMSE performance with correlated data for a single snapshot problem with $N/L = 0.27$ and $SNR = 20$ dB are given in Fig. 5.2. FP SBL represents a sparse Bayesian learning algorithm with a Type II likelihood maximization with a fixed point update rule [63, 64]. FP PCSBL is the pattern-coupled version of that algorithm, which is proposed in this work. We compare our algorithm with EM update-based SBL algorithms which are classical SBL (EM SBL), PCSBL (EM PCSBL), and CSBL (EM CSBL). Even though we consider correlated data, FP PCSBL provides a considerable improvement compared to regular FP SBL. Note that FP PCSBL exploits the statistical dependence of the sparsity patterns of the neighboring coefficients when the data is uncorrelated. However, it still provides a huge improvement for correlated data. Similarly, EM PCSBL and EM CSBL significantly improve EM SBL. On the other hand, EM PCSBL, EM CSBL, and FP PCSBL have similar performances. However, while overall EM PCSBL and EM CSBL algorithms take around $0.5 - 1.5$ seconds with a Macbook Pro 2019 (16 GB of RAM and 6-core Intel Core i7 2.6 GHz processor), FP PCSBL converges in $0.03 - 0.05$ seconds for a single snapshot problem thanks to the fast convergence of the fixed point update rule. The NMSE performance of the reconstructions with correlated data for a single snapshot problem with different N/L, SNR, and snapshot values are given in Fig. 5.3a,5.3b, and 5.3c, respectively. All results are averaged 100 Monte Carlo simulations. While FP SBL performs better than EM SBL for different N/L and SNR values, we observe similar performances for FP PCSBL, EM PCSBL, and EM CSBL. For small SNR values, FP PCSBL has slightly better performance than its counterparts, but we observe the opposite for small N/L values. Lastly, the performance of all the algorithms is increased by increasing the number of snapshots to some extent. However, in the multi-snapshot problem, with an increasing number of snapshots, we do not see a considerable benefit of using pattern coupling.

The algorithm is also tested with different values of a, (i.e. $0 \leq a \leq 0.5$) and we observe similar results as in Figs. 5.2, 5.3a, 5.3b and 5.3c, including for the case of uncorrelated data (i.e. $a = 0$). Hence, the correlations in the data for given values of a do not have a significant impact on the reconstruction performance.

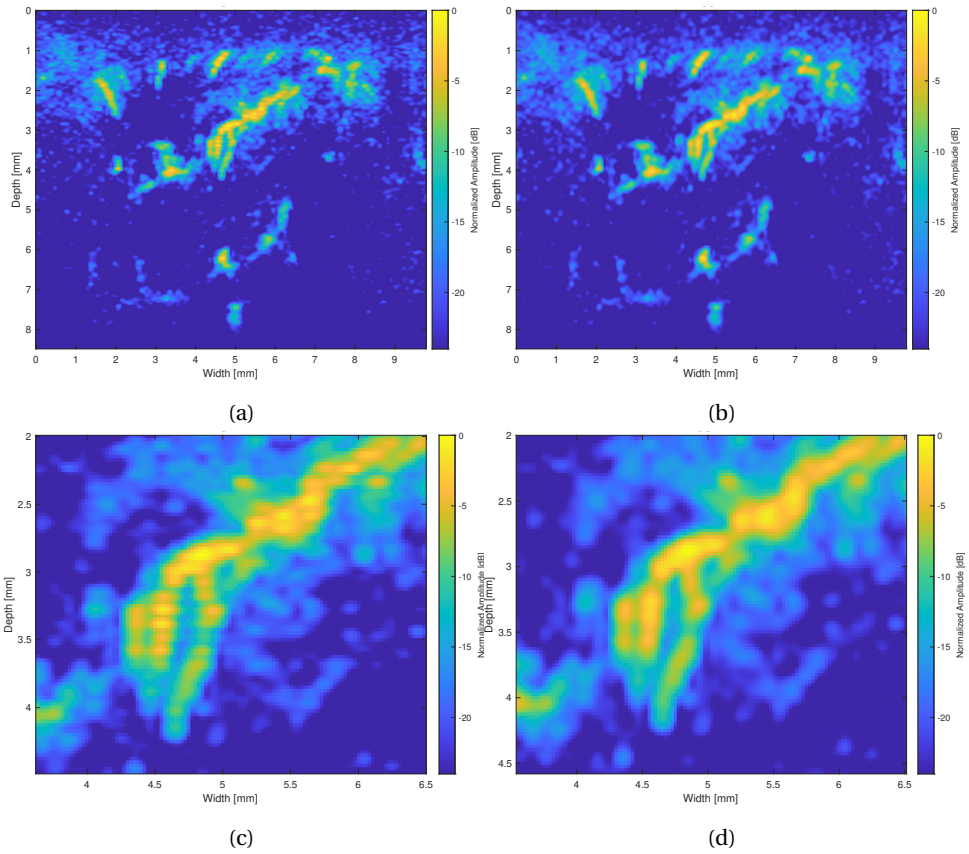

Figure 5.4: Comparison of (a), (c) FP SBL and (b), (d) FP PCSBL for mouse brain with 16 measurements and 20 steering angles when we image them in the same dynamic range

5.4.2. RESULTS FOR VASCULAR ULTRASOUND IMAGING

Now, we apply the proposed algorithm to the mouse brain data with the presented configurations in Chapter 4. The number of frames for the mouse brain data is $M = 197$. The corresponding PDI reconstructions are shown in 5.4 and 5.5 with 16 measurements and 20 steering angles and with 128 measurements and 2 steering angles, respectively. While Fig. 5.4a, 5.4b, 5.5a and 5.5b show the reconstructions, Fig. 5.4c, 5.4d, 5.5c and 5.5d are zoomed version of those reconstructed images.

We observe a grainy structure with the classical FP SBL algorithm, which is slightly mitigated by FP PCSBL. The grainy structure is due to the independent selection of hyperparameters in FP SBL. Since we enforce the dependence between neighboring hyperparameters in FP PCSBL, the grainy effect is reduced. However, this improvement did not substantially affect the SNR. In Fig. 5.3c, we have already analyzed the NMSE versus the number of snapshots for the DOA and amplitude estimation problem. After $10-20$ snapshots, FP SBL and FP PCSBL perform similarly in the NMSE sense. Since

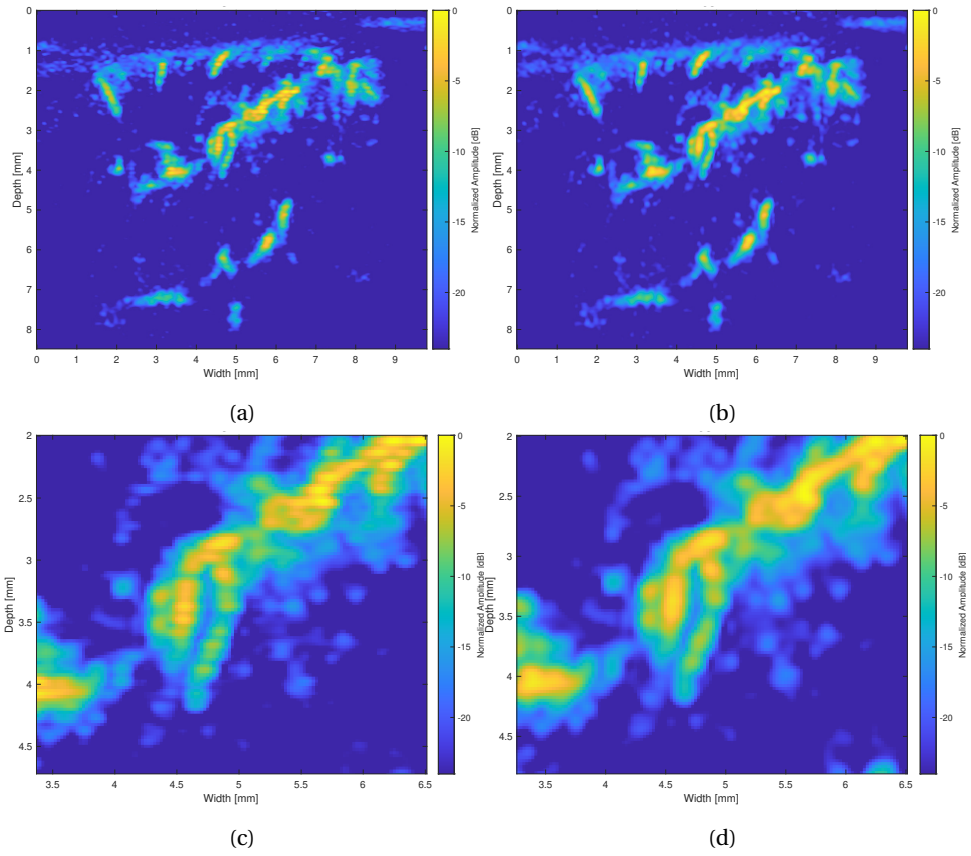

Figure 5.5: Comparison of (a), (c) FP SBL and (b), (d) FP PCSBL for mouse brain with 128 measurements with 2 steering angles when we image them in the same dynamic range

the number of frames for the mouse brain data equals $M = 197$, the difference between FP SBL and FP PCSBL might not be pronounced. Reducing the number of frames below 20 might make the differences more apparent; however, we needed at least 50 frames to obtain a convenient vasculature PDI image. Hence, it did not present a suitable scenario to observe the clear distinction between FP SBL and FP PCSBL for the mouse brain imaging data. Nonetheless, removing the grainy structure shows that the relationship between neighboring elements still provides some performance gain.

Due to their computational demands, we did not test EM SBL, EM PCSBL, and EM CSBL algorithms on the mouse brain dataset. Since the performance of the FP SBL and EM SBL are almost the same, and EM PCSBL, EM CSBL, and FP PCSBL show comparable results in DOA and amplitude estimation, we expect similar outcomes in vascular ultrasound imaging as well.

5.5. CONCLUSION AND DISCUSSION

In this work, we proposed a pattern coupling algorithm with fixed point iterations based on the update rule for the hyperparameters instead of using the EM algorithm. It does not require further assumptions on the hyperparameters and provides a simple update rule. The proposed algorithm was first tested on a simple DOA and amplitude estimation problem, and its performance was close to that of both EM PCSBL and EM CBSL; however, it was faster than both counterparts, thanks to the fixed-point iterations method. We also applied the proposed FP PCSBL algorithm to the mouse brain imaging data. However, as the number of frames is high for the data, we could not observe a significant improvement apart from the reduction of the grainy structure.

6

CORRELATED SPARSE BAYESIAN LEARNING FOR RECOVERY OF BLOCK SPARSE SIGNALS

We consider the problem of recovering complex valued block sparse signals with unknown borders. Such signals arise naturally in numerous applications. Several algorithms have been developed to solve the problem of unknown block partitions. In pattern-coupled sparse Bayesian learning (PCSBL), each coefficient involves its own hyperparameter and those of its immediate neighbors to exploit the block sparsity. Extended block sparse Bayesian learning (EBSBL) assumes the block sparse signal consists of correlated and overlapping blocks to enforce block correlations. We propose a simpler alternative to EBSBL and reveal the underlying relationship between the proposed method and a particular case of EBSBL. The proposed algorithm uses the fact that immediate neighboring sparse coefficients are correlated. The proposed model is similar to classical sparse Bayesian learning (SBL). However, unlike the diagonal correlation matrix in conventional SBL, the unknown correlation matrix has a tridiagonal structure to capture the correlation with neighbors. Due to the entanglement of the elements in the inverse tridiagonal matrix, instead of a direct closed-form solution, an approximate solution is proposed. The alternative algorithm avoids the high dictionary coherence issue in EBSBL, reduces the unknowns of EBSBL, and is hence computationally more efficient. The sparse reconstruction performance of the algorithm is evaluated with both correlated and uncorrelated block sparse coefficients. Results of comprehensive simulations demonstrate that the proposed algorithm outperforms PCSBL and correlation-based methods such as EBSBL in terms of reconstruction quality. The numerical results also show that the proposed correlated SBL algorithm is able to deal with isolated zeros and isolated nonzeros as well as block sparse patterns.

Part of this chapter is published as: D. Dogan, G. Leus, Correlated Sparse Bayesian Learning for Recovery of Block Sparse Signals with Unknown Borders, IEEE Open Journal of Signal Processing (2024) [34].

6.1. INTRODUCTION

Block sparsity has been observed for signals in a wide range of applications, such as the cluster structure of scatterers in radar images [23, 24, 25], fetal ECG [26], ultrasound signals [27] and so on. The structured sparse model can be naturally exploited by including further the dependencies among sparse coefficients, such as the correlations between coefficients or dependence of the sparsity patterns. Under noisy environments or with very compressive measurements, algorithms properly leveraging such an underlying structure could achieve a robust recovery compared to their counterparts which merely exploit the sparsity.

A number of algorithms have been proposed for block sparse signal recovery when the block partition is known a priori, including greedy pursuit algorithms like Model-based Compressive Sampling Matching Pursuit (CoSaMp) [102], Block Orthogonal Matching Pursuit (Block OMP) [103], and regularized convex optimizations, such as group Lasso [104], group basis pursuit [105], mixed ℓ_1/ℓ_2 programming [106] and block sparse Bayesian learning (BSBL) [107, 33]. These algorithms require knowledge of the cluster pattern (block partition) a priori. However, prior knowledge of the block partition of sparse coefficients is practically unavailable. To address this problem, a particular structure is imposed on the support of sparse coefficients in the first category of algorithms [108, 109]. For instance, the Clustered Sparse Solver (Cluss) algorithm in [108] employs a hierarchical Bayesian "spike-and-slab" prior model to encourage the sparseness and promote the cluster patterns simultaneously. However, since the resulting posterior distribution of the Bayesian cluster sparse model cannot be analytically derived, Markov chain Monte Carlo (MCMC) sampling [110] has to be employed for Bayesian inference. Similarly, the Boltzmann machine is employed on the support of sparse coefficients in [109] to model the dependencies and an approximate model of the maximum a posterior (MAP) estimator is used to estimate hidden variables with exhaustive search.

In another category of algorithms, different block sparsity priors are imposed directly on the sparse coefficients. Algorithms such as extended block sparse Bayesian learning (EBSBL) [33], pattern-coupled sparse Bayesian learning (PCSBL) [28], cluster structured sparse Bayesian learning (CSBL) [30] and total variation regularized sparse Bayesian learning (TVSBL) [111] are evaluated under this category. EBSBL is an extension of the block sparse Bayesian learning algorithm which is designed for known block partitions. In EBSBL, it is assumed that the nonzero blocks are arbitrarily located and their size is unknown. Then the signal is partitioned into a number of overlapping and fully correlated blocks with user-defined block size. By expanding the overlapping blocks to a non-overlapping block structure, an extended set of fully correlated blocks is introduced for the unknown sparse coefficients. Based on this block structure, an expanded sensing matrix is constructed by adding redundant columns to the original sensing matrix. Similarly, the unknown coefficient vectors introduced for each block are concatenated as an augmented vector. Thereafter, the measurements are expressed as a linear combination of the expanded measurement matrix and concatenation of the block vectors. Then, the problem can be effectively solved by the traditional BSBL algorithm to find the augmented block vector. Finally, the unknown sparse coefficients can be computed by using the relation between the original sparse coefficients and the blocks. PCSBL, on

the other hand, introduces a pattern-coupled hierarchical Gaussian prior for each coefficient involving its own hyperparameter and those of its immediate neighbors to exploit interactions between neighboring coefficients. A suboptimal solution is attained for the hyperparameters; however, the performance of PCSBL heavily depends on a proper selection of the hyperparameters. Extensions of PCSBL to two-dimensional cases are further addressed in [31, 32]. CSBL takes on a similar formula as the pattern-coupled prior used in PCSBL without relying on the hierarchical distribution over the hyperparameters. As a result, no proper hyperparameter selection is required in contrast to PCSBL. For both the PCSBL and CSBL, the expectation-maximization (EM) is developed to learn the hidden variables and the unknown parameters. Lastly, in TVSBL, a block SBL method has been developed inspired by total variation (TV) denoising [111].

In the mentioned category, algorithms such as EBSBL, PCSBL, CSBL, and TVSBL exploit the EM algorithm in update rules. Instead of EM, the variational Bayesian inference can be exploited. As an alternative to PCSBL with EM, [112] develops an algorithm using variational Bayesian inference, and it has a noticeable performance for the MIMO channel estimation problem. [113] introduces a method that exploits variational Bayesian inference instead of EM, which can be considered an alternative version of EBSBL (BSBL). Although it performs similarly to BSBL, it is faster than BSBL as it is a covariance-free algorithm. [114] also presents both EM and variational Bayesian inference methods for Kalman smoothing, reporting that they have similar performance, but the variational Bayesian method is slower due to the high number of iterations required for convergence. Although there is no clear consensus on which family of methods is faster or has better performance, we prefer EM-based update rules for a fair comparison with the existing methods. However, the variational Bayesian method can also be exploited as future work.

In the second category, where different group-structured priors are imposed on the sparse coefficients, only a few existing algorithms consider intra-block correlation, i.e., the correlation among the elements within each block. In practical applications intra-block correlation widely exists in signals, such as physiological signals [26] and images [27]. In this chapter, we review several algorithms that explore and exploit intra-block correlation to improve performance. These algorithms are based on block sparse Bayesian learning (BSBL) and extended block sparse Bayesian learning (EBSBL) [33]. However, BSBL requires knowledge of the block partition and EBSBL suffers from several key drawbacks leading to high computational complexity and coherence, and a larger dictionary matrix. Note that high number of unknowns deteriorates the performance of EBSBL.

In this chapter, a new algorithm dealing with the problem of an unknown block partition of the correlated signal is proposed to alleviate the challenges of recently reported methods. This chapter is motivated by the disadvantages of EBSBL, where the interactions among neighboring coefficients are implicitly modeled by a linear transformation of the artificially constructed augmented vector. A new structured sparse prior can be derived based on the underlying relationship between the correlation matrices in the augmented EBSBL model and the original signal model. The proposed algorithm uses the fact that immediate neighboring sparse coefficients are correlated. It is also inspired by PCSBL [28] and CSBL [30] in the sense that it considers the relation between neigh-

boring sparse coefficients. However, it is different than PCSBL and CSBL since they do not leverage the existing correlations among the data. We naturally exploit these correlations instead of relating the hyperparameters. In this chapter, we only focus on the correlations between immediate neighbors. Hence, the unknown correlation matrix has a tridiagonal structure, which is different than the diagonal correlation matrix used in conventional SBL algorithms [37, 63]. The proposed algorithm with a tridiagonal correlation matrix is a simple extension of the classical sparse Bayesian learning algorithm which has a diagonal correlation matrix. On the other hand, our algorithm improves the group sparsity performance as it does not ignore the correlation with the neighbors.

While classical SBL assumes the sources are uncorrelated, EBSBL assumes the different blocks share a common correlation structure [33]. In this chapter, we claim that if there is an intra-block correlation in the data, modeling an inter-element correlation can already trigger a grouping effect. In other words, without building a new block-based data model, assuming inter-element correlation in the classical SBL model already promotes group sparsity. It is also shown that there is a grouping effect even when the true data does not have intra-block correlations but only contains the block structure without correlations.

There are three contributions of this chapter, which can concisely be summarized as follows. First, a new structured sparse recovery algorithm is proposed, which can be considered a better alternative to EBSBL. The algorithm avoids the high dictionary coherence in EBSBL and also reduces the unknowns of EBSBL, making it computationally more efficient. Second, we provide an analysis of the relation between our algorithm and a particular case of EBSBL. The intuitions given here can be used to enhance the approximate update rule for the proposed algorithm with a tridiagonal structure. The third contribution of our chapter is the ability of the proposed algorithm to tackle irregular sparsity patterns where the sparse vector contains both block sparse and isolated coefficients. Once there are isolated zeros and nonzeros in the data, the group sparsity algorithms might not perform well as their assumptions enforce only the grouping effect. However, the proposed algorithm is also able to deal with isolated zeros and isolated nonzeros as well as block sparse patterns.

The rest of the chapter is organized as follows. Section II provides a review of classical sparse Bayesian learning and extended block SBL algorithms. A tridiagonal correlation based prior on the sparse coefficients is derived from the classical SBL algorithm in Section III. Section IV discusses the relationship of the proposed method to EBSBL. Comparisons of the proposed method with the state-of-the-art are shown in Section V. Conclusions are drawn in Section VI.

6.1.1. NOTATION

Throughout the chapter, bold symbols in small and capital fonts are used for vectors and matrices, respectively. $||\mathbf{x}||_2^2$ denotes the l_2-norm of vector $\mathbf{x}$. $\mathbf{x}_i$ denotes the i-th block of $\mathbf{x}$. And the i-th element of $\mathbf{x}$ is either denoted by $\mathbf{x}(i)$, $(\mathbf{x})_i$ or x_i. Furthermore, $(\mathbf{A})_{ij}$ and A_{ij} represent the element in ith row and jth column of an A matrix. For matrix $\mathbf{A}$, $\mathbf{A}^{\mathsf{H}}$ and $\mathbf{A}^{-1}$ denote the Hermitian and the inverse of the matrix, respectively. tr($\mathbf{A}$) is the trace of a matrix $\mathbf{A}$. Notation diag($\mathbf{A}$) denotes a column vector composed of the diagonal elements of a matrix $\mathbf{A}$. rank($\mathbf{A}$) denotes the rank of matrix $\mathbf{A}$. $|\mathbf{A}|$ is the determinant of

the matrix $\mathbf{A}$. $\mathscr{CN}(.)$ denotes the multivariate complex Gaussian distribution.

6.2. REVIEW OF SBL ALGORITHMS

Sparse signal recovery problems attempt to recover the unknown sparse coefficient vector $\mathbf{s} \in \mathbb{C}^L$ from noisy and distorted measurements $\mathbf{z} \in \mathbb{C}^N$. More specifically, we consider the model

$$\mathbf{z} = \mathbf{A}\mathbf{s} + \mathbf{n} \tag{6.1}$$

where $\mathbf{n} \in \mathbb{C}^N$ is the additive white noise and $\mathbf{A} \in \mathbb{C}^{N \times L}$ is the measurement matrix with $N \ll L$. A block structure in $\mathbf{s}$ is commonly observed in practice, where elements of $\mathbf{s}$ tend to be nonzero in multiple groups with unknown block sizes and arbitrary locations. Let us first give a detailed review of the considered structure in classical SBL. Such a detailed review is given to show the relation between our method to the classical SBL. Then we provide a brief review on the EBSBL [33].

6.2.1. CLASSICAL SBL

Using Bayesian inference to solve the linear problem in (6.1) involves determining the posterior distribution of the complex amplitudes $\mathbf{s}$ from the likelihood and prior distribution. The conditional probability density function (PDF) for $\mathbf{z}$ given the sources $\mathbf{s}$ is complex Gaussian with noise variance σ^2:

$$p(\mathbf{z}|\mathbf{s};\sigma^2) = \frac{\exp\left(-\frac{1}{\sigma^2}||\mathbf{z}-\mathbf{A}\mathbf{s}||_2^2\right)}{(\pi\sigma^2)^N}. \tag{6.2}$$

The unknown coefficients s_l are assumed to be independent across different coefficients l and to follow a zero-mean complex Gaussian distribution:

$$p_l(s_l;\gamma_l) = \frac{1}{\pi\gamma_l} e^{-|s_l|^2/\gamma_l}. \tag{6.3}$$

Then the variances of the elements of $\mathbf{s}$ can be stacked into $\boldsymbol{\gamma} = [\gamma_1, \ldots, \gamma_L]^T$ and we get

$$p(\mathbf{s};\boldsymbol{\gamma}) = \prod_{l=1}^{L} p_l(s_l;\gamma_l) = \mathscr{CN}(\mathbf{0}, \boldsymbol{\Gamma}) \tag{6.4}$$

with $\boldsymbol{\Gamma} = \mathrm{diag}(\boldsymbol{\gamma})$. When the variance $\gamma_l = 0$, then $s_l = 0$ with probability 1. Hence the sparsity of the model is controlled by the hyper-parameters $\boldsymbol{\gamma}$. It has been shown that such a model enforces sparsity.

By using the likelihood in (6.2) and the prior in (6.4), the posterior PDF of $\mathbf{s}$ can be found using the Bayes rule conditioned on $\boldsymbol{\gamma}$ and σ^2 and neglecting the denominator

$$\begin{aligned} p(\mathbf{s}|\mathbf{z};\boldsymbol{\gamma},\sigma^2) &= \frac{p(\mathbf{z}|\mathbf{s};\sigma^2)\,p(\mathbf{z};\boldsymbol{\gamma})}{p(\mathbf{z};\boldsymbol{\gamma},\sigma^2)} \propto p(\mathbf{z}|\mathbf{s};\sigma^2)\,p(\mathbf{s};\boldsymbol{\gamma}) \\ &\propto \frac{e^{-\mathrm{tr}((\mathbf{s}-\boldsymbol{\mu}_\mathbf{s})^H \boldsymbol{\Sigma}_\mathbf{s}^{-1}(\mathbf{s}-\boldsymbol{\mu}_\mathbf{s}))}}{\pi^L \det(\boldsymbol{\Sigma}_s)} = \mathscr{CN}(\boldsymbol{\mu}_\mathbf{s}, \boldsymbol{\Sigma}_\mathbf{s}). \end{aligned} \tag{6.5}$$

Since both $p(\mathbf{z}|\mathbf{s};\sigma^2)$ in (6.2) and $p(\mathbf{s};\boldsymbol{\gamma})$ in (6.4) are Gaussians, their product (6.5) is Gaussian with posterior mean $\boldsymbol{\mu}_\mathbf{s}$ and covariance $\boldsymbol{\Sigma}_\mathbf{s}$ given by

$$\begin{aligned}\boldsymbol{\mu}_\mathbf{s} &= E[\mathbf{s}|\mathbf{z};\boldsymbol{\Gamma},\sigma^2] = \boldsymbol{\Gamma}\mathbf{A}^\mathsf{H}\boldsymbol{\Sigma}_\mathbf{z}^{-1}\mathbf{z} \\ &= \sigma^{-2}(\sigma^{-2}\mathbf{A}^\mathsf{H}\mathbf{A}+\boldsymbol{\Gamma}^{-1})^{-1}\mathbf{A}^\mathsf{H}\mathbf{z}\end{aligned} \tag{6.6}$$

and

$$\begin{aligned}\boldsymbol{\Sigma}_\mathbf{s} &= E[(\mathbf{s}-\boldsymbol{\mu}_\mathbf{s})(\mathbf{s}-\boldsymbol{\mu}_\mathbf{s})^\mathsf{H}|\mathbf{z};\boldsymbol{\Gamma},\sigma^2] \\ &= (\frac{1}{\sigma^2}\mathbf{A}^\mathsf{H}\mathbf{A}+\boldsymbol{\Gamma}^{-1})^{-1} = \boldsymbol{\Gamma}-\boldsymbol{\Gamma}\mathbf{A}^\mathsf{H}\boldsymbol{\Sigma}_\mathbf{z}^{-1}\mathbf{A}\boldsymbol{\Gamma}\end{aligned} \tag{6.7}$$

where the covariance matrix of the measurements $\boldsymbol{\Sigma}_\mathbf{z}$ is given by

$$\boldsymbol{\Sigma}_\mathbf{z} = \sigma^2\mathbf{I}_N + \mathbf{A}\boldsymbol{\Gamma}\mathbf{A}^\mathsf{H}. \tag{6.8}$$

Here, to estimate the $\boldsymbol{\Gamma}$ and σ^2, we perform expectation-maximization (EM) to maximize $p(\mathbf{z};\boldsymbol{\Gamma},\sigma^2)$. The actual EM formulation proceeds by treating the $\mathbf{s}$ as a hidden variable and then by maximizing

$$Q(\boldsymbol{\Gamma},\sigma^2) = E_{\mathbf{s}|\mathbf{z};\boldsymbol{\Gamma},\sigma^2}[\log p(\mathbf{z},\mathbf{s};\boldsymbol{\Gamma},\sigma^2)] \tag{6.9}$$

with respect to the hyperparameters $\boldsymbol{\Gamma}$ and σ^2 to find their estimates, where $E_{\mathbf{s}|\mathbf{z};\boldsymbol{\Gamma},\sigma^2}[.]$ denotes an expectation with respect to the posterior distribution of $\mathbf{s}$. By substituting the joint distribution $p(\mathbf{z},\mathbf{s};\boldsymbol{\Gamma},\sigma^2) = p(\mathbf{z}|\mathbf{s};\sigma^2)p(\mathbf{s};\boldsymbol{\Gamma})$ into (6.9) we obtain

$$\begin{aligned}E_{\mathbf{s}|\mathbf{z};\boldsymbol{\Gamma},\sigma^2}[\log p(\mathbf{z},\mathbf{s};\boldsymbol{\Gamma},\sigma^2)] = &E_{\mathbf{s}|\mathbf{z};\sigma^2}[\log p(\mathbf{z}|\mathbf{s};\sigma^2)]+ \\ &E_{\mathbf{s}|\mathbf{z};\boldsymbol{\Gamma}}[\log p(\mathbf{s};\boldsymbol{\Gamma})].\end{aligned} \tag{6.10}$$

Ignoring the terms independent from $\boldsymbol{\Gamma}$, we can estimate the $\boldsymbol{\Gamma}$ by maximizing $E_{\mathbf{s}|\mathbf{z},\boldsymbol{\Gamma}}[\log p(\mathbf{s};\boldsymbol{\Gamma})]$. Starting from

$$\log p(\mathbf{s};\boldsymbol{\Gamma}) = -\frac{1}{2}\log(|\boldsymbol{\Gamma}|) - \frac{1}{2}\mathbf{s}^\mathsf{H}\boldsymbol{\Gamma}^{-1}\mathbf{s} \tag{6.11}$$

and using the fact that $\mathbf{s}^\mathsf{H}\boldsymbol{\Gamma}^{-1}\mathbf{s} = \mathrm{tr}(\boldsymbol{\Gamma}^{-1}\mathbf{s}\mathbf{s}^\mathsf{H})$ and $E[\mathbf{s}\mathbf{s}^\mathsf{H}] = \boldsymbol{\Sigma}_\mathbf{s} + \boldsymbol{\mu}_\mathbf{s}\boldsymbol{\mu}_\mathbf{s}^\mathsf{H}$ we attain the following expression:

$$E_{\mathbf{s}|\mathbf{z};\boldsymbol{\Gamma}}[\log p(\mathbf{s};\boldsymbol{\Gamma})] = -\frac{1}{2}\log(|\boldsymbol{\Gamma}|) - \frac{1}{2}\mathrm{tr}(\boldsymbol{\Gamma}^{-1}(\boldsymbol{\Sigma}_\mathbf{s} + \boldsymbol{\mu}_\mathbf{s}\boldsymbol{\mu}_\mathbf{s}^\mathsf{H})). \tag{6.12}$$

This function is also called as Q function. Since we have a diagonal $\boldsymbol{\Gamma}$, we can maximize this function only for the diagonal elements in $\boldsymbol{\Gamma}$. Hence, we can take the derivative as follows:

$$\frac{\partial E_{\mathbf{s}|\mathbf{z};\boldsymbol{\Gamma}}[p(\mathbf{s};\boldsymbol{\Gamma})]}{\partial\gamma_l} = \frac{(\boldsymbol{\Sigma}_\mathbf{s} + \boldsymbol{\mu}_\mathbf{s}\boldsymbol{\mu}_\mathbf{s}^\mathsf{H})_{ll}}{\gamma_l^2} - \frac{1}{\gamma_l} = 0. \tag{6.13}$$

Then, the closed-form solution for $\boldsymbol{\Gamma}_l$ is given by

$$\gamma_l = (\boldsymbol{\Sigma}_\mathbf{s})_{ll} + (\boldsymbol{\mu}_\mathbf{s})_l(\boldsymbol{\mu}_\mathbf{s}^\mathsf{H})_l. \tag{6.14}$$

Note that in classical SBL, the sources are assumed uncorrelated.

6.2.2. EXTENDED BLOCK SBL (EBSBL)

The BSBL method is proposed to solve the group sparsity problem with a known block partition [33] in which both the block size and the border locations of the blocks are known. Group sparsity is enforced by considering a separate covariance matrix per block, with a common structure over the different blocks and potentially a specific structure within every block (e.g., Toeplitz). The extension of this method, the extended BSBL (EBSBL) deals with unknown block partitions. EBSBL considers an extended set of hidden blocks $\mathbf{x}_i$ with hidden block size h for $i = 1 \dots g$ ($g = L-h+1$ is the number of blocks). More specifically, the unknown signal $\mathbf{s}$ is represented as

$$\mathbf{s} = \sum_{i=1}^{g} \mathbf{E}_i \mathbf{x}_i \tag{6.15}$$

where $\mathbf{E}_i \in \mathbb{R}^{L \times h}$ contains an identity matrix from the ith row to the $(i+h-1)$th row and zeros for the other entries. This idea allows for blocks of size h with unknown border locations but it can also handle blocks that might have a size different from h as discussed in [33]. Under (6.15), the model in (6.1) can be written as follows:

$$\mathbf{z} = \sum_{i=1}^{g} \mathbf{A}\mathbf{E}_i \mathbf{x}_i + \mathbf{n} = \Theta \mathbf{x} + \mathbf{n} \tag{6.16}$$

where $\mathbf{x} = [\mathbf{x}_1^T \dots \mathbf{x}_g^T]^T$ and $\Theta = [\Theta_1 \dots \Theta_g]$ with $\Theta_i = \mathbf{A}\mathbf{E}_i$. The problem in (6.16) becomes a block sparsity problem with a known block partition and is solvable by BSBL. Specifically, $\mathbf{x}$ is assumed to follow the given distribution:

$$p(\mathbf{x}; \{\beta_i, \mathbf{B}\}_{i=1}^{g}) = \mathscr{CN}(0, \mathbf{\Gamma}_0), \tag{6.17}$$

where $\mathbf{\Gamma}_0 = \text{diag}(\beta_1 \mathbf{B}, \dots, \beta_g \mathbf{B})$ and where each block satisfies the parameterized multivariate Gaussian distribution of $p(\mathbf{x}_i; \beta_i, \mathbf{B}) = \mathscr{CN}(0, \beta_i \mathbf{B})$ with β_i determining the degree of block sparsity. Then we can find the MAP estimate of $\mathbf{x}$ using the given formulas in (6.6), (6.7) as follows:

$$\boldsymbol{\mu}_{\mathbf{x}} = E[\mathbf{x}|\mathbf{z}; \mathbf{\Gamma}_0, \sigma^2] = \mathbf{\Gamma}_0 \Theta^{\mathsf{H}} (\sigma^2 \mathbf{I}_N + \Theta \mathbf{\Gamma}_0 \Theta^{\mathsf{H}})^{-1} \mathbf{z} \tag{6.18}$$

$$\begin{aligned} \mathbf{\Sigma}_{\mathbf{x}} &= E[(\mathbf{x} - \boldsymbol{\mu}_{\mathbf{x}})(\mathbf{x} - \boldsymbol{\mu}_{\mathbf{x}})^{\mathsf{H}} | \mathbf{z}; \mathbf{\Gamma}_0, \sigma^2] \\ &= (\frac{1}{\sigma^2} \Theta^{\mathsf{H}} \Theta + \mathbf{\Gamma}_0^{-1})^{-1}. \end{aligned} \tag{6.19}$$

After iteratively finding the hyperparameters, finally, the estimate of the unknown signal $\mathbf{s}$ is given by

$$\hat{\mathbf{s}} = \sum_{i=1}^{g} \mathbf{E}_i \boldsymbol{\mu}_{\mathbf{x}_i}. \tag{6.20}$$

EBSBL is designed to cope with block-sparse recovery under the assumption of an unknown block partition. However, it suffers from several disadvantages. First, it leads to a higher computational complexity, as the augmented vector $\mathbf{x}$ is of size $h \times (L-h+1)$, which is almost h times the size of the original signal $\mathbf{s}$. More importantly, since the expanded measurement matrix Θ is constructed by adding redundant columns to the original measurement matrix $\mathbf{A}$, dictionary Θ will be of high coherence. It affects the efficiency of the sparse coefficient estimation in SBL [30].

6.3. CORRELATED SPARSE BAYESIAN LEARNING ALGORITHM

As we mentioned before, classical SBL assumes the sources are uncorrelated, whereas EBSBL assumes the different blocks share a common correlation structure, which includes intra-block correlation or not. Related to the latter, it has been shown that if the data contains an intra-block correlation, the performance of EBSBL improves if it is taken into account. On the other hand, the performance of EBSBL ignoring intra-block correlation does not change with the amount of intra-block correlation in the data. The claim we make in this chapter is that if there is an intra-block correlation in the data, just modeling an inter-element correlation can already trigger a grouping effect. In other words, assuming inter-element correlation in the classical SBL model already promotes group sparsity without the need for building a new block-based data model first. Experimental results (shown later on) show that this grouping effect is even there when the true data has no intra-block correlations.

In this section, we, therefore, discuss how the classical SBL can be extended for correlated sources, where we assume for simplicity that only neighboring elements are correlated.

6.3.1. PRIORS ON THE SOURCES

In this section, the complex coefficients s_l, which were assumed to be independent and uncorrelated in the classical SBL, are assumed to be correlated with their immediate neighbors. In other words, $\mathbf{s}$ has the following distribution:

$$p(\mathbf{s};\boldsymbol{\Gamma}) = \mathscr{CN}(\mathbf{0},\boldsymbol{\Gamma}) \tag{6.21}$$

with the following tri-diagonal structure for $\boldsymbol{\Gamma}$:

$$\boldsymbol{\Gamma} = E[\mathbf{s}\mathbf{s}^{\mathsf{H}}] = \begin{bmatrix} \Gamma_{11} & \Gamma_{12} & 0 & \dots & 0 \\ \Gamma_{21} & \Gamma_{22} & \Gamma_{23} & \dots & 0 \\ 0 & \Gamma_{32} & \Gamma_{33} & \dots & 0 \\ \vdots & \vdots & \vdots & \ddots & \vdots \\ 0 & \dots & \dots & \dots & \Gamma_{LL} \end{bmatrix}. \tag{6.22}$$

Hence, we assume to have nonzero elements in the tridiagonal elements of $\boldsymbol{\Gamma}$, $\Gamma_{ll'}$ where $l' = l, l' = l+1, l' = l-1$, by ignoring the other elements of $\boldsymbol{\Gamma}$. Note that $\boldsymbol{\Gamma}$'s diagonal elements represent the power of the coefficients and $\Gamma_{ll} \geq 0$. When the variance $\Gamma_{ll} = 0$, then $s_l = 0$. Hence, the sparsity of the model is controlled by the diagonal elements of $\boldsymbol{\Gamma}$. For that problem, the likelihood is given by

$$p(\mathbf{s}|\mathbf{z};\boldsymbol{\Gamma},\sigma^2) = \mathscr{CN}(\boldsymbol{\mu}_{\mathbf{s}},\boldsymbol{\Sigma}_{\mathbf{s}}), \tag{6.23}$$

which is similar to the formulation in (6.21). Based on the likelihood in (6.23) and the prior of $\mathbf{s}$ in (6.21), it is easy to show that the posterior of $\mathbf{s}$ is a Gaussian with mean and covariance

$$\hat{\mathbf{s}} = \boldsymbol{\mu}_{\mathbf{s}} = \boldsymbol{\Gamma}\mathbf{A}^{\mathsf{H}}(\sigma^2\mathbf{I}_N + \mathbf{A}\boldsymbol{\Gamma}\mathbf{A}^{\mathsf{H}})^{-1}\mathbf{z}, \tag{6.24}$$

$$\boldsymbol{\Sigma}_{\mathbf{s}} = (\frac{1}{\sigma^2}\mathbf{A}^{\mathsf{H}}\mathbf{A} + \boldsymbol{\Gamma}^{-1})^{-1}, \tag{6.25}$$

where $\mathbf{\Gamma}$ is a tridiagonal matrix but the inverse $\mathbf{\Gamma}^{-1}$ does not have a simple structure as in the diagonal case. However, a fast inverse of this tridiagonal matrix is available with recursive methods [115].

6.3.2. DISCUSSION

Once we insert (6.22) into (6.24), while attaining $\boldsymbol{\mu}_s$ or $\hat{\mathbf{s}}$, we can see how the structure of $\mathbf{\Gamma}$ affects the relation with the neighboring elements. For the computation of $\boldsymbol{\mu}_\mathbf{s}$, we can see that in each row there are contributions from the sub-diagonals (the correlations with the neighbors) in the multiplication of the $\mathbf{\Gamma}$ and $\mathbf{A}^\mathsf{H}(\sigma^2\mathbf{I}_N + \mathbf{A}\mathbf{\Gamma}\mathbf{A}^\mathsf{H})^{-1}\mathbf{z}$. Here, in addition to Γ_{ll}, both $\Gamma_{l(l-1)}$ and $\Gamma_{l(l+1)}$ contribute to $(\boldsymbol{\mu}_\mathbf{s})_l$.

For the correlated block sparse data, the correlations with the neighboring elements (correlations in the sub-diagonals) become nonzero inside the group, and they become zero outside the group or for the corner elements of the group. The nonzero elements on the sub-diagonals enforce the neighboring elements to be nonzero in the group. Likewise, the corners of the groups can be clearly separated as the diagonals for the corner elements are nonzero, but the correlation with the neighboring zero element which is in the sub-diagonal is zero. If we focus on a single nonzero element surrounded by zeros (isolated nonzero element), its autocorrelation is nonzero, but the elements in the sub-diagonal are zero. Similarly, for a zero element inside a nonzero group (isolated zero elements), the correlations in the sub-diagonal become zero and are not affected by the neighboring nonzeros.

Once these elements of the $\mathbf{\Gamma}$ are used in (6.24), it can be seen that the contributions are only between consecutive nonzero elements. If there is a zero neighbor, then it does not have any contribution. Furthermore, if the nonzero element is a corner element or an isolated nonzero element, it also does not have a contribution to the zero neighbors. Only the nonzero elements in the group contribute to each other as given in (6.24) and provide a grouping effect. As a result, the proposed algorithm does not have any exponential decay around the corners of the groups or isolated zero and nonzero coefficients. Hence, unlike pattern coupling approaches [28, 30], the proposed algorithm tackles both isolated nonzero and zero elements in addition to the block sparse patterns.

6.3.3. ESTIMATION OF $\mathbf{\Gamma}$

By following the derivations from (6.9) to (6.12) to derive the EM-based update rule for $\mathbf{\Gamma}$, we attain the minimization function for $\mathbf{\Gamma}$. Since we assume a structure over $\mathbf{\Gamma}$, we can minimize the function in (6.12) only for the tridiagonal elements in (6.22). Note that we have complex-valued data and $\mathbf{\Gamma}$ is Hermitian symmetric but not symmetric, and thus each entry in the matrix is considered as a unique entry. Hence, we can take the derivative of all tridiagonal entries and set them to zero, leading to

$$\frac{\partial E_{\mathbf{s}|\mathbf{z};\mathbf{\Gamma}}[p(\mathbf{s};\mathbf{\Gamma})]}{\partial \Gamma_{ll'}} = [\mathbf{\Gamma}^{-1}(\mathbf{\Sigma}_\mathbf{s} + \boldsymbol{\mu}_\mathbf{s}\boldsymbol{\mu}_\mathbf{s}^\mathsf{H})\mathbf{\Gamma}^{-1} - \mathbf{\Gamma}^{-1}]_{ll'} = 0 \quad \text{for } l = l',\ l = l'+1 \text{ and } l = l'-1. \tag{6.26}$$

Note that while $\mathbf{\Gamma}$ has a particular tridiagonal structure, $\mathbf{\Gamma}^{-1}$ does not have a simple particular structure, unlike the diagonal version of $\mathbf{\Gamma}$. Hence, finding a closed-form solution

to this problem is tricky as the $\Gamma_{ll'}$ terms are entangled. Alternatively, we can use iterative algorithms to maximize (6.12), such as gradient-ascent [116] or fixed-point iterations [39]. However, they might be time-consuming as we need to take the inverse of $\mathbf{\Gamma}$ several times during the update steps of the iterative algorithms. Instead of solving the problem with iterative methods, we propose an approximation for the solution of $\mathbf{\Gamma}$.

To propose an approximation for the tridiagonal $\mathbf{\Gamma}$, we first consider the update rule for $\mathbf{\Gamma}$ without any structure, and then try to relate this to the solution for the tridiagonal $\mathbf{\Gamma}$. If we consider all the correlations in $\mathbf{\Gamma}$ without any structure, the derivative of (6.12) with respect to $\mathbf{\Gamma}$ is expressed as follows:

$$\frac{\partial E_{\mathbf{s}|\mathbf{z},\mathbf{\Gamma}}[p(\mathbf{s};\mathbf{\Gamma})]}{\partial \mathbf{\Gamma}} = \mathbf{\Gamma}^{-1}(\mathbf{\Sigma_s} + \boldsymbol{\mu_s}\boldsymbol{\mu_s}^{\mathsf{H}})\mathbf{\Gamma}^{-1} - \mathbf{\Gamma}^{-1}. \tag{6.27}$$

Setting this derivative to zero, we obtain the following closed-form solution

$$\bar{\mathbf{\Gamma}} = \mathbf{\Sigma_s} + \boldsymbol{\mu_s}\boldsymbol{\mu_s}^{\mathsf{H}}. \tag{6.28}$$

Here $\bar{\mathbf{\Gamma}}$ notation is used for the full $\mathbf{\Gamma}$. However, using all the correlations does not lead to a sparse solution. In classical SBL, the sparse coefficients are generally assumed to be uncorrelated and result in a diagonal $\mathbf{\Gamma}$. Note that the $\mathbf{\Gamma}$ estimated in (6.14) corresponds to the diagonal of $\bar{\mathbf{\Gamma}}$ and is also the closed-form solution to the problem in (6.13). Likewise, in the tridiagonal case, although it is not a closed-form solution to the problem in (6.26), we can use the following approximation

$$\begin{aligned} \Gamma_{ll'} &\approx (\mathbf{\Sigma_s})_{ll'} + (\boldsymbol{\mu_s})_l(\boldsymbol{\mu_s}^{\mathsf{H}})_{l'} \\ \text{for } l = l', l &= l'+1 \text{ and } l = l'-1 \end{aligned} \tag{6.29}$$

as a solution for the tridiagonal elements. Note that this solution contains the elements in the diagonal and main sub-diagonals of $\bar{\mathbf{\Gamma}}$. The intuition behind such an update rule is using the neighboring correlations that come from the full correlation matrix $\bar{\mathbf{\Gamma}}$. Since extracting a tridiagonal submatrix from the correlation matrix $\bar{\mathbf{\Gamma}}$ preserves the relation between neighboring elements, we embrace this approach. However, the convergence of such an update rule cannot be guaranteed as the proposed $\mathbf{\Gamma}$ matrix is not guaranteed to be positive definite anymore. Then, $\log(|\mathbf{\Gamma}|)$ might be undefined, and it might become complex valued at certain points, and it cannot guarantee the increment of the Q function in (6.12) during EM steps.

To guarantee the positive definiteness of $\mathbf{\Gamma}$ and obtain a generalized update rule for $\mathbf{\Gamma}$, we multiply the sub-diagonals by a parameter β to reduce their values:

$$\begin{aligned} &\Gamma_{ll'} \approx (\mathbf{\Sigma_s})_{ll'} + (\boldsymbol{\mu_s})_l(\boldsymbol{\mu_s}^{\mathsf{H}})_{l'} \text{ for } l = l' \\ &\Gamma_{ll'} \approx \beta((\mathbf{\Sigma_s})_{ll'} + (\boldsymbol{\mu_s})_l(\boldsymbol{\mu_s}^{\mathsf{H}})_{l'}) \\ &\text{for } l = l'+1 \text{ and } l = l'-1. \end{aligned} \tag{6.30}$$

Still, the correlation between neighboring elements is preserved which causes the group sparsity thanks to the relation between neighboring zeros and nonzeros. For values of $\beta \in [0, 0.5]$, we empirically observe that $\mathbf{\Gamma}$ stays positive definite and the Q function (6.12)

does not result in complex values. Here, the most efficient β is observed to be 0.5. Although the update rule proposed for the sub-diagonal elements is intuitive, it provides a significant performance improvement for block sparse and isolated elements.

To provide theoretical bounds of β for the positive definiteness of $\mathbf{\Gamma}$, we use the following proposition from [117]:

Proposition 1: Let $\mathbf{\Gamma}_t = \begin{bmatrix} a_1 & b_1 & 0 & \dots & 0 \\ b_1^* & a_2 & b_2 & \dots & 0 \\ 0 & b_2^* & a_3 & \dots & 0 \\ \vdots & \vdots & \vdots & \ddots & \vdots \\ 0 & \dots & \dots & \dots & a_L \end{bmatrix}$ be a Hermitian symmetric tridiagonal matrix with diagonal entries positive and real. If

$$b_i b_i^* < \frac{1}{4} a_i a_{i+1} \frac{1}{\cos^2(\frac{\pi}{L+1})} \tag{6.31}$$

then $\mathbf{\Gamma}_t$ is positive definite. Using this proposition, we can introduce the following theorem.

Theorem 1: For $\beta^2 < \frac{1}{4} \frac{1}{\cos^2(\frac{\pi}{L+1})}$, $\mathbf{\Gamma}$ in (6.30) is positive definite.

Proof. First, we prove this for the second part of (6.30) which includes $\boldsymbol{\mu}_\mathbf{s}\boldsymbol{\mu}_\mathbf{s}^\mathsf{H}$. Assuming that $\boldsymbol{\mu}_\mathbf{s} = \mathbf{c}$, we have the following

$$\begin{aligned} \text{tridiag}(\boldsymbol{\mu}_\mathbf{s}\boldsymbol{\mu}_\mathbf{s}^\mathsf{H}) &= \text{tridiag}(\mathbf{c}\mathbf{c}^\mathsf{H}) \\ &= \begin{bmatrix} c_1 c_1^* & \beta c_1 c_2^* & 0 & \dots & 0 \\ \beta c_2 c_1^* & c_2 c_2^* & \beta c_2 c_3^* & \dots & 0 \\ 0 & \beta c_3 c_2^* & c_3 c_3^* & \dots & 0 \\ \vdots & \vdots & \vdots & \ddots & \vdots \\ 0 & 0 & 0 & \dots & c_L c_L^* \end{bmatrix} \end{aligned} \tag{6.32}$$

where tridiag(.) is defined as the extraction of the tridiagonal part of a given matrix and multiplication of the subdiagonals by β. For $\beta^2 < \frac{1}{4} \frac{1}{\cos^2(\frac{\pi}{L+1})}$, we can write $\beta^2 c_i c_{i+1}^* c_{i+1} c_i^* < \frac{1}{4} c_i c_i^* c_{i+1} c_{i+1}^* \frac{1}{\cos^2(\frac{\pi}{L+1})}$ using the *Proposition 1*. Therefore, for the values of $\beta^2 < \frac{1}{4} \frac{1}{\cos^2(\frac{\pi}{L+1})}$, we can conclude that tridiag(.) results in a positive definite matrix from rank-one matrices and tridiag($\boldsymbol{\mu}_\mathbf{s}\boldsymbol{\mu}_\mathbf{s}^\mathsf{H}$) is positive definite.

Now, we generalize this approach for any positive definite matrix. Note that all positive definite matrices can be written as $\mathbf{C}\mathbf{C}^\mathsf{H} = \sum_{i=1}^N \mathbf{c}_i \mathbf{c}_i^\mathsf{H}$ which is a summation of multiple rank-one matrices. Here, $\mathbf{c}_i$ is the ith column of $\mathbf{C}$. As tridiag(.) is a linear operator, it can be written as follows:

$$\text{tridiag}(\mathbf{C}\mathbf{C}^\mathsf{H}) = \sum_{i=1}^{N} \text{tridiag}(\mathbf{c}_i \mathbf{c}_i^\mathsf{H}). \tag{6.33}$$

Since tridiag(.) results in a positive definite matrix for each $\mathbf{c}_i\mathbf{c}_i^\mathsf{H}$, and the summation of positive definite matrices is also a positive definite, tridiag($\mathbf{C}\mathbf{C}^\mathsf{H}$) is positive definite.

Note that $\mathbf{\Sigma_s}$ is positive definite for a positive definite $\mathbf{\Gamma}$. Therefore, tridiag($\mathbf{\Sigma_s}$) is positive definite. As a final step, it can be concluded that,

$$\mathbf{\Gamma} = \text{tridiag}(\mathbf{\Sigma_s}) + \text{tridiag}(\boldsymbol{\mu_s}\boldsymbol{\mu_s}^{\mathsf{H}}) \tag{6.34}$$

is positive definite since it is a summation of positive definite matrices. □

Remark 1: From *Theorem 1*, $-\frac{1}{2cos(\frac{\pi}{L+1})} < \beta < \frac{1}{2cos(\frac{\pi}{L+1})}$ guarantees the positive definiteness of $\mathbf{\Gamma}$. To choose a safe boundary for β, we keep it in the range $[0, 0.5]$ for values of $L > 50$. Note that we keep β positive so as not to change the sign of the correlation between the neighboring elements.

Remark 2: Note that it is important to show the proposed update rule increases the Q function (6.12) in every iteration. Because then we can draw from the generalized EM theory [118]: any hyperparameter update rule that ensures that the Q function is non-decreasing in each EM iteration will ensure convergence of the EM iterations to a local maximum or saddle point. Once we consider the case $\beta \in [0.0.5]$ for (6.30), we empirically observe that the Q function in (6.12) increases in each iteration, and it has a higher increase in each EM iteration compared to the one in (6.14). Although the theoretical convergence proof is unavailable, we have never encountered a case where the algorithm's convergence is not satisfied with a high number of trials of simulations and various problem models.

Remark 3: The choice of β seems slightly important for the recovery performance, as demonstrated by our simulation results. Although our simulations suggest that choosing a non-zero β mostly improves the performance compared to the setting with $\beta = 0$, the best choice of β appears to be around 0.5. However, for cases where the signal structure is unknown, the β parameter might be adjusted for the structure of the data by setting it to another value in the range $\beta \in [0, 0.5]$.

6.3.4. ESTIMATION OF THE NOISE PARAMETER σ^2

To estimate σ^2, we maximize $E_{\mathbf{s}|\mathbf{z};\mathbf{\Gamma},\sigma^2}[p(\mathbf{z},\mathbf{s};\mathbf{\Gamma},\sigma^2)]$ with respect to σ^2 [28]. Now, we only focus on the σ^2 related terms on the right-hand side of (6.10) as follows:

$$\begin{aligned} & E_{\mathbf{s}|\mathbf{z};\sigma^2}[\log p(\mathbf{z}|\mathbf{s};\sigma^2)] \\ & \propto -N\log\sigma^2 - \frac{E_{\mathbf{s}|\mathbf{z};\sigma^2}[||\mathbf{z}-\mathbf{A}\mathbf{s}||_2^2]}{\sigma^2} \\ & = -N\log\sigma^2 - \frac{||\mathbf{z}-\mathbf{A}\boldsymbol{\mu_s}||_2^2 + \text{tr}(\mathbf{\Sigma_s}\mathbf{A}^{\mathsf{H}}\mathbf{A})}{\sigma^2}. \end{aligned} \tag{6.35}$$

The second equality can be derived as follows:

$$\begin{aligned} & E_{\mathbf{s}|\mathbf{z};\sigma^2}[||\mathbf{z}-\mathbf{A}\mathbf{s}||_2^2] \\ & = \mathbf{z}^{\mathsf{H}}\mathbf{z} - 2E[\mathbf{s}^{\mathsf{H}}\mathbf{A}^{\mathsf{H}}\mathbf{z}] + E[\mathbf{s}^{\mathsf{H}}\mathbf{A}^{\mathsf{H}}\mathbf{A}\mathbf{s}] \\ & = \mathbf{z}^{\mathsf{H}}\mathbf{z} - 2\boldsymbol{\mu_s}^{\mathsf{H}}\mathbf{A}^{\mathsf{H}}\mathbf{z} + \boldsymbol{\mu_s}^{\mathsf{H}}\mathbf{A}^{\mathsf{H}}\mathbf{A}\boldsymbol{\mu_s} + \text{tr}(\mathbf{\Sigma_s}\mathbf{A}^{\mathsf{H}}\mathbf{A}) \\ & = ||\mathbf{z}-\mathbf{A}\boldsymbol{\mu_s}||_2^2 + \text{tr}(\mathbf{\Sigma_s}\mathbf{A}^{\mathsf{H}}\mathbf{A}). \end{aligned} \tag{6.36}$$

Algorithm 4: Correlated SBL

Output: S: unknown data

Initialize $\sigma^2 = 1$, diag(Γ) = $\mathbf{1}$, $\epsilon_{min} = 0.001$, $E_{max} = 100$

while $e < E_{max}$ *and* $\epsilon_{min} < \epsilon$ **do**

$e = e+1$, $\boldsymbol{\mu}_{\mathbf{s}}^{old} = \boldsymbol{\mu}_{\mathbf{s}}^{new}$, $\Gamma_{ll'}^{old} = \Gamma_{ll'}^{new}$,

Γ = tridiag($\Gamma_{ll'}^{new}$)

compute $\boldsymbol{\Sigma}_{\mathbf{s}} = (\frac{1}{\sigma^2}\mathbf{A}^H\mathbf{A} + \boldsymbol{\Gamma}^{-1})^{-1}$

update $\Gamma_{ll'}^{new}$ with (6.30)

update $(\sigma^2)^{new}$ with (6.37)

$\epsilon = ||\boldsymbol{\mu}_{\mathbf{s}}^{new} - \boldsymbol{\mu}_{\mathbf{s}}^{old}||_2$

end

$\hat{\mathbf{s}} = \boldsymbol{\mu}_{\mathbf{s}}^{new}$

Then, we set the derivative of (6.35) with respect to σ^2 to 0 and we obtain the update for σ^2 as

$$\hat{\sigma}^2 = \frac{||\mathbf{z} - \mathbf{A}\boldsymbol{\mu}_{\mathbf{s}}||_2^2 + \text{tr}(\boldsymbol{\Sigma}_{\mathbf{s}}\mathbf{A}^{\mathsf{H}}\mathbf{A})}{N}. \tag{6.37}$$

The estimate of $\mathbf{s}$ is finally given by $\boldsymbol{\mu}_{\mathbf{s}}$ in (6.6) by iteratively calculating the $\Gamma_{ll'}$'s in (6.29) and σ^2 in (6.37) till convergence. The iterative steps of the proposed algorithm are given in Algorithm 9. For the convergence, we use the stopping criterion that the maximum absolute error of two successive estimates of $\mathbf{s}$ is smaller than a threshold, or the number of iterations exceeds the maximum number of iterations.

6.3.5. COMPUTATIONAL COMPLEXITY

The computational complexity of the proposed algorithm is similar to the classical SBL, PCSBL, and CSBL. Here, the main computational task at each iteration is to calculate the covariance matrix $\boldsymbol{\Sigma}_{\mathbf{s}}$ as it requires computing the inverse of an $L \times L$ matrix. By using the matrix inversion lemma [119], this matrix inversion can be converted to an $N \times N$ matrix inversion. Hence the computational complexity is of order $\mathcal{O}(N^3)$. However, for the computation of the tridiagonal $\boldsymbol{\Gamma}$, there is a slight increase in the computational cost, but its effect on the overall computational complexity is negligible.

6.4. RELATION TO EBSBL

To show the relation between our method and EBSBL, we consider EBSBL with $h = 2$ and hence $g = L - 1$. In such case, $s_i = \mathbf{x}_{i-1}(2) + \mathbf{x}_i(1)$, where (.) shows the entry indice in $\mathbf{x}_i$. Different than EBSBL, where there is a single $\mathbf{B}$ for each block, we use different $\mathbf{B}_i$s for each block. We then have $E[\mathbf{x}_i\mathbf{x}_j^{\mathsf{H}}] = \delta_{i,j}\beta_i\mathbf{B}_i$ ($\delta_{i,j} = 1$ if $i = j$; otherwise $\delta_{i,j} = 0$). Note that, to avoid ambiguities, we also take $\beta_i = 1$. In our approach, we assume each s_i is correlated to the neighboring elements s_{i-1} and s_{i+1} and ignore the other correlations. By interpreting the $E[\mathbf{s}\mathbf{s}^{\mathsf{H}}]$ in (6.22) in terms of the $\mathbf{B}_i$ matrices our entries in the tridiagonal

$\mathbf{\Gamma}$ matrix are given as follows:

$$\begin{aligned}
\Gamma_{ii} &= E[s_i s_i^{\mathsf{H}}] \\
&= E[(\mathbf{x}_{i-1}(2)+\mathbf{x}_i(1))(\mathbf{x}_{i-1}(2)^*+\mathbf{x}_i(1)^*)] \\
&= E[\mathbf{x}_i(1)\mathbf{x}_i(1)^*+\mathbf{x}_{i-1}(2)\mathbf{x}_{i-1}(2)^*] \\
&= \mathbf{B}_i^{(11)}+\mathbf{B}_{i-1}^{(22)} \\
\Gamma_{i(i+1)} &= E[s_i s_{i+1}^{\mathsf{H}}] \\
&= E[(\mathbf{x}_{i-1}(2)+\mathbf{x}_i(1))(\mathbf{x}_i(2)^*+\mathbf{x}_{i+1}(1)^*)] \\
&= E[\mathbf{x}_i(1)\mathbf{x}_i(2)^*] = \mathbf{B}_i^{(12)} \\
\Gamma_{(i+1)i} &= \Gamma_{i(i+1)}^* \text{ for } L>i>1,
\end{aligned} \tag{6.38}$$

where $\mathbf{B}_i^{(.)}$ corresponds to the (.)th entry of the $\mathbf{B}_i$ matrix. Here, the intermediate terms in $E[s_i s_i^{\mathsf{H}}]$ and $E[s_i s_{i+1}^{\mathsf{H}}]$ are $E[(\mathbf{x}_{i-1}(2)\mathbf{x}_i(1)^*+\mathbf{x}_i(1)\mathbf{x}_{i-1}(2)^*]=0$ and $E[(\mathbf{x}_{i-1}(2)\mathbf{x}_i(2)^*+\mathbf{x}_i(1)\mathbf{x}_{i+1}(1)^*+\mathbf{x}_{i-1}(2)\mathbf{x}_{i+1}(1)^*]=0$, respectively as $E[\mathbf{x}_i\mathbf{x}_j^{\mathsf{H}}]=0$ for $i\neq j$).

The equations in (6.38) can also be written as follows:

$$E[\mathbf{s}_{i:i+1}\mathbf{s}_{i:i+1}^{\mathsf{H}}] = \begin{bmatrix} \mathbf{B}_i^{(11)}+\mathbf{B}_{i-1}^{(22)} & \mathbf{B}_i^{(12)} \\ \mathbf{B}_i^{(21)} & \mathbf{B}_{i+1}^{(11)}+\mathbf{B}_i^{(22)} \end{bmatrix} \tag{6.39}$$

where $\mathbf{s}_{i:j}$ represents the elements of $\mathbf{s}$ from i to j. Therefore, our model can be interpreted as an alternative to the EBSBL for $h=2$ when there are separate correlation matrices $\mathbf{B}_i$ for each group.

To show the equivalence between the MAP estimates of $\hat{\mathbf{s}}$ in EBSBL and in the proposed method, we give an examination of the updating rule of $\hat{\mathbf{s}}$ in (6.20) that comes from (6.18), and the updating rule of $\hat{\mathbf{s}}$ in (6.24), respectively. Rewriting the first part of (6.18) and (6.24) as

$$\mathbf{\Gamma}\mathbf{A}^{\mathsf{H}} = \begin{bmatrix} \mathbf{B}_1^{(11)}\mathbf{a}_1^{\mathsf{H}}+\mathbf{B}_1^{(12)}\mathbf{a}_2^{\mathsf{H}} \\ \mathbf{B}_1^{(21)}\mathbf{a}_1^{\mathsf{H}}+(\mathbf{B}_1^{(22)}+\mathbf{B}_2^{(11)})\mathbf{a}_2^{\mathsf{H}}+\mathbf{B}_2^{(12)}\mathbf{a}_3^{\mathsf{H}} \\ \vdots \\ \mathbf{B}_{L-2}^{(21)}\mathbf{a}_{L-2}^{\mathsf{H}}+(\mathbf{B}_{L-2}^{(22)}+\mathbf{B}_{L-1}^{(11)})\mathbf{a}_{L-1}^{\mathsf{H}}+\mathbf{B}_{L-1}^{(12)}\mathbf{a}_L^{\mathsf{H}} \\ \mathbf{B}_{L-1}^{(21)}\mathbf{a}_{L-1}^{\mathsf{H}}+\mathbf{B}_{L-1}^{(22)}\mathbf{a}_L^{\mathsf{H}} \end{bmatrix} \tag{6.40}$$

$$\mathbf{\Gamma}_0\Theta^{\mathsf{H}} = \begin{bmatrix} \mathbf{B}_1^{(11)}\mathbf{a}_1^{\mathsf{H}}+\mathbf{B}_1^{(12)}\mathbf{a}_2^{\mathsf{H}} \\ \mathbf{B}_1^{(21)}\mathbf{a}_1^{\mathsf{H}}+\mathbf{B}_1^{(22)}\mathbf{a}_2^{\mathsf{H}} \\ \vdots \\ \mathbf{B}_{L-1}^{(11)}\mathbf{a}_1^{\mathsf{H}}+\mathbf{B}_{L-1}^{(12)}\mathbf{a}_L^{\mathsf{H}} \\ \mathbf{B}_{L-1}^{(21)}\mathbf{a}_1^{\mathsf{H}}+\mathbf{B}_{L-1}^{(22)}\mathbf{a}_L^{\mathsf{H}} \end{bmatrix}. \tag{6.41}$$

where $\mathbf{a}_i$ represents the ith column of the $\mathbf{A}$ matrix. It is straightforward to see that $\mathbf{\Gamma}\mathbf{A}^{\mathsf{H}} = \sum_{i=1}^{L-1}\mathbf{E}_i\mathbf{\Gamma}_0\Theta^{\mathsf{H}}$. Now, we need to show the equivalence of the second part of (6.18) and (6.24), which is given by $(\sigma^2\mathbf{I}_N+\Theta\mathbf{\Gamma}_0\Theta^{\mathsf{H}})^{-1}\mathbf{Z}$ and $(\sigma^2\mathbf{I}_N+\mathbf{A}\mathbf{\Gamma}\mathbf{A}^{\mathsf{H}})^{-1}\mathbf{Z}$. Using the simple

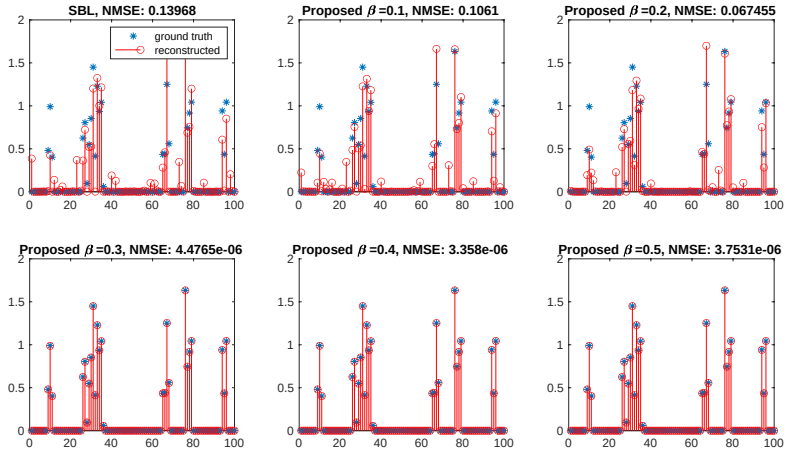

(a)

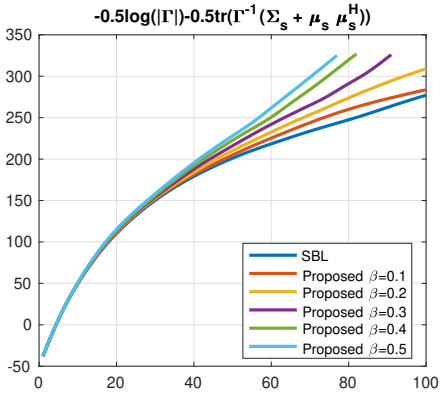

(b)

Figure 6.1: (a) The magnitudes of reconstructed group sparse data with $K = 25$, $N = 35$ and $L = 100$ for SBL and the proposed method with noiseless data and (b) the value of the Q function for SBL and the proposed one.

diagonal structure of $\mathbf{\Gamma}_0$ we attain the following:

$$\Theta\mathbf{\Gamma}_0\Theta^{\mathsf{H}} = \sum_{i=1}^{L-1} (\mathbf{a}_i\mathbf{B}_i^{(11)}\mathbf{a}_i^{\mathsf{H}} + \mathbf{a}_{i+1}\mathbf{B}_i^{(21)}\mathbf{a}_i^{\mathsf{H}} + \mathbf{a}_i\mathbf{B}_i^{(12)}\mathbf{a}_{i+1}^{\mathsf{H}} + \mathbf{a}_{i+1}\mathbf{B}_i^{(22)}\mathbf{a}_{i+1}^{\mathsf{H}}), \tag{6.42}$$

and using the tridiagonal structure of $\mathbf{\Gamma}$ we obtain

$$\begin{aligned}\mathbf{A\Gamma A}^{\mathsf{H}} = \mathbf{a}_1\mathbf{B}_1^{(11)}\mathbf{a}_1^{\mathsf{H}} + \mathbf{a}_2\mathbf{B}_1^{(21)}\mathbf{a}_1^{\mathsf{H}} + \\ \sum_{i=1}^{L-2}(\mathbf{a}_i\mathbf{B}_i^{(12)}\mathbf{a}_{i+1}^{\mathsf{H}} + \mathbf{a}_{i+1}(\mathbf{B}_i^{(22)} + \mathbf{B}_{i+1}^{(11)})\mathbf{a}_{i+1}^{\mathsf{H}} + \\ \mathbf{a}_{i+2}\mathbf{B}_i^{(21)}\mathbf{a}_{i+1}^{\mathsf{H}}) + \mathbf{a}_{L-1}\mathbf{B}_{L-1}^{(12)}\mathbf{a}_L^{\mathsf{H}} + \mathbf{a}_L\mathbf{B}_{L-1}^{(22)}\mathbf{a}_L^{\mathsf{H}}.\end{aligned} \tag{6.43}$$

It is easy to see the equivalence of the expressions in (6.42) and (6.43). Therefore, the MAP estimates of $\hat{\mathbf{s}}$ are the same for both algorithms.

The difference between the algorithms can be seen in the update rules for $\mathbf{B}_i$ in EBSBL and the proposed algorithm. The update rules for EBSBL in [33] are given as follows:

$$\beta_i = \mathrm{tr}[\mathbf{B}_i^{-1}(\mathbf{\Sigma}_{\mathbf{x}_i} + \boldsymbol{\mu}_{\mathbf{x}_i}\boldsymbol{\mu}_{\mathbf{x}_i}^{\mathsf{H}})], \tag{6.44}$$

$$\mathbf{B} = \frac{1}{g}\sum_{i=1}^{g}\frac{\mathbf{\Sigma}_{\mathbf{x}_i} + \boldsymbol{\mu}_{\mathbf{x}_i}\boldsymbol{\mu}_{\mathbf{x}_i}^{\mathsf{H}}}{\beta_i}. \tag{6.45}$$

Normally, in EBSBL, β_i is also learned during the iterations but once we assume $\beta_i = 1$ we cancel that step and only have the iterations for $\mathbf{B}_i$ and σ^2. Our update rule can be considered a counterpart of the case without averaging the $\mathbf{B}_i$s in EBSBL as follows:

$$\mathbf{B}_i = \mathbf{\Sigma}_{\mathbf{x}_i} + \boldsymbol{\mu}_{\mathbf{x}_i}\boldsymbol{\mu}_{\mathbf{x}_i}^{\mathsf{H}}, \tag{6.46}$$

where $\mathbf{\Sigma}_{\mathbf{x}_i} \in \mathbb{C}^{2\times 2}$ corresponds to the ith diagonal block in $\mathbf{\Sigma}_{\mathbf{x}}$ in (6.19) and $\boldsymbol{\mu}_{\mathbf{x}_i} \in \mathbb{C}^2$ is the ith block of $\boldsymbol{\mu}_{\mathbf{x}}$ in (6.18). We already showed that $\boldsymbol{\mu}_{\mathbf{s}} = \sum_{i=1}^{L-1}\mathbf{E}_i\boldsymbol{\mu}_{\mathbf{x}}$. However, now we cannot obtain the tridiagonal part of $\boldsymbol{\mu}_{\mathbf{s}}\boldsymbol{\mu}_{\mathbf{s}}^{\mathsf{H}}$, which is included in our update rule in (6.29), by the overlapping block diagonal sum of blocks in $\boldsymbol{\mu}_{\mathbf{x}}\boldsymbol{\mu}_{\mathbf{x}}^{\mathsf{H}}$ in the way that we obtained (6.39). Another difference between our algorithm and EBSBL is in the update of $\mathbf{\Sigma}_{\mathbf{x}}$ in (6.19) and $\mathbf{\Sigma}_{\mathbf{s}}$ in (6.25) due to the inversion terms. While $\mathbf{\Gamma}_0$ in (6.19) is a block diagonal matrix, $\mathbf{\Gamma}$ in (6.25) is a tridiagonal matrix, and relating their inverses is not straightforward. Besides, the outmost inverse term entangles the relationship between $\mathbf{\Sigma}_{\mathbf{x}}$ and $\mathbf{\Sigma}_{\mathbf{s}}$.

Note that the number of unknown variables in EBSBL when $h = 2$ is almost two times the one required in the proposed algorithm. The reduced number of unknowns enhances the performance of the proposed algorithm. Lastly, the proposed method has around $\mathcal{O}(h^3) = \mathcal{O}(2^3)$ times lower computational complexity than EBSBL.

6.5. NUMERICAL RESULTS

In this section, we conduct numerical experiments to evaluate the performance of the proposed algorithm in comparison with the existing literature. The performance of the algorithms is examined for both synthetic and real data. The benchmark algorithms include SBL [37], BSBL [33], EBSBL [33], CSBL [30], PCSBL [28], and the proposed method. For EBSBL, we use EBSBL-BO: the bound-optimization presented in [33], as it is used as a reference method for comparison and it is stated that it has a similar performance to EBSBL-EM: the expectation-maximization method.

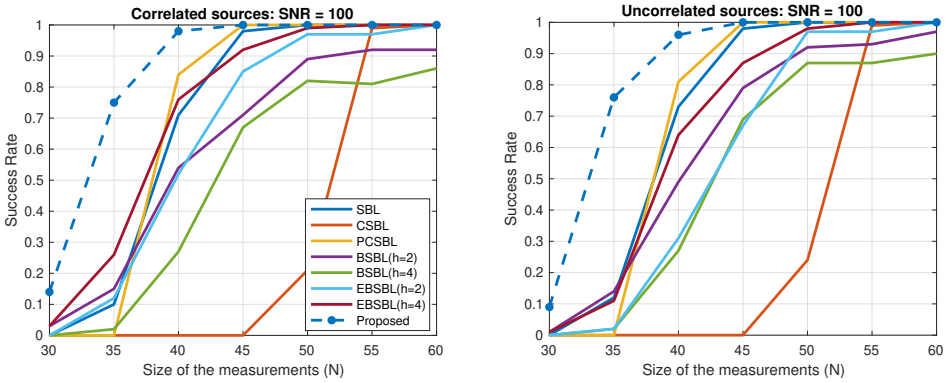

(a) (b)

Figure 6.2: Success rate performance comparison of the sparse Bayesian learning algorithms with correlated (a) and uncorrelated (b) noiseless data for the sparsity level $K = 25$ and different sizes of the measurements N

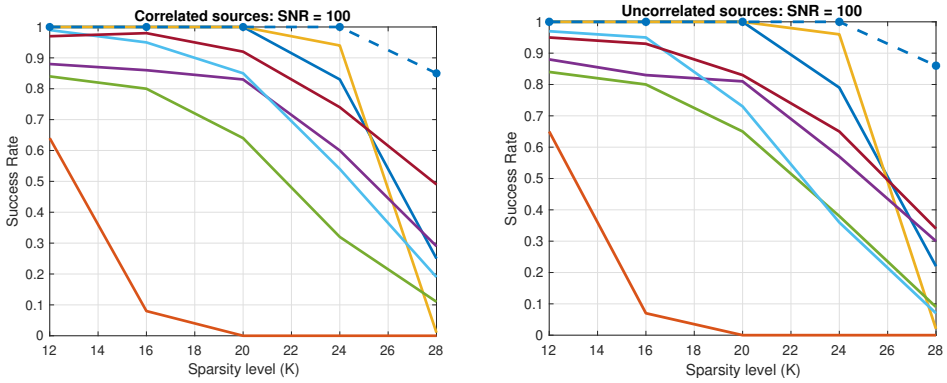

(a) (b)

Figure 6.3: Success rate performance comparison of the sparse Bayesian learning algorithms with correlated (a) and uncorrelated (b) noiseless data for the size of the measurements $N = 40$ and different sparsity levels K.

6.5.1. SYNTHETIC DATA AND SYNTHETIC SYSTEM MATRIX

The measurement matrix $\mathbf{A}$ is randomly generated with each entry independently drawn from a normal distribution, and the columns are normalized to unit norm. Likewise, the nonzero coefficients of $\mathbf{s}$ are drawn from a complex normal distribution. Complex Gaussian white noise is added with a signal-to-noise ratio of $SNR(dB) = 20\log 10(||\mathbf{As}||_2/||\mathbf{n}||_2)$.

We use the success rate and the support recovery rate under the noiseless case for performance evaluation. On the other hand, the normalized mean squared error (NMSE) is used under noisy cases. The NMSE is calculated by averaging the normalized

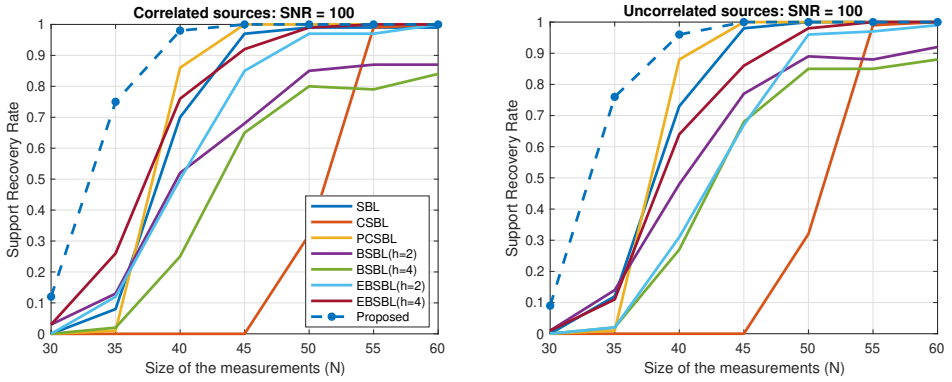

(a) (b)

Figure 6.4: Support recovery rate performance comparison of the sparse Bayesian learning algorithms with correlated (a) and uncorrelated (b) noiseless data for for the sparsity level $K = 25$ and different sizes of the measurements N.

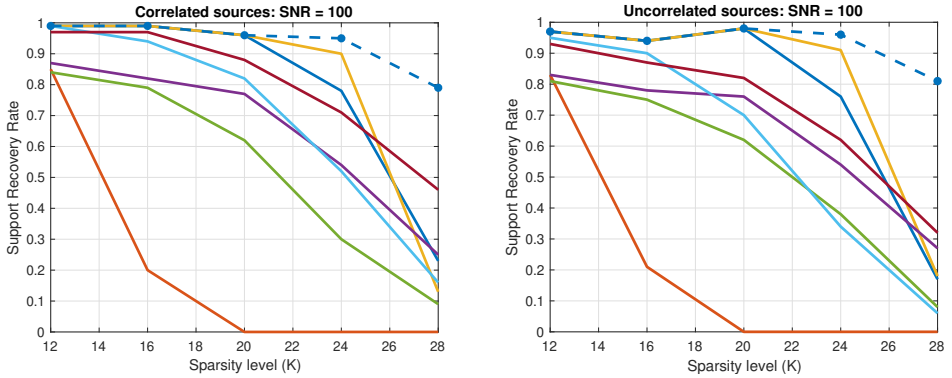

(a) (b)

Figure 6.5: Support recovery rate performance comparison of the sparse Bayesian learning algorithms with correlated (a) and uncorrelated (b) noiseless data for the size of the measurements $N = 40$ and different sparsity levels K.

squared errors $||\mathbf{s} - \hat{\mathbf{s}}||_2^2 / ||\mathbf{s}||_2^2$. The success rate is defined as the percentage of successful trials in a total of T independent runs. A successful trial is defined as one with NMSE being less than 10^{-3}. A total number of $T = 100$ independent trials are conducted. Besides, for the identification of the true support of sparse signals, we consider the "pattern recovery success rate". Similar to the regular success rate, it is the ratio of the number of successful trials to the total number of independent runs. However, each trial is considered successful if the support of the block-sparse signal is recovered. A coefficient whose magnitude is less than 10^{-2} is assumed as a zero coefficient for the calculation of the pattern recovery success rates (but not for the regular success rate).

For the proposed method, $\epsilon = 0.001$ and $E_{max} = 100$ in Algorithm 9 are used in our experiments. Similarly, for PCSBL and CSBL, we used the same values. On the other hand, the probability distribution relies on hierarchical parameters a and b in $p(\mathbf{\Gamma}|a,b)$ in PCSBL. It should be noted that the choice of the hyperparameter a of PCSBL affects dramatically the algorithm's performance [30]. The parameter a is always set to 0.5 to achieve its best performance in the following experiments. Also, the parameter $b = 10^{-10}$. To make a fair comparison, the block size h is first set to be 2 for both BSBL and EBSBL. However, we also consider $h = 4$ for BSBL and EBSBL, as it is used for comparison in the literature [33, 28]. Note that the algorithms are modified to handle the complex data.

For the proposed algorithm, we use the update rule in (6.30) with $\beta = 0.5$. For this, we observe the behavior of the Q function in (6.12) during EM iterations both for SBL and the proposed method with different β values. For a sample realization, the objective function increase during EM iterations for all of them is shown in Fig. 6.1b, and the reconstructed data for different methods are shown in 6.1a with a noiseless case. Note that the proposed method further increases the value of the objective function compared to classical SBL for values of $\beta \in [0, 0.5]$. Since the highest increment is observed with $\beta = 0.5$ among several realizations, we select $\beta = 0.5$ to test our algorithm.

In the numerical simulations, sparse signals with dimensionality of $N = 40$, $L = 100$ and $K = 25$ nonzero coefficients are partitioned into five arbitrary blocks with random sizes and arbitrary locations. For these arbitrary groups, we generate them in the same way with [28]. Here, the group sizes are likely to be higher than two and the nonzero groups are apart from each other. Hence, in this setting, the chance of there being isolated zeros and nonzeros among the groups is very small. The sources are chosen to be both uncorrelated and correlated which matches our tridiagonal correlation assumption. The correlated sources are created as $\mathbf{s} = \mathbf{R}^{1/2}\mathbf{w}$ where $\mathbf{w}$ is complex random noise with unit variance. We choose

$$\mathbf{R} = \begin{bmatrix} 1 & c & \dots & 0 \\ c & 1 & \dots & 0 \\ \vdots & \vdots & \ddots & \vdots \\ 0 & \dots & \dots & 1 \end{bmatrix} \tag{6.47}$$

where $c = 0.3$. $\mathbf{R}$ is chosen to be a tridiagonal correlation matrix; hence, only the neighboring correlations are considered. As a second setting, the sources are chosen to be uncorrelated to see the robustness of the algorithms with such a setting and $c = 0$.

PERFORMANCE IN NOISELESS ENVIRONMENTS

The success rates of the exact recovery of different algorithms the noiseless case ($SNR = 100$ dB) are provided from the viewpoint of the size of the measurements N for the purpose of comparison. Fig. 6.2 and 6.3 give the success rates of different algorithms against the size of the measurements N and the sparsity level K for both correlated and uncorrelated data, respectively. Simulation results with correlated complex-valued data in Fig. 6.2a and 6.3a show that the proposed method outperforms all other methods in terms of success rate. Note that the main counterpart of our method is EBSBL ($h = 2$) and

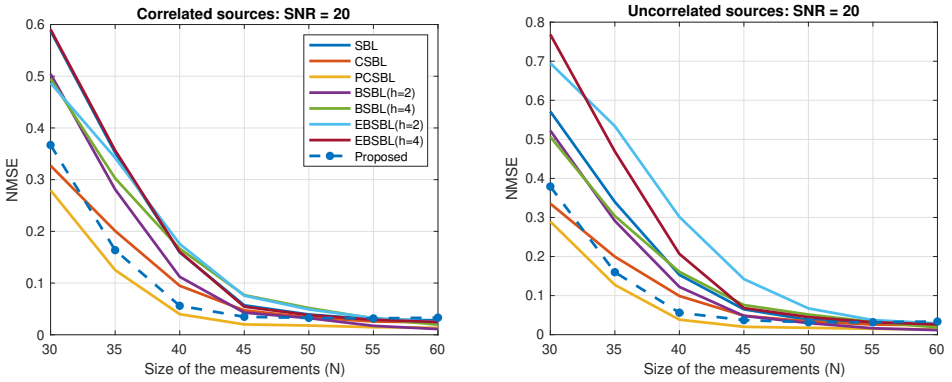

(a) (b)

Figure 6.6: NMSE performance comparison of the sparse Bayesian learning algorithms with correlated (a) and uncorrelated (b) noisy data (20 dB SNR) for the sparsity level $K = 25$ and different sizes of the measurements N.

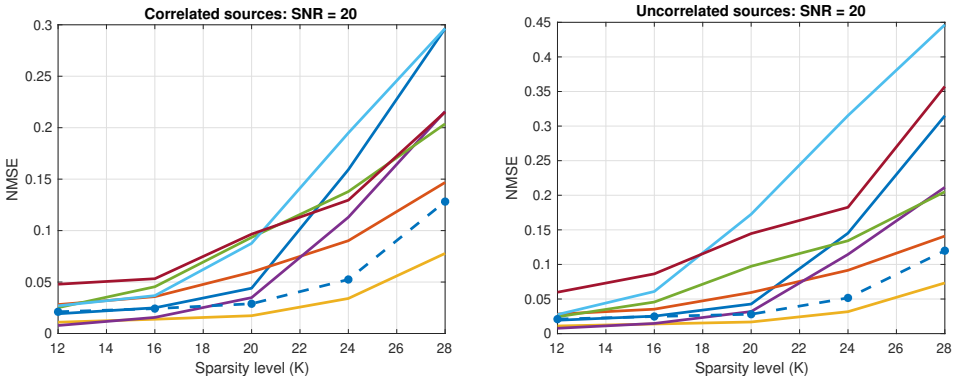

(a) (b)

Figure 6.7: NMSE performance comparison of the sparse Bayesian learning algorithms with correlated (a) and uncorrelated (b) noisy data (20 dB SNR) for the size of the measurements $N = 40$ and different sparsity levels K.

there is a significant difference between EBSBL and the proposed one in terms of success rate. Furthermore, our method has lower computational complexity. Surprisingly, CSBL's success rate is lower than other algorithms. It has been reported that CSBL performs similarly to PCSBL [30]. It still has good performance in terms of NMSE, but since the preselected threshold is set at 10^{-3}, its success rate is low. If we select it as 10^{-1}, the success rate of CSBL would be higher. However, for the noiseless case, 10^{-3} seems to be a good choice to evaluate the performances of the algorithms. On the other hand, BSBL might not be a suitable algorithm to test the performances of the data with varying block sizes and varying block partition locations. While BSBL performs well with the data that

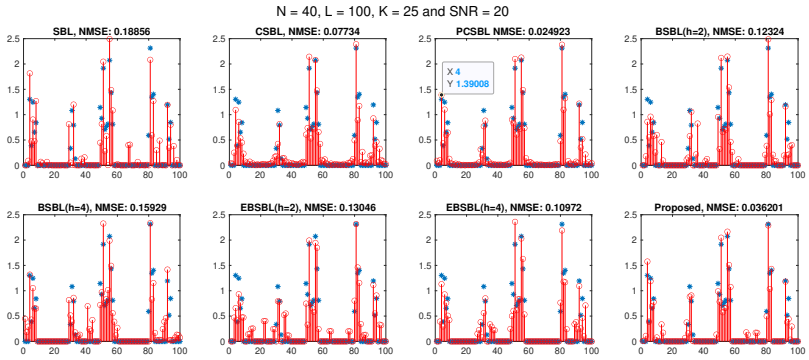

Figure 6.8: The magnitudes of the reconstructions of SBL algorithms with group sparse noisy data (20 dB SNR).

might fit into the considered block partition assumption, it does not perform well with the other data.

With uncorrelated data, again the proposed method has a higher success rate than the existing literature. Compared to the correlated case in Fig. 6.2 and 6.3, the EBSBL method has lower performance with uncorrelated data. This is expected as it directly uses the correlations. However, surprisingly our method's and PCSBL's performances did not change significantly. While we exploit the correlations of the neighboring elements, PCSBL assumes them uncorrelated and enforces the statistical dependence between sparsity patterns. Although these two methods utilize different motivations for correlated neighboring coefficients, they seem not to be affected by the level of the correlation.

In the support recovery rate graphs in Fig. 6.4 and 6.5, the performances of the algorithms are similar to the success rate performances given in Fig. 6.2 and 6.3. Although we observe small variations over the methods, again the proposed method outperforms the existing literature.

PERFORMANCE IN NOISY ENVIRONMENTS

The performances of different algorithms in terms of the NMSE against the size of the measurements N and the sparsity level K are given in Fig. 6.6 and 6.7, respectively. Under noisy environments, the NMSEs of all algorithms consistently decrease as the size of the measurements N increases and the sparsity degree K decreases as shown in Fig. 6.6 and 6.7, where PCSBL with $a = 0.5$ achieves the lowest NMSE and proposed method achieves lower performance than the best performance of PCSBL. Note that the tested data consists of sparse groups and the chance of isolated zeros and nonzero elements in the data is very small. Different from the noiseless case, CSBL is better at dealing with noise than other correlation-based methods. However, in noiseless cases, it does not provide a perfect estimation of $\mathbf{s}$ while other methods can produce a very low reconstruction error and high success rate.

Illustrative examples of sparse coefficient recovery of different algorithms with the

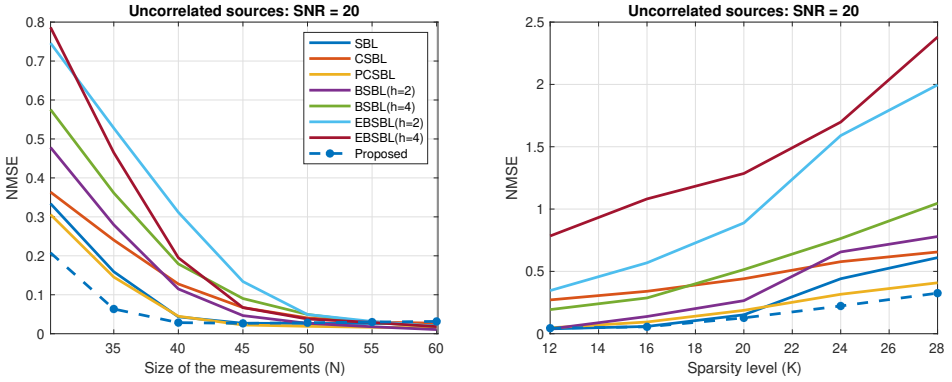

(a) (b)

Figure 6.9: NMSE performance comparison of the SBL algorithms with the data that has isolated zeros for (a) the sparsity level $K = 25$ and different the size of the measurements N; (b) the size of the measurements $N = 30$ and different sparsity level K.

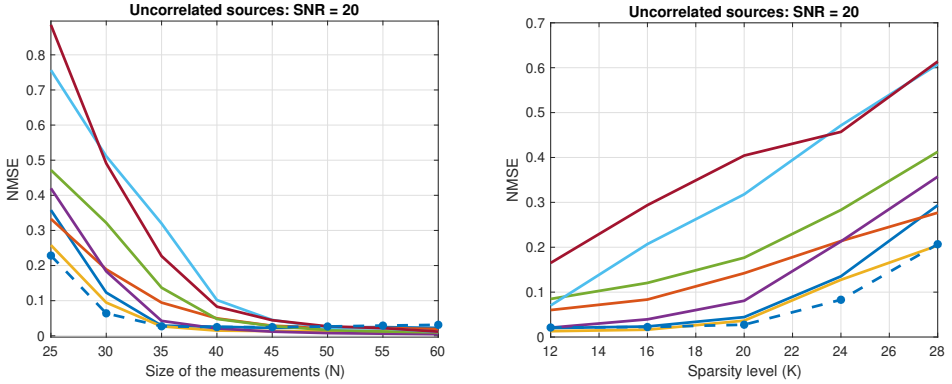

(a) (b)

Figure 6.10: NMSE performance comparison of the SBL algorithms with the data that has isolated zeros for (a) the sparsity level $K = 25$ and different the size of the measurements N; (b) the size of the measurements $N = 35$ and different sparsity level K.

size of the measurements N being 40 are given in Fig. 6.8, respectively. PCSBL and our proposed method provide the most accurate estimates of the original sparse coefficients with fewer measurements, especially for those significant elements inside blocks. By closely looking at CSBL and PCSBL, we observe smooth decay around the corners of the groups. This effect is stronger in CSBL due to the modeling difference between CSBL and PCSBL. On the other hand, although the proposed method is able to reconstruct sharp edges, the proposed one and other correlation-based methods suffer from reconstructing some off-group elements. This is possibly arising from the effect of the noise correlation. In CSBL and PCSBL, we observe smooth edges and the boundaries of the

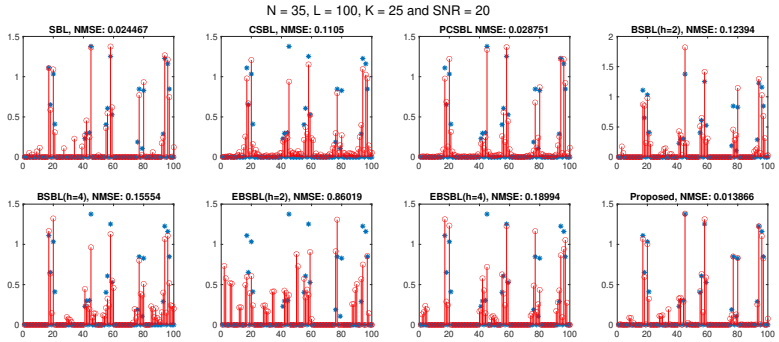

(a)

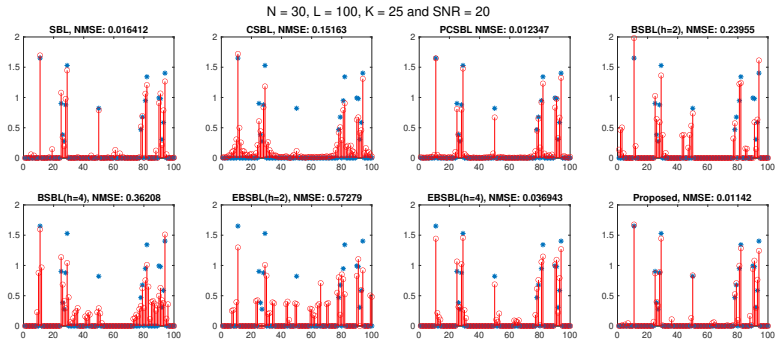

(b)

Figure 6.11: The magnitudes of the reconstructions of SBL algorithms with (a) noisy data (20 dB SNR) which has isolated zeros in each group (b) the data with mixed groups, isolated zeros, and isolated nonzeros.

groups are indistinct but we do not observe reconstructed elements that are not close to the groups.

In addition to testing with group sparse data, we test our algorithm for a new setting where each group has an isolated zero element inside the group. For such a scenario, the proposed method achieves the best performance in terms of NMSE with 20 dB SNR as shown in Figs. 6.9a and 6.9b for varying numbers of N and K respectively. The reconstructions are shown in Fig. 6.11a for a single realization. As CSBL and PCSBL algorithms consider contributions from the neighboring elements, the isolated zero element is affected by the surrounding nonzeros. On the other hand, the proposed algorithm considers the correlation with the neighbors in a multiplication form. When the sub-diagonal elements become zero they do not negatively affect the reconstruction of the isolated zero elements. Note that with such data, the classical SBL algorithm is also performing better than most of the other group sparsity-based algorithms. For BSBL and EBSBL, the performance varies significantly depending on different Monte Carlo realizations. Again

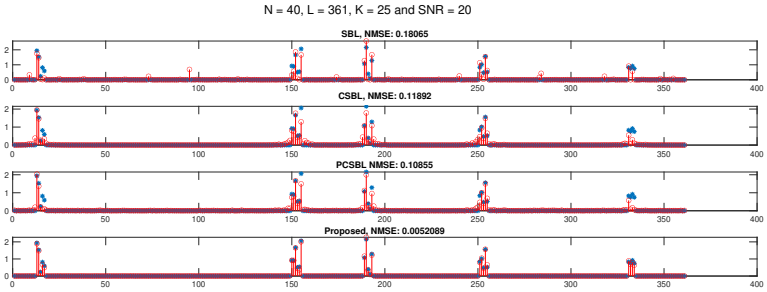

Figure 6.12: The magnitudes of the reconstructions of SBL algorithms with noisy group sparse data (20 dB SNR) for DOA and amplitude estimation.

it possibly arises from the block partition assumption of the algorithms.

We also tested these algorithms with a mixed scenario which consists of two isolated zero elements, two full group elements, and one group with an isolated nonzero element. As shown in Figs. 6.10a and 6.10b, we attain the best performance with the proposed method as it tackles the isolated nonzeros and isolated zeros more successfully compared to the existing literature. As the groups do not have a specific size, other correlation-based algorithms such as BSBL and EBSBL might fail to reconstruct the groups. We again demonstrate the reconstructions in Fig. 6.11b and observe a similar effect.

6.5.2. DOA AND AMPLITUDE ESTIMATION WITH SYNTHETIC DATA

Now, the proposed algorithm is tested on a DOA and amplitude estimation problem with block sparse sources. It should be noted that most analysis in the literature has been done with randomly designed sensing matrices [28, 33]. However, such a random design is not realistic to evaluate the performance of these algorithms. Hence, we tested and compared their performance for a simple DOA and amplitude estimation problem. Here, we consider an array with various numbers of elements. The DOAs are on an angular grid $[-90:0.5:90]^\circ$, and $L = 361$. The noise is modeled as i.i.d. complex Gaussian. Here, we examine a scenario with $K = 25$ random sources in five random groups. DOA groups collect s_l values having random complex amplitudes. The sources are chosen to be correlated and $c = 0.5$.

The performances of different algorithms in terms of the NMSE against the size of the measurements N and the sparsity level K are given in Fig. 6.13, 6.14, 6.15 and 6.16 for 20 dB SNR and 10 dB SNR, respectively. With such a realistic setting where the system model $\mathbf{A}$ is a realistic matrix, the best performance is attained by the proposed algorithm, especially for the 20 dB SNR case. The performance of the proposed algorithm is still comparable to or better than the state-of-the-art under the 10 dB SNR case. Note that the DOA matrix $\mathbf{A}$ has a higher coherence compared to a randomly generated $\mathbf{A}$ matrix. Illustrative examples of the sparse coefficient recovery of different algorithms with the size of the measurements N being 40 are given in Fig. 6.12. Here, the proposed method provides the most accurate estimates of the original sparse coefficients. By closely look-

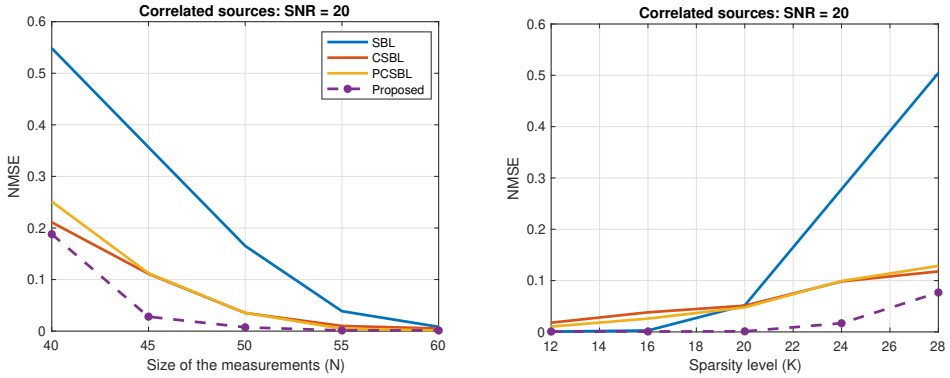

(a) (b)

Figure 6.13: NMSE performance comparison of the SBL algorithms with noisy data (20 dB SNR) for (a) the sparsity level $K = 25$ and different the size of the measurements N; (b) the size of the measurements $N = 45$ and different sparsity level K for a single snapshot problem with correlated data.

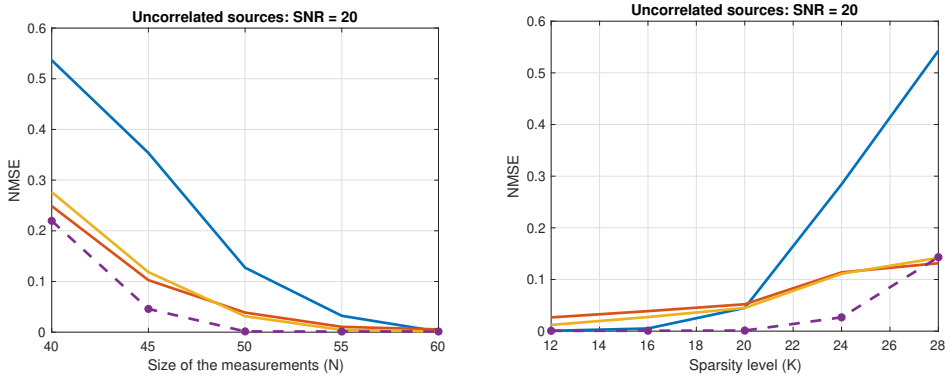

(a) (b)

Figure 6.14: NMSE performance comparison of the SBL algorithms with noisy data (20 dB SNR) ffor (a) the sparsity level $K = 25$ and different the size of the measurements N; (b) the size of the measurements $N = 45$ and different sparsity level K for a single snapshot problem with uncorrelated data.

ing at CSBL and PCSBL, we again observe a smooth decay around the corners of the groups. On the other hand, the proposed method is able to reconstruct sharp edges.

6.6. CONCLUSION

In this chapter, we have proposed a correlated sparse Bayesian learning algorithm for block sparse signals with arbitrary block sizes and locations under the Bayesian frame-

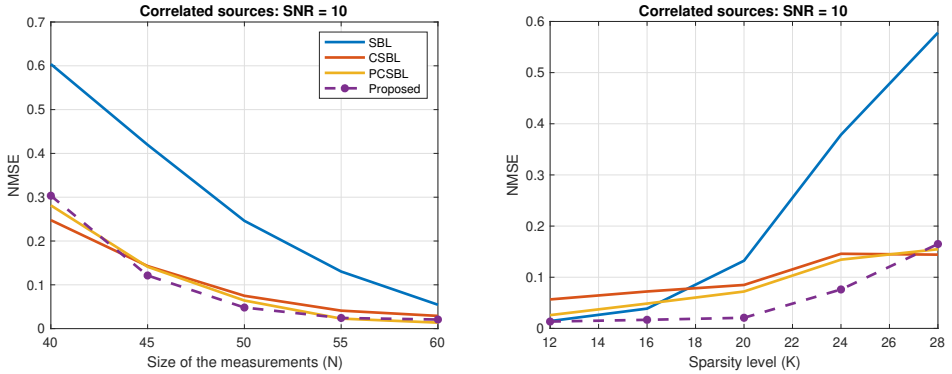

(a) (b)

Figure 6.15: NMSE performance comparison of the SBL algorithms with noisy data (10 dB SNR) for (a) the sparsity level $K = 25$ and different the size of the measurements N; (b) the size of the measurements $N = 45$ and different sparsity level K for a single snapshot problem with correlated.

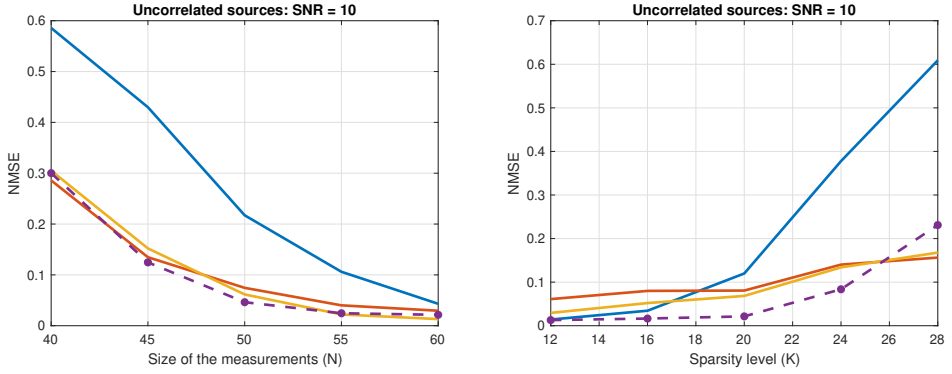

(a) (b)

Figure 6.16: NMSE performance comparison of the SBL algorithms with noisy data (10 dB SNR) for (a) the sparsity level $K = 25$ and different the size of the measurements N; (b) the size of the measurements $N = 45$ and different sparsity level K for a single snapshot problem with uncorrelated data.

work. This is a simpler alternative to EBSBL and we explain the underlying relationship between the proposed method and a particular case of EBSBL. The proposed algorithm uses the fact that immediate neighboring sparse coefficients are correlated. Unlike the diagonal correlation matrix in conventional SBL, the unknown correlation matrix has a tridiagonal structure to capture the correlation with neighbors. Due to the entanglement of the elements in the inverse tridiagonal matrix, instead of a direct closed-form solution, an approximate solution is proposed. The sparse reconstruction performance of the algorithm is evaluated with both correlated and uncorrelated block sparse coefficients. Results of comprehensive simulations demonstrate that the proposed algorithm

outperforms CSBL and PCSBL and other correlation-based methods such as EBSBL in terms of reconstruction quality. The numerical results also show that the proposed correlated SBL algorithm is capable of recovering signals with both block patterns and isolated coefficients.

6.7. DISCUSSION

The correlated sparse Bayesian learning algorithm can be modified for the two-dimensional scenario. However, now the matrix given in (6.22) does not have a simple tridiagonal structure. Instead, it is block tridiagonal with tridiagonal blocks to capture all the correlations between neighboring elements. Estimating the correlations cannot be simply extended but requires significant computations.

At first, the correlated sparse Bayesian algorithm is developed for vascular ultrasound imaging to be used with the mouse brain data tested in Chapter 4 and 5. However, due to the high computational complexity of the expectation-maximization algorithms with large-size data and the complicated derivations in the two-dimensional case, the proposed method has not been developed for and applied to the ultrasound imaging problem. In future work, estimating the non-zero elements in the block tridiagonal with tridiagonal blocks correlation matrix is required. Furthermore, the algorithm's speed can be boosted with an inversion-free method [120, 121]. Alternatively, the problem can be solved via the fixed-point iteration method, as in the previous chapter, which focused on pattern-coupling in sparse Bayesian learning. However, again, the block tridiagonal with tridiagonal blocks structure requires investigation of suitable parameter estimation rules.

Unfortunately, the previously proposed algorithms generally provided limited improvements and demanded high computational power, as illustrated in Chapters 4 and 5. Since we aim to balance image quality and computational requirements, the proposed algorithms were impractical. Hence, we did not endeavor to develop the two-dimensional version of the correlated sparse Bayesian learning algorithm. Ultimately, we decided to focus on the developments in ultrasound transmissions instead of image reconstruction algorithms. Such an approach seems more promising than making more algorithmic advances.

Although we did not apply the correlated sparse Bayesian learning algorithm to the vascular ultrasound imaging problem, we have gladly developed an efficient algorithm that outperformed the literature in one-dimensional problems such as DOA estimation. It is a novel contribution to the literature and a valuable part of the thesis as it provides mathematical insights into this application-focused thesis.

7

Optimizing Coded Excitation for Model-based Ultrasound Imaging with Unfocused Transmissions

Ultrafast imaging, which uses unfocussed transmissions to form images, provides very high frame rates at the cost of low signal-to-noise ratio (SNR). This loss of SNR becomes especially apparent when imaging deeper structures. Ultrafast imaging is mostly used in combination with Doppler processing. Even if we apply tissue-separation filters, they lead to significant energy loss and decrease the SNR. Previous work showed that this loss in SNR and, hence, penetration depth can be partially regained using coded transmissions. However, these codes are mostly either standard or randomly generated and can be improved with a design rooted in an optimization scheme. To address this limitation, we design an optimized code tailored to ultrasound imaging with unfocused transmissions represented by a generalized encoding matrix in a linear signal model. We employ the minimization of the Cramér-Rao lower bound (CRB) over the unknown coding matrix as a way to optimize the code. Due to the high computational cost of the resulting optimization problems, we also introduce a trace-constraint optimization problem based on the Fisher information matrix (FIM). Simulation results show that the optimized code provides higher SNR in deep image regions than previously tested coding schemes such as the Barker code, albeit with a trade-off for decreased resolution. On the other hand, the application of least-squares QR (LSQR) mitigates this resolution degradation. Lastly, the optimized code was tested in simulations using a numerical model of a clinical transducer setting, demonstrating its potential for higher SNR in ultrafast Doppler imaging.

This chapter is accepted for a publication in IEEE Transactions on Computational Imaging as "Optimizing Coded Excitation for Model-based Imaging with Unfocused Transmissions".

7.1. INTRODUCTION

Doppler ultrasound imaging is a well-established technique widely used for imaging blood flow inside the human body, leveraging the principles of ultrasound and the interaction of mechanical pressure waves with tissue and red blood cells[122, 123]. Unfocused transmissions are advantageous for Doppler ultrasound compared to conventional ultrasound imaging [124]. The latter employs focused ultrasonic waves and sends a single focused wave during each transmission, reconstructing one image line at a time. However, this might not achieve a high sampling frequency and could result in inaccuracies for Doppler imaging [125]. In contrast, in unfocused transmissions such as plane-wave imaging, receivers capture the backscattered echoes from the entire imaging area. This enables the reconstruction of a full image from a single transmission using beamforming. It can obtain much more images compared to conventional ultrasound for the same number of firings and acquisition time.

Unfocussed transmissions trade image quality (specifically SNR) for temporal resolution, which is beneficial for Doppler imaging [126]. This gain allows for novel imaging applications such as functional ultrasound [125], pulse wave velocity imaging [127], etc. Although they also notably trade-off (reduce) spatial resolution, we are particularly interested in imaging blood flow inside the brain, where the SNR is of paramount importance. A higher SNR contributes to a high-quality image, enhancing diagnostic capabilities in clinical applications [128]. Unfocused transmissions face challenges in visualizing vasculature due to a low SNR. Echo signals from blood cells are considerably weaker than surrounding tissue. This leads to limitations in visualizing small blood vessels and deep areas.

There are advanced filtering methods for visualization of the microvasculature especially at greater depths. While some of these filters can be classified as beamforming methods, many others can be categorized as post-processing methods for detailed visualization. Examples of beamforming approaches include MVDR [129], LSQR (Least Squares QR, an iterative algorithm used for solving large linear systems of equations) [130], sparse reconstruction methods [21], and deep learning-based methods [131]. In terms of post-processing, methods like SVD filtering [50] and super-resolution techniques such as TMSBL [132] and SUSHI [133] improve the quality of the beamformed image and enable better visualization at deeper levels. However, these methods often face challenges related to computational complexity, particularly when applied to real-time imaging.

It is also observed in ultrasound literature that applying coded excitation [14, 15, 16, 134, 135], which means sending out longer encoded pulses, can enhance the SNR of ultrasound images and improve the penetration depth. Coded excitation achieves a high main lobe-to-side lobe ratio after pulse compression, with an axial resolution comparable to or slightly worse than a single short pulse. Note that pulse compression is a signal processing technique where a long-duration coded pulse is transmitted and its echo is processed via decoding filtering to compress energy into a narrow peak [136, 137]. The design of coded excitation pulses typically utilizes frequency or phase encoding techniques based on the impulse response of the transducer [68]. Frequency encoding involves linearly modulating a carrier signal frequency, often achieved through linear fre-

quency modulation (FM), also known as chirp excitation [15]. On the other hand, phase encoding is achieved by modulating the phase of the transmitted pulse, such as linear phase modulation and bi-phase modulation [14]. In linear phase modulation, the phase changes linearly with time across the pulse duration. This creates a smooth phase transition and can contribute to the signal's resilience against distortion and interference. In bi-phase modulation, the transmitted pulse is encoded with either a 0-degree shift (represented by 1) or a 180-degree shift (represented by -1).

The two commonly used bi-phase modulation sequences are the Golay and Barker codes, which have found extensive applications in ultrasound imaging thanks to their favorable autocorrelation properties and ability to generate high-quality images with improved signal-to-noise ratio [35, 36]. A Barker code is a binary sequence that leads to a high main lobe-to-side lobe ratio after matched filtering, with good autocorrelation properties. However, existing Barker codes only have specific lengths, restricting the total transmitted energy. The Golay code consists of a pair of finite equal-length binary sequences. Unlike single transmit signals like Barker codes, which exhibit range side lobes after pulse compression, the Golay pair is designed to cancel out these range side lobes. However, the drawback of Golay pairs is that the frame rate will be halved since it requires two transmissions to obtain a single image. Note that these two transmissions are added to cancel out the side lobes. A major weakness of Golay code pairs is incomplete cancellation caused by target motion between transmissions, even when complementary orthogonal codes are used. This problem has been tackled in [69] by transmitting two pairs of mutually complementary orthogonal codes, which can achieve the same frame rate as a single transmission code.

Instead of applying the same code for every transmitting element, the random code is an alternative to Barker and Golay encoding, incorporating the time and space domains [18]. Instead of transducer elements transmitting the same encoded pulse, this method excites each element with a different randomly encoded pulse. The resulting randomly transmitted waves constructively and destructively interfere in the imaging area, creating spatio-temporal interference patterns. This leads to low pixel-to-pixel correlations, which might yield a high-resolution image. However, the SNR improvement is quite limited compared to Barker and Golay codes. Furthermore, there are also complete complementary codes that offer better side lobe suppression and higher SNR improvement compared to random codes [138]. Hence, they are more effective for high-quality imaging while maintaining low pixel-to-pixel correlations.

Coded excitation in ultrasound imaging can be refined using diverse methods. One promising way involves investigating hybrid coding techniques, combining different coding sequences to combine their strengths. For instance, [65] suggests the convolution of Barker and Golay codes to effectively mitigate side lobe levels, leading to a notable increase in SNR. Similarly, [66] introduces chirp-modulated Golay codes, integrating orthogonal binary codes with a chirp, which results in a substantial enhancement. Another approach is integrating advanced signal processing algorithms to decode and reconstruct received echoes efficiently. Decoding filtering techniques, such as mismatched or adaptive filters [139, 140], play a critical role in balancing side lobe suppression and SNR gain during pulse compression. For instance, the work [67] uses a finite impulse response (FIR) filter, to decode echoes transmitted with Barker codes, effectively sup-

pressing the side lobe energy at the expense of decreased SNR. This approach further facilitates the design of longer Barker codes using Kronecker products, enabling applications such as functional ultrasound neuroimaging, but it may degrade the autocorrelation properties.

There is a potential for utilizing optimized code design to enhance SNR in ultrasound imaging with unfocused transmissions. While substantial research has been dedicated to optimized code design in the radar domain, emphasizing robustness and high-resolution [141] [142] and demonstrating significant improvements in radar detectability, a notable gap exists for unfocused transmissions in ultrasound imaging. Therefore, this chapter explores optimized code sequences for ultrasound imaging with unfocused transmissions. We first present a linear signal model where the code sequences appear in a coding matrix. To optimize this coding matrix, we employ the minimization of the Cramér-Rao lower bound (CRB) [40] as a proxy to minimize the mean square error[42]. In that sense, the minimization of the maximum eigenvalue, determinant, and trace of the CRB matrix has been proposed to find the optimized encoding matrix for a specific imaging area [143]. Since the original problem is non-convex, some relaxations are imposed to ensure a feasible solution [144]. The drawback of this approach is its computational complexity and memory challenge for large imaging areas. A suboptimal formulation is proposed to address this by maximizing the trace of the Fisher information matrix (FIM) instead of minimizing the trace of the CRB. Fortunately, the maximization of the trace of the FIM results in a small-scale problem that can be solved by finding the eigenvector of a small-sized matrix corresponding to the largest eigenvalue. Therefore, the proposed approach is computationally more efficient.

The rest of this chapter is organized as follows: Section 7.2 presents the signal model and the associated image reconstruction. The subsequent section, Section 7.3, focuses on articulating the optimization methods applicable to the encoding matrix. Further, Section 7.4 shows the results, delving into the application scenario for the proposed method and discussing its limitations. Conclusions are drawn in Section 7.6.

7.2. SIGNAL MODEL

In this work, model-based beamforming is employed instead of the conventional delay-and-sum (DAS) approach. In our approach, each transmitter sends different pulses, while DAS is useful in the case where all transmitters share the same coding pattern. Model-based beamforming provides more flexibility in handling the diverse coded excitation scheme. In model-based ultrasound imaging, we first construct the image formation model and represent this in the form of a matrix-vector multiplication [21]. In the ultrasound imaging system, there are I elements where all the elements transmit and receive the backscattered signal. The imaging area is discretized into a grid of L pixels. Using the Born approximation [145], each measurement is represented as a linear combination of the pulse-echo signals from the scatterers [49] weighted by their scattering coefficient. Throughout this chapter, we will work in the frequency domain instead of the time domain since it allows for faster computation. More specifically, we only consider a limited set of F frequencies given by $\Omega = \{\omega_1, \omega_2, \cdots, \omega_F\}$, which are assumed equidistant and within the positive side of the frequency spectrum. Defining $z_j[\omega]$ as

the signal received by the jth element at frequency ω, we can write

$$z_j[\omega] = \sum_{l=1}^{L} s_l \sum_{i=1}^{I} g_{j,l,i}[\omega] u_i[\omega]. \tag{7.1}$$

Here, s_l represents each pixel's unknown reflection coefficient, and $u_i[\omega]$ represents the excitation pulse sent by element i at frequency ω. Furthermore, $g_{j,l,i}[\omega]$ is the overall Green's function for the wave propagating from the transmitting element i to pixel m and from the pixel l to the receiving element j. The computation of Green's function considers factors such as the distance between the transmitting/receiving elements and each pixel, attenuation during propagation in the tissue, and the impulse responses of the transducers. The overall function $g_{j,l,i}[\omega]$ is given by

$$g_{j,l,i}[\omega] = \frac{h_t[\omega] h_r[\omega]}{4\pi(d_{i,l} + d_{l,j})} \exp\Big(-j\frac{\omega}{v_0}(d_{i,l} + d_{l,j})\Big), \tag{7.2}$$

where $h_t[\omega]$ and $h_r[\omega]$ respectively correspond to the known transmit and receive impulse responses of the transducer, $d_{i,l}$ denotes the distance from the transmitting element i to pixel l, and $d_{l,j}$ is the distance covered by the backscattered signal from pixel l to sensor j. Further, v_0 corresponds to the speed of sound in the medium. The denominator in equation (7.2) stands for the geometric spreading of the pressure field, considering the entire distance the wave travels from the source to the pixel and back to the sensor. The exponential term in (7.2) represents the phase shift caused by the delay from the source to the pixel and back to the sensor.

Note that the excitation pulse $u_i[\omega]$ in equation (7.1) depends on the transmitting elements. For this scenario, we consider a case where all I elements transmit longer pulses consisting of an equal number K of base pulses. Every base pulse is amplitude and bi-phase encoded with a weight denoted by $c_{i,k}$. Hence, the excitation pulse $u_i[\omega]$ at transmitting element i and frequency ω can be written as

$$u_i[\omega] = \sum_{k=1}^{K} c_{i,k} p_k[\omega] = \mathbf{c}_i^{\mathsf{T}} \mathbf{p}[\omega], \tag{7.3}$$

where $p_k[\omega]$ denotes the kth base pulse. The relation between two consecutive base pulses is $p_{k+1}[\omega] = p_k[\omega] e^{-j\omega\tau}$ where τ is the delay between two base pulses. Further, $\mathbf{p}[\omega] = [p_1[\omega], p_2[\omega], \ldots, p_K[\omega]]^{\mathsf{T}}$ is the base pulse vector and $\mathbf{c}_i = [c_{i,1}, c_{i,2}, \ldots, c_{i,K}]^{\mathsf{T}}$ is the amplitude and bi-phase code related to transmit element i. Here, we also concatenate the $\mathbf{c}_i$'s as $\mathbf{C} \in \mathbb{R}^{I \times K}$, which is called the encoding matrix, i.e., $\mathbf{C} = [\mathbf{c}_1, \mathbf{c}_2, \ldots, \mathbf{c}_I]^{\mathsf{T}}$.

The measurements from all elements are stacked in a vector $\mathbf{z}[\omega] \in \mathbb{C}^I$, and the part related to the Green's functions can be stored in a matrix $\mathbf{A}_\mathbf{c}[\omega]$. The measurement model for all elements at frequency ω is then expressed as

$$\mathbf{z}[\omega] = \begin{bmatrix} z_1[\omega] \\ \vdots \\ z_I[\omega] \end{bmatrix} = \mathbf{A}_\mathbf{c}[\omega]\mathbf{s}, \tag{7.4}$$

where the mth entry of the vector $\mathbf{s} \in \mathbb{R}^L$ is $[\mathbf{s}]_l = s_l$ and the (j,l)th entry of the matrix $\mathbf{A_c}[\omega] \in \mathbb{C}^{I\times L}$ is written as

$$[\mathbf{A_c}[\omega]]_{j,l} = \sum_{i=1}^{I} g_{j,l,i}[\omega]\mathbf{c}_i^{\mathsf{T}}\mathbf{p}[\omega] = \mathbf{g}_{j,l}^{\mathsf{T}}[\omega]\mathbf{C}\mathbf{p}[\omega], \tag{7.5}$$

where $\mathbf{g}_{j,l}[\omega] = [g_{j,l,1}[\omega],\ldots,g_{j,l,I}[\omega]]^{\mathsf{T}}$. Now we can also write $\mathbf{A_c}[\omega]$ in (7.4) as follows

$$\begin{aligned}\mathbf{A_c}[\omega] &= \begin{bmatrix} \mathbf{g}_{1,1}^{\mathsf{T}}[\omega] & \ldots & \mathbf{g}_{1,L}^{\mathsf{T}}[\omega] \\ \vdots & \ddots & \vdots \\ \mathbf{g}_{I,1}^{\mathsf{T}}[\omega] & \ldots & \mathbf{g}_{I,L}^{\mathsf{T}}[\omega] \end{bmatrix} [\mathbf{I}_L \otimes (\mathbf{C}\mathbf{p}[\omega])] \\ &= \mathbf{G}[\omega][\mathbf{I}_L \otimes (\mathbf{C}\mathbf{p}[\omega])]. \end{aligned} \tag{7.6}$$

where $\mathbf{I}_L$ is an $L \times L$ identity matrix. It is clear from (7.6) that $\mathbf{A_c}[\omega]$ is linear in every element of the encoding matrix $\mathbf{C}$. As a result, (7.6) can be written as

$$\mathbf{A_c}[\omega] = \sum_{i=1}^{I}\sum_{k=1}^{K} c_{i,k}\mathbf{A}_{i,k}[\omega], \tag{7.7}$$

where $\mathbf{A}_{i,k}[\omega] \in \mathbb{C}^{N\times M}$ is given by

$$\mathbf{A}_{i,k}[\omega] = \mathbf{G}[\omega][\mathbf{I}_L \otimes (\mathbf{E}_{i,k}\mathbf{p}[\omega])], \tag{7.8}$$

with $\mathbf{E}_{i,k} \in \mathbb{R}^{I\times K}$ a matrix with only one non-zero entry, i.e., $[\mathbf{E}_{i,k}]_{i,k} = 1$. The matrix $\mathbf{E}_{i,k}$ basically selects which code entry is active.

Finally, all the frequency components are computed and concatenated vertically. Adding zero-mean white Gaussian noise with variance σ^2 to the model, this leads to

$$\mathbf{z} = \begin{bmatrix} \mathbf{z}[\omega_1] \\ \vdots \\ \mathbf{z}[\omega_F] \end{bmatrix} = \begin{bmatrix} \mathbf{A_c}[\omega_1] \\ \vdots \\ \mathbf{A_c}[\omega_F] \end{bmatrix} \mathbf{s} + \mathbf{n} = \mathbf{A_c}\mathbf{s} + \mathbf{n}. \tag{7.9}$$

Here, $\mathbf{z} \in \mathbb{R}^{FI}$ contains all measured samples from the array transducer in the frequency domain and $\mathbf{A_c} \in \mathbb{R}^{FI\times M}$ collects as columns the impulse responses related to the different pixels. Here, $\mathbf{n} \in \mathbb{R}^{FI}$ represents the additive white Gaussian noise. Due to (7.7) we can write

$$\mathbf{A_c} = \sum_{i=1}^{I}\sum_{k=1}^{K} c_{i,k}\mathbf{A}_{i,k}, \tag{7.10}$$

where

$$\mathbf{A}_{i,k} = \begin{bmatrix} \mathbf{A}_{i,k}[\omega_1] \\ \vdots \\ \mathbf{A}_{i,k}[\omega_F] \end{bmatrix}.$$

For simplicity, we will group the two indices i and k into a single index p as $p = (k-1)I+i$, where $p = 1,2,\ldots,IK$. In this context, we will also define $c_{(k-1)I+i} = c_{i,k}$ and $\mathbf{A}_{(k-1)I+i} =$

$\mathbf{A}_{i,k}$, which allows us to rewrite (7.10) as

$$\mathbf{A_c} = \sum_{p=1}^{IK} c_p \mathbf{A}_p, \tag{7.11}$$

Finally note that we can view c_p as the pth entry of the vector $\mathbf{c} = \text{vec}(\mathbf{C})$, where vec(.) vectorizes a matrix columnwise.

In the remainder of this chapter, coded excitation techniques are generalized using the encoding matrix $\mathbf{C}$. The rows of $\mathbf{C}$ are identical for Barker and Golay codes, as the same signal is transmitted from all transducers while the elements are randomly generated for the random code case. For all those schemes, the entries of $\mathbf{C}$ are 1 or -1. In addition to bi-phase encoding, we also consider amplitude encoding in the proposed optimized coding scheme, as it has proven its advantages in radar applications [146]. The modulus of each entry in $\mathbf{C}$ is the weight for amplitude encoding, while its polarity stands for the phase encoding of the transmitted ultrasound pulses.

7.2.1. IMAGING TECHNIQUES

Before optimizing the code, let us present imaging methods that solve (7.9). The simplest one is matched filtering, which maximizes the SNR under additive Gaussian noise and has the following solution:

$$\hat{\mathbf{s}} = \mathbf{A}_\mathbf{c}^\mathsf{H} \mathbf{z}. \tag{7.12}$$

Secondly, least squares estimation can be considered, which minimizes the sum of squared differences between the measurement vector $\mathbf{z}$ and the modeled measurement vector based on the estimated vector $\mathbf{s}$. It has the following closed-form solution:

$$\hat{\mathbf{s}} = (\mathbf{A}_\mathbf{c}^\mathsf{H} \mathbf{A}_\mathbf{c})^{-1} \mathbf{A}_\mathbf{c}^\mathsf{H} \mathbf{z}, \tag{7.13}$$

which only holds when $\mathbf{A_c}$ is full rank.

Note that matched filtering (7.12) will be the main technique employed in this work, thanks to its efficiency and ease of implementation. On the other hand, the least squares estimation in (7.13) has a large inverse, and its computational complexity is significantly high. Instead of solving the large inverse, an iterative LSQR algorithm will be used [130].

7.3. OPTIMIZATION OF THE ENCODING MATRIX

Based on the earlier developed linear measurement model, we are now ready to find the optimal coded excitation scheme. Therefore, we first focus on estimating the image $\mathbf{s}$, and we then optimize the related estimation error for $\mathbf{s}$ with respect to $\mathbf{c}$ (the vectorized version of the coded excitation matrix $\mathbf{C}$). Suppose $\mathbf{s}$ is deterministic and unknown. In that case, we can estimate $\mathbf{s}$ using an unbiased estimator leading to an error covariance matrix $\mathbf{R_e} = \mathbb{E}(\mathbf{e}\mathbf{e}^\mathsf{H})$ [42], with $\mathbf{e} = \mathbf{s} - \hat{\mathbf{s}}$. This could be any of the previously considered estimators, including (if needed) a proper normalization for making the estimator unbiased. The trace of the error covariance matrix $\mathbf{R_e}$ yields the mean square error (MSE) of the estimator [42]. For any unbiased estimator, the error covariance matrix $\mathbf{R_e}$ is bounded below by the Cramér–Rao lower bound (CRB) matrix. So, instead of finding an expression for

$\mathbf{R_e}$ related to a specific unbiased estimator, we will make use of the CRB matrix, which is often easier to derive. We thereby also remark that the CRB matrix is the inverse of the Fisher information matrix (FIM) $\mathbf{F}$, which quantifies how much information a dataset provides about the parameter of interest. So in general, we have $\mathbf{R_e} \succeq \mathbf{F}^{-1}$, where $\mathbf{F}$ could potentially depend on the unknown image $\mathbf{s}$. For our specific data model, which is a linear additive Gaussian model, the FIM is independent of $\mathbf{s}$ and is given by

$$\mathbf{F} = \sigma^{-2}\mathbf{A}_\mathbf{c}^\mathsf{H}\mathbf{A}_\mathbf{c}. \tag{7.14}$$

As can be seen, it does not depend on $\mathbf{s}$ but it does depend on the code $\mathbf{c}$. We make this explicit by writing $\mathbf{F}(\mathbf{c})$ instead of $\mathbf{F}$.

7.3.1. CRB Minimization

There are three ways of minimizing the CRB matrix: minimization of the largest eigenvalue of the CRB matrix (Eig-Opt), minimization of the determinant of the CRB matrix (Det-Opt), or minimization of the trace of the CRB matrix (Trace-Opt) [143].

Eig-Opt: We first formulate the problem for Eig-Opt, which minimizes the largest eigenvalue of the CRB matrix. Note that using the maximum eigenvalue ensures that the CRB is minimized on all elements simultaneously. On the other hand, they might compensate for each other within the trace or determinant. In that sense, Eig-Opt can be more efficient for minimizing the CRB [143]. The Eig-Opt problem can be written as follows:

$$\begin{aligned} \min_{\mathbf{c}} \quad & \lambda_{\max}(\mathbf{F}^{-1}(\mathbf{c})) \\ \text{s.t.} \quad & ||\mathbf{c}||_2^2 = 1, \end{aligned} \tag{7.15}$$

where $\lambda_{\max}(\mathbf{F}^{-1}(\mathbf{c}))$ is the maximum eigenvalue of $\mathbf{F}^{-1}(\mathbf{c})$. Note that minimizing the maximum eigenvalue of the CRB matrix is equivalent to maximizing the minimum eigenvalue of its inverse. As such, we can also write

$$\begin{aligned} \max_{\mathbf{c}} \quad & \lambda_{\min}(\mathbf{A}_\mathbf{c}^\mathsf{H}\mathbf{A}_\mathbf{c}) \\ \text{s.t.} \quad & ||\mathbf{c}||_2^2 = 1, \end{aligned} \tag{7.16}$$

where $\lambda_{\min}(\mathbf{F}^{-1}(\mathbf{c}))$ is the minimum eigenvalue of $\mathbf{F}^{-1}(\mathbf{c})$. Here, (7.16) is equivalent to

$$\begin{aligned} \max_{\lambda,\mathbf{c}} \quad & \lambda \\ \text{s.t.} \quad & \mathbf{A}_\mathbf{c}^\mathsf{H}\mathbf{A}_\mathbf{c} - \lambda\mathbf{I}_L \succeq \mathbf{0}, \\ & ||\mathbf{c}||_2^2 = 1, \end{aligned} \tag{7.17}$$

where the first constraint is not linear in $\mathbf{c}$, and the problem in (7.17) is thus not convex. More specifically, we can write

$$\begin{aligned} \mathbf{A}_\mathbf{c}^\mathsf{H}\mathbf{A}_\mathbf{c} &= \left(\sum_{p=1}^{IK} c_p\mathbf{A}_p\right)^\mathsf{H}\left(\sum_{q=1}^{IK} c_q\mathbf{A}_q\right) \\ &= \sum_{p=1}^{IK}\sum_{q=1}^{IK} c_p^* c_q \mathbf{A}_p^\mathsf{H}\mathbf{A}_q, \end{aligned} \tag{7.18}$$

where c_p^* represents the complex conjugate of c_p. Solving nonconvex problems can be challenging due to the potential of traditional optimization algorithms getting trapped in local optima or encountering convergence issues. As a result, some relaxation is introduced to turn the nonconvex problem into a convex one. Here, a common relaxation technique is employed, which involves absorbing the quadratic term $c_p^* c_q$ into a single variable $C_{p,q}$ [42]. As such, (7.18) can be transformed into

$$\mathbf{A}_\mathbf{c}^\mathsf{H}\mathbf{A}_\mathbf{c} = \sum_{p=1}^{IK}\sum_{q=1}^{IK} C_{p,q}\mathbf{A}_p^\mathsf{H}\mathbf{A}_q, \tag{7.19}$$

which is linear in $C_{p,q}$ instead of quadratic in c_p. Introducing the matrix $\mathscr{C} \in \mathbb{C}^{IK\times IK}$ with $[\mathscr{C}]_{p,q} = C_{p,q}$, the equivalence between (7.18) and (7.19) only holds when $\mathscr{C} = \mathbf{c}\mathbf{c}^\mathsf{H}$. This requires $\mathscr{C}$ to be a rank-one matrix, and this constraint is not convex. One way to relax this rank-one constraint is by replacing it with $\mathscr{C} \succeq \mathbf{0}$. Defining $\mathbf{A} = [\mathbf{A}_1^\mathsf{T}, \ldots, \mathbf{A}_{IK}^\mathsf{T}]^\mathsf{T}$, this allows us to relax (7.17) as the following semidefinite program (SDP) [144]:

$$\begin{aligned} \max_{\mathscr{C},\lambda} \quad & \lambda \\ \text{s.t.} \quad & \mathbf{A}^\mathsf{H}(\mathscr{C}\otimes\mathbf{I}_{FI})\mathbf{A} - \lambda\mathbf{I}_L \succeq \mathbf{0} \\ & \mathscr{C} \succeq \mathbf{0} \\ & \mathbf{1}^\mathsf{T}\mathrm{diag}(\mathscr{C}) = 1. \end{aligned} \tag{7.20}$$

Note that $||\mathbf{c}||_2^2 = 1$ is equivalent to $\mathbf{1}^\mathsf{T}\mathrm{diag}(\mathscr{C}) = 1$. The matrix inequality constraint is now linear in $\mathscr{C}$, and thus, the whole problem is convex.

Based on this formulation, we can also modify the problem to a subsampled scenario by defining $\mathbf{z} = \mathbf{A}_\mathbf{c}\mathbf{R}\mathbf{s}_r + \mathbf{n}$ where $\mathbf{R} \in \mathbb{R}^{L\times S}$ is a subsampling matrix, S is the number of subsamples and $\mathbf{s}_r$ contains only the pixels from the subsampled area. Note that this scenario ignores the contribution of most of the pixels in the area, and it does not give the optimal solution for the overall area. However, it is applied because of the substantial computational complexity of solving the SDP (7.20). The subsampled problem formulation is given by:

$$\begin{aligned} \max_{\mathscr{C},\lambda} \quad & \lambda \\ \text{s.t.} \quad & \mathbf{R}^\mathsf{T}\mathbf{A}^\mathsf{H}(\mathscr{C}\otimes\mathbf{I}_{FI})\mathbf{A}\mathbf{R} - \lambda\mathbf{I}_S \succeq \mathbf{0} \\ & \mathscr{C} \succeq \mathbf{0} \\ & \mathbf{1}^\mathsf{T}\mathrm{diag}(\mathscr{C}) = 1. \end{aligned} \tag{7.21}$$

Note that the size of the first constraint significantly decreases due to subsampling the data.

Det-Opt: Second, we can consider minimizing the determinant of the CRB matrix, which is referred to as the Det-Opt criterion. The problem can then be formulated as

$$\begin{aligned} \min_{\mathbf{c}} \quad & \det(\mathbf{F}^{-1}(\mathbf{c})) \\ \text{s.t.} \quad & ||\mathbf{c}||_2^2 = 1. \end{aligned} \tag{7.22}$$

Since the CRB matrix is the inverse of the Fisher information matrix, (7.22) is equivalent to

$$\begin{aligned} \max_{\mathbf{c}} \quad & \det(\mathbf{A}_{\mathbf{c}}^{\mathsf{H}}\mathbf{A}_{\mathbf{c}}) \\ \text{s.t.} \quad & ||\mathbf{c}||_2^2 = 1. \end{aligned} \tag{7.23}$$

Applying the same relaxation techniques and replacing $\det(\mathbf{F}(\mathbf{c}))$ with $\log(\det(\mathbf{F}(\mathbf{c})))$ we obtain the problem

$$\begin{aligned} \max_{\mathscr{C}} \quad & \log(\det(\mathbf{A}^{\mathsf{H}}(\mathscr{C} \otimes \mathbf{I}_{FI})\mathbf{A})) \\ \text{s.t.} \quad & \mathscr{C} \succeq \mathbf{0} \\ & \mathbf{1}^{\mathsf{T}}\operatorname{diag}(\mathscr{C}) = 1. \end{aligned} \tag{7.24}$$

Since $\log(\det(\mathbf{F}(\mathbf{c})))$ is known to be concave for a positive semidefinite matrix $\mathbf{F}(\mathbf{c})$, the above optimization problem is convex [147].

Trace-Opt: Third, we consider minimizing the trace of the CRB matrix, called Trace-Opt, which is given by

$$\begin{aligned} \min_{\mathbf{c}} \quad & \operatorname{trace}(\mathbf{F}^{-1}(\mathbf{c})) \\ \text{s.t.} \quad & ||\mathbf{c}||_2^2 = 1. \end{aligned} \tag{7.25}$$

By again applying the same convex relaxation techniques, we attain the following minimization problem:

$$\begin{aligned} \min_{\mathscr{C}} \quad & \operatorname{trace}((\mathbf{A}^{\mathsf{H}}(\mathscr{C} \otimes \mathbf{I}_{FI})\mathbf{A})^{-1}) \\ \text{s.t.} \quad & \mathscr{C} \succeq \mathbf{0} \\ & \mathbf{1}^{\mathsf{T}}\operatorname{diag}(\mathscr{C}) = 1. \end{aligned} \tag{7.26}$$

To eliminate the large inverse term from the objective function, we first reformulate the problem as follows:

$$\begin{aligned} \min_{\mathscr{C},\mathbf{T}} \quad & \operatorname{trace}(\mathbf{T}) \\ \text{s.t.} \quad & \mathbf{T} - (\mathbf{A}^{\mathsf{H}}(\mathscr{C} \otimes \mathbf{I}_{FI})\mathbf{A})^{-1} \succeq \mathbf{0} \\ & \mathscr{C} \succeq \mathbf{0} \\ & \mathbf{1}^{\mathsf{T}}\operatorname{diag}(\mathscr{C}) = 1. \end{aligned} \tag{7.27}$$

where $\mathbf{T}$ is introduced as the upper bound of the term inside the trace(.). Now, we minimize $\operatorname{trace}(\mathbf{T})$ instead of $\mathbf{A}^{\mathsf{H}}(\mathscr{C} \otimes \mathbf{I}_{FI})\mathbf{A})^{-1}$ [144]. Using the Schur complement method [148], we finally obtain

$$\begin{aligned} \min_{\mathscr{C},\mathbf{T}} \quad & \operatorname{trace}(\mathbf{T}) \\ \text{s.t.} \quad & \begin{bmatrix} \mathbf{T} & \mathbf{I}_L \\ \mathbf{I}_L & \mathbf{A}^{\mathsf{H}}(\mathscr{C} \otimes \mathbf{I}_{FI})\mathbf{A} \end{bmatrix} \succeq \mathbf{0} \\ & \mathscr{C} \succeq \mathbf{0} \\ & \mathbf{1}^{\mathsf{T}}\operatorname{diag}(\mathscr{C}) = 1. \end{aligned} \tag{7.28}$$

Similar to (7.21), we can apply subsampling to Det-Opt criterion in (7.24) and Trace-Opt criterion in (7.28).

Now, solving (7.20),(7.24) or (7.28) for $\mathscr{C}$ yields the optimized encoding matrix. As the resulting solution $\hat{\mathscr{C}}$ from (7.20),(7.24) or (7.28) is not guaranteed to have rank one, an approximate rank-one solution can be found by choosing the largest eigenvector of $\hat{\mathscr{C}}$. However, the effectiveness of this method depends on the low rankness of $\hat{\mathscr{C}}$. Another widely employed approach is the randomization method, where we treat $\hat{\mathscr{C}}$ as a covariance matrix to generate multiple candidate random vectors from $\hat{\mathbf{c}} \sim \mathcal{N}(0, \hat{\mathscr{C}})$. Subsequently, these solutions are projected onto the original constraint set. In our case, every randomization is normalized here to satisfy the energy constraint. Each candidate is then applied to the original problem (7.15),(7.22) or (7.25), and the realization that optimizes the related cost is selected as the solution[149]. This approach is regularly used in literature thanks to its proven success in many studies and its theoretical performance guarantees for several discrete optimization problems [150, 149]. While we cannot establish a lower bound on the optimality of this method, empirical observations demonstrate that this approach consistently outperforms solutions derived from the leading eigenvector. Note that if $\hat{\mathscr{C}}$ is found to have rank one, the random vectors generated using $\hat{\mathscr{C}}$ as covariance matrix will be identical to the leading eigenvector of $\hat{\mathscr{C}}$, up to a scalar value.

The previous optimization schemes in (7.15),(7.22), or (7.25) represent the optimal MSE solution. However, due to the substantial pixel count in the imaging area, the computational demands of the cost function become significant. This involves calculating and storing a significant number of $\mathbf{A}_p^{\mathsf{H}}\mathbf{A}_q \in \mathbb{C}^{L\times L}$ matrices, making it computationally challenging and memory-intensive to implement and solve in cvx, which is a MATLAB toolbox for solving convex optimization problems [151]. One way is to optimize the codes for the subsampled imaging area with fewer pixels, such as proposed in (7.21). However, this solution will be suboptimal as the new CRB for the subsampled data will not be optimal for the overall system. Another way to address this limitation is to explore a suboptimal optimization function that is less complex and more efficient.

7.3.2. FIM MAXIMIZATION

Rather than minimizing the trace of the CRB matrix in (7.25), an alternative approach involves maximizing the trace of the FIM. An optimized encoding matrix can be obtained by maximizing the Fisher information within a region of interest (ROI). Thanks to the linearity of the trace operator, this proposed approach becomes computationally more efficient than the optimization schemes outlined in (7.20),(7.24) or (7.28). However, it may not achieve the optimal MSE, potentially resulting in a degradation of image quality. This degradation results from the fact that trace-based FIM maximization and trace-based CRB minimization are not mathematically equivalent optimization problems since the trace(.) operator is not linear.

Although this is not equivalent to the minimization problem in (7.25), we can maximize the trace of the FIM as expressed in (7.14) which leads to

$$\begin{aligned} \max_{\mathbf{c}} \quad & \text{trace}(\mathbf{A}_{\mathbf{c}}^{\mathsf{H}}\mathbf{A}_{\mathbf{c}}) \\ \text{s.t.} \quad & ||\mathbf{c}||_2^2 = 1. \end{aligned} \tag{7.29}$$

Through the transformation of $\mathbf{A}_\mathbf{c}^\mathsf{H}\mathbf{A}_\mathbf{c}$ using (7.18), its trace can be written as

$$\begin{aligned}\text{trace}(\mathbf{A}_\mathbf{c}^\mathsf{H}\mathbf{A}_\mathbf{c}) &= \sum_{p=1}^{IK}\sum_{q=1}^{IK} c_p^* c_q \text{trace}(\mathbf{A}_p^\mathsf{H}\mathbf{A}_q) \\ &= \mathbf{c}^\mathsf{H}\mathscr{A}\mathbf{c},\end{aligned} \tag{7.30}$$

where $\mathscr{A}$ is given by

$$\mathscr{A} = \begin{bmatrix} \text{trace}(\mathbf{A}_1^\mathsf{H}\mathbf{A}_1) & \dots & \text{trace}(\mathbf{A}_1^\mathsf{H}\mathbf{A}_{IK}) \\ \vdots & & \vdots \\ \text{trace}(\mathbf{A}_{IK}^\mathsf{H}\mathbf{A}_1) & \dots & \text{trace}(\mathbf{A}_{IK}^\mathsf{H}\mathbf{A}_{IK}) \end{bmatrix}. \tag{7.31}$$

As a result, (7.29) can be simplified as

$$\begin{aligned} \max_{\mathbf{c}} \quad & \mathbf{c}^\mathsf{H}\mathscr{A}\mathbf{c} \\ \text{s.t.} \quad & \|\mathbf{c}\|^2 = 1. \end{aligned} \tag{7.32}$$

The solution to this problem is well-known by Lagrange multipliers and is given by the eigenvector of $\mathscr{A}$ corresponding to the largest eigenvalue [152].

Notably, the matrix $\mathscr{A}$ is complex and has complex eigenvectors. However, we need to narrow its focus to amplitude and bi-phase encoding. In other words, the encoding vector $\mathbf{c}$ is constrained to the real domain. By decomposing the cost function in (7.32) using real and complex parts, it can be expressed as

$$\mathbf{c}^\mathsf{H}\mathscr{A}\mathbf{c} = \begin{bmatrix}\text{Re}(\mathbf{c})^\mathsf{T} & \text{Im}(\mathbf{c})^\mathsf{T}\end{bmatrix} \begin{bmatrix}\text{Re}(\mathscr{A}) & -\text{Im}(\mathscr{A}) \\ \text{Im}(\mathscr{A}) & \text{Re}(\mathscr{A})\end{bmatrix} \begin{bmatrix}\text{Re}(\mathbf{c}) \\ \text{Im}(\mathbf{c})\end{bmatrix}. \tag{7.33}$$

Since only the real part of $\mathbf{c}$ is considered for amplitude and bi-phase encoding, the imaginary part can be set to zero, i.e., $\text{Im}(\mathbf{c}) = \mathbf{0}$. As a result, (7.33) can be expressed as

$$\text{Re}(\mathbf{c})^\mathsf{T}\text{Re}(\mathscr{A})\text{Re}(\mathbf{c}). \tag{7.34}$$

The amplitude and bi-phase encoding vector can thus be determined by extracting the leading eigenvector from the real part of the matrix $\mathscr{A}$. We will call this method the FIM-Opt approach.

7.3.3. Encoding Matrix Optimization for Multiple Transmissions

For multiple transmissions, D distinct encoding matrices are designed to construct a more accurate compounded ultrasound image. Assuming the pixel intensity $\mathbf{s}$ remains constant across these D transmissions, a signal model for the D transmissions and measurements can be expressed as follows

$$\begin{bmatrix}\mathbf{z}_1 \\ \mathbf{z}_2 \\ \vdots \\ \mathbf{z}_D\end{bmatrix} = \begin{bmatrix}\mathbf{A}_{\mathbf{c}_1} \\ \mathbf{A}_{\mathbf{c}_2} \\ \vdots \\ \mathbf{A}_{\mathbf{c}_D}\end{bmatrix} \mathbf{s} + \begin{bmatrix}\mathbf{n}_1 \\ \mathbf{n}_2 \\ \vdots \\ \mathbf{n}_D\end{bmatrix}. \tag{7.35}$$

It is important to note that the model (7.35) remains linear concerning both $\mathbf{s}$ and the encoding matrices $\mathbf{C}_d$. Consequently, the optimization methods detailed in Sections 7.3.1 and 7.3.2 can again be employed to address and solve the code design for this model.

Solving for the encoding matrices in (7.35) using the optimization methods(7.20),(7.24) or (7.28) described in Section 7.3.1 would still encounter memory issues when implemented due to the large number of pixels. Alternatively, for the solution based on the minimization of the CRB, we can use the same method as before but adopt the randomization method in the subsampled scenario to obtain L distinct encoding matrices instead of creating the formulation based on (7.35). We first generate many random vectors from the distribution $\hat{\mathbf{c}} \sim \mathcal{N}(0,\hat{\mathscr{C}})$. Then, we apply them to the original problem and choose L candidates that give the minimum value for (7.15),7.22, or 7.25. Hence, we find L solutions that minimize the CRB, and these L transmissions are coherently compounded. For the solution based on the maximization of the FIM, it is observed that multiple large eigenvalues of $\mathscr{A}$ are close to each other, suggesting the presence of multiple suboptimal solutions. Therefore, a potential solution could involve the first few leading eigenvectors corresponding to these largest eigenvalues for multiple transmissions. Then, each eigenvector is normalized and selected as a coding vector of each transmission, and finally, these L transmissions are compounded.

7.3.4. COMPUTATIONAL COMPLEXITY

The FIM-Opt approach requires the computation of the $\mathscr{A}$ matrix in (7.31). Because of the trace operator, this requires calculating the diagonal of I^2K^2 matrices of the form $\mathbf{A}_p^{\mathsf{H}}\mathbf{A}_q \in \mathbb{C}^{L\times L}$ (see (7.19); for the subsampled scenario, we can simply change L by S). Computing the diagonal of each $\mathbf{A}_p^{\mathsf{H}}\mathbf{A}_q$ requires a complexity of $\mathscr{O}(LFI)$ and the overall cost becomes $\mathscr{O}(I^3K^2LF)$. Taking the traces of all terms in (7.31) has complexity $\mathscr{O}(I^2K^2L)$; which is relatively negligible. Later, computing the eigenvectors of the resulting $\mathscr{A}$ matrix brings a computational complexity of $\mathscr{O}(I^3K^3)$, which is again negligible. Note that I in our case is of size 80 or 128 and $2 \le K \le 5$. Hence, the optimization procedure with FIM-Opt has an overall computational complexity of $\mathscr{O}(I^3K^2LF)$.

In Eig-Opt, Dep-Opt and Trace-Opt scenarios, calculating the I^2K^2 entries of the $\mathbf{A}_p^{\mathsf{H}}\mathbf{A}_q \in \mathbb{C}^{L\times L}$ matrices in (7.19) has a computational complexity of $\mathscr{O}(I^3K^2L^2F)$ which is already L times the complexity of the FIM-Opt scenario. Moreover, the computational complexity of the SDP given in (7.20) or (7.28) has a complexity of $\mathscr{O}(I^4K^2F^2L+L^2I^2KF)$ per iteration because $\mathbf{A}^{\mathsf{H}}(\mathscr{C}\otimes\mathbf{I}_{FI})\mathbf{A}$ is computed in every iteration with respect to updated codes in SDP. Note that instead of actually implementing the Kronecker product, an equivalent expression in (7.19) is used. Then, the computational complexity of the SDP per iteration becomes $\mathscr{O}(I^3K^2L^2F)$. Besides, the cost of the first and second positive semidefinite constraints are $\mathscr{O}(L^3)$ and $\mathscr{O}(I^3K^3)$, respectively, in (7.20) and (7.28). Since these terms are generally negligible, the overall computational cost of Eig-Opt or Trace-Opt becomes $\mathscr{O}(I^3K^2L^2FT)$ where T is given by the number of iterations in the SDP solver. Note that cvx uses interior point methods, where each iteration has additional costs, increasing the computation time even further.

While FIM-Opt requires a single step with the complexity of $\mathscr{O}(I^3K^2LF)$, Eig-Opt,

Trace-Opt, and Det-Opt require a notably higher cost, which makes FIM-Opt more useful in practical scenarios. Furthermore, $\mathcal{O}(I^3K^2L^2FI)$ quadratically increases by L, and the number of pixels can be significantly high in ultrasound imaging, which requires subsampling. Nonetheless, the optimization of the codes is performed only once and can be used in imaging tasks repeatedly.

Finally, the computational cost of matched filtering after the optimization procedure is $\mathcal{O}(LFI)$, which is equivalent for all coding schemes of comparison.

7.4. Numerical Results

Simulation experiments are conducted using the k-Wave toolbox [153]. In all k-Wave simulated measurements, the attenuation coefficient has a frequency-dependent power law model for realistic nonlinear ultrasound wave propagation in biological soft tissue. The attenuation is defined as $\alpha(f) = \alpha_0 f^y$ where $\alpha_0 = 0.75$ dB/(MHz^y·cm) is the attenuation coefficient and $y = 1.5$ is the power law exponent.

Two scenarios are considered to evaluate the performance of the proposed optimized code. The first scenario presented in Section 7.4.1 involves a densely sampled high-frequency array with an element pitch-to-wavelength ratio less than 0.5. The second scenario in Section 7.4.2 aims to test the optimized code on a numerical model of the clinical transducer array again with an element pitch-to-wavelength ratio less than 0.5. We used both a high-frequency array and a lower-frequency clinical probe to test our method's robustness across different transducer simulations. Note that high-frequency arrays offer a better resolution for detailed analysis in superficial imaging [154], while low-frequency arrays are useful in practical deep imaging scenarios [122, 123]. In a densely sampled high-frequency array with 128 elements, we first start with a toy example (a simplified simulation) to compare the proposed algorithm with the state-of-the-art. Then, we compare the performance of CRB minimization and FIM maximization for point scatterers data for a highly subsampled optimization scheme. Lastly, the computationally efficient FIM method is chosen to compare its performance with the state-of-the-art. These comparisons are also carried out with the simulated clinical transducer for both point scatterers data and a simulated flow phantom in Doppler imaging.

First, the transmitted pulse length $t_{pulse} \leq 5.19$ μs was chosen to limit the dead-zone to 4 mm. Second, the total pulse length is the length of the base pulse multiplied by the number of bits since we do not consider any overlap between consecutive pulses. In other words, the delay τ between two base pulses is considered equal to the base pulse length. Third, the number of transmissions D is important for the imaging quality. For the initial toy example, we pick $D = 1$ in Section 7.4.1. For the cases in Section 7.4.1, we select various values of $D = 1, 3, 5, 10$ for comprehensive analysis between CRB minimization and FIM maximization. In ultrafast compounded Doppler imaging, it is experimentally validated that when D reaches 9, the resulting contrast and SNR are satisfying, and image contrast will only slightly improve for $D > 16$ assuming plane-wave imaging [124]. Hence, D bounded between 10 and 16 should be sufficient in literature. Hence, we pick $D = 10$ for the comparisons with the state-of-the-art in Sections 7.4.1 and 7.4.2. Hence, we make sure that all the compared methods are tested with a sufficient number of transmissions. Those methods involve Barker coding, random coding,

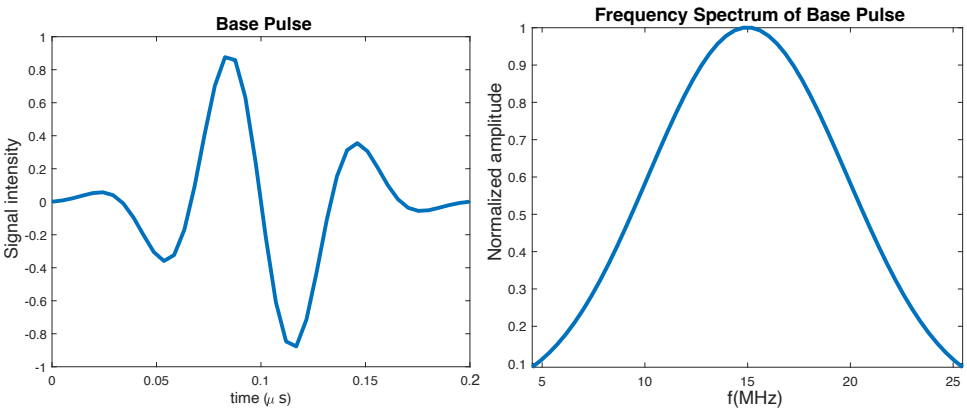

(a) (b)

Figure 7.1: Transmit pulse shape: (a) single short pulse (base pulse), (b) frequency spectrum of base pulse

and plane-wave transmissions.

7.4.1. DENSELY SAMPLED HIGH-FREQUENCY ARRAY

The densely sampled high-frequency array consists of 128 elements spaced with 25 μm pitch. The ultrasound transducer emits a base pulse with a center frequency of 15 MHz. The base pulse and its frequency spectrum are given in Fig. 7.1. The imaging region of interest extends from 4 mm to 11 mm in depth and from -1.25 mm to 1.225 mm in width, aligning with the area typically studied in mouse brain imaging. The interpixel spacing is picked as $dz = dx = 25$ μm.

TOY EXAMPLE

In this section, we compare the results of the approaches that rely on the minimization of the CRB and the maximization of the FIM with the state-of-the-art for a single scatterer. For the former approach, we solve the problem given in (7.20) and (7.28) using cvx software [151]. However, due to the high computational complexity of the problem, we only focus on a small optimization area with a single pixel. For the latter approach, the solution is given by the leading eigenvector of $\mathrm{Re}(\mathscr{A})$.

Due to the high computational complexity of the CRB-based solution, an optimized encoding matrix of size 128×2 is designed, with the pulse having a short bit-length of 2. To evaluate the performance of the algorithms, we first consider a single scatterer image where the codes are optimized with respect to the known scatterer point, which is located at $[x, y] = [0, 8]$ mm. Since we test only for a single scatterer, such an optimization scheme is sufficient. Ideally, for a larger area of distributed scatterers, the optimization should be performed on the pixels taken from the entire area to improve the SNR performance. Here, we only consider a single transmission, i.e., $D = 1$. We use random rounding for the CRB minimization method, and the single realization that maximizes (7.20) (Eig-Opt) or minimizes (7.28) (Trace-Opt) is picked among 100 random vectors

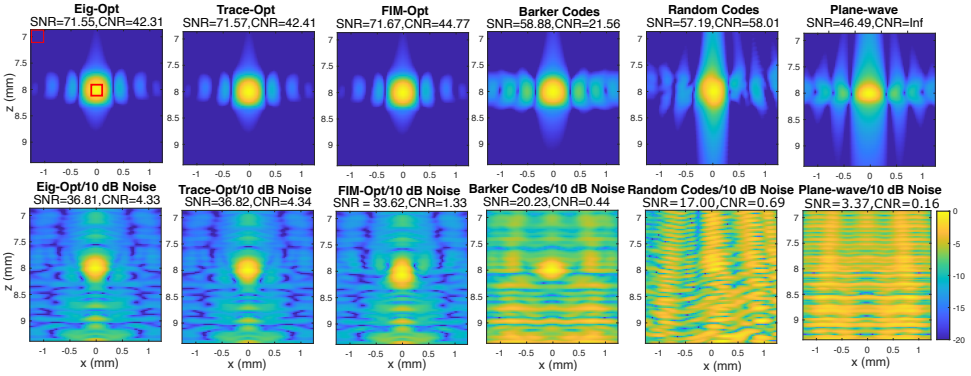

Figure 7.2: The single transmission imaging results for optimized transmissions with Eig-Opt, Trace-Opt, FIM-Opt, Barker code, random code, and plane-wave transmission for noiseless data (top) and noisy data with 10 dB SNR (bottom)

that belong to the following distribution $\hat{\mathbf{c}} \sim \mathcal{N}(0, \hat{\mathscr{C}})$. Here, further increasing the number of random vectors did not visibly affect the performance. For the solution based on the maximization of the FIM (FIM-Opt), the leading eigenvector of $\mathrm{Re}(\mathscr{A})$ is selected for transmission. The performance of the methods is compared to the Barker code, random code, and plane-wave transmission under noiseless and noisy conditions with 10 dB SNR. Before transmission, all pulses undergo normalization to ensure uniform average energy levels. Except for the plane-wave transmission, all transmission codes have a length of 2. All results obtained with matched filtering in (7.12) for these six scenarios are shown in Fig. 7.2.

The results are numerically analyzed by comparing the SNR and CNR in the four scenarios, where SNR = $10\log_{10}(\frac{P_s}{P_n})$. P_s and P_n are the average power of the point scatterer and background noise, respectively. In noise-free cases, P_n corresponds to the average power of the low-intensity background region across the image. Here, $CNR = 10\log_{10}(|\frac{\mu_s - \mu_n|}{\sigma_n})$ where μ_s and μ_n are mean values of the intensities of point scatterer and background regions, and σ_n is the standard deviation of the noise. To compute the SNR and CNR, the red rectangles are used for the scatterer and background noise. Eig-Opt, Trace-Opt, and FIM-Opt perform similarly in noiseless and noisy cases with 10 dB SNR noise, outperforming the plane-wave, random code, and Barker code reconstructions. Since the formulations in (7.21) and (7.28) are the same for the single pixel scenario, it is expected that we observe that both Eig-Opt and Trace-Opt results in the same reconstructions. We also observe that in the noisy case, while Eig-Opt, Trace-Opt, FIM-Opt, and the Barker code approach could reconstruct the scatterer, the other methods could not provide a proper view of the scatterer. The Eig-Opt, Trace-Opt and FIM-Opt results outperform the Barker code in the noisy case. Thanks to the computational efficiency of the FIM-Opt approach, it is more advantageous than both Eig-Opt and Trace-Opt methods.

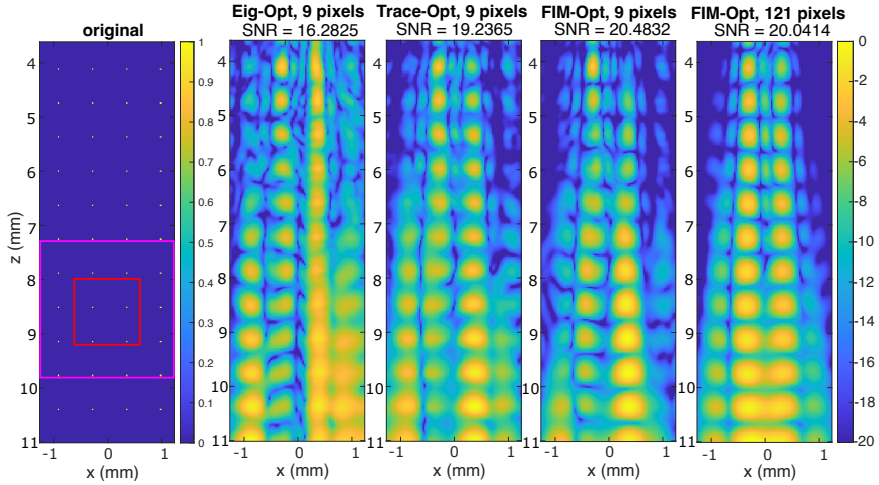

(a)

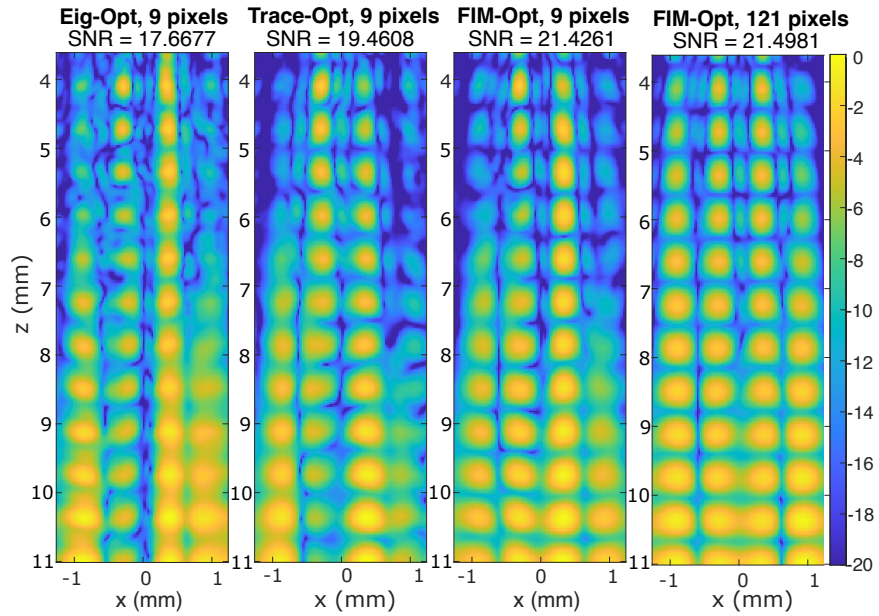

(b)

Figure 7.3: Simulated imaging performance for densely sampled high-frequency array. The compounded image results for optimized transmissions with Eig-Opt, Trace-Opt, and FIM-Opt using 9 and 121 pixels for (a) single transmission, (b) 3 transmissions

CRB MINIMIZATION VERSUS FIM MAXIMIZATION

Now, instead of a single scatterer, we consider uniformly distributed point scatterers in Fig. 7.3. The scatterers are placed 0.625 mm apart both in z and x directions. We com-

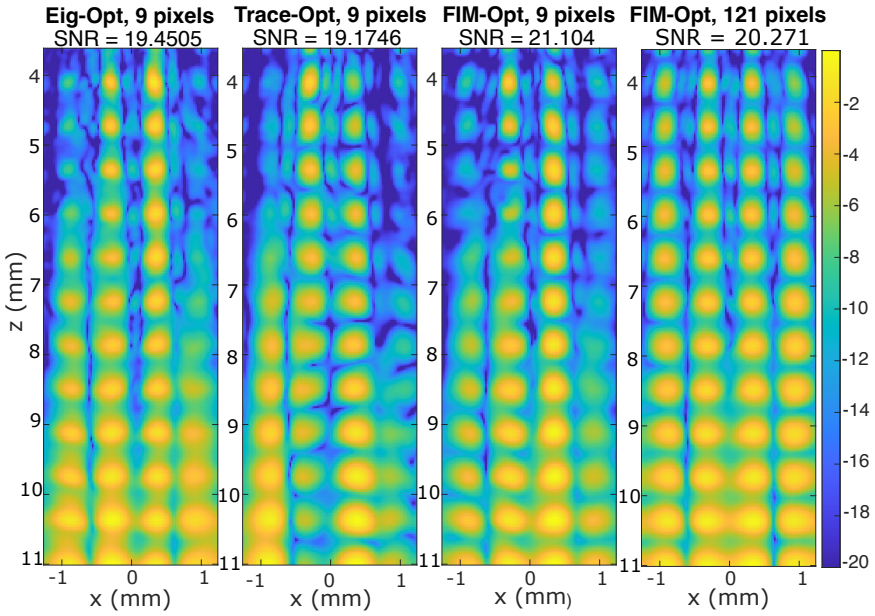

(a)

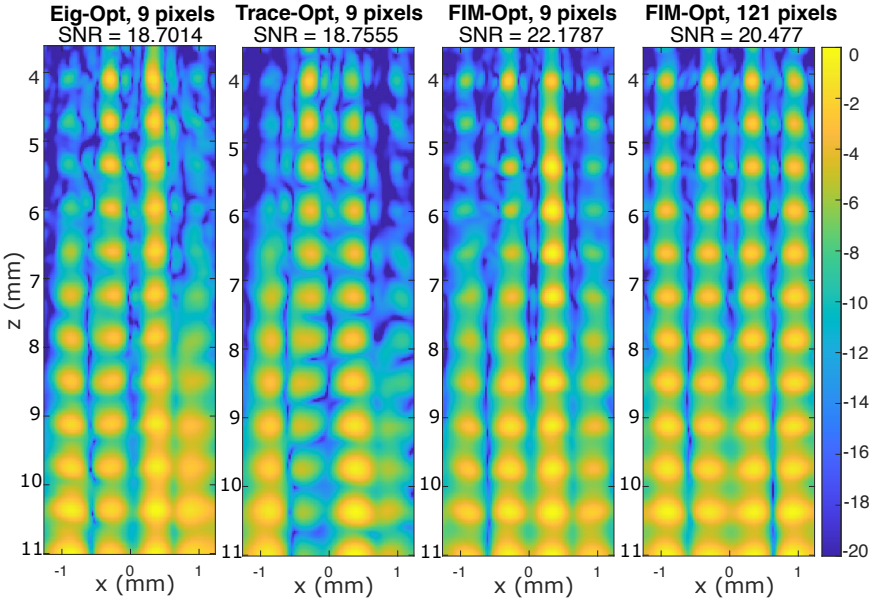

(b)

Figure 7.4: Simulated imaging performance for densely sampled high-frequency array. The compounded image results for optimized transmissions with Eig-Opt, Trace-Opt, and FIM-Opt using 9 and 121 pixels for (a) 5 transmissions, and (b) 10 transmissions

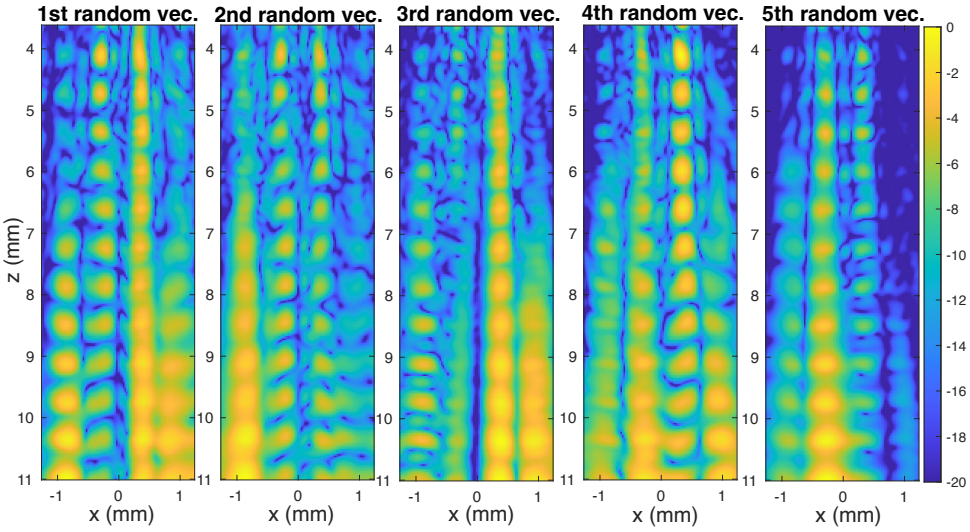

Figure 7.5: Simulated imaging performance for the densely sampled high-frequency array with the imaging results of $D = 5$ transmissions for Eig-Opt

pare the imaging performance of three transmission methods: Eig-Opt, Trace-Opt, and FIM-Opt, using 2-bit codes. However, due to the high computational complexity of the problem, we only focus on a small optimization area with few pixels (9 or 121 pixels). Since we optimize the codes for a small area, comparing them with the state-of-the-art would be unfair. It was fair for the single scatterer as the codes are optimized with respect to the specific location of the scatterer. Now, the optimization area is significantly smaller than the extent of the uniformly distributed scatterers, and the subset of pixels selected does not overlap with the scatterers. Therefore, only the proposed methods are compared to choose the best one for more comparisons in the next section. Before transmission, all codes undergo normalization to ensure uniform average energy levels.

An image subset of $3 \times 3 = 9$ equidistantly distributed pixels from 8 to 9.3 mm on the z-axis and from -0.65 to 0.65 mm on the x-axis in Fig. 7.3a was chosen for optimization. Note that this area is shown with a red rectangle where the scatterers and selected pixels do not overlap. This area is chosen in the middle of the region of interest between 6 mm to 11 mm. Such a low number of pixels is selected due to the computational complexity of the semidefinite program in (7.20) for Eig-Opt and (7.28) for Tra-Opt, which is solved via the cvx toolbox. On a Dell server with dual AMD EPYC 7551 processors (64 cores total, 128 threads, 128 GB RAM, 1 TB SSD), optimization with Eig-Opt takes approximately 1800 seconds, Tra-Opt takes about 2600 seconds, and FIM-Opt completes in around 20 seconds for 9 pixels. While this server is optimized for fast computation, running the same algorithms on a standard MacBook Pro 2019 (2.6 GHz 6-core Intel Core i7) takes roughly 10,000 seconds for Eig-Opt and Tra-Opt. The middle three plots in Fig. 7.3a and the first three plots in Fig. 7.3b, 7.4a and 7.4b are obtained with the optimized code that relies on 9 pixels. Hence, we compare the results for minimizing the CRB based on the

Eig-Opt and Trace-Opt criterion and maximizing the FIM for the same pixels.

In the second scenario, a subset of pixels comprising $11 \times 11 = 121$ equidistantly distributed pixels spanning from 7.3 to 9.9 mm on the z-axis and from -1.3 to 1.3 mm on the x-axis in Fig. 7.3a was chosen to maximize the FIM where the area is shown with a magenta rectangle. Although there is not a specific reason for the exact choice of 11×11, we aim to exceed the performance of the CRB minimization for a small area (9 pixels) by maximizing the FIM for a larger area (121 pixels), with lower computational complexity. Indeed, it is significantly lower as it only takes around 160 seconds with the given Dell server. However, Eig-Opt and Tra-Opt algorithms exceed 36 hours for 121 pixels scenario; hence, it is not practical. The last plots are obtained with the optimized code concerning 121 pixels in Figs. 7.3 and 7.4. Note that the computational cost of FIM-Opt, even with more pixels, is still lower than the Eig-Opt and Trace-Opt methods.

For each method $D = 1$, $D = 3$, $D = 5$ and $D = 10$ transmissions are compounded. These codes are generated randomly for the Eig-Opt and Trace-Opt which employ the mentioned random rounding method in Section 7.3.3, and D realizations that minimize (7.15) or (7.25) are picked, respectively. With FIM-Opt, the leading D eigenvectors of $\mathrm{Re}(\mathscr{A})$ are selected for transmission. All results obtained with matched filtering from $D = 1$, $D = 3$, $D = 5$, and $D = 10$ transmissions for these four scenarios are shown in Figs. 7.3 and 7.4. We only show the results without noise in Figs. 7.3 and 7.4. Moreover, Fig. 7.5 shows individual transmissions of the Eig-Opt algorithm compounded in Fig. 7.4a. Here, each transmission focuses on a different part of the image, hence showing the necessity of various transmissions.

The SNR values given in Figs. 7.3 and 7.4 are obtained by taking the average power of all the known scatterer locations for P_s. To compute P_n, noise locations are selected at the central points between every four scatterers, where the scatterers form the corners of a rectangle. These central points represent regions expected to contain minimal signal, primarily dominated by noise. Across the reconstructions, single transmission is insufficient for a good reconstruction quality for all methods, as shown in Figs. 7.3 and 7.4. The resolution of the scatterers increases with $D = 5$ transmissions especially for FIM-Opt method and the entire ROI even becomes more resolvable with $D = 10$ transmissions. In terms of the clarity of all scatterers, the Eig-Opt performs similarly to the FIM-Opt, where the performance of Trace-Opt seems to be slightly weaker than the others. FIM-Opt outperforms both Eig-Opt and Trace-Opt in terms of SNR. When the region of interest for maximizing the FIM is extended from 9 pixels to 121 pixels, the scatterers in the entire ROI become more resolvable. In contrast, the SNR values for FIM-Opt for 9 pixels seem higher. This is due to scatterers in the middle of the x-axis seeming to be very bright and increasing the average SNR for FIM-Opt with 9 pixels. Here FIM-Opt optimized based on 121 pixels and with 10 transmissions seems to provide a good balance between resolution and SNR by capturing the entire area of scatterers.

The computational complexity of the CRB minimization is significantly higher than the FIM maximization, and hence, FIM-Opt is more advantageous than others also in terms of computational cost. While the Eig-Opt and Trace-Opt require solving a high-cost SDP given in (7.20) or (7.28) using a toolbox such as cvx, the FIM-Opt only takes D eigenvectors of $\mathrm{Re}(\mathscr{A})$ in (7.31). In the FIM-Opt method, irrespective of the area of interest, the size of the $\mathscr{A}$ matrix in (7.31) is the same for the same code length and number

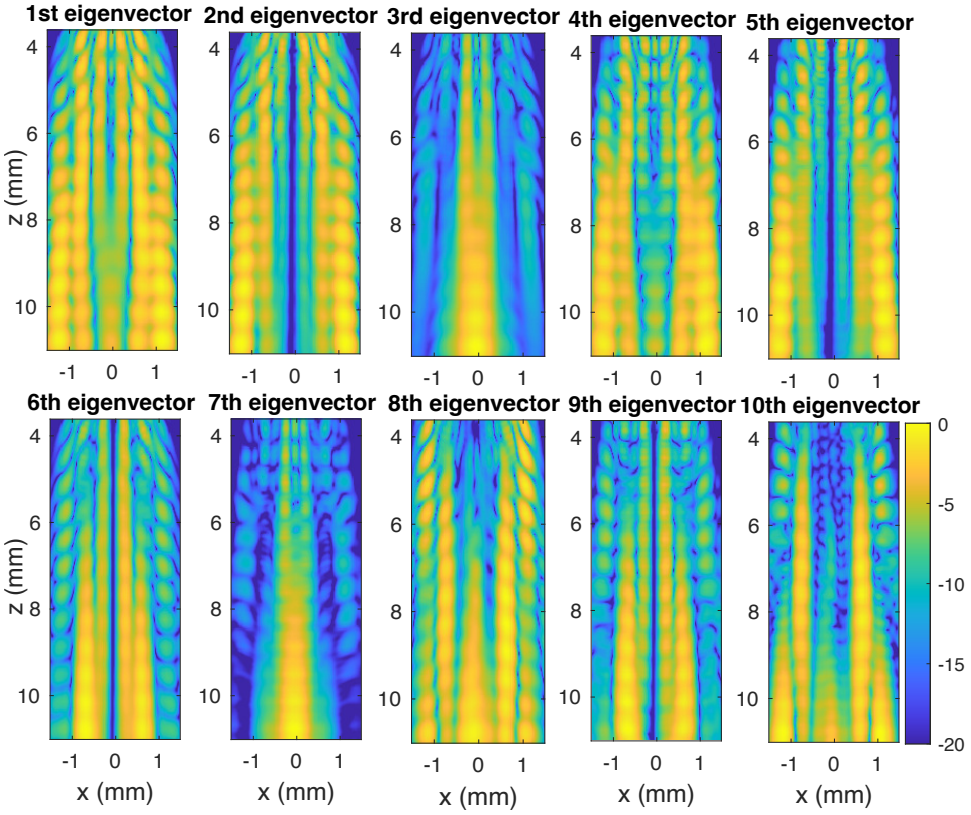

Figure 7.6: Simulated imaging performance for a probe geometry matching that of a densely sampled high-frequency array based on the 10 leading eigenvectors with FIM-Opt Method

of transmitters. The only increment in the computational complexity is calculating the $\mathscr{A}$ matrix. In the end, FIM-Opt is exploited for the rest of the simulations thanks to its reconstruction quality and computational efficiency.

FIM MAXIMIZATION VERSUS THE STATE-OF-THE-ART

In this section, an optimized encoding matrix of size 128×5 is designed, with the pulse having a bit-length of $K = 5$. We compare the imaging performance of four transmission methods: single short pulse plane-wave, 5-bit Barker code, 5-bit random code, and 5-bit optimized code with FIM-Opt. Before transmission, all codes are normalized to ensure uniform average energy levels. Here, images from $D = 10$ transmissions are compounded. The scatterers are placed 0.625 mm apart in the z direction and 0.45 mm apart in the x direction, respectively. For FIM-Opt, an image subset between 6 to 11 mm in the z-axis and between -1.5 mm to 1.5 mm in the x-axis was chosen for optimization, as shown with the red rectangle in Fig. 7.7. This image subset contains $50 \times 30 = 1500$ equidistantly distributed pixels. The distance between each pixel used for optimization is 0.1 mm in the z and x directions, four times the interpixel distance. Since the construction of $\mathscr{A}$ takes time when the area is extended, the optimization region is limited.

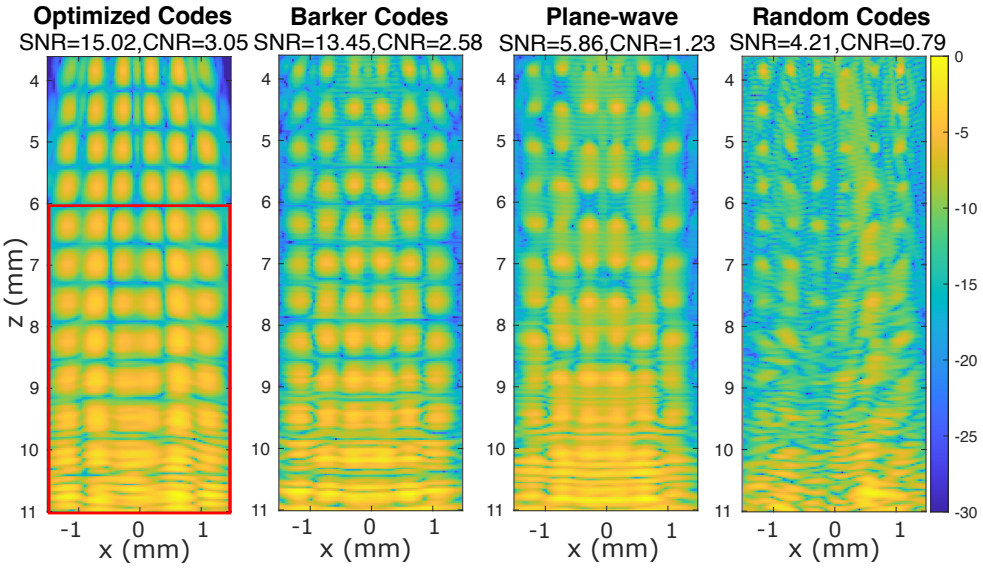

Figure 7.7: Simulated imaging performance for densely sampled high-frequency array for optimized code, Barker code, plane-wave, and random transmission with SNR = 10 dB

Fig. 7.6 shows the matched filter imaging results from the optimized (FIM-Opt) code based on the 10 leading eigenvectors. It shows that each eigenvector transmission produces a different focusing area in the image, leading to varying imaging results. This finding highlights the need for different optimized encoding matrices for multiple transmissions. Then, the compounded imaging results are shown in Fig. 7.7 for all methods. These are reconstructed from measurements with the same additive white Gaussian complex noise at SNR of 10 dB. The left-most image is obtained with the optimized code by compounding data from the 10 leading eigenvectors. The subsequent two images display results from Barker-5 transmissions and single pulse plane-wave transmissions by compounding the data from 10 insonified angles spanning $[-12°, 12°]$. Meanwhile, the fourth image is acquired and compounded through 10 instances of 5-bit random code transmissions.

The SNR values in Fig. 7.7 are obtained by taking the average power of all the known scatterer locations as P_s and picking a low-intensity point between every four scatterers for P_n, where the scatterers form the corners of a rectangle. Although the optimization of the codes is performed for an area smaller than the ROI, the SNR values are acquired with the points picked from the entire ROI. The CNR values are also attained in a similar fashion. The results show that the optimized transmission produces the highest SNR and CNR, and the reconstructions appear brighter in the deeper area ranging from 7 to 9 mm. Conversely, the Barker code and plane-wave transmissions show distortions starting from approximately 8 mm depth. Distortions are also present for the optimized codes, but their effect is less severe thanks to the higher SNR of optimized codes. Lastly, a random transmission appears to be the most sensitive to additive noise, leading to significant degradation in image quality. In summary, Barker codes outperform plane-wave

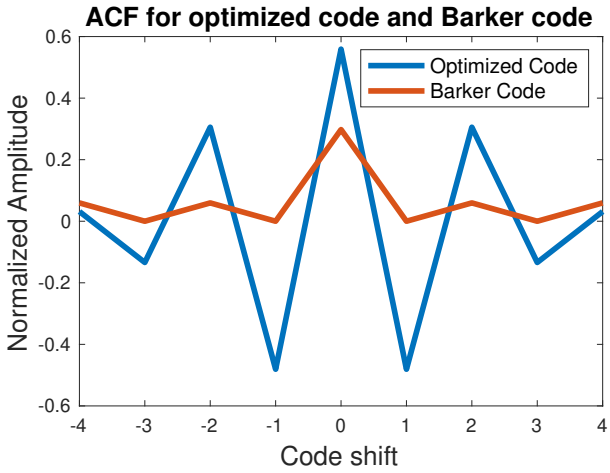

Figure 7.8: Normalized autocorrelation function for optimized code on the 80th element, $[0.75,-1.58,1.88,-1.51,0.70]$, and Barker code of length 5, $[1,1,1,-1,1]$. These codes are scaled with the same factor after normalization to show the magnitude of the optimized codes compared to standard Barker codes.

and random codes in the deeper region but still fall short compared to the optimized transmission regarding SNR and noise sensitivity.

To measure resolution, we used the full width at half maximum (FWHM) of the point spread function (PSF) at the scatterer locations. The FWHM represents the width of the PSF at 50% of its peak value and indicates how well nearby points can be distinguished. We report both axial and lateral FWHM values as indicators of spatial resolution. The FWHM of the PSF for resolution is given in Table 7.1 for the images in Fig. 7.7. The twelve scatterers inside the region over the $[6,7.5]$ mm across z-axis have been used and their FWHM values are averaged. These scatterers are chosen as they are in the optimization area, and they do not suffer from the degradations starting around 8 mm for random codes. The optimized codes present the worst resolution and the highest FWHM value. Then, Barker codes and plane-wave produce better axial and lateral resolution, and random codes result in the best resolution values.

A trade-off between SNR and resolution (both axial and lateral) for the optimized code is observed. This trade-off arises from the limitation in the optimization formulation (7.32), where the autocorrelation property of the code is not considered. The autocorrelation function (ACF) of the optimized code (on the 80th element) and the 5-bit Barker code is plotted in Fig. 7.8. It can be seen that the normalized main lobe amplitude (the highest peak) of the optimized code (0.55) is higher than the Barker code (0.25) by a factor of 2. However, the main lobe-to-side lobe (the second highest peak) ratio of the optimized code 1.89 is considerably lower than that of the Barker code (5). A lower

FWHM (mm)	Optimized	Barker	PW	Random
Axial	0.423	0.342	0.327	0.266
Lateral	0.333	0.323	0.310	0.262

Table 7.1: Axial and lateral FWHM of PSF

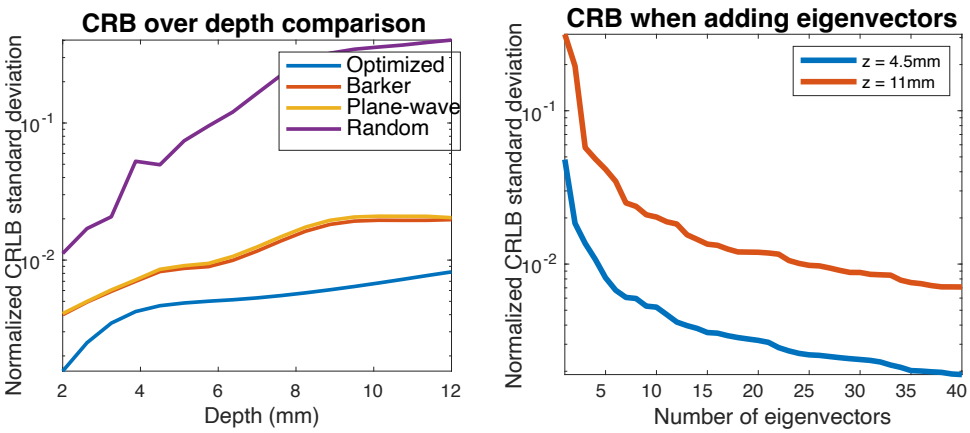

(a) (b)

Figure 7.9: (a) CRB versus depth for random, Barker, plane-wave, and optimized code at -0.7 mm on x-axis; (b) CRB versus D, the number of compounded eigenvectors, for a pixel at depth 4.5 mm and depth 11 mm

main lobe-to-side lobe ratio increases interference and artifacts caused by side lobe energy and results in smoother images with worse resolution. Although a high main lobe level can result in a higher SNR in the image; a low main lobe-to-side lobe ratio causes a degraded resolution for optimized codes.

We evaluate the CRB of the four methods across different imaging depths, as shown in Fig. 7.9a. The results reveal that the FIM-Opt code yields the lowest CRB, indicating superior estimation precision of optimized codes, meaning it provides the most accurate estimation of scatterer intensities among the tested methods. Meanwhile, the Barker code and short pulse plane-wave exhibit similar CRB curves and the random code displays the highest CRB values. These SNR values align with the trends observed in the imaging results. Hence, this analysis confirms the effectiveness of the FIM-Opt code compared to the other tested methods in terms of increased SNR.

Remark 1: Note that number of transmissions D can also be analyzed from the CRB perspective. Thus, how the CRB changes when compounding more leading eigenvectors for multiple transmissions is investigated. In Fig. 7.9b, the normalized CRB is plotted for a pixel located at depths of 4.5 mm and 11 mm when compounding 1 to 40 leading eigenvectors. It becomes evident that after compounding 5 transmissions, the CRB no longer decreases significantly. Still, to accommodate the literature, the number of transmissions D is set to 10 for good compounded image quality.

7.4.2. SIMULATED CLINICAL TRANSDUCER RESULTS

Here, the M5Sc-D phased array transducer manufactured by General Electric (GE) with its 80×3 elements and a pitch of 0.27 mm is used. This transducer complies with the Nyquist sampling requirement, operating at a center frequency of 2.8 MHz with wavelength $\lambda = 0.55$ mm. We only consider using the middle row elements, resulting in 80 active elements. The choice was made for computational efficiency, as it reduces the number of elements. Although this limits the shape of the beam in the elevation di-

rection, it allows for a focused investigation of beamforming performance in the lateral direction. The pixel spacing is $dz = dx = 90\ \mu m$.

MATCHED FILTER RESULTS

Simulations are conducted using equidistantly distributed point scatterers within the imaging area. The encoding matrix $\mathbf{C}$ was optimized with dimensions 80×5, focusing on an image subset ranging from around 50 mm to 90 mm in the z-axis and -12 mm to 12 mm in the x-axis which is shown with the red rectangle in Fig. 7.10a. This image subset contains $90 \times 44 = 3960$ equidistantly distributed pixels. Here, the distance between each pixel used for the optimization is 0.54 mm in the z and x directions, 6 times the interpixel distance. Its performance was compared to the 5-bit Barker code, single pulse plane-wave, and 5-bit random code. The imaging region ranges from 5 mm to 90 mm. Fig. 7.10a displays the results obtained from compounding 10 transmissions, all subject to the same level of additive white Gaussian noise (SNR = 10 dB).

In Fig. 7.10a, the imaging result beginning at 55 mm with the optimized code is more detectable and more robust to the noise than the Barker code, the plane-wave, and random codes in the deeper regions. Note that the proposed coding scheme is optimized for the area between 50 mm and 90 mm. Therefore, the performance enhancement is expected in that area. As a trade-off, the optimized code has a lower resolution than the other alternatives. Another trade-off of the optimized code is that it results in a narrower field of view compared to other methods. The top left and right point scatterers are not detectable since the near field between 5 mm to 50 mm is ignored for optimization, and some information loss may exist in the near field area. Among other methods, the 5-bit Barker code seems to have higher SNR than the other but slightly degrades the axial resolution compared to the plane-wave or random codes, leading to visible side lobes at point targets as the Barker code does not possess perfect side lobe cancellation after pulse compression[67]. To quantify this, a vertical line at $x = [-0.6875]$ mm is analyzed. Along the axial direction, 19 scatterers are considered to compute the average main lobe-to-side lobe ratio, which is found to be 8.46 dB. The optimized code performs even worse in this regard, yielding a lower ratio of 3.38 dB. Conversely, the random code exhibits better axial resolution than the other methods, particularly in the near-field area[18]. However, the SNR of the random code is notably lower than other methods. In conclusion, the trade-off between the SNR of the optimized code and axial resolution is also observed in Figure 7.10a.

The results are numerically analyzed by comparing the SNR in the four scenarios. For this calculation, a line at $x = [-0.6875]$ mm is picked. We aim to give the reader a richer view of what is happening with the SNR at various depths. The middle line is chosen as the limited optimization region affects the field of view in the corners. Boundary effects have less influence on the middle. This region is where the optimization is most effective, providing a more reliable and representative evaluation of the method. The highest-intensity and lowest-intensity regions are determined on this line. It results in 19 high-intensity regions, corresponding to approximate locations of 19 point scatterers at $x = [-0.6875]$ mm. Then 19 lowest intensity regions in this line are selected and considered as background noise. Each SNR value is computed between a high-intensity region and neighboring a low-intensity region and results in 19 SNR values. Using these 19 SNR

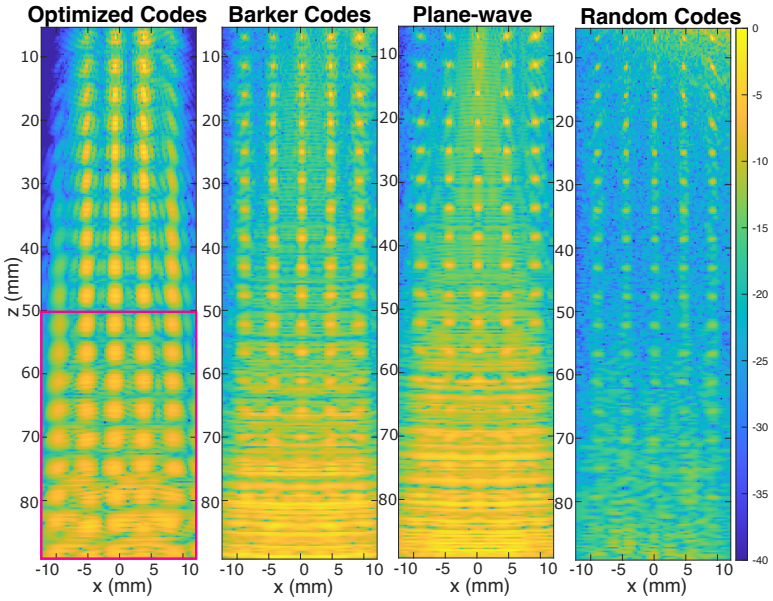

(a)

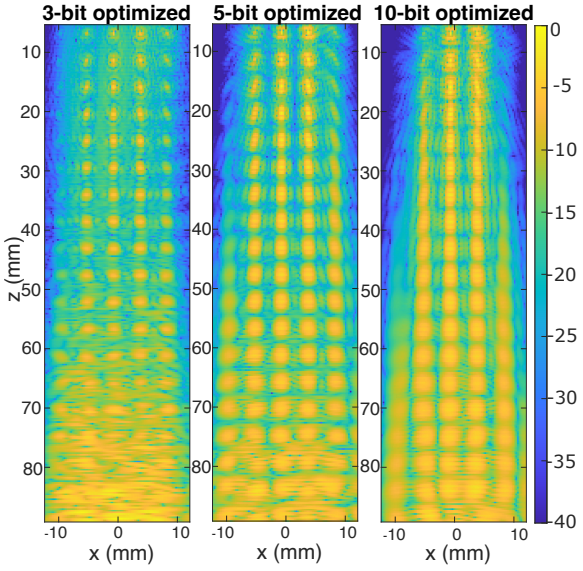

(b)

Figure 7.10: Simulated imaging performance for a probe geometry matching that of a clinical transducer (a) Imaging results for optimized code, Barker codes, plane-wave, and random transmissions with SNR = 10 dB. (b) Imaging results for 3-bit, 5-bit, and 10-bit optimized codes with SNR = 10 dB.

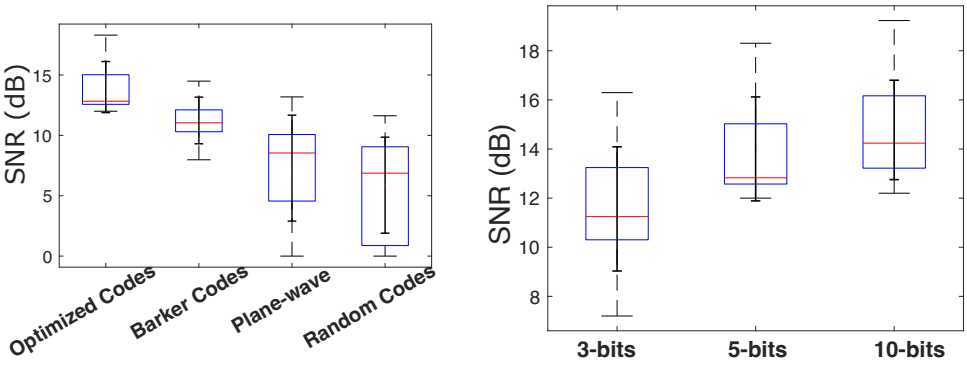

(a) (b)

Figure 7.11: (a) The SNR boxplot analysis for point scatterer images with optimized codes, Barker codes, single pulse plane-wave, and random codes. In each box, the bottom and top edges of the box represent the 25th and 75th percentiles in the data, and the red line inside the box marks the median. The whiskers represent the highest and lowest values in the data. (b) The SNR boxplot analysis for point scatterer images with 3-bit, 5-bit, and 10-bit optimized codes.

values, the box plots of the SNR data from each method are shown in Fig. 7.11b. The optimized code has the highest SNR among all methods. A single pulse plane-wave has the highest variation. If we look at the median SNR value, the optimized code has an SNR gain of 4.4 dB, while the Barker code has a gain of 2.5 dB compared to the single short pulse. Note that the optimized and Barker codes maintain a more consistent SNR performance than single pulse and random code.

Furthermore, the performance of different bit-length optimized codes (3-bit, 5-bit, and 10-bit) is compared. The results are shown in Figs. 7.10b and 7.11b. As the bit-length increases, the SNR also increases. Note that longer codes have higher main lobe levels after pulse compression, resulting in a stronger signal relative to the noise, especially in the deeper regions. However, the use of longer codes also involves a trade-off. Specifically, a 10-bit code exhibits lower resolution for point scatterers compared to the 3-bit and 5-bit codes. As can be seen from the autocorrelation function of optimized codes in Fig. 7.12, the 10-bit code has the highest main lobe amplitude but the lowest

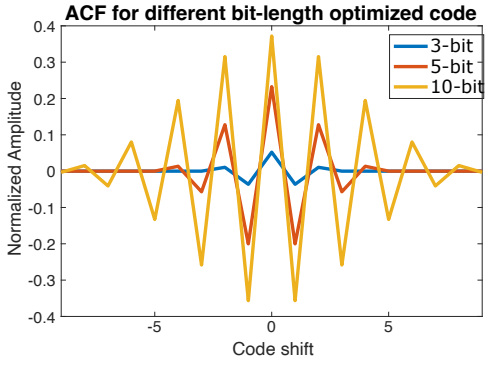

Figure 7.12: Autocorrelation function for 3-bit, 5-bit, and 10-bit optimized codes

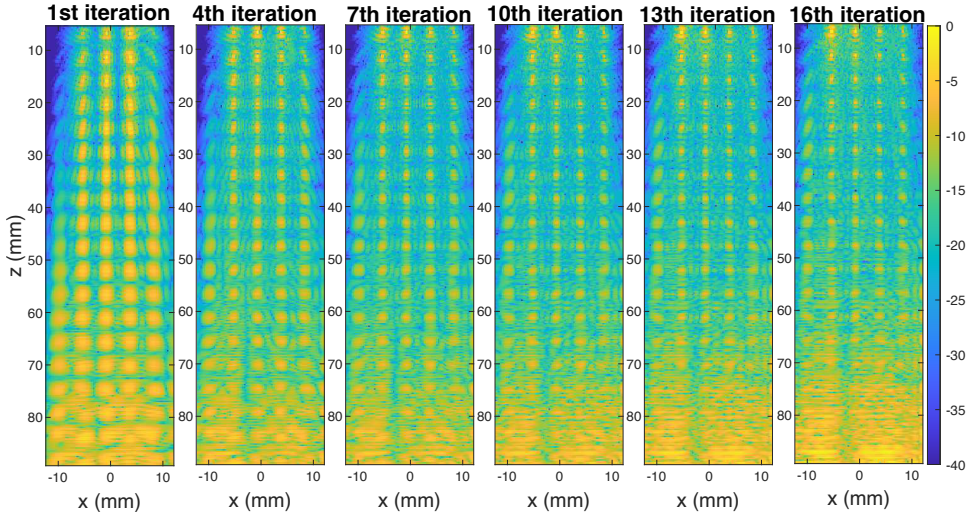

(a)

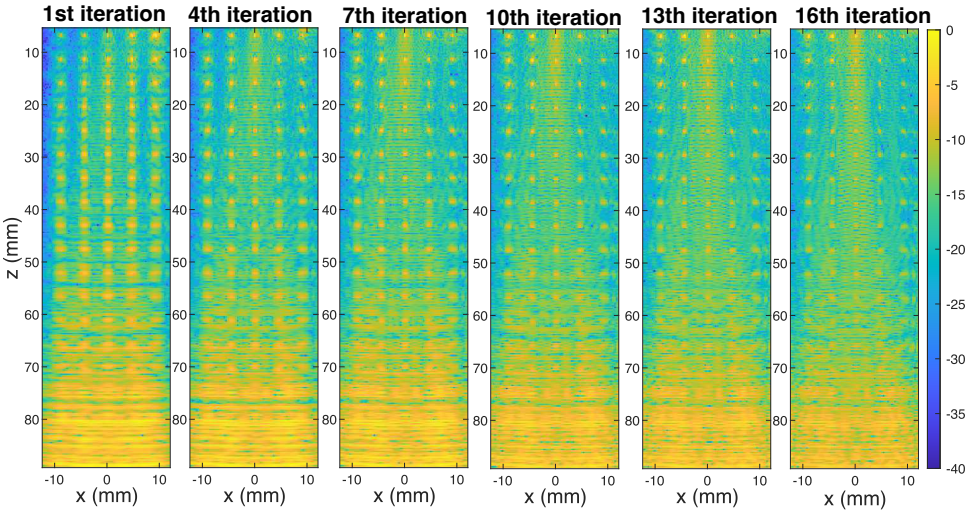

(b)

Figure 7.13: Simulated imaging performance for a probe geometry matching that of a clinical transducer for (a) Optimized code using Least Squares QR (LSQR) algorithm (b) Barker code using LSQR algorithm. Here, we show the images after 1 to 16 iterations.

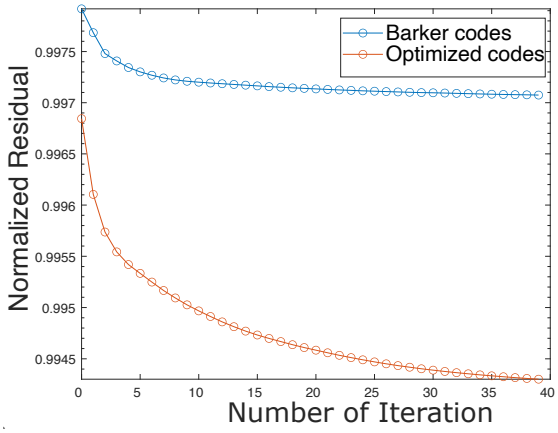

Figure 7.14: Normalized residual curves for Barker code and optimized code when adding iteration in LSQR.

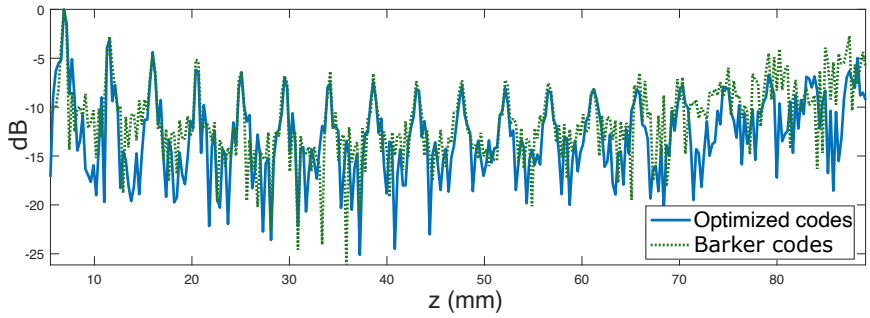

Figure 7.15: Image contrast of a vertical line from the image at 0.24 mm on x-axis to noise comparison between optimized code at 10th and Barker code at 4th iteration.

main lobe to side lobe ratio which is only 1.19. The 3-bit code has the lowest main lobe level but has a main lobe-to-side lobe ratio of 5, which is equal to the 5-bit Barker code.

LSQR RESULTS

Instead of reconstructing the image with the matched filter, we can also seek a better fit between the data and the model by applying LSQR to improve the resolution of the optimized code results. Experiments with the number of iterations from 1 to 16 were conducted. Fig. 7.13a displays images obtained at different iteration steps. The optimized code results show that the image resolution improves as the number of iterations increases. However, after around 10 iterations, the image starts to overfit with the noise. Especially in deeper areas with lower signal levels, it leads to a decrease in the SNR and overall image quality. We observed this effect visually in the reconstructed images, where noise patterns become more prominent. Furthermore, the point scatterers at two sides at the top of the image become visible within the increasing number of iterations, which were not clear in matched filter reconstructions in Fig. 7.10a with optimized code.

The LSQR results from the optimized code are compared to those from the Barker code, as shown in Fig. 7.13b. The results indicate that LSQR does not significantly im-

prove the SNR for the Barker code. Although the resolution improves slightly with an increase in the number of iterations, the near-field area starts to overfit with the noise after 7 iterations. Analyzing the normalized residual curve for these two coded excitation schemes reveals that the residual does not decrease significantly for Barker codes compared to optimized codes with the addition of more iterations (Fig. 7.14).

In a direct comparison of the best performance image using LSQR between these two transmission schemes (e.g., the 10th iteration for optimized codes and the 7th iteration for Barker codes), the optimized codes still outperform Barker codes in terms of SNR in deeper areas while achieving a decent resolution. Fig. 7.15 shows the contrast signal for a vertical line located at position 0.24 mm on x-axis in the image. The scatterers show clear peaks before 60 mm for both methods. The Barker code starts to fail in the area deeper than 60 mm, while the optimized code still maintains a good contrast.

7.4.3. Doppler Flow Simulations

In this section, the blood flow imaging simulation is done in k-Wave using MATLAB. The clinical transducer setting described in Section 7.4.2 is used here. A flow phantom with a size of 90 × 20 mm is generated with a 9 mm diameter parabolic blood vessel that is placed 55 mm away and angled at 25° from the transducer surface. The flow velocity is 9 cm/s, and the blood-to-tissue level is −67 dB. The simulated number of frames is 30. The tissue density is modeled as a random distribution with a mean value of approximately 1000 kg/m^3. The scatterer density in the blood vessel region is also randomly distributed with values ranging from 1000 kg/m^3 to 1020 kg/m^3, where the vessel wall is assumed static. The imaging performance of the 5-bit optimized code and 5-bit Barker code is compared for 10 transmissions. The matched filter is used for beamforming, and after compounding, an SVD filter is applied to all the temporal compounded images to gain the final power Doppler image [50].

Different levels of white Gaussian noise at the noise-to-blood level of −30, −15, and 0 dB are added to the measurement data. The results are shown in Figures 7.16 and 7.17. The SNR and the contrast-to-noise ratio (CNR) are calculated for each image, where the blood vessel area and the tissue area are indicated by the black and white rectangular in Fig. 7.16 respectively. These regions are selected considering the actual locations of the blood vessel and the tissue area in the simulated flow image. We aimed to observe the effect of different codes around the boundaries of the blood vessel. After SVD filtering, the PDI results at a noise level of 0 and −15 dB show that the blood vessel images from the optimized code exhibit a better distinction between vessel and background regions and have stronger intensity compared to the ones from the Barker code (Fig. 7.16). In the deeper area (below 60 mm), the optimized code exhibits an improved contrast between the vessel and the background compared to the Barker code. The optimized code exhibits a clear advantage over the Barker code for a high noise level (−30 dB). The numerical results show that the optimized code has consistent and higher SNR and CNR across different noise levels. For the noise levels 0, −15, and −30 dB, the optimized code has SNR gains of 2.33, 4.3, and 7.78 dB compared to the Barker code. The optimized code is more robust for high-level noise. The blood flow simulation result demonstrates the ability of the proposed optimized code to improve the SNR of the Doppler images in deep areas. The resolution problems exhibited by the optimized code in the previous

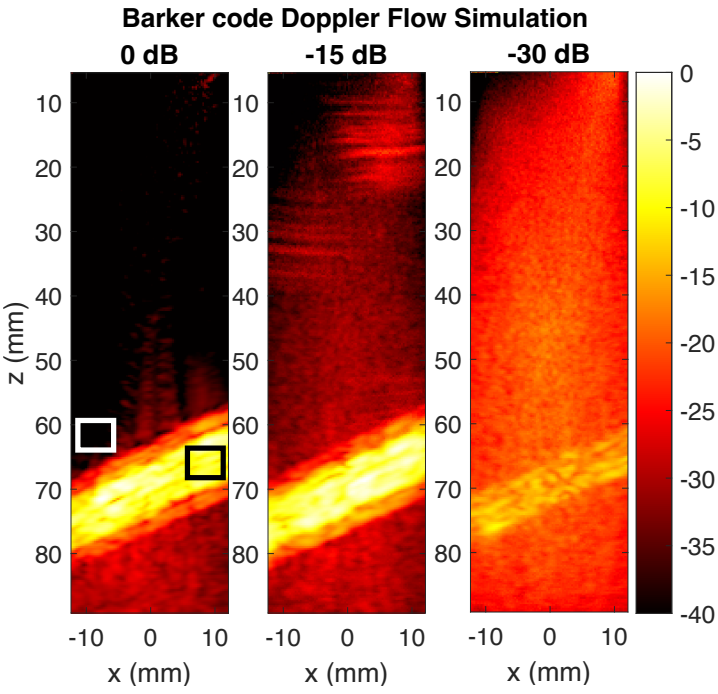

(a)

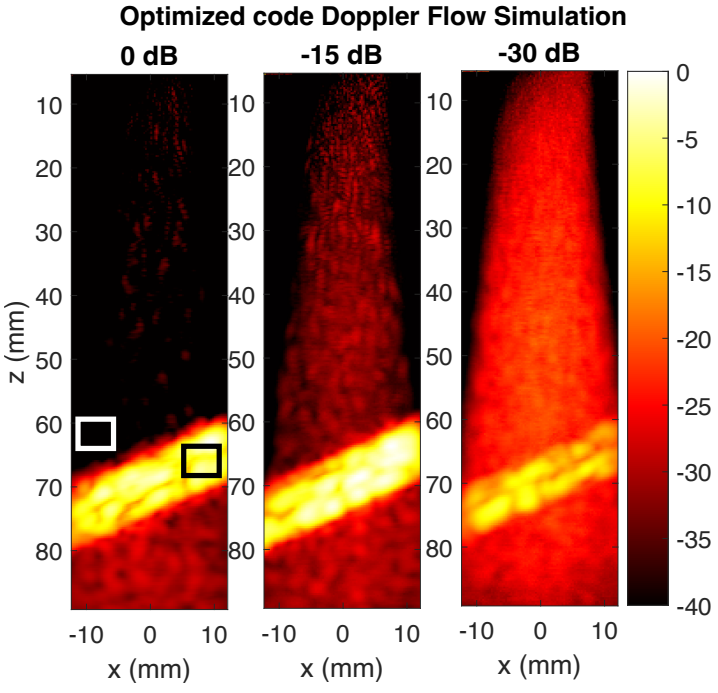

(b)

Figure 7.16: (a) shows the Power Doppler images from 5-bit Barker code with noise-to-blood levels at 0, −15, and −30 dB. (b) is the Power Doppler images from the optimized code. All the images are shown with the same colormap spectrum from 0 to −40 dB.

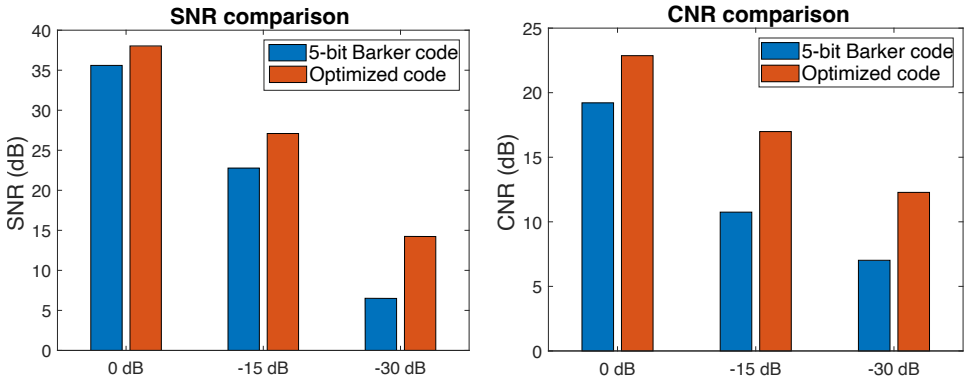

(a) (b)

Figure 7.17: (a) SNR of the Barker code and optimized code; (b) CNR of the Barker code and optimized code. They are calculated using the ROI shown in Fig. 7.16, where the black and white rectangular shows the blood vessel and the background region, respectively.

sections are not very severe in the Doppler flow simulation.

7.5. Discussions and Future Work

7.5.1. Discussions

In this work, a model-based approach is embraced as it allows for more flexibility in handling the diverse coded excitation scheme used in our method. For a fair comparison between different coding schemes, we applied model-based beamforming to all coded excitations in order to ensure that any differences in performance are not due to the choice of beamforming. This approach allowed for the design of the coded excitation scheme with CRB minimization (Eig-Opt, Det-Opt, Trace-Opt) or FIM maximization (FIM-Opt). Note that the matched filter method prioritizes SNR, which is maximized by the matched filter, over spatial resolution. Therefore, all methods can suffer from slight resolution loss.

Theoretically, we can obtain the optimal solution with an exhaustive search for CRB minimization, resulting in a single transmission that captures the entire region of interest but has a high computational cost. Since the optimization problem is non-convex, convex relaxation and subsampling are used, leading to suboptimal solutions and performance degradation. A more feasible FIM-Opt approach is proposed to reduce the complexity further, providing practical solutions that approximate the ideal case, with multiple randomizations to compensate. Diverse codes ensure that different parts of the region of interest are emphasized with each transmission, producing a more comprehensive and meaningful image. This diversity benefits scenarios with multiple transmissions.

Simulations in Section 7.4.1 and 7.4.1 concluded that FIM-Opt is a cost-efficient solution that performs slightly better than the Eig-Opt and Trace-Opt for the same optimization area. Besides, FIM-Opt with an enlarged optimization area outperforms the Trace-Opt and Eig-Opt optimized for a small area in terms of resolution, although FIM-

Opt is still computationally more efficient.

In Section 7.4.1 FIM-optimized code achieves the highest SNR and robustness to the noise and lowest CRB. However, its lower main lobe-to-side lobe ratio introduces a trade-off between SNR and resolution. For example, Barker codes are specifically designed to have good autocorrelation properties, allowing for axial resolution retrieval comparable to a single short pulse. The findings in Section 7.4.2 also support these arguments. Moreover, increasing bit lengths results in higher SNR but in lower resolution and hence suffers from this trade-off. To establish a balance between SNR and resolution, LSQR is employed in Section 7.4.2, and an improvement is observed until the 10th iteration for the optimized code. However, there is still a need for optimized codes that maximize the main lobe-to-side lobe ratio while minimizing CRB without using any advanced beamforming methods.

The simulation results in Section 7.4.3 demonstrate that the optimized code offers improved SNR and CNR compared to the Barker code, again with a trade-off for the resolution. This is common in clinical imaging and often depends on the diagnostic context. For example, in scenarios where noise dominates, stronger vessel contrast can improve overall visibility, even if boundaries appear smoother. Our results indicate that small vessel visibility is not significantly compromised, as shown by the improved CNR metrics.

7.5.2. LIMITATIONS AND FUTURE WORK

Our work can be considered as an initial attempt for the usage of optimized coded-excitation and it has a lot of potential for future research direction.

- As highlighted before, future work needs to achieve balanced enhancement of SNR and resolution. For example, adding a resolution-related constraint (e.g., related to the autocorrelation property) to the problems in (7.15), (7.25), (7.22) or (7.29) can improve the resolution.

- This work considered amplitude encoding. However, bi-phase encoding can be easier to implement for more practical purposes with the Verasonics system. In the optimization function, we then need a binary constraint where $\mathbf{c} \in \{-1, 1\}^{IK}$.

- The optimization problem poses a computational complexity challenge. Future research on developing efficient algorithms rather than subsampling can be more useful.

- Another computational problem is due to the model-based approach. Although a direct application of DAS beamforming is not possible as each transmitter sends a different coded pulse, a decoding matrix for the optimized encoding matrix can be developed. Then, an initial implementation of the decoding matrix makes applying the DAS beamforming possible. Still, the design of the decoding matrix poses a computational challenge. For a similar discussion, [155] can be considered.

- Conducting *Phantom* and *in Vivo* experiments with the Verasonics can validate the applicability of the proposed method and are needed as future work.

- The proposed model-based framework for coded excitation can be useful for systems with compressive sensing or more advanced image reconstruction techniques with fewer sensors [11].

7.6. CONCLUSIONS

In this work, we have proposed optimizing a coded excitation scheme. For this, we designed an optimized code represented by a generalized encoding matrix in a linear signal model. Then, we employed the minimization of the CRB for the unknown coding matrix. The minimization of the maximum eigenvalue, determinant, and trace of the CRB matrix has been proposed, but its computational complexity makes the optimization infeasible for a large area of interest. Therefore, instead of minimizing the trace of the CRB, maximizing the trace of the FIM has been proposed. It results in a computationally less complex problem that can be solved by finding the eigenvector of a small-sized matrix corresponding to the largest eigenvalue. We used a densely sampled high-frequency array to compare the performance of the CRB's minimization and the FIM's maximization for point scatterer data. Then, the suboptimal FIM-based method is chosen to compare its performance with the state-of-the-art. It is observed that while the SNR increases, the resolution decreases as the autocorrelation property is not considered. We also tested the suboptimal FIM-based method with a numerical model of the clinical transducer on the point scatterer data. Again, we obtained a tradeoff between SNR and resolution. We also observed that LSQR can drastically improve the resolution of the optimized code with a slight decrease in SNR. Finally, blood flow simulations are done using a clinical transducer, and the optimized code exhibits consistent and higher SNR and CNR at different noise levels. Future work highlights the need to balance SNR and resolution and computationally more efficient optimization schemes.

8

CONCLUSIONS AND FUTURE WORK

8.1. CONCLUSIONS

This thesis has presented advanced methods and optimization techniques in ultrasound imaging to address some challenges in the field. This work focused on enhancing imaging quality (resolution, SNR) by proposing novel algorithms and optimizing transmit signal designs within the imaging system. The key contributions can be summarized as follows:

Chapter 2 briefly explores the fundamental principles of model-based vascular imaging focusing on power Doppler imaging (PDI). The chapter emphasizes the advantages of the model-based approach over the traditional DAS approach. Using mathematical models and regularization techniques, model-based approaches improve the image quality. The chapter first presents the basic model-based image reconstruction techniques such as matched filter and least squares estimation. Then, it continued with deterministic and probabilistic frameworks to exploit the prior image information. On the other hand, model-based methods face challenges in balancing computational efficiency and image quality, especially for real-time applications. While the image quality can be improved with those methods, they still require advancements, especially in compressive scenarios. Hence, this thesis aims to overcome these issues by developing an advanced reconstruction algorithm and imaging system to improve SNR, resolution, penetration depth, noise reduction, and so on.

To answer **Q1**, Chapter 3 proposes an image reconstruction method leveraging the joint sparse structure of the vasculature at different time instants. The ℓ_1-SVD algorithm is performed over the measurements, to reduce the computational complexity of this MMV model. We evaluated the performance of the proposed method within two different simulation settings. In the first set of simulations, where an ultrasound super-resolution problem is considered, it has been shown that the proposed method improves the spatial resolution and provides a clear separation between very close vessels compared to the state-of-the-art. In the second setting, where the image reconstruction is directly applied to the RF measurements, our method seems slightly slower than SUSHI,

which is a state-of-the-art method. Still, its image reconstruction quality is better under appropriate settings. This chapter also discussed why joint sparsity with deterministic priors might not be sufficient for the ultrasound imaging data. Due to the limited prior information associated with deterministic sparsity, this chapter points out the motivation for the need for statistical sparsity in the upcoming chapters.

To answer **Q1**, Chapter 4 proposes using the SBL algorithm with fixed-point iterations for vascular ultrasound imaging. Instead of deterministic methods, joint sparsity is now enforced using statistical methods. Further, the performance of the MMV FISTA and SBL algorithms have been compared with mouse brain image data. Both methods slightly outperform the matched filter; however, the improvements are limited to noise suppression and increased contrast ratio and did not contribute to visualizing the detailed structure of vasculature. This chapter also noted that since vasculature seems to be a connected network, more advanced priors considering the relations between neighboring pixels might improve the reconstruction quality.

To answer **Q2**, Chapter 5 introduced a pattern coupling algorithm with fixed-point iterations, FP PCSBL, which is computationally faster than the EM algorithm. The performance of the proposed method has been tested with DOA and amplitude estimation, and FP PCSBL shows results similar to those of EM PCSBL. The proposed algorithm is then tested on mouse brain imaging data to see if pattern coupling enhances the reconstruction performance of the SBL algorithm with fixed-point iterations. While the method eliminates the grainy structure observed in the vasculature, it does not improve the visualization of the detailed structure. Finally, this chapter suggested using the correlations between hyperparameters of each pixel instead of only a simple dependence.

To answer **Q2**, Chapter 6 proposed a correlated sparse Bayesian learning (SBL) algorithm for block sparse signal reconstruction with unknown partition. This algorithm is proposed as a computationally more efficient version of EBSBL by explaining the underlying relation between these two algorithms. We assume that neighboring sparse coefficients are correlated, resulting in a tridiagonal correlation matrix. We proposed an approximate solution as the inverse of a tridiagonal matrix is cumbersome. The sparse reconstruction performance of the algorithms is evaluated for randomly generated synthetic data and DOA, focusing on the amplitude estimation problem. The proposed block sparsity algorithm outperforms EBSBL and methods that do not rely on correlations, such as CSBL and PCSBL. Furthermore, the proposed algorithm recovers both block patterns and isolated coefficients.

We also noted that a two-dimensional version of the algorithm can be derived. However, the correlation matrix becomes block tridiagonal with tridiagonal blocks to capture the correlation with the pixels in the horizontal and vertical directions. Such an approach requires further discovery on the estimation of the parameters. We decided not to pursue that approach due to the computational inefficiency of the SBL algorithms with the EM method for the two-dimensional ultrasound imaging data. As in Chapter 5, the fixed-point iterations version of the correlated SBL algorithm can be derived. However, since the previously proposed algorithms, such as classical SBL and PCSBL, did not significantly contribute to the image quality, we also did not pursue that direction. Henceforth, we decided to continue our search for improved image quality through the design of coded transmissions.

To answer **Q3**, Chapter 7 addressed the optimization of coded excitation schemes with a generalized encoding matrix in a linear signal model. Initially, we employed the minimization of the CRB matrix's maximum eigenvalue, determinant, and trace, but the high computational complexity made this approach infeasible for large areas. Instead, the maximization of the trace of the FIM is proposed, simplifying the problem by finding the eigenvector of the largest eigenvalue in a small matrix. First, a tight array is used to compare the performance of the CRB minimization and the FIM maximization for point scatterer data. Thanks to the computational simplicity, the suboptimal FIM-based method is chosen to be compared with the state-of-the-art such as plane-wave imaging, Barker codes and random codes. While the SNR increases, resolution decreases as the autocorrelation property is ignored. Testing the FIM-based method with a clinical transducer exhibited a tradeoff between SNR and resolution, and the LSQR method improved resolution at a small expense of SNR. Lastly, blood flow simulations demonstrated that the optimized code consistently offers higher SNR and CNR among different noise levels. This chapter also noted that future work should investigate optimization strategies to balance SNR and resolution enhancement. Moreover, multiphase encoding can be focused on in addition to the bi-phase encoding.

8.2. FUTURE WORK

Here, we present the limitations and future work regarding image reconstruction algorithms presented in Chapters 3, 4, 5 and 6, and ultrasound transmission in Chapter 7.

8.2.1. IMAGE RECONSTRUCTION ALGORITHMS

This thesis focused on enhancing image quality (SNR and resolution) and reducing artifacts to overcome model-based vascular ultrasound imaging challenges. However, the improvements achieved with deterministic and statistical priors were not sufficient to reveal the detailed structure of the vasculature and were computationally expensive.

Firstly, the way of incorporating deterministic and statistical priors can be improved. We first determined the number of tissue-related components using empirical observations on the matched filter data in deterministic and probabilistic cases. Then, we separated the tissue via SVD filtering from the RF measurements as it is a linear operation. Finally, we enforced joint sparsity in Chapters 3 and 4 or jointly block sparsity in Chapter 5. Although this procedure is theoretically convenient, the linearity of the SVD filtering might be distorted by the noise present in the RF data. Thus, selecting the tissue-related components was applied as an empirical procedure, and the exact number of tissue-related components in the SVD filtering step was determined roughly. In future work, this issue can be addressed by integrating tissue-related priors with blood flow-related priors. Instead of separating the tissue with an SVD filter on the RF data, tissue separation can be handled during the inverse problem solution step. In the deterministic approach in Chapter 3, the tissue-related components can be represented with a smooth prior, such as low-rankness, as in [156]. This approach may provide flexibility in extracting the vasculature data.

Another drawback of the proposed deterministic approach is that considering the tissue-separated vasculature as purely joint sparse or jointly block sparse in the spatial

domain is not proven empirically and remains an assumption. Note that rapid temporal fluctuations can be present in the data, which may violate the joint-sparsity assumption. Therefore, searching for a transform domain may produce a better sparse representation for the unknown vectorized image stack **S** as given with the following formulation:

$$\hat{\mathbf{S}} = \arg\min_{\mathbf{S}} \frac{1}{2}||\mathbf{Z} - \mathbf{AS}||_F^2 + \lambda||\mathbf{TS}||_0 \tag{8.1}$$

or

$$\hat{\mathbf{S}} = \arg\min_{\mathbf{S}} \frac{1}{2}||\mathbf{Z} - \mathbf{AS}||_F^2 + \lambda||\mathbf{TS}||_{2,1} \tag{8.2}$$

where **T** represents a suitable transform. This can be handled by a standard known transform. For instance, [156] considered taking the temporal Fourier transform of the **S** where Doppler shifts can be represented by few spectral samples. Still, such an approach has not been proven to be the most efficient way of exploiting suitable prior information. To mitigate this, a dictionary or transform learning step for the ultrasound images can be implemented [96, 97]. Moreover, deep learning can be an alternative solution [157]. However, the common pitfall of learning-based approaches is the computational complexity of the large imaging data in vascular ultrasound imaging. Still, since the learning step can be applied once to the training data, extra costs would not be incurred when solving the inverse problem in real-time.

The main concern of future work should be alleviating the computational inefficiencies related to model-based imaging for real-time applications. Using fewer sensors or taking the Fourier transform of the RF data reduces the computational complexity arising in model-based approaches. However, DAS beamforming still seems to be the fastest approach, and computational demands in model-based image reconstruction techniques limit their practical usage. In the probabilistic approach, SBL requires taking the large inverse in the iterations. One approach employs an inversion-free method to reduce the computational burden [120, 121]. In particular, for correlated SBL, the fixed-point iterations method could be advantageous for one-dimensional and two-dimensional scenarios. Although updating the diagonal non-zero elements of the correlation matrix can be handled by simple update rules, the non-zero off-diagonal elements require further exploration. We tried to develop the fixed-point iterations version of the correlated SBL but have not achieved a successful result yet. Henceforth, it can be addressed as a part of future work. However, it would not yet be the most computationally efficient algorithm even with fixed-point iterations.

8.2.2. ULTRASOUND TRANSMISSIONS

The algorithms proposed in Chapters 3, 4, 5, and 6 have shown limited improvements with high computational cost. The main challenge is balancing the image quality and computational efficiency. Consequently, our focus has shifted to advancements in Chapter 7 in the transmit-receive data acquisition process by developing advanced transmission codes instead of advancements in image reconstruction algorithms.

In Chapter 7, the proposed optimization method still poses computational challenges for one-time optimization before real-time imaging. Optimizing the coded excitation matrix becomes impractical when applied to larger areas. The second challenge is

related to the beamforming process of the optimized code transmissions. As each transmitted pulse differs for the transducer elements, a traditional DAS beamformer could not be applied, but a model-based approach has been exploited. Note that a decoding matrix can also be designed to provide geometric focusing and proper application of an algorithm similar to DAS. However, the design of such a decoding matrix poses a new challenge. Unlike the transmit code design based on matched filtering, the decoding matrix must be compatible with delay-and-sum beamforming. In matched filtering, the focus is optimizing the transmission codes to maximize SNR by assuming a straightforward relationship between the transmitted and received signals. However, the decoding matrix must account for the complex changes over the signals after transmission, such as reflections and scattering. The decoding matrix needs to reverse these effects while also managing the delays and geometrical properties of the system; and hence the decoding matrix requires a more careful design. The third avenue can be incorporating multi-phase encoding, which is not explored in Chapter 7. Multi-phase encoding, along with the phase delays in the encoding matrix, can improve the focusing and steering capacity of the transmissions and result in focused beams or angled plane waves. Fourthly, bi-phase encoding can be considered for future work to reduce the computational complexity. It requires more sophisticated relaxation techniques but can be solved with greedy algorithms instead of forming a semidefinite program [10]. Note that it also provides simplicity for the Verasonics system. As a fifth suggestion, the balance between SNR and resolution should be established. Future research could investigate optimization techniques that use autocorrelation property constraints in the convex optimization problem. Finally, the proposed coding scheme should be tested in experimental setups and in-vivo.

ACKNOWLEDGEMENTS

I want to start by thanking my supervisor and promotor, Geert Leus, for the opportunity he gave me to work with him. He is an excellent professor in his area, and I am super proud to work with him and have all the meetings with him. Since he is brilliant and very good in his area, I was always surprised by his intelligence and the highlights of our meetings. Furthermore, he was very supportive when I could not focus on PhD due to my severe medical condition for some months. His kindness and patience helped me to overcome those challenging times. Next, I thank Pieter Kruizinga from Erasmus MC for the joy and positivity he brings to our project. Although our perspectives on science differ at certain times, he always gave me good vibes and supported me. He helped me to work in an interdisciplinary area and extended my perspective on signal processing. Next, I would like to thank Hans Bosch, who is always very kind, calm and supportive. Whenever I go to Erasmus MC, I've enjoyed our conversations about the projects and our holidays. Dear Professors, I am fortunate to work on such an interdisciplinary project with you.

Next, I would like to thank Fox, my fantastic colleague and friend, with whom I collaborated significantly on our project. You are a very funny, friendly, helpful, and understanding person. I learned a lot from you, especially when I had difficulty understanding the interdisciplinary aspects of the project. You were always a bridge between me, Pieter, and Hans to express my work from their perspective. I also would like to thank Michael, who helped me a lot during the project and impressed me with his knowledge of ultrasound imaging. Dear Pim, I was clueless at the beginning of PhD during COVID-19; and you explained all the details regarding ultrasound imaging with your emails. We couldn't meet often after your contract ended, but thanks for all the help!

At TU Delft, I also have a lovely bond with other professors. I am incredibly grateful to Geethu, who significantly helped me in the mathematical parts of my project and inspired me a lot as a very smart and hard-working woman in the engineering area. She encouraged me by sharing her PhD journey and showing me how to stay strong during challenging times. I thank Alle-Jan for his psychological support during the times when I had medical troubles. He always cheered me for reminding me to be kind to myself. I am also grateful to Raj; he always gave me motivational talks and raised my mood significantly. Also Bori, who is the sunshine of our group! Her attitude has always cheered me up and enlightened my mood.

When I first came to Delft, I did not know anyone except Aybuke, my good friend and officemate. You were my first friend in the Netherlands and always supported me in my PhD and personal life. Thank you for all your support and all the joy you have brought to my life! I cannot believe we haven't met before while doing our master's at the same university. My friend and officemate, Dear Hanie, you might be the kindest person I have ever met; you are friendly, mature, patient, a good listener, and a supporter. You always have inspired me with your research and personal attitudes. And Sofia, you were

a cheerful person who always brightened my mood. Your stories are always interesting, and I can listen to you forever. I cannot think of anyone who doesn't like you girls! Thank you, my officemates, for all the support you gave me!

Metin, you have been one of my best friends in the office. We always have good conversations about our research, personal lives, psychology, philosophy, and all the various domains anyone can imagine. Anurodh, you are a very kind, caring, and understanding person. Your friendship has a warm, healing effect on anyone. I also always enjoyed your interesting philosophic questions. Furthermore, thank you for all the research-related discussions.

Dear Chang Heng, you are one of the most intelligent people I've ever met. I have always been impressed by your knowledge of mathematics and your humble demeanor. Although you seem silent from the outside, you are a great friend once you open up! Besides, you have always helped me with my research. Alberto, your enthusiasm for research always impressed me. You have been a supportive and realistic friend to me. Mainly, I thank you for your contributions to my research. Yanbin, I received much help from you for one of my papers. You are a very smart, friendly and funny person. I will never forget about your sarcastic and witty jokes! Dear guys, although your names aren't in my papers, you are secret supporters of my research.

Dear Miao, Mario, Cristian, Jordi, Ellen, Antonio, Ruben, Yanbo, Yujie, Sinian, Shouyan, Giovanni, Peiyuan, Zhonghang, Seline, Costas... Thank you for all the great conversations during our drinks, office lunches, and meetings. You were great colleagues!

Now, I want to express my gratitude to my mother and father, Zeynep and Unal. Dear Mom, although you have never had the opportunity to attend school, you have always supported my education and academic career as a single mom. I have always felt your unconditional love. Dear Dad, although you have not been in this world for over 20 years, I have always felt your love, support, and best wishes from heaven. Dear sister Ayse, you have been like a second mother since my childhood. I am lucky to have such a joyful, helpful, and wise sister around me. You, my brother-in-love Yusuf, my niece Fatima Beyza (also one of my best friends), and my nephew Muhammed provided me with the family environment I needed in the Netherlands! Dear sister Funda, I would never have imagined such a career path without your support, as you taught me to love science from a young age. You are a great listener and better than all the psychologists! Dear niece Elif, you have been my best friend with your mature and calm character. You are the best listener I have ever met! I am so lucky to have a niece like you, who is like my sister! Dear Brother Alper, I owe my ambition to your great talks and my humor to your witty jokes! Thanks for everything!

Finally, my dear husband Hasan Can, I don't know how to thank you. In addition to being my lover, you become my family and the best friend in my life. You moved to another country with me to support my career; we always had great travel adventures and looked at the best landscapes together (although your smile looks even more beautiful than the landscapes). Whenever I had research trouble, you pushed me to focus on my work and finish my PhD. Sometimes, you even became like my secret second supervisor. When I had medical troubles during my PhD, you have always been there for me. You have significantly contributed to my life and research; I will be grateful to you forever!

BIBLIOGRAPHY

[1] S.R. Ghorayeb, W. Lord, and S.S. Udpa. “Application of a beamforming technique to ultrasound imaging in nondestructive testing”. In: *IEEE Transactions on Ultrasonics, Ferroelectrics, and Frequency Control* 41.2 (1994), pp. 199–208.

[2] Salavat R Aglyamov et al. “Model-based reconstructive elasticity imaging using ultrasound”. In: *International journal of biomedical imaging* 2007.1 (2007), p. 035830.

[3] Chengpu Yu, Cishen Zhang, and Lihua Xie. “A blind deconvolution approach to ultrasound imaging”. In: *IEEE Transactions on Ultrasonics, Ferroelectrics, and Frequency Control* 59.2 (2012), pp. 271–280.

[4] Tanya Chernyakova and Yonina C. Eldar. *Fourier Domain Beamforming: The Path to Compressed Ultrasound Imaging*. 2013.

[5] P. Pal and P. P. Vaidyanathan. “Pushing the Limits of Sparse Support Recovery Using Correlation Information”. In: *IEEE Transactions on Signal Processing* 63.3 (2015), pp. 711–726.

[6] D. Cohen and Y. C. Eldar. “Sub-Nyquist Sampling for Power Spectrum Sensing in Cognitive Radios: A Unified Approach”. In: *IEEE Transactions on Signal Processing* 62.15 (2014), pp. 3897–3910.

[7] A. Bar-Zion et al. “Fast Vascular Ultrasound Imaging With Enhanced Spatial Resolution and Background Rejection”. In: *IEEE Transactions on Medical Imaging* 36.1 (2017), pp. 169–180.

[8] A. Bar-Zion et al. “SUSHI: Sparsity-Based Ultrasound Super-Resolution Hemodynamic Imaging”. In: *IEEE Transactions on Ultrasonics, Ferroelectrics, and Frequency Control* 65.12 (2018), pp. 2365–2380.

[9] Pieter Kruizinga et al. “Compressive 3D ultrasound imaging using a single sensor”. In: *Science Advances* 3.12 (2017).

[10] P. van der Meulen et al. “Coding Mask Design for Single Sensor Ultrasound Imaging”. In: *IEEE Transactions on Computational Imaging* 6 (2020), pp. 358–373.

[11] Yuyang Hu et al. “Compressive Imaging with Spatial Coding Masks on Low Number of Elements: An Emulation Study”. In: *2022 IEEE International Ultrasonics Symposium (IUS)*. 2022, pp. 1–4.

[12] Yuyang Hu et al. “3D Carotid Artery Flow Imaging Using Compressive Sensing with a Spatial Coding Mask: A Simulation Study”. In: *2023 IEEE International Ultrasonics Symposium (IUS)*. 2023, pp. 1–4.

[13] Yuyang Hu et al. “Computational Ultrasound Carotid Artery Imaging with a Few Transceivers: An Emulation Study”. In: *IEEE Transactions on Ultrasonics, Ferroelectrics, and Frequency Control* (2025), pp. 1–1.

[14] Thanassis Misaridis and Jørgen Arendt Jensen. “Use of modulated excitation signals in medical ultrasound. Part I: Basic concepts and expected benefits”. In: *IEEE transactions on ultrasonics, ferroelectrics, and frequency control* 52.2 (2005), pp. 177–191.

[15] Thanassis Misaridis and Jørgen Arendt Jensen. “Use of modulated excitation signals in medical ultrasound. Part II: Design and performance for medical imaging applications”. In: *IEEE transactions on ultrasonics, ferroelectrics, and frequency control* 52.2 (2005), pp. 192–207.

[16] Thanassis Misaridis and Jørgen Arendt Jensen. “Use of modulated excitation signals in medical ultrasound. Part III: High frame rate imaging”. In: *IEEE transactions on ultrasonics, ferroelectrics, and frequency control* 52.2 (2005), pp. 208–219.

[17] Heng Zhao, Larry Y. L. Mo, and Shangkai Gao. “Barker-coded ultrasound color flow imaging: theoretical and practical design considerations”. In: *IEEE Transactions on Ultrasonics, Ferroelectrics, and Frequency Control* 54.2 (2007), pp. 319–331.

[18] Pavel Ni and Heung-No Lee. “High-Resolution Ultrasound Imaging Using Random Interference”. In: *IEEE Transactions on ultrasonics, ferroelectrics, and frequency control* 67.9 (2020), pp. 1785–1799.

[19] Christoph F Dietrich et al. “How to perform contrast-enhanced ultrasound (CEUS)”. In: *Ultrasound international open* 4.01 (2018), E2–E15.

[20] Stephanie R Wilson, Lennard D Greenbaum, and Barry B Goldberg. “Contrast-enhanced ultrasound: what is the evidence and what are the obstacles?” In: *American Journal of Roentgenology* 193.1 (2009), pp. 55–60.

[21] Didem Dogan et al. “Multiple Measurement Vector Model for Sparsity-Based Vascular Ultrasound Imaging”. In: *2021 IEEE Statistical Signal Processing Workshop (SSP)*. 2021, pp. 501–505.

[22] Ying Liu et al. “Super-resolution ultrasound imaging by sparse Bayesian learning method”. In: *IEEE Access* 7 (2019), pp. 47197–47205.

[23] Lu Wang et al. “Enhanced ISAR Imaging by Exploiting the Continuity of the Target Scene”. In: *IEEE Transactions on Geoscience and Remote Sensing* 52.9 (2014), pp. 5736–5750.

[24] Lu Wang et al. “Sparse Representation-Based ISAR Imaging Using Markov Random Fields”. In: *IEEE Journal of Selected Topics in Applied Earth Observations and Remote Sensing* 8.8 (2015), pp. 3941–3953.

[25] Lifan Zhao et al. “The Race to Improve Radar Imagery: An overview of recent progress in statistical sparsity-based techniques”. In: *IEEE Signal Processing Magazine* 33.6 (2016), pp. 85–102.

[26] Zhilin Zhang et al. “Compressed Sensing for Energy-Efficient Wireless Telemonitoring of Noninvasive Fetal ECG Via Block Sparse Bayesian Learning”. In: *IEEE Transactions on Biomedical Engineering* 60.2 (2013), pp. 300–309.

[27] Oana Lorintiu, Hervé Liebgott, and Denis Friboulet. “Compressed Sensing Doppler Ultrasound Reconstruction Using Block Sparse Bayesian Learning”. In: *IEEE Transactions on Medical Imaging* 35.4 (2016), pp. 978–987.

[28] Jun Fang et al. “Pattern-Coupled Sparse Bayesian Learning for Recovery of Block-Sparse Signals”. In: *IEEE Transactions on Signal Processing* 63.2 (2015), pp. 360–372.

[29] Didem Dogan and Geert Leus. “Pattern Coupled Sparse Bayesian Learning with Fixed Point Iterations for DOA and Amplitude Estimation”. In: *2023 57th Asilomar Conference on Signals, Systems, and Computers*. 2023, pp. 1303–1307.

[30] Lu Wang et al. “Alternative to Extended Block Sparse Bayesian Learning and Its Relation to Pattern-Coupled Sparse Bayesian Learning”. In: *IEEE Transactions on Signal Processing* 66.10 (2018), pp. 2759–2771.

[31] Huiping Duan et al. “Pattern-Coupled Sparse Bayesian Learning for Inverse Synthetic Aperture Radar Imaging”. In: *IEEE Signal Processing Letters* 22.11 (2015), pp. 1995–1999.

[32] Jun Fang, Lizao Zhang, and Hongbin Li. “Two-Dimensional Pattern-Coupled Sparse Bayesian Learning via Generalized Approximate Message Passing”. In: *IEEE Transactions on Image Processing* 25.6 (2016), pp. 2920–2930.

[33] Zhilin Zhang and Bhaskar D. Rao. “Extension of SBL Algorithms for the Recovery of Block Sparse Signals With Intra-Block Correlation”. In: *IEEE Transactions on Signal Processing* 61.8 (2013), pp. 2009–2015.

[34] Didem Dogan and Geert Leus. “Correlated Sparse Bayesian Learning for Recovery of Block Sparse Signals With Unknown Borders”. In: *IEEE Open Journal of Signal Processing* 5 (2024), pp. 421–435.

[35] Heng Zhao, Larry Y. L. Mo, and Shangkai Gao. “Barker-coded ultrasound color flow imaging: theoretical and practical design considerations”. In: *IEEE Transactions on Ultrasonics, Ferroelectrics, and Frequency Control* 54.2 (2007), pp. 319–331.

[36] István A. Veres et al. “Golay code modulation in low-power laser-ultrasound”. In: *Ultrasonics* 53.1 (2013), pp. 122–129.

[37] Michael E. Tipping. “Sparse Bayesian Learning and the Relevance Vector Machine”. In: *Journal of Machine Learning Research* 1 (2001), pp. 211–244.

[38] Shihao Ji, Ya Xue, and Lawrence Carin. “Bayesian Compressive Sensing”. In: *IEEE Transactions on Signal Processing* 56.6 (2008), pp. 2346–2356.

[39] Homer F. Walker and Peng Ni. “Anderson Acceleration for Fixed-Point Iterations”. In: *SIAM Journal on Numerical Analysis* 49.4 (2011), pp. 1715–1735.

[40] T.A. Schonhoff and A.A. Giordano. *Detection and Estimation Theory and Its Applications*. PearsonPrentice Hall, 2006. ISBN: 9780130894991.

[41] Sundeep Prabhakar Chepuri. “Sparse sensing for statistical inference: Theory, algorithms, and applications”. PhD Thesis. Delft University of Technology, 2016.

[42] Pim van der Meulen et al. “Coding mask design for single sensor ultrasound imaging”. In: *IEEE Transactions on Computational Imaging* 6 (2019), pp. 358–373.

[43] Emilie Mace et al. “Functional ultrasound imaging of the brain: theory and basic principles”. In: *IEEE transactions on ultrasonics, ferroelectrics, and frequency control* 60.3 (2013), pp. 492–506.

[44] J.A. Jensen et al. “Ultrasound research scanner for real-time synthetic aperture data acquisition”. In: *IEEE Transactions on Ultrasonics, Ferroelectrics, and Frequency Control* 52.5 (2005), pp. 881–891.

[45] Pieter Kruizinga et al. “Compressive 3D ultrasound imaging using a single sensor”. In: *Science Advances* 3.12 (2017), e1701423.

[46] C. Kargel et al. “Doppler ultrasound systems designed for tumor blood flow imaging”. In: *IEEE Transactions on Instrumentation and Measurement* 53.2 (2004), pp. 524–536.

[47] JM Rubin and RS Adler. “Power Doppler expands standard color capability.” In: *Diagnostic imaging* 15.12 (1993), pp. 66–69.

[48] Vincent Perrot et al. “So you think you can DAS? A viewpoint on delay-and-sum beamforming”. In: *Ultrasonics* 111 (2021), p. 106309.

[49] R. Lavarello, F. Kamalabadi, and W.D. O’Brien. “A regularized inverse approach to ultrasonic pulse-echo imaging”. In: *IEEE Transactions on Medical Imaging* 25.6 (2006), pp. 712–722.

[50] Charlie Demené et al. “Spatiotemporal Clutter Filtering of Ultrafast Ultrasound Data Highly Increases Doppler and fUltrasound Sensitivity”. In: *IEEE Transactions on Medical Imaging* 34.11 (2015), pp. 2271–2285.

[51] Meghan L Thorne, Richard N Rankin, and Steinman. “In vivo Doppler ultrasound quantification of turbulence intensity using a high-pass frequency filter method”. In: *Ultrasound in medicine & biology* 36.5 (2010), pp. 761–771.

[52] Daniel Król, Anita Lorenc, and Radosław Świcęiński. “Detecting laterality and nasality in speech with the use of a multi-channel recorder”. In: *2015 IEEE International Conference on Acoustics, Speech and Signal Processing (ICASSP)*. 2015, pp. 5147–5151.

[53] Didem Dogan et al. “Multiple Measurement Vector Model for Sparsity-Based Vascular Ultrasound Imaging”. In: *2021 IEEE Statistical Signal Processing Workshop (SSP)*. 2021, pp. 501–505.

[54] J. T. Fokkema and P. M. van de Berg. “Seismic applications of acoustic reciprocity”. In: cp-46-00204 (1993).

[55] Martin Verweij, Bradley Treeby, and Libertario Demi. *Simulation of Ultrasound Fields in Comprehensive Biomedical Physics Volume 2: X-Ray and Ultrasound Imaging*. Vol. 2. Sept. 2014. ISBN: 978-0-444-53633-4.

[56] S.G. Mallat and Zhifeng Zhang. “Matching pursuits with time-frequency dictionaries”. In: *IEEE Transactions on Signal Processing* 41.12 (1993), pp. 3397–3415.

[57] Joel A. Tropp and Anna C. Gilbert. “Signal Recovery From Random Measurements Via Orthogonal Matching Pursuit”. In: *IEEE Transactions on Information Theory* 53.12 (2007), pp. 4655–4666.

[58] I.F. Gorodnitsky and B.D. Rao. “Sparse signal reconstruction from limited data using FOCUSS: a re-weighted minimum norm algorithm”. In: *IEEE Transactions on Signal Processing* 45.3 (1997), pp. 600–616.

[59] Scott Shaobing Chen, David L. Donoho, and Michael A. Saunders. “Atomic Decomposition by Basis Pursuit”. In: *SIAM Journal on Scientific Computing* 20.1 (1998), pp. 33–61.

[60] R. Tibshirani. “Regression Shrinkage and Selection via the Lasso”. In: *Journal of the Royal Statistical Society (Series B)* 58 (1996), pp. 267–288.

[61] D Malioutov, M Cetin, and A.S Willsky. “A sparse signal reconstruction perspective for source localization with sensor arrays”. eng. In: *IEEE transactions on signal processing* 53.8 (2005), pp. 3010–3022.

[62] Erik G. Larsson and Yngve Selen. “Linear Regression With a Sparse Parameter Vector”. In: *IEEE Transactions on Signal Processing* 55.2 (2007), pp. 451–460.

[63] Peter Gerstoft et al. “Multisnapshot Sparse Bayesian Learning for DOA”. In: *IEEE Signal Processing Letters* 23.10 (2016), pp. 1469–1473.

[64] Christoph F. Mecklenbriiuker, Peter Gerstoft, and Geert Leus. “Sparse Bayesian Learning for DOA Estimation of Correlated Sources”. In: *2018 IEEE 10th Sensor Array and Multichannel Signal Processing Workshop (SAM)*. 2018, pp. 533–537.

[65] Zeng Fan et al. “Convolution of Barker and Golay Codes for Low Voltage Ultrasonic Testing”. In: *Technologies* 7.4 (2019), p. 72.

[66] Yanis Mehdi Benane et al. “An enhanced chirp modulated Golay code for ultrasound diverging wave compounding”. In: *2018 26th European Signal Processing Conference (EUSIPCO)*. IEEE. 2018, pp. 81–85.

[67] Emelina P. Vienneau and Brett C. Byram. “A coded excitation framework for increased signal-to-noise ratio of in vivo ultrasound power Doppler imaging”. In: *Proceedings Volume 11602, Medical Imaging 2021: Ultrasonic Imaging and Tomography; 116020P (2021)* ().

[68] Richard Y Chiao and Xiaohui Hao. “Coded excitation for diagnostic ultrasound: A system developer’s perspective”. In: *IEEE transactions on ultrasonics, ferroelectrics, and frequency control* 52.2 (2005), pp. 160–170.

[69] Ihor Trots. “Mutually orthogonal Golay complementary sequences in synthetic aperture imaging systems”. In: *Archives of Acoustics* 40.2 (2015), pp. 283–289.

[70] Cynthia Peterson Ammar Hindi and Richard G Barr. “Artifacts in diagnostic ultrasound”. In: *Reports in Medical Imaging* 6 (2013), pp. 29–48.

[71] Frederick W Kremkau and KJ Taylor. “Artifacts in ultrasound imaging.” In: *Journal of ultrasound in medicine* 5.4 (1986), pp. 227–237.

[72] Marie Ploquin, Adrian Basarab, and Denis Kouamé. “Resolution enhancement in medical ultrasound imaging”. In: *Journal of Medical Imaging* 2.1 (2015), pp. 017001–017001.

[73] Abdulrahman M. Alanazi et al. “Model-Based Reconstruction for Multi-Frequency Collimated Beam Ultrasound Systems”. In: *IEEE Transactions on Computational Imaging* 9 (2023), pp. 904–916.

[74] Pieter Kruizinga et al. “Plane-wave ultrasound beamforming using a nonuniform fast fourier transform”. In: *IEEE Transactions on Ultrasonics, Ferroelectrics, and Frequency Control* 59.12 (2012), pp. 2684–2691.

[75] Rakesh K. Jain. “Normalization of Tumor Vasculature: An Emerging Concept in Antiangiogenic Therapy”. In: *Science* 307.5706 (2005), pp. 58–62.

[76] Yonina C. Eldar. *Sampling Theory: Beyond Bandlimited Systems*. Cambridge University Press, 2015.

[77] Michael Elad. *Sparse and Redundant Representations: From Theory to Applications in Signal and Image Processing*. 1st. Springer Publishing Company, Incorporated, 2010. ISBN: 144197010X.

[78] R. Baraniuk and P. Steeghs. “Compressive Radar Imaging”. In: *2007 IEEE Radar Conference*. 2007, pp. 128–133.

[79] Michael Lustig, David Donoho, and John M. Pauly. “Sparse MRI: The application of compressed sensing for rapid MR imaging”. In: *Magnetic Resonance in Medicine* 58.6 (2007), pp. 1182–1195.

[80] E. J. Candes, J. Romberg, and T. Tao. “Robust Uncertainty Principles: Exact Signal Reconstruction from Highly Incomplete Frequency Information”. In: *IEEE Trans. Inf. Theor.* 52.2 (Feb. 2006), pp. 489–509.

[81] J. Yang et al. “Multiple-Measurement Vector model and its application to Through-the-Wall Radar Imaging”. In: *2011 IEEE International Conference on Acoustics, Speech and Signal Processing (ICASSP)*. 2011, pp. 2672–2675.

[82] A. Rakotomamonjy. “Surveying and comparing simultaneous sparse approximation (or group-lasso) algorithms”. In: *Signal Processing* 91.7 (2011), pp. 1505–1526.

[83] Christoph Dalitz, Regina Pohle-Fröhlich, and Thorsten Michalk. “Point spread functions and deconvolution of ultrasonic images”. In: *IEEE transactions on ultrasonics, ferroelectrics, and frequency control* 62 (Mar. 2015), pp. 531–544.

[84] Ho-Chul Shin et al. “Sensitivity to point-spread function parameters in medical ultrasound image deconvolution”. In: *Ultrasonics* 49.3 (Mar. 2009), pp. 344–357.

[85] J. Baranger et al. “Adaptive Spatiotemporal SVD Clutter Filtering for Ultrafast Doppler Imaging Using Similarity of Spatial Singular Vectors”. In: *IEEE Transactions on Medical Imaging* 37.7 (2018), pp. 1574–1586.

[86] Shaoguang Huang, Hongyan Zhang, and Aleksandra Pižurica. “Joint sparsity based sparse subspace clustering for hyperspectral images”. In: *IEEE Conference on International Conference on Image Processing (ICIP)*. Athens, Greece, Oct. 2018, pp. 3878–3882. ISBN: 978-1-4799-7061-2.

[87] Amir Beck and Marc Teboulle. “A Fast Iterative Shrinkage-Thresholding Algorithm for Linear Inverse Problems”. In: *SIAM Journal on Imaging Sciences* 2.1 (2009), pp. 183–202.

[88] Rafal Zdunek and Andrzej Cichocki. “Improved M-FOCUSS Algorithm With Overlapping Blocks for Locally Smooth Sparse Signals”. In: *IEEE Trans. Signal Process.* 56.10-1 (2008), pp. 4752–4761.

[89] Jian A. Zhang et al. “Multiple-measurement vector based implementation for single-measurement vector sparse Bayesian learning with reduced complexity”. In: *Signal Processing* 118 (2016), pp. 153–158.

[90] H. Duan et al. “Fast Inverse-Free Sparse Bayesian Learning via Relaxed Evidence Lower Bound Maximization”. In: *IEEE Signal Processing Letters* 24.6 (2017), pp. 774–778.

[91] Stephen Boyd et al. “Distributed Optimization and Statistical Learning via the Alternating Direction Method of Multipliers”. In: *Found. Trends Mach. Learn.* 3.1 (Jan. 2011), pp. 1–122.

[92] Alexandre Gramfort, Matthieu Kowalski, and Matti Hämäläinen. “Mixed-norm estimates for the M/EEG inverse problem using accelerated gradient methods”. In: *Physics in Medicine and Biology* 57.7 (Mar. 2012), pp. 1937–1961.

[93] Bradley E. Treeby and Benjamin T. Cox. “k-Wave: MATLAB toolbox for the simulation and reconstruction of photoacoustic wave fields”. In: *Journal of Biomedical Optics* 15.2 (2010), pp. 1–12.

[94] Tanya Chernyakova and Yonina Eldar. “Fourier Domain Beamforming: The Path to Compressed Ultrasound Imaging”. In: *Ultrasonics, Ferroelectrics, and Frequency Control, IEEE Transactions on* 61 (July 2013).

[95] Fabio Procopio et al. “Anatomical liver resection using the ultrasound-guided compression technique in minimal access surgery”. In: *Surgical Endoscopy* 38.1 (2024), pp. 193–201.

[96] Didem Dogan and Figen S. Oktem. “Convolutional Inverse Problems in Imaging with Convolutional Sparse Models”. In: *Imaging and Applied Optics 2019 (COSI, IS, MATH, pcAOP)*. Optica Publishing Group, 2019, JW2A.9.

[97] Didem Dogan and Figen S. Oktem. “Model-based Inversion Methods for Compressive Spectral Imaging with Diffractive Lenses”. In: *Imaging and Applied Optics Congress*. Optica Publishing Group, 2020, CW4B.4.

[98] D.P. Wipf and B.D. Rao. “Sparse Bayesian learning for basis selection”. In: *IEEE Transactions on Signal Processing* 52.8 (2004), pp. 2153–2164.

[99] Pim van der Meulen et al. “Impulse response estimation method for ultrasound arrays”. In: *2017 IEEE International Ultrasonics Symposium (IUS)*. 2017, pp. 1–4.

[100] Huiping Huang, Michael Faußß, and Abdelhak M. Zoubir. “Block Sparsity-Based DOA Estimation with Sensor Gain and Phase Uncertainties”. In: *2019 27th European Signal Processing Conference (EUSIPCO)*. 2019, pp. 1–5.

[101] A. Jaffer. “Maximum likelihood direction finding of stochastic sources: a separable solution”. In: *ICASSP-88., International Conference on Acoustics, Speech, and Signal Processing*. Los Alamitos, CA, USA: IEEE Computer Society, Apr. 1988, pp. 2893, 2894, 2895, 2896.

[102] Richard G. Baraniuk et al. “Model-Based Compressive Sensing”. In: *IEEE Transactions on Information Theory* 56.4 (2010), pp. 1982–2001.

[103] Yonina C. Eldar, Patrick Kuppinger, and Helmut Bolcskei. “Block-Sparse Signals: Uncertainty Relations and Efficient Recovery”. In: *IEEE Transactions on Signal Processing* 58.6 (2010), pp. 3042–3054.

[104] Xiaolei Lv, Guoan Bi, and Chunru Wan. “The Group Lasso for Stable Recovery of Block-Sparse Signal Representations”. In: *IEEE Transactions on Signal Processing* 59.4 (2011), pp. 1371–1382.

[105] Ewout van den Berg and Michael P. Friedlander. “Probing the Pareto Frontier for Basis Pursuit Solutions”. In: *SIAM Journal on Scientific Computing* 31.2 (2009), pp. 890–912.

[106] Yonina C. Eldar and Moshe Mishali. “Robust Recovery of Signals From a Structured Union of Subspaces”. In: *IEEE Transactions on Information Theory* 55.11 (2009), pp. 5302–5316.

[107] Zhilin Zhang and Bhaskar D. Rao. “Sparse Signal Recovery With Temporally Correlated Source Vectors Using Sparse Bayesian Learning”. In: *IEEE Journal of Selected Topics in Signal Processing* 5.5 (2011), pp. 912–926.

[108] Lei Yu et al. “Bayesian Compressive Sensing for clustered sparse signals”. In: *2011 IEEE International Conference on Acoustics, Speech and Signal Processing (ICASSP)*. 2011, pp. 3948–3951.

[109] Angélique Dremeau, Cédric Herzet, and Laurent Daudet. “Boltzmann Machine and Mean-Field Approximation for Structured Sparse Decompositions”. In: *IEEE Transactions on Signal Processing* 60.7 (2012), pp. 3425–3438.

[110] Christophe Andrieu et al. “An Introduction to MCMC for Machine Learning”. In: *Machine Learning* 50.1–2 (2003), pp. 5–43.

[111] Aditya Sant, Markus Leinonen, and Bhaskar D. Rao. “Block-Sparse Signal Recovery via General Total Variation Regularized Sparse Bayesian Learning”. In: *IEEE Transactions on Signal Processing* 70 (2022), pp. 1056–1071.

[112] Jisheng Dai, An Liu, and Hing Cheung So. “Non-Uniform Burst-Sparsity Learning for Massive MIMO Channel Estimation”. In: *IEEE Transactions on Signal Processing* 67.4 (2019), pp. 1075–1087.

[113] Anupama Rajoriya, Alok Kumar, and Rohit Budhiraja. “Covariance-Free Variational Bayesian Learning for Correlated Block Sparse Signals”. In: *IEEE Communications Letters* 27.3 (2023), pp. 966–970.

[114] Rupam Kalyan Chakraborty, Geethu Joseph, and Chandra R. Murthy. *Joint State and Input Estimation for Linear Dynamical Systems with Sparse Control*. 2023.

[115] Gérard Meurant. “A Review on the Inverse of Symmetric Tridiagonal and Block Tridiagonal Matrices”. In: *SIAM Journal on Matrix Analysis and Applications* 13.3 (1992), pp. 707–728.

[116] Shun-ichi Amari. “Backpropagation and stochastic gradient descent method”. In: *Neurocomputing* 5.4 (1993), pp. 185–196.

[117] Milica Andelic and Carlos da Fonseca. “Sufficient conditions for positive definiteness of tridiagonal matrices revisited”. In: *Positivity* 15 (Mar. 2011).

[118] Radford M. Neal and Geoffrey E. Hinton. “A View of the EM Algorithm that Justifies Incremental, Sparse, and other Variants”. In: *Learning in Graphical Models*. Ed. by Michael I. Jordan. Dordrecht: Springer Netherlands, 1998, pp. 355–368.

[119] Daniel J Tylavsky and Guy RL Sohie. “Generalization of the matrix inversion lemma”. In: *Proceedings of the IEEE* 74.7 (1986), pp. 1050–1052.

[120] Huiping Duan et al. “Fast Inverse-Free Sparse Bayesian Learning via Relaxed Evidence Lower Bound Maximization”. In: *IEEE Signal Processing Letters* 24.6 (2017), pp. 774–778.

[121] Alexander Lin et al. “Covariance-Free Sparse Bayesian Learning”. In: *IEEE Transactions on Signal Processing* 70 (2022), pp. 3818–3831.

[122] Rune Aaslid, Thomas-Marc Markwalder, and Helge Nornes. “Noninvasive transcranial Doppler ultrasound recording of flow velocity in basal cerebral arteries”. In: *Journal of neurosurgery* 57.6 (1982), pp. 769–774.

[123] Spyretta Golemati, Aimilia Gastounioti, and Konstantina S. Nikita. “Toward Novel Noninvasive and Low-Cost Markers for Predicting Strokes in Asymptomatic Carotid Atherosclerosis: The Role of Ultrasound Image Analysis”. In: *IEEE Transactions on Biomedical Engineering* 60.3 (2013), pp. 652–658.

[124] Jeremy Bercoff et al. “Ultrafast compound Doppler imaging: Providing full blood flow characterization”. In: *IEEE transactions on ultrasonics, ferroelectrics, and frequency control* 58.1 (2011), pp. 134–147.

[125] Emilie Mace et al. “Functional ultrasound imaging of the brain: theory and basic principles”. In: *IEEE Transactions on Ultrasonics, Ferroelectrics, and Frequency Control* 60.3 (2013), pp. 492–506.

[126] Giulia Matrone et al. “High Frame-Rate, High Resolution Ultrasound Imaging With Multi-Line Transmission and Filtered-Delay Multiply And Sum Beamforming”. In: *IEEE Transactions on Medical Imaging* 36.2 (2017), pp. 478–486.

[127] Jianwen Luo, Ronny X. Li, and Elisa E. Konofagou. “Pulse wave imaging of the human carotid artery: an in vivo feasibility study”. In: *IEEE Transactions on Ultrasonics, Ferroelectrics, and Frequency Control* 59.1 (2012), pp. 174–181.

[128] Elisabetta Sassaroli et al. “Image quality evaluation of ultrasound imaging systems: advanced B-modes”. In: *Journal of Applied Clinical Medical Physics* 20.3 (2019), pp. 115–124.

[129] Jayaraj U Kidav et al. “A broadband MVDR beamforming core for ultrasound imaging”. In: *Integration* 81 (2021), pp. 221–233.

[130] Michael A. Saunders Christopher C. Paige. “LSQR: An Algorithm for Sparse Linear Equations and Sparse Least Squares”. In: *ACM Transactions on Mathematical Software* 8.1 (1982), pp. 43–71.

[131] Ben Luijten et al. “Adaptive Ultrasound Beamforming Using Deep Learning”. In: *IEEE Transactions on Medical Imaging* 39.12 (2020), pp. 3967–3978.

[132] Ying Liu et al. “Super-Resolution Ultrasound Imaging by Sparse Bayesian Learning Method”. In: *IEEE Access* 7 (2019), pp. 47197–47205.

[133] Avinoam Bar-Zion et al. “SUSHI: Sparsity-Based Ultrasound Super-Resolution Hemodynamic Imaging”. In: *IEEE Transactions on Ultrasonics, Ferroelectrics, and Frequency Control* 65.12 (2018), pp. 2365–2380.

[134] Emelina P. Vienneau and Brett C. Byram. “A Coded Excitation Framework for High SNR Transcranial Ultrasound Imaging”. In: *IEEE Transactions on Medical Imaging* 42.10 (2023), pp. 2886–2898.

[135] A Nowicki, J Tasinkiewicz, and I Trots. “Flow imaging using differential Golay encoded ultrasound”. In: *Ultrasonics* 126 (2022), p. 106825.

[136] Changhan Yoon et al. “An efficient pulse compression method of chirp-coded excitation in medical ultrasound imaging”. In: *IEEE Transactions on Ultrasonics, Ferroelectrics, and Frequency Control* 60.10 (2013), pp. 2225–2229.

[137] Vera Behar and Dan Adam. “Parameter optimization of pulse compression in ultrasound imaging systems with coded excitation”. In: *Ultrasonics* 42.10 (2004), pp. 1101–1109.

[138] Mohamed Tamraoui, Herve Liebgott, and Emmanuel Roux. “Complete complementary coded excitation scheme for SNR improvement of 2D sparse array ultrasound imaging”. In: *IEEE Transactions on Biomedical Engineering* 71.3 (2023), pp. 1043–1055.

[139] Chang-Hong Hu et al. “Coded excitation using biphase-coded pulse with mismatched filters for high-frequency ultrasound imaging”. In: *Ultrasonics* 44.3 (2006), pp. 330–336.

[140] Kie B. Eom. “Speckle Reduction in Ultrasound Images Using Nonisotropic Adaptive Filtering”. In: *Ultrasound in Medicine & Biology* 37.10 (2011), pp. 1677–1688.

[141] Emanuele Grossi et al. “Robust waveform design for MIMO radars”. In: *2010 IEEE International Symposium on Information Theory*. 2010, pp. 1633–1637.

[142] Huaping Xu et al. “High-Resolution Radar Waveform Design Based on Target Information Maximization”. In: *IEEE Transactions on Aerospace and Electronic Systems* 56.5 (2020), pp. 3577–3587.

[143] Jian Li et al. “Range Compression and Waveform Optimization for MIMO Radar: A CramÉr–Rao Bound Based Study”. In: *IEEE Transactions on Signal Processing* 56.1 (2008), pp. 218–232.

[144] Stephen Boyd and Lieven Vandenberghe. “Semidefinite programming relaxations of non-convex problems in control and combinatorial optimization”. In: *Communications, Computation, Control, and Signal Processing: a tribute to Thomas Kailath* (1997), pp. 279–287.

[145] Jacob T Fokkema and Peter M van den Berg. *Seismic applications of acoustic reciprocity*. Elsevier, 1993.

[146] Mark A Richards et al. *Principles of modern radar*. Citeseer, 2010.

[147] Adrien Saumard and Jon A Wellner. "Log-concavity and strong log-concavity: a review". In: *Statistics surveys* 8 (2014), p. 45.

[148] Jean Gallier et al. "The Schur complement and symmetric positive semidefinite (and definite) matrices". In: *Penn Engineering* (2010), pp. 1–12.

[149] Zhi-Quan Luo et al. "Semidefinite relaxation of quadratic optimization problems". In: *IEEE Signal Processing Magazine* 27.3 (2010), pp. 20–34.

[150] Eric Feron. "Nonconvex quadratic programming, semidefinite relaxations and randomization algorithms in information and decision systems". In: *System Theory: Modeling, Analysis and Control* (2000), pp. 255–274.

[151] Michael Grant, Stephen Boyd, and Yinyu Ye. *CVX: Matlab software for disciplined convex programming*. 2009.

[152] Dimitri P Bertsekas. *Constrained optimization and Lagrange multiplier methods*. Academic press, 2014.

[153] Bradley E Treeby and Benjamin T Cox. "k-Wave: MATLAB toolbox for the simulation and reconstruction of photoacoustic wave fields". In: *Journal of biomedical optics* 15.2 (2010), pp. 021314–021314.

[154] Jack Levy et al. "High-frequency ultrasound in clinical dermatology: A review". In: *The Ultrasound Journal* 13 (2021), pp. 1–12.

[155] Nick Bottenus, Jacob Spainhour, and Stephen Becker. "Comparison of spatial encodings for ultrasound imaging". In: *IEEE Transactions on Ultrasonics, Ferroelectrics, and Frequency Control* 70.1 (2022), pp. 52–63.

[156] Mahdi Bayat and Mostafa Fatemi. "Concurrent Clutter and Noise Suppression via Low Rank Plus Sparse Optimization for Non-Contrast Ultrasound Flow Doppler Processing in Microvasculature". In: *2018 IEEE International Conference on Acoustics, Speech and Signal Processing (ICASSP)*. 2018, pp. 1080–1084.

[157] Sam Ehrenstein et al. "Rank-Assisted Deep Residual Reconstruction Network for Non-Contrast Ultrasound Imaging of Blood Microvessels". In: *2021 IEEE International Ultrasonics Symposium (IUS)*. 2021, pp. 1–4.

GLOSSARY

NOTATION

SETS

$\mathbb{N}$	Natural numbers.
$\mathbb{N}_+$	Positive natural numbers.
$\mathbb{Z}$	Integer numbers.
$\mathbb{R}$	Real numbers.
$\mathbb{R}_+$	Nonnegative real numbers.
$\mathbb{R}^N$	Real length-N vectors.
$\mathbb{R}^{M\times N}$	Real $M \times N$ matrices.
$\mathbb{C}$	Complex numbers.
$\mathbb{C}^N$	Complex length-N vectors.
$\mathbb{C}^{M\times N}$	Complex $M \times N$ matrices.

VECTORS AND MATRICES

x, X	Plain lowercase and uppercase letters denote scalar.
$\mathbf{x}$	Lowercase boldface letters denote vectors.
$\mathbf{X}$	Uppercase boldface letters denote matrices.
$\mathbf{X}^\mathsf{T}$	Transpose of matrix $\mathbf{X}$.
$\mathbf{X}^*$	Complex conjugate of the elements in matrix $\mathbf{X}$.
$\mathbf{X}^\mathsf{H}$	Complex conjugate transpose, i.e., Hermitian, of matrix $\mathbf{X}$.
$\mathrm{diag}(\mathbf{x})$	Diagonal matrix with entries on the main diagonal collected in $\mathbf{x}$.
$\mathbf{0}_N$	$N \times 1$ vector of all ones.
$\mathbf{0}_{N,M}$	$N \times M$ matrix of all zeros.
$\mathbf{I}_N$	$N \times N$ matrix of all ones.
$\mathrm{trace}(\mathbf{X})$	Trace of matrix $\mathbf{X}$.
$\mathbf{X}^{-1}$	Inverse of matrix $\mathbf{X}$.
$\mathbf{X}^\dagger := (\mathbf{X}^H\mathbf{X})^{-1}\mathbf{X}^H$	Pseudo inverse (or the left-inverse) of a full-column rank tall matrix $\mathbf{X}$.
$\mathbf{X} \succcurlyeq \mathbf{Y}$	$\mathbf{X}-\mathbf{Y}$ is a positive semidefinite matrix.
$\mathbf{X} \odot \mathbf{Y}$	Hadamard product of matrix $\mathbf{X}$ and matrix $\mathbf{Y}$.
$\mathbf{X} \otimes \mathbf{Y}$	Kronecker product of matrix $\mathbf{X}$ and matrix $\mathbf{Y}$.
$\mathbf{X} \circ \mathbf{Y}$	Khatri-Rao product of matrix $\mathbf{X}$ and matrix $\mathbf{Y}$.

$\text{vec}(\mathbf{X})$	$MN \times 1$ vector formed by stacking the columns of an $M \times N$ matrix $\mathbf{X}$.

NORMS

$\|\mathbf{x}\|_0$	ℓ_0-(quasi) norm, i.e., number on non-zero entries of vector $\mathbf{x}$.
$\|\mathbf{x}\|_1$	ℓ_1-norm of vector $\mathbf{x}$.
$\|\mathbf{x}\|_2$	Euclidean (or ℓ_2-)norm of vector $\mathbf{x}$.
$\|\mathbf{X}\|_{2,1} := \sum_{i=1}^{N} \|\mathbf{x}_i\|_2$	$\ell_{2,1}$ norm of matrix $\mathbf{X}$ that has columns $\mathbf{x}_i, i = 1, \ldots, N$.
$\|\mathbf{X}\|_F := \sqrt{\text{Tr}(\mathbf{X}\mathbf{X}^H)}$	Frobenious norm of matrix $\mathbf{X}$.
$\mathbf{X}$.	

STOCHASTIC PROCESSES

$E(\mathbf{x})$	Expected value of random vector $\mathbf{x}$.
$\mathcal{N}(\boldsymbol{\mu}, \boldsymbol{\Sigma})$	Gaussian distribution with mean vector $\boldsymbol{\mu}$ and covariance matrix $\boldsymbol{\Sigma}$.
$p(x; \boldsymbol{\theta})$	Probability density function of x parameterized by $\boldsymbol{\theta}$.

ABBREVIATIONS

LSQR	least squares QR
SNR	signal-to-noise ratio
CNR	contrast-to-noise ratio
PDI	power Doppler image
SBL	sparse Bayesian Learning

CURRICULUM VITÆ

DIDEM DOĞAN was born in Yozgat in Türkiye. She received her B.Sc. in Electrical and Electronics Engineering from Bilkent University in Ankara in 2017. Shortly after that, she followed her passion for signal processing and obtained her M.Sc. from Middle East Technical University (METU) in Ankara in 2020. She is interested in computational imaging and was particularly focused on spectral and solar imaging during her master's studies. She had long dreamt of pursuing a Ph.D., though she hesitated for a while between continuing in the USA or in Europe. In the end, she chose Europe, aiming for a healthier work-life balance. Luckily, a great Ph.D. position at TU Delft in ultrasound imaging popped up. She then joined the Signal Processing Systems (SPS) group of Delft University of Technology, and now she is wrapping up her Ph.D. adventure.

She has always been fascinated by the beauty of mathematics, the elegance of algorithms, and the hidden patterns in physics. She also loves coding, where ideas quickly turn into something real. In her research, she especially loves the idea of "making the invisible visible", whether it's finding hidden structures or creating images from waves that the eye can't normally see. This led her to computational imaging, where math, physics, and a bit of creativity all come together. She doesn't really see herself as a professor, but she hopes to stay a lifelong research scientist: always asking questions and finding new ways to uncover the unseen. Apart from research, she enjoys traveling, running, cycling, watching TV series, and cooking. She is also into philosophy, nature, photography, decoration, and fashion. The photo on the right is evidence that she is happiest when she is traveling in nature.